POLYGENERATION PLANT BASED ON INTEGRATING BIOMASS GASIFIER AND ALKALINE ELECTROLYZER FOR DISTRICT ENERGY NETWORKS

Jimmy Barco Burgos

UNIVERSITAT ROVIRA i VIRGILI

Polygeneration plant based on integrating biomass gasifier and alkaline electrolyzer for district energy networks

Jimmy Barco Burgos

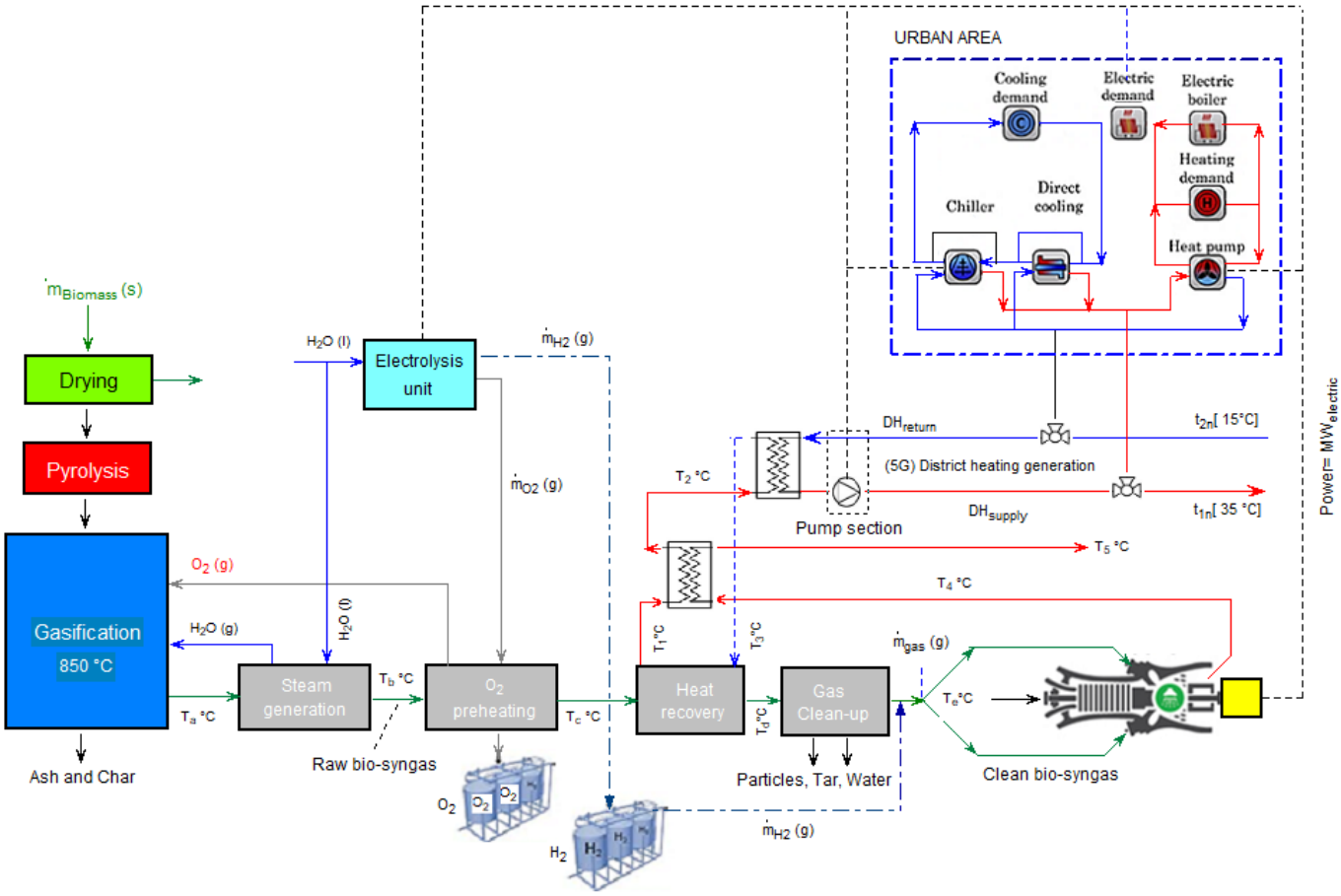

DOCTORAL THESIS
2022

Polygeneration plant based on integrating biomass gasifier and alkaline electrolyzer for district energy networks

Jimmy Barco Burgos

DOCTORAL THESIS

Supervised by
Dr. Joan Carles Bruno

Fluid Thermodynamics Engineering
Research Group of Applied Thermal Engineering

UNIVERSITAT
ROVIRA i VIRGILI

Department of Mechanical Engineering
2022

(Acknowledgements)

¡¡Si lo crees, se crea!!

Con este documento se cierra uno de los capítulos más importantes, el sueño académico de ser doctor en ingeniería. Dedicado a mis padres, en especial a José Barco Ahumedo quien partió antes de lo esperado. A mi hija Paulina Barco y a mi mejor amigo Jhosimar Fuentes quienes me motivaron y apoyaron en la transición a nuevas tierras. Asimismo, dedicado a tí quien me retó a soltar e ir por mis sueños.

“Hold my beer and watch this!”

UNIVERSITAT ROVIRA i VIRGILI

Department of Mechanical Engineering
Av. Paisos Catalans, 26
43007 Tarragona, Spain

I STATE that the present study entitled "**Polygeneration plant based on integrating biomass gasifier and alkaline electrolyzer for district energy networks**," presented by Jimmy Barco Burgos for the award of the degree of doctor, has been carried out under my supervision at the Department of Mechanical Engineering of this University in the framework of the PhD program on Fluid Thermodynamics Engineering.

Tarragona, June 27th, 2022

Doctoral Thesis Supervisor

Dr. Joan Carles Bruno Argilaguet

SUMMARY

Polygeneration systems allow to produce four or more useful commodities by using one or multiple input energy resources, increasing energy efficiency and conserving natural resources. Despite increasing system complexity, properly designed polygeneration enhances energy efficiency, reduces emissions, and wastes and increases economic benefit. In this way, polygeneration systems minimize carbon footprint, contribute to solve the problem of fossil resource scarcity and increase energy efficiency compared to separately operated units. Likewise, decentralized polygeneration in remote areas also increases energy access to energy in rural areas. For waste-based systems, polygeneration with carbon capture and utilization is not only beneficial from an environmental perspective but also offers an opportunity for net-negative emissions.

Although many polygeneration systems have been proposed and studied it was seen that there is no detailed information on a new promising configuration integrating organic waste gasification and water electrolysis systems. Therefore, for this configuration it is necessary to improve its modeling and design, operation modes and strategies and optimize the performance of its main system components gasifier and electrolyzer gathering experimental data. This PhD thesis investigates this proposed polygeneration concept able to produce power, heat and store electricity as biofuels based on an integrated gasifier/electrolyzer system connected to a low-temperature district energy network and using heat pumps for the effective delivery of the produced energy in a very efficient and flexible way. A case study is performed to obtain the benefit of the electrolyzer integration comparing to options: 1) In the first one, no electrolyzer is used and the gasifier operates with air or steam as the gasifying agent. The resulting product gas is fed to heat recovery units, later to a clean-up section and finally to a gas turbine connected with the District energy network; 2) the second one, the system is operated with the same gasifier but integrated with electrolysis units. The electrolyzer converts electricity and water into H_2 and O_2, providing O_2 as gasifying agent. At the same time, H_2 is directly sent to the syngas stream to improve the heating value of the syngas generated, producing a N_2-free gas suited for biofuel synthesis, power, heating, and cooling production. These two options or operation modes are connected with district energy networks to distribute power and heat to nearby locations.

This doctoral thesis aims to study the mentioned polygeneration concept based on biomass gasification integrated with an electrolyzer to maximize the hydrogen content of the syngas. The use of steam is one of the routes to improve the content

in hydrogen in the syngas and the application of alkaline electrolysis will reduce the cost and hence the application feasibility of this system for medium to large scale capacities. That is why the experimental part of this thesis has been oriented to deeply study the use of steam as biomass gasification agent and also the alkaline electrolyzer process. The complete integration of both systems is investigated in a realistic case study.

The methodology to perform the mentioned investigation is focused in performing an experimental study of some aspects of gasification and electrolysis processes to complement and provide the required information for the modeling and simulation of the complete system as a preliminary assessment of its viability. First it is developed a general thermodynamic modelling approach of the different units of the polygeneration system paying special attention to the complex gasification process for which a dedicated rigorous but straightforward gasification model is done using the Engineering Equation Solver (EES) software. The experimental investigation consists of two parts: First, it is studied a steam gasification plant using palm kernel shells (PKS) for hydrogen-rich N_2-free syngas production in a pilot-scale atmospheric downdraft allothermal gasifier; and secondly, an experimental characterization of an alkaline electrolysis cell for hydrogen production at atmospheric pressure is performed to obtain enough understanding and data to feed the developed theoretical models. Additionally, is carried out a review and analysis of different District Energy Networks (DEN) and the integration of high-temperature commercial heat pumps to efficiently deliver power and heating to buildings and small industries. Likewise, to describe placement options and connection modes of a heat pump unit in DEN networks. Finally, implement the proposed polygeneration system configuration integrated in a very low-temperature district energy networks using real data from a neighborhood in Montreal (Canada) known as Lachine Est.

This thesis is organized and presented in eight chapters. Chapter 1 provides the planned objectives and methodology of this PhD thesis along with the background information on polygeneration systems based on the integration of biomass gasification and renewable-driven water electrolysis systems to produce hydrogen and other energy commodities. Chapter 2 proposes a general modelling approach to analyze the polygeneration system connected with a very low-temperature district energy network. The specific details of the gasification model for designing and simulating a biomass gasification plant using the equation solver program Engineering Equation Solver (EES) are presented separately in Chapter 3. The experimental parameters required for the accurate modeling of the biomass plant

are obtained using an experimental investigation of the steam gasification of palm kernel shells (PKS) for hydrogen-rich N_2- free syngas production in a pilot-scale atmospheric downdraft allothermal gasifier (Chapter 4). The electrolyzer, the second main component of the system, is experimentally studied in Chapter 5. In this chapter is presented the design and thermal characterization of an alkaline electrolysis cell for hydrogen generation at atmospheric pressure to get the operation data for its modelling. The purpose is to analyze the electrolyzer unit and how its integration affects the consumption of syngas and biomass using the production of the oxygen for the gasification process. Chapter 6 reviews the integration of electrical heat pumps into DEN (District Energy Networks) and how it could be an innovative and profitable solution for decarbonizing buildings and small industries using green electricity. Finally, in chapter 7, all previously developed models (gasifier, electrolyzer, and DEN) and the gathered experimental data (gas compositions, efficiencies, and power consumption) are considered to analyze a polygeneration system serving a low-temperature district energy network in the neighborhood of Lachine Est in Montreal, Canada. Finally, Chapter 8 provides the conclusions and the perspective for further work.

The gasification model developed in this thesis was a revised version of a previous biomass gasification plant model using the equation solver program Engineering Equation Solver (EES) including some modifications for adaptation to real processes, in which only a partial approach to chemical equilibrium is achieved. The model developed, which has been validated with, provides the opportunity to evaluate different variations in biomass fuel and operating conditions. A variation of less than 10% was obtained when validating the results with own and other authors' experimental data. The model has been used to evaluate the influence of temperature and the type of oxidizing agent in the syngas' hydrogen production and the Lower heating value (LHV). Comparing the three considered oxidizing agents, steam showed a higher capacity to generate hydrogen than air + steam and air, by 52% and 63%, respectively. Likewise, a higher capacity to generate syngas with superior LHV, than air + steam and air, by 44 % and 51%, respectively.

Another contribution of this thesis has been the experimental investigation of the steam gasification of palm kernel shells (PKS) for hydrogen-rich N_2-free syngas production in a pilot-scale atmospheric downdraft allothermal gasifier (Chapter 4) in order to explore a potential route to generate syngas with a high content of hydrogen. Likewise, the experimental study provides the key parameters (temperature profiles, pressure, and gas residence times) that allows to improve the definition and selection of the equilibrium constants that allow to improve the

prediction capacity of the mathematical model with a deviation of less than 10%. The feedstock material characterization, description of the gasifier design, auxiliary systems, operating conditions, and evaluation of the operating methodology for obtaining fuel gas are presented. The gasification equipment was tested under gasification temperatures between $800 \text{ and } 950\ ℃$ and steam-biomass mass ratios between 0,2 and 1,2. The maximum H_2 generation is achieved with a gasification temperature of $850\ ℃$, steam/biomass ratio of $0{,}85$, particle sizes of 2 - 3 mm, and biomass feed of $57{,}1\ \text{kg/h}$. The volume fraction of $H_2 + CO$ can reach 80,4 %, and maximum cold gas efficiency of 80 % with an average lower calorific value of $11{,}5\ \text{MJ/Nm}^3$.

The design and thermal characterization of the alkaline electrolysis cell for hydrogen generation at atmospheric pressure is presented in chapter 5. The objective is to get a better understanding of a type of electrolyzer of low cost and able to meet the medium to large capacities required for the proposed polygeneration system. The experimental electrolytic cell was manufactured from acrylic, using 316 L stainless steel electrodes, and considering a membrane separation for gases. The effect of current conditions, the distance between electrodes on the production efficiency of hydrogen and the distribution and variation of temperatures on the surface of the electrodes in operation were evaluated. The measurement of temperature in electrodes allows for improving the selection of the faraday efficiency coefficients that are a function of the temperature to improve the prediction capacity of the model for the production of hydrogen and the general balance of energy (Energy consumption per flow of hydrogen and oxygen generated). Maximum hydrogen generation (0,026 Nm^3/h) was achieved with a separation between electrodes (anode and cathode) of 3 mm and a current of 30 A at 12 V. Furthermore, the thermoelectric effects on the electrodes were analyzed, and the presence of areas of higher activity was discussed for oxidation and reduction reactions.

Other important contribution is the integration of heat pumps into DEN (District Energy Networks) that provides significant environmental and performance improvements, an innovative and profitable solution for different decarbonizing sectors, alternative to the use of just boilers or heat recovery heat exchangers. Chapter 6 reviews different district energy networks and the integration of high-temperature commercial heat pumps. Likewise, it describes placement options and connection modes of a heat pump unit in DEN networks, identifying twelve (12) generic configurations of heat pumps and how they can be integrated into DEN systems, where four (4) of them have not been studied in the literature yet.

Finally, Chapter 7 studies the combination of biomass gasification and electrolyzer as a potential solution to reduce the emission problem and replace fossil fuels at the Lachine-Est area using the proposed plant concept. The gasification produces syngas and electricity from biomass, and at the same time provides heat for the heating demand. Specifically, a district network is proposed that uses all the heat available from the gasification process and turbine to feed a central pump that allows covering the entire demand of the Lachine est area in Canada. The electrolyzer converts water into chemical products (i.e., O_2 or H_2) with the help of electricity from the cogeneration system using syngas. A gas turbine cogeneration system is selected for this case study. In this scheme, biomass plays a key role as a CO_2 capture system as it grows by consuming CO_2 from the air. The overall efficiency ranges from about 44-88%, depending on the oxidizing agent and operating conditions used. Specifically, using only oxygen in the gasifier, 1428 kg/hr of synthesis gas (60,25 H_2 vol.%) with a calorific value of 37,02 MJ/kg is available to be used to operate the gas turbine and generate 6 MW_e of electrical power (2,2 MW_e to cover the power demand in the Lachine area and 3,8 MW_e to operate the electrolyzer). In this case, are consumed 1442 kg/hr of typical biomass considering an elemental composition of 48% C, 44% O, 6% H, 0,1% N, and 11% of moisture. The syngas composition and heating value can be adjusted by changing the flow rate of the gasifying agent. The flow rate of syngas strictly depends on the desired syngas properties (i.e., composition or heating value). In terms of chemical products, the production rate of CO or H_2 can be adjusted by changing the O_2 supplied by the electrolyzer.

While the proposed integration process is promising, there are several challenges to make this process more efficient. We believe that the improvement in the geometry of the gasifier, the performance of the electrolyzer and heat recovery exchanger system and the development of a CO_2 electrolyzer (using CO_2 available in the gasification system) will bring the proposed system to be more efficient in the future.

TABLE OF CONTENTS.

Nomenclature

Abbreviations and parameters

DEN	District energy network	LRT	Low refrigerant temperature
1G	First generation	HS	Heat sources
2G	Second generation	AHP	Absorption heat pump
3G	Third generation	CC	Compression chiller
4G	Fourth generation	C_HP_Ts_DHs	Central heat pump, Tsource low-grade heat and the DH supply used as a heat sink
5G	Fifth generation	L_HP_DHs_DHs	Local heat pump, DH supply line as heat source Sink to DH supply.
CHP	Combined heat and power	L_HP_DHr_DHs:	Local heat pump DH return line as a heat sourc Sink to DH supply
COSP	Coefficient of system performance	L_HP_DHs_DHs a	Local heat pump DH return line as a heat source Sink DH supply alternative.
COP	Coefficient of performance	I_HP_DHs_PH_DHW	Individual heat pump directly connected DH supply line as a heat source, heat sink connect to PH and DHW.
HP	Heat pump	I_HP_DHr_Tdemand	Individual heat pump directly connected DH return line as a heat source, Sink to Tdemand.
PtH	Power-to-Heat	I_HP_DHs_Tdemand	Individual heat pump directly connected DH supply line as a heat source, Sink to Tdemand.
DH	District heating	I_HP_Ts_DHs	Individual heat pump directly connected, Tsource low-grade heat, DH return line as a heat source, Sink to DH supply.
PV	Photovoltaic	I_HP_Ts_DHs-a	Individual heat pump directly connected Tsource low-grade heat as a heat source, Sink to DH supply alternative
SCOP	Seasonal coefficient of performance	I_HP_Ts_DHr	Individual heat pump directly connected Tsource low-grade heat as a heat source, Sink to DH return.
VHC	Volumetric heating capacity	I_HP_Ts_ DHr-a	Individual heat pump directly connected Tsource low-grade heat as a heat source Sink to DH return alternative
GHG	Greenhouse gas	I_HP_Ts_Tdemand	Individual heat pumps indirectly connected Tsource low-grade heat as a heat source Sink to Tdemand.
RES	Renewable energy sources	Tsink	Sink temperature
HX	Heat exchangers	Tsource	Source temperature
SH	Space heating	Tsupply	Supply temperature
DHW	Domestic hot water	Treturn	Return temperature
PH	Process heating	Tdemand	Demand temperature
HTHP	High-temperature heat pump		
VHTHl	Very high-temperature heat pump		
IHX	Internal heat exchanger		
HRT	High refrigerant temperature		

Chapter I INTRODUCTION, OBJECTIVES AND SCOPE

The world's energy systems are undergoing a radical transformation driven by the need to mitigate climate change. The development of an at-scale, clean hydrogen economy is a strategic priority for Canada, needed to diversify our future energy mix, generate economic benefits, and achieve net-zero emissions by 2050. Hydrogen is a technically viable energy vector for applications ranging from small-scale power supply in off-grid modes to large-scale chemical energy exports. However, with hydrogen being naturally unavailable in its pure form, it can be produced from renewable energy sources, biomass, waste, and wastewater using thermochemical (pyrolysis and gasification), electrochemical (water electrolysis) and biological (microbial electrolysis cells-MEC) processes. Important factors for a future hydrogen economy include storage (hydrogenation of carbon dioxide and others), distribution (pipelines, gas grid), and re-conversion concepts (fuel cells, turbines, and internal combustion engines)[1][2][3].

Canada has played a major role in the development of the growing global hydrogen economy, starting more than a century ago with innovation in hydrogen production technology and four decades ago as pioneers in fuel cell technology. Today Canada continues to be R&D and technology leaders in the hydrogen sector. From a systems perspective substantial change in energy distribution and storage infrastructure are required to handle the fluctuating production of renewables. In cities as the world's dominant energy consumers, hydrogen can become an essential clean energy carrier with the potential to link the buildings, mobility, industry, and waste sectors. Hydrogen is emerging as an alternative carrier of energy [4]. It can play a key role in the energy sector's decarbonization if produced by zero or low emissions sources in future cities [5]. Likewise, there is a strong need to identify reliable, affordable, abundant, and clean sources for H_2 production [6]. Also, the production of hydrogen using renewable resources plays a crucial role in the sustainable transformation of the energy and mobility systems because it is a multi-use energy carrier that can be used directly for clean mobility in fuel-cell vehicles, as a store for variable renewable energy sources, or as a starting point for the production of synthetic fuels [7][8].

Hydrogen can be made from widely available primary energy sources, including coal, natural gas, ammonia, methane, biomass, wind, water, and wastes [9]. Indeed, biomass can be transformed into solid, liquid, or gaseous fuels through physicochemical (extraction and transesterification), biochemical (alcoholic fermentation, anaerobic digestion, and aerobic digestion), and thermochemical

conversion processes (torrefaction, pyrolysis, gasification, and liquefaction)[10][11]. Despite the widespread use of biomass, this is not yet fully exploited and is awaiting improved conversion methods to produce solid, liquid, and gaseous energy for commercial purposes [11][12].The gasification process is one of the frontier technologies to convert biomass into energy, is commonly used to convert biomass into syngas (H_2, CO, CH_4, and CO_2), which can be used as to produce electricity, heat, cold, and chemical feedstock. In the short term, gasification has more significant commercial potential than other thermochemical processes (liquefaction, pyrolysis, and combustion), due to its greater flexibility in terms of energy application for power generation and raw materials for industrial chemicals, to its greater efficiency due to that it can be integrated into combined systems and to its potential for low environmental impact [13][14][15].

Water electrolysis (WE) powered by renewable sources is one of the options to produce hydrogen, which is generated by passing an electric current through a conductive substance (electrolyte) to conduct a non-spontaneous reaction. The reaction of interest is the decomposition of water into hydrogen and oxygen, which is endothermic and requires energy input to be carried out. WE offer several advantages over other production methods such as steam reforming, giving pure hydrogen (98 %) with no carbon emissions as there is no dependence on hydrocarbon sources. Also, it has the simplicity of small scale/real time supplies, utilization of renewable primary energy sources and pure oxygen as a by-product. The literature review revealed that the hydrogen production of low cost alkaline electrolyzer has not been fully explored under different operating environments [16][17]. Specifically, the challenges of reducing energy consumption, cost and maintenance persist. At the same time, an increase in reliability, durability, and safety is required by integrating renewable energy [16][18].

A fast replacement of fossil fuels by renewable resources is not possible, maintaining the present economic growth rate. During this transition, more efficient systems will help reduce CO_2 emissions for the same utility output (figure 1-1). The combination of technologies (gasifier-electrolyzer) can produce several outputs, for instance, heating, cooling, power, hydrogen, and oxygen together with a single power source (figure 1-1). Combined integrated systems have several advantages: (i) highly efficient plant processing, (ii) fewer thermal losses, (iii) diminished material residual, (iv) lower operating maintenance costs, and (v) low emissions. After cogeneration and trigeneration, polygeneration emerges as a sustainable solution with optimum resource utilization, better efficiency, and environmental friendliness using renewable resources (figure 1-2). Various

methods have been proposed to enhance syngas heating value by increasing the concentration of H_2 and CO. Co- gasification of biomass using coal [19] or plastic waste [20] are the most common methods to boost the H_2 concentration. However, these methods lead to worse CO_2 emissions due to the utilization of fossil fuel-based sources. Recently, the electrochemical routes (WE) start receiving attention to improve H_2 concentration. For instance, water electrolysis can provide the O_2 as the gasifying agent, while H_2 is directly sent to the syngas stream to improve the heating value of syngas generated. Another way to increase H_2 concentration is by removing inert species (i.e., CO_2) from the syngas stream and use it with water electrolysis for producing H_2 and O_2 to upgrade syngas composition and produce methane.

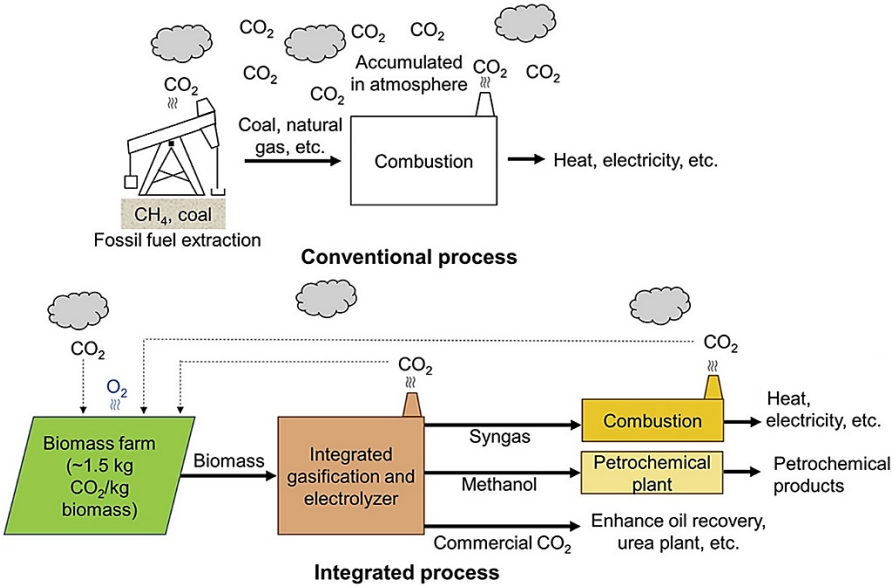

Figure 1-1: Comparison of CO_2 emissions for the conventional generation of heat and electricity (above) and the integrated gasification-electrolyzer (bottom) [21].

Polygeneration systems allow producing four or more useful commodities by using one or more input energy resources increasing energy efficiency and conserving natural resources [21][22]. Despite it increases system complexity, properly designed polygeneration enhances energy efficiency, reduces emission, waste, and increases the economic benefit [23]. There are several advantages to polygeneration. For example, gasification-electrolyzer-based polygenerations systems could be a good integrated technology to reduce carbon footprint, contribute to resolves the problem of fossil resource scarcity, and increases energy efficiency compared to separate production units [24]. Likewise, decentralized polygeneration in remote areas also increases energy access to rural people [25],

and for waste-based systems, polygeneration with carbon capture and utilization is beneficial from environmental and economic viewpoints [26].

Figure 1-2 shows the classification of generation systems. Specifically, in a power plant, electricity is produced from fuel energy. At the same time, effluents are rejected to the environment in form of flue gas, hot wastewater, etc. Similarly, electricity and utility heat are produced in cogeneration plants. When three outputs are produced from a single plant, it is called a trigeneration plant. These outputs are electricity, cooling, and heating. When multiple utilities are produced in a single plant from one or multiple resources, that plant is called a multi-generation or polygeneration plant. Apart from energy services, chemicals may be outputs of polygeneration [25]. As polygeneration is a combination of multiple processes, the design of polygeneration is important and it varies widely [27]. Polygeneration delivers multiple outputs by using single or multiple inputs. Hence, its performance assessment is also very crucial. This performance may be measured by different types of metrics and its sustainability assessment is critical from multi-dimensional aspects.

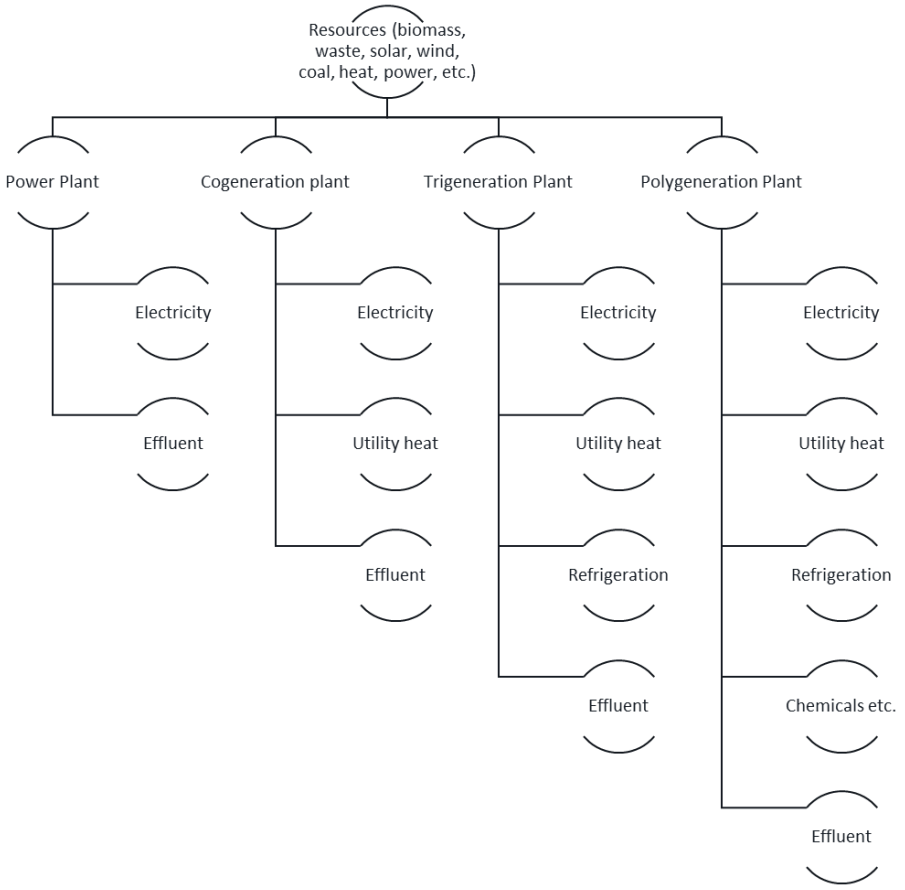

Figure 1-2: Classification of generation systems

The studies on polygeneration systems can classify into theoretical, experimental (lab scale), and pilot plant studies. From the literature review, most polygeneration systems are not operating at a commercial scale. Most of the papers available in the literature on polygeneration are based on theoretical studies. A summary of the paper on different polygeneration modeling and simulation is given in table 1-1. Information is classified according to sources of input energy, outputs, energy conversion devices, and objectives are indicated on the table.

Table 1-1: Summary of polygeneration design and simulation- literature review

Author	Input energy sources	Outputs	Energy conversion devices for power/electricity	Objectives
Soutullo et al. [28]	Solar thermal, PV, PEM fuel cell, biomass	Heating, cooling, electricity	PV, PEM fuel cell	TRNSYS simulation and performance assessment
Mohan et al. [29]	Solar thermal	Chill, clean water, domestic hot water	-	Dynamic simulation (by TRNSYS) and economic modeling
Kieffer et al. [30]	Natural gas, municipal solid waste	Electricity, transportation fuel (FT)	Combined Cycle Gas Turbines (**CCGT**)	Techno-economic modeling
Calise et al. [31]	Solar PV/T	Electricity, space heating, chilling, hot water	PV	Dynamic simulation and thermoeconomic optimization.
Farhat and Reichelstein [32]	Coal	Hydrogen, power, urea, ammonia	Combined Cycle Gas Turbines (**CCGT**)	Economic modeling
Zhu et al. [33]	Coal	Hydrogen, power	Combined Cycle Gas Turbines (**CCGT**)	Modeling (dual chemical loping process)
Hao et al. [34]	Coal and coke oven gas	Dimetrhyl ether, methanol and electricity	Combined Cycle Gas Turbines (**CCGT**)	System modeling
Lythcke-Jørgensen and Haglind [35]	Biomass (straw)	Power, heat, ethanol	Steam turbine	Design optimization
Tock and Marechal [36]	Biomass, coal, natural gas	Hydrogen, electricity, heat and captured CO_2	Gas turbine, steam turbine, fuel cell.	Multi-objective optimization
Jana and De [22]	Biomass (Coconut fiber)	Power, desalinated water, heat, chill	Combined Cycle Gas Turbines (**CCGT**)	Process design (Aspen Plus simulation)
Jana and De [37]	Biomass (Agricultural waste)	Power, heat, chill, ethanol	Combined Cycle Gas Turbines (**CCGT**)	Process design (Aspen Plus simulation)
Salkuyeh and Adams II [38]	Coal	Power, methanol, DME	Gas turbine, steam turbine	Chemical looping
Lythcke-Jørgensen et al [39]	Biomass	Power, heat, ethanol	Steam turbine	Exergy analysis
Li et al. [40]	Coal	Methanol, power	Combined Cycle	Aspen Plus

			Gas Turbines (**CCGT**)	simulation
Yi et al. [41]	Coke-oven gas and coal gasified gas	Electricity, methanol, DME	Combined Cycle Gas Turbines (**CCGT**)	Aspen Plus simulation and optimization
Song et al. [42]	Biomass	Ethanol, power, heat	Steam turbine	Influence of drying process
Samavati et al. [43]	Syngas and hydrogen	Electricity and heating	Solid oxide fuel cell	Design and simulation
Calise et al. [44]	Hybrid solar photovoltaic/thermal collectors (PVT)	Electricity, space heating, cooling, domestic hot water.	PV	Dynamic simulation (by TRNSYS)
Calise et al. [45]	Vegetable oil, solar thermal	Electricity, space heating, cooling, domestic hot water.	Reciprocating engine	Dynamic simulation (by TRNSYS)
Maraver et al. [46]	Biomass	Power, cooling, desalinated water	Organic rankine cycle	Simulation and performance assessment
Ahmadi et al. [47]	Fossil fuel	Power, cooling, heating	Combined Cycle Gas Turbines (**CCGT**)	Multi-objective optimization
Ilic et al. [48]	Biomass, molasses	Ethanol, biogas, electricity, and heat	Steam turbine	Optimization
Li et al. [49]	Coal, coke oven gas	Methanol, dimethyl ether, dimethyl carbonate.	Steam turbine	Simulation and exergoeconomic analysis
Pellegrini and Oliveira Jr. [50]	Surgarcane	Sugar, ethanol, electricity	Steam turbine	Exergy optimization
Kyriakarakos et al. [25]	Wind energy, solar energy	Electricity, water, hydrogen.	Wind turbine, fuel cell	Simulation and optimization
Rubio-Maya et al. [51]	Natural gas, solar energy	Electricity, heating, cooling fresh water	Gas turbine, fuel cell, Stirling engine	Design optimization
De Kam et al. [52]	Biomass	Ethanol, power, heat	Steam turbine	Aspen Plus simulation
Gao et al. [53]	Natural gas	Power, methanol	Combined Cycle Gas Turbines (**CCGT**)	System design

From table 1-1, it is noted that configurations of polygeneration systems vary widely. It mainly depends on input energy sources and outputs in polygeneration systems (renewable or non-renewable), and outputs are mainly electricity, heating, cooling, chemicals, liquid or gaseous fuels, potable water, etc. To convert primary to secondary energy different energy conversion devices can be used as shown in table 1-1 and these are selected depending on configurations and technological and socio-economical viewpoints.

A few experimental and pilot plants of polygeneration are also considered in a few studies. For example, Hossain et al. [54] developed a polygeneration system

for electricity, food preparation, cold storage, and pure water. The plant was based on a compression ignition engine of 9.9 kW power, and it was run by plant oil. Likewise, Ma et al. [55] reported design and experimental investigation of the pilot plan of polygeneration (190 kW biomass fixed bed gasifier). Also, Paleta et al. [56] designed and tested a polygeneration energy container for remote communities to test design issues and solve operation and maintenance challenges associated with autonomous electricity production systems.

In addition, Ferrari et al. [57] analyzed the performance curves for different prime movers of polygeneration systems. In this paper, micro-turbines, internal combustion engines, SOFC-hybrid systems, absorption chillers were selected as prime movers for this experimental facility. Based on laboratory scale experimental results, a pilot plant of polygeneration process with moving bed coal pyrolysis was developed and they reported successful scaling up of the polygeneration process. In the same manner, Mohan et al. [29] investigated a solar thermal-based polygeneration experimentally. This polygeneration pilot plant was designed and developed to produce chilled water for air conditioning by absorption chillers, clean drinking water with membrane distillation units, and domestic hot water by utilizing heat recovery. Finally, Ortiga et al. [58] presented the first results of a polygeneration plant recovering heat at different temperatures levels. They reported the operational and start-up results for the polygeneration of electricity, heating, and cooling. Rossi et al. [59] analyzed and compared experimentally the real-time management of a smart micro-grid under economic and environmental viewpoints.

Other authors like Anghilante et al. [24] proposed the water electrolysis to provide O_2 as the gasifying agent, while H_2 is directly sent to the syngas stream. The identical method is also reported by Ali et al. [60] using Solid Oxide Electrolysis Cell (SOEC) to convert water into O_2 and H_2. Another way to increase H_2 concentration is by removing inert species (i.e., CO_2) from the syngas stream. The Anghilante research group proposed utilizing post-combustion CO_2 capture to remove CO_2 from the syngas stream [61]. There are various options of CO_2 capture, including absorption, adsorption, or membrane separation, which can be applied to the gasification system [62]. Recently, amine-based CO_2 capture is technologically advanced due to its flexibility for retrofitting into the available plants [63].

In resume, developing efficient utility experimental and pilot plants using renewable resources is an imperative need of the present. Gasification-electrolyzer- based polygenerations systems are such systems with strong potential for this purpose. A holistic and interdisciplinary research approach is necessary to create new solutions and opportunities which can enable cities – and energy actors in cities – to address these challenges in a new and potentially more effective way. For example, in electrolysis, water could be splited into its constituent elements – hydrogen and oxygen – using renewable electricity. The challenge in a possible project could be the implementation of biomass-based flexible energy plants that can go beyond the current state of the art of the grids and convert power into practical and easily storable energy carriers. Another example could be how synthetic fuels can be produced using biomass and electrolysis processes and which concepts are best suited for the reconversion of these fuels. As well, to work on emission-optimized transport fuels and designer-fuels. Last, to provide systems analysis and technology evaluation that looks at future fuel's topic from a holistic perspective and includes factors such as cost-effectiveness, performance, the security of supply, and social acceptance [64].

1.1 CRITICAL ANALYSIS

1.1.1 CURRENT STATUS, RESEARCH TRENDS, AND CHALLENGES IN WATER ELECTROLYSIS SCIENCE AND TECHNOLOGY

Grigoriev et al. [65] provide a review of the state-of the-art in the field of water electrolysis science and technology, including a description of the various water electrolysis technologies, and a discussion of the associated challenges and opportunities. The authors discuss the advantages and disadvantages of an Alkaline Water Electrolyzer (AWE), Proton Exchange Membrane cell (PEM), and a Solid Oxide Electrolysis cell (SOEC). Likewise, the electrochemical performances and limitations are presented and analyzed. Some cost elements are also reported. Research trends in the field are discussed. Possible solutions for performance improvements are offered. The paper concludes with a discussion of several perspectives in terms of future applications. In resume, the objective of most R&D activities is to increase the operating current density (to reduce the capital expenditures (Capex) and at the same time, to improve efficiency (to reduce the operating expenses (Opex)). Simultaneously, it is necessary to optimize existing systems (electrolyzer + hydrogen compressor) so that high-pressure hydrogen can be delivered on-site in a cost-efficient and safety-satisfying way. In addition, in most applications, the

target product of water electrolysis is pressurized hydrogen; oxygen is a by-product, usually released into the atmosphere.

1.1.2 HIGH TEMPERATURE STEAM GASIFICATION : PREPARATION OF HYDROGEN-RICH SYNGAS

Pang et. al. [66] present a study to investigate the high-temperature steam gasification of biomass in a downdraft gasifier to prepare hydrogen-rich gas, including the effects of some parameters, such as temperature and flow rate, on product gas composition. The authors evaluated experimentally an indirect heating (allothermal) biomass gasification system. The biomass pellets were used as raw material for preparing hydrogen-rich gas in a downdraft gasifier. The experimental results show that the higher the temperature, the higher the $H_2 + CO$ content. However, the higher the amount of water vapor, the lower the $H_2 + CO$ content. Another influencing factor is the gasification temperature. When the gasification reaction temperature is higher than $750\ °C$, the volume fraction of H_2 in the product gas is higher than $50\ \%$ with little effect of temperature, the variation range is less than $3\ \%$, and the maximum value is $56{,}7\%$. The volume fraction of CO is up to $43{,}42\%$, and the $H_2 + CO$ can reach $94{,}62\%$. Finally, the steam/biomass (S/B) relation is another essential factor in water steam gasification. H_2 and CO_2 were increased with the increase of S/B, while CO decreased. The volume fraction of H_2, CO_2, CO and $H_2 + CO$ were $51{,}2$ to $56{,}70\ \%$, $4{,}63$ to $13{,}59\%$, $28{,}35 - 40{,}21\%$ and $84{,}13 - 92{,}43\%$, respectively.

In this work (Pang et. al. [66]), only steam was used as an oxidizing agent. Compared with the air or oxygen gasification process, the high-temperature steam gasification also has some shortcomings: the process is more energy consuming, as it is endothermic. High-temperature steam gasification needs to put an external heat source to provide the heat (and gasification does not require oxygen or air) required for the reaction, leading to increased cost in energy. For that reason, is necessary to continue advancing in gasification technology to develop, optimize and implement this technology for the alternative use of residual biomass from many of our industries' (wood, brick, solid urban waste, coal, and agro-industrial) waste. Specifically, hydrogen production using allothermal gasification of biomass has not been fully explored under different operating environments.

1.1.3 BIOMASS UPGRADING TO HIGH-VALUE CHEMICALS VIA GASIFICATION AND ELECTROLYSIS

Adnan et al. [21] provided a thermodynamic analysis of biomass upgrading to high-value chemicals via gasification and electrolysis. The authors proposed an integrated biomass gasification process with electrolysis to produce syngas and chemical products using a modified downdraft gasifier with the focus of minimizing tar and maximizing syngas production. Specifically, the electricity from char combustion and syngas-fueled power generation is used to drive the electrochemical reaction. The effect of the gasifying agent on the gasification performance is evaluated at different split ratios of the syngas for power generation. Finally, the authors included a new perspective introducing retrofitting of CO_2 electrolysis and utilizing gasification-generated electricity to convert CO_2 into methanol. A parametric study is conducted to evaluate the effects of the gasifying agents on biomass gasification performance. To evaluate the effect of O_2 injection, different flow rates of O_2 are fed to the syngas reform, while the biomass and steam flow rates are kept constant. This study sheds light on the techno-economic feasibility of implementing such systems, specifically at high latitudes where energy costs are relatively high. The article concludes that the combination of biomass gasification and electrochemical process can be a potential solution to the emission and energy problem. In this scheme, biomass plays a key role as a CO_2 capture system as it grows by consuming CO_2 from the air. Also, the electrolyzer converts CO_2 emission into chemical products (i.e., CO or methanol) with the help of electricity from gasification. Likewise, the overall exergy efficiency ranges about 17-40%, and the largest exergy loss lays on the coolers, which discharge the energy in the process stream into the environment. This finding indicates that the room for performance improvement of the present integrated gasification process is still widely open. One way to minimize the exergy loss is to develop a sophisticated heat integration system to bring the flue gas temperature as close as possible the ambient temperature. Despite the great focus of the authors, they do not include other possible configurations related to taking advantage of syngas to produce other useful products like power, heat, cooling, hydrogen, and synthetic fuels.

1.2 LITERATURE REVIEW AND RESEARCH JUSTIFICATION

As mentioned before, polygeneration systems allow producing four or more useful commodities by using the same or multiple input energy resources. The polygeneration approach offers an opportunity to find synergies between different technologies so that the potential negative environmental impacts of energy

systems are substantially diminished. For example, the integration of exothermic and endothermic processing units or blending the different qualities of syngas generated to provide the correct H_2/CO ratio for integrate the power, heat, transport, and downstream synthesis processes [67][68].

The literature review showed that the main problems related to the integration of waste gasification syngas and renewable-energies-driven water electrolysis for hydrogen-rich syngas production are: (i) the alkaline electrolyzer hydrogen production had not been fully explored under different operating environments. Specifically, the challenges of reducing energy consumption, cost, and maintenance persist. Simultaneously, an increase in reliability, durability, and safety is required by integrating renewable energy [16][17] [18]; (ii) the necessity exists to continue advancing in gasification technology to develop, optimize and implement this technology for the alternative use of residual biomass from many of our industries' (wood, brick, solid urban waste, coal, and agro-industrial) waste [69]. Specifically, hydrogen production from a separation of syngas produced by allothermal gasification of biomass has not been fully explored under different operating environments [70][71][72]. Finally, (iii) there is a need for the analysis of realistic case studies based on flexible waste-driven energy plants to prove the polygeneration concept to advance the current state of the art.

The fundamental concepts underlying the major shortcomings identified in the papers mentioned above include: (i) In the case of the electrolyzer, identify the interaction between the electrical, thermal phenomena, and gas bubble dynamics in electrodes to pursued the lower total cost of hydrogen maximizing the operating current density and the optimization of the overall power consumption (increasing efficiency and operating pressure) while maintaining a low manufacturing cost of the electrolyzer [73][74][75]; (ii) the necessity to continue advancing in the experimental investigation of the gasification technology to develop, optimize and implement this technology for the alternative use of residual biomass from many of our industries. Specifically, to use a downdraft gasifier with indirect heating (allothermal) through the combustion of gases and water vapor or oxygen as an oxidizing agent [76][77][78][79]. The technological advantages of this type of gasifier are related to the simplicity of operation and maintenance. Downdraft configuration allows obtaining a gas of low tar content, and indirect heating allows obtaining a gas with a higher calorific value by not having a combustion zone inside it. Also, water vapor or oxygen are excellent options as oxidizing agent due to its availability and capacity to increase the calorific value of the syngas obtained due to its high reactivity. Finally, (iii) propose the full thermal integrations of the

different units of a polygeneration systems (electrolysis unit, gasification unit, internal combustion engine/turbine and heat exchangers).

Future research on polygeneration systems for successful development may be in developing prototypes based on optimal theoretical results and subsequent experimental performance and feasibility assessment. With variable inputs and outputs, intelligent monitoring and control are critical for efficient polygeneration. Performance being multi-dimensional, criteria of assessment of polygeneration may be several, based on the objective of assessment or weighted average of several objectives. Defining such criteria will be another interesting issue for future polygeneration research. Integrating multiple utility outputs in efficient ways was the basic motive of developing polygeneration and this will remain for the future development of innovative integrated systems considering availability of resources and utility demands. Integrating new devices/components with newer inventions will always remain scope for developing more efficient waste-based flexible energy plants and easily storable energy carriers.

1.3 **OBJECTIVES**

The following general and specific objectives are set according to the performed review and identified research gaps:

GENERAL OBJECTIVE

The main objective is to propose and investigate a polygeneration plant based on integrating biomass gasifier and alkaline electrolyzer for district energy networks

SPECIFICS OBJECTIVES

- Develop a simple mathematical model of the integrated gasification-electrolyzer polygeneration system for its evaluation.
- Develop a rigorous but straightforward gasification model for designing and simulating a biomass gasification plant using the equation solver program Engineering Equation Solver (EES).
- Experimental investigation of the steam gasification of palm kernel shells (PKS) for hydrogen-rich N_2-free syngas production in a pilot-scale atmospheric downdraft allothermal gasifier.
- Thermal characterization of alkaline electrolysis cell for hydrogen production at atmospheric pressure.
- Review and analysis of different District energy networks and the integration of high-temperature commercial heat pumps to efficiently deliver the

heating to building and small industries. Likewise, to describe placement options and connection modes of a heat pump unit in DEN networks.

- Implement the proposed configuration case of polygeneration systems in a very low-temperature district energy networks. The case study will use real data from of the Lachine Est neighborhood in Montreal, Canada.

1.4 METHODOLOGY

Figure 1-3 shows a schematic representation of the polygeneration plant concept to develop in the present work. Organic waste that could be provided from different sources such as agrofood industry byproducts or municipal waste is converted into syngas using an appropriate gasifier. Optionally some preprocessing operation such as torrefaction of biomass could be used but not included in the present work. The syngas is used in a cogeneration system to produce power and heating. A fraction of the power generated is used in an water electrolyzer to generate hydrogen that and be used to increase the heating value of the syngas or stored as a fuel or a commodity. The oxygen co-generated at the electrolyzer is used in the gasification process to generate a higher quality syngas. The electricity generated in this system can be also applied to drive heat pumps to provide efficient heating using a low temperature District Heating network. In some cases, heat pumps are considered also a renewable energy technology and are potentially more efficient than boilers. According to the literature reviewed and the defined objectives in this first chapter, the designed methodology to carry out this thesis is based in the following steps:

1 - Develop a mathematical model of the main components of the polygeneration plant (Chapter 2), except the more complex and detailed model of the core unit gasification system that is presented later in Chapter 3.

2 - Develop a specific mathematical model of the gasification system due to its relevance and complexity. This is a straightforward gasification model for the design and simulation of a biomass gasification plant using the software Engineering Equation Solver (EES) to predict the gasifier performance. The model includes some modifications for its adaptation to real processes, in which only a partial approach to chemical equilibrium is achieved. The model will be validated with experimental data to evaluate variations in fuel and operating conditions previous to an experimental test namely, the influence of temperature and the oxidizing agent on the syngas' hydrogen production and the determination of the Lower heating value (LHV). The experimental test will be also used to get performance parameters to feed the model.

3 - Experimental investigation of the steam biomass gasification process. The parameters required to drive the developed models are obtained from experimental investigations of the gasifier unit (Chapter 4). The experimental investigation is on a steam gasification of biomass for hydrogen-rich N_2-free syngas production in a pilot-scale atmospheric downdraft allothermal gasifier. This experimental data will be used to improve the mathematical model and increase the capacity to predict the gas composition in the gasification of various biomass and oxidizing agents (air + steam, steam, and oxygen) other than just air. The theoretical model has been validated with own experimental data and used to create an improved model will allow better theoretical/simulation analysis in waste-based flexible energy plants.

4 – Experimental investigation of an alkaline electrolyzer. The experimental results are used to get knowledge on its performance and obtain data for its modelling. The experimental results of an alkaline electrolyzer (Chapter 5), mainly the calculation of the electrical power consumed, the efficiency of the cell and the distribution of temperatures on the electrodes will be used to complete the mentioned electrolyzer mathematical model. Likewise, in order to find strategies to reduce manufacturing costs and increase efficiency, this research analyzes the distribution and variation of temperature on the surface of the electrodes while they are in operation, managing to set as these changes are related to thermoelectric phenomena, the presence of areas of higher activity for oxidation and reduction reactions in metals widely used in alkaline electrolysis, such as stainless steel.

5 – Use of heat pumps to provide heating through a low-temperature District Network. The waste heat from the gasification process is used to increase the plant efficiency. The heating demand of the nearby users is intended to be covered using electrically driven heat pumps using efficient low-temperature District heating networks. Therefore, different district energy networks are reviewed along with how to integrate high-temperature commercial heat pumps in them. Likewise, is necessary to describe and analyze placement options and connection modes of a heat pumps in district heating networks and identify new generic configurations of heat pumps and how they can be integrated into polygeneration systems. This last point is performed in the case study based on the Dominion Bridge area in Lachine-Est in Montreal.

6 – Test of the proposed polygeneration system in a case study. A case study using the developed models and operation parameters is performed in the last chapter to present the potential of the proposed polygeneration system. The case study is based on the Dominion Bridge area in the Lachine-Est quartier in Montreal. Developers intend to design an eco-quartier with a district heating network and an

energy-efficient and cost-effective energy system. Two configurations are compared considering the energy consumption for the same sets of buildings. In the first configuration, just the gasifier operates. Using air or steam as the gasifying agent. The resulting product gas is fed to heat recovery units, a clean-up section, and a gas turbine coupled with a district energy network in the Lachine-Est area. In contrast, in the second configuration, the system consists of a gasifier plus an electrolyzer. The electrolyzer converts electricity and water into H_2 and O_2. O_2 is used as the gasifying agent. At the same time, H_2 is directly sent to the syngas stream to improve the heating value of syngas generated, producing an N_2-free gas suited for biofuel synthesis, hydrogen, power, heating, and cooling production.

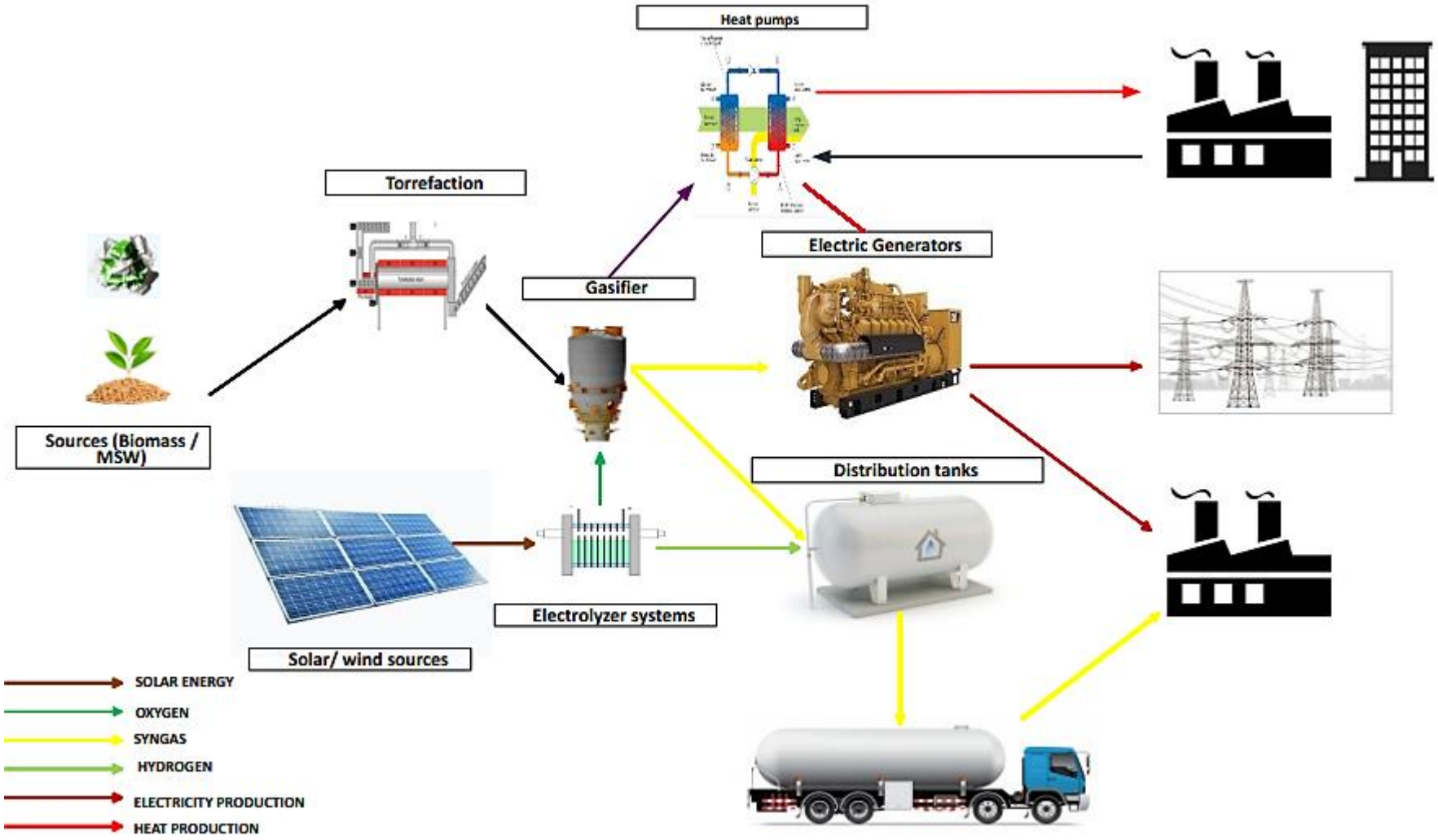

Figure 1-3: Schematic representation of possible polygeneration plant concepts for syngas upgrading.

1.5 **REFERENCES**

[1] A. Steiner, K. K. Yumkella, J. Clos, and G. Van Begin, "District Energy in Cities Unlocking the Potential of Energy Efficiency and Renewable Energy," [Online]. Available: https://wedocs.unep.org/bitstream/handle/20.500.11822/9317/-District_energy_in_cities_unlocking_the_potential_of_energy_efficiency_and_renewable_ene.pdf?sequence=2&isAllowed=y.

[2] IRENA, "Renewable Power-To-Heat Innovation Landscape Brief," 2019.

[3] IRENA, "Renewable Energy in District Heating and Cooling, A sector roadmap for REmap," Int. Renew. Energy Agency, no. March, 2017, [Online]. Available: http://www.irena.org/-/media/Files/IRENA/Agency/Publication/2017/Mar/IRENA_REmap_DEN_Report_2017.pdf.

[4] Natural Resources Canada (NRCan), "Hydrogen strategy for Canada Seizing the Opportunities for Hydrogen," 2020.

[5] K. Mazloomi and C. Gomes, "Hydrogen as an energy carrier: Prospects and challenges," Renew. Sustain. Energy Rev., vol. 16, no. 5, pp. 3024–3033, 2012, doi: 10.1016/j.rser.2012.02.028.

[6] R. P. Menon, M. Paolone, and F. Maréchal, "Study of optimal design of polygeneration systems in optimal control strategies," Energy, vol. 55, pp. 134–141, 2013, doi: 10.1016/j.energy.2013.03.070.

[7] A. D. Celebi, S. Sharma, A. V. Ensinas, and F. Maréchal, "Next generation cogeneration system for industry – Combined heat and fuel plant using biomass resources," Chem. Eng. Sci., vol. 204, pp. 59–75, 2019, doi: 10.1016/j.ces.2019.04.018.

[8] DLR, "DLR researchers achieve high-temperature electrolysis with solar-thermal steam for the first time," Effic. Hydrog. Prod., pp. 1–2, 2018, [Online]. Available: https://www.dlr.de/dlr/en/desktopdefault.aspx/tabid-10202/334_read-27203/#/gallery/30470.

[9] O. Bičáková and P. Straka, "Production of hydrogen from renewable resources and its effectiveness," Int. J. Hydrogen Energy, vol. 37, no. 16, pp. 11563–11578, 2012, doi: 10.1016/j.ijhydene.2012.05.047.

[10] H. Balat and E. Kirtay, "Hydrogen from biomass - Present scenario and future prospects," Int. J. Hydrogen Energy, vol. 35, no. 14, pp. 7416–7426, 2010, doi: 10.1016/j.ijhydene.2010.04.137.

[11] J. S. Tumuluru, Biomass Preprocessing and Pretreatments for Production of Biofuels. 2018.

[12] I. Hannula, "Hydrogen production via thermal gasification of biomass in near-to-medium term Hydrogen production via thermal gasification of biomass in near-to-medium term," 2009. [Online]. Available: http://www.vtt.fi/publications/index.jsp.

[13] A. Indarto, Syngas Production, Applications and environmental impact. 2554.

[14] I. Dincer, "Green methods for hydrogen production," Int. J. Hydrogen Energy, vol. 37, no. 2, pp. 1954–1971, 2012, doi: 10.1016/j.ijhydene.2011.03.173.

[15] S. Heidenreich and P. Ugo, "New concepts in biomass gasi fi cation," Prog. Energy Combust. Sci., vol. 46, pp. 72–95, 2015, doi: 10.1016/j.pecs.2014.06.002.

[16] M. David, C. Ocampo-Martínez, and R. Sánchez-Peña, "Advances in alkaline water electrolyzers: A review," J. Energy Storage, vol. 23, no. January, pp. 392–403, 2019, doi: 10.1016/j.est.2019.03.001.

[17] S. Marini et al., "Advanced alkaline water electrolysis," Electrochim. Acta, 2012, doi: 10.1016/j.electacta.2012.05.011.

[18] S. Niaz, T. Manzoor, and A. H. Pandith, "Hydrogen storage: Materials, methods and perspectives," Renewable and Sustainable Energy Reviews. 2015, doi: 10.1016/j.rser.2015.05.011.

[19] A. Seçer, N. Küçet, E. Fakı, and A. Hasanoğlu, "Comparison of co–gasification efficiencies of coal, lignocellulosic biomass and biomass hydrolysate for high yield hydrogen production," Int. J. Hydrogen Energy, vol. 3, pp. 21269–21278, 2018, doi: 10.1016/j.ijhydene.2018.09.144.

[20] R. Alipour Moghadam Esfahani, L. Osmieri, S. Specchia, S. Yusup, A. Tavasoli, and A. Zamaniyan, "H2-rich syngas production through mixed residual biomass and HDPE waste via integrated catalytic gasification and tar cracking plus bio-char upgrading," Chem. Eng. J., vol. 308, pp. 578–587, 2017, doi: 10.1016/j.cej.2016.09.049.

[21] M. A. Adnan, M. M. Hossain, and M. G. Kibria, "Biomass upgrading to high-value chemicals via gasification and electrolysis: A thermodynamic analysis," Renew. Energy, vol. 162, pp. 1367–1379, Dec. 2020, doi: 10.1016/j.renene.2020.08.075.

[22] K. Jana and S. De, "Sustainable polygeneration design and assessment through combined thermodynamic, economic and environmental analysis," Energy, vol. 91, pp. 540–555, 2015, doi: 10.1016/j.energy.2015.08.062.

[23] F. Calise, M. D. d'Accadia, and M. Vicidomini, "Optimization and dynamic analysis of a novel polygeneration system producing heat, cool and fresh water," Renew.

Energy, vol. 143, pp. 1331–1347, 2019, doi: 10.1016/j.renene.2019.05.051.

[24] R. Anghilante et al., "Innovative power-to-gas plant concepts for upgrading of gasification bio-syngas through steam electrolysis and catalytic methanation," Energy Convers. Manag., vol. 183, no. January, pp. 462–473, 2019, doi: 10.1016/j.enconman.2018.12.101.

[25] G. Kyriakarakos, A. I. Dounis, S. Rozakis, K. G. Arvanitis, and G. Papadakis, "Polygeneration microgrids: A viable solution in remote areas for supplying power, potable water and hydrogen as transportation fuel," Appl. Energy, vol. 88, no. 12, pp. 4517–4526, 2011, doi: 10.1016/j.apenergy.2011.05.038.

[26] K. Jana, A. Ray, M. M. Majoumerd, M. Assadi, and S. De, "Polygeneration as a future sustainable energy solution – A comprehensive review," Appl. Energy, vol. 202, pp. 88–111, 2017, doi: 10.1016/j.apenergy.2017.05.129.

[27] U. Sahoo, R. Kumar, S. K. Singh, and A. K. Tripathi, "Energy, exergy, economic analysis and optimization of polygeneration hybrid solar-biomass system," Appl. Therm. Eng., vol. 145, no. August, pp. 685–692, 2018, doi: 10.1016/j.applthermaleng.2018.09.093.

[28] S. Soutullo et al., "Energy performance assessment of a polygeneration plant in different weather conditions through simulation tools," Energy Build., vol. 124, pp. 7–18, 2016, doi: 10.1016/j.enbuild.2016.04.031.

[29] G. Mohan, U. Kumar, M. K. Pokhrel, and A. Martin, "A novel solar thermal polygeneration system for sustainable production of cooling, clean water and domestic hot water in United Arab Emirates: Dynamic simulation and economic evaluation," Appl. Energy, vol. 167, pp. 173–188, 2016, doi: 10.1016/j.apenergy.2015.10.116.

[30] M. Kieffer, T. Brown, and R. C. Brown, "Flex fuel polygeneration: Integrating renewable natural gas into Fischer-Tropsch synthesis," Appl. Energy, vol. 170, pp. 208–218, 2016, doi: 10.1016/j.apenergy.2016.02.115.

[31] F. Calise, M. Dentice d'Accadia, R. D. Figaj, and L. Vanoli, "A novel solar-assisted heat pump driven by photovoltaic/thermal collectors: Dynamic simulation and thermoeconomic optimization," Energy, vol. 95, pp. 346–366, 2016, doi: 10.1016/j.energy.2015.11.071.

[32] K. Farhat and S. Reichelstein, "Economic value of flexible hydrogen-based polygeneration energy systems," Appl. Energy, vol. 164, pp. 857–870, 2016, doi: 10.1016/j.apenergy.2015.12.008.

[33] L. Zhu, Z. Zhang, J. Fan, and P. Jiang, "Polygeneration of hydrogen and power based

on coal gasification integrated with a dual chemical looping process: Thermodynamic investigation," Comput. Chem. Eng., vol. 84, pp. 302–312, 2016, doi: 10.1016/j.compchemeng.2015.09.010.

[34] Y. Hao, Y. Huang, M. Gong, W. Li, J. Feng, and Q. Yi, "A polygeneration from a dual-gas partial catalytic oxidation coupling with an oxygen-permeable membrane reactor," Energy Convers. Manag., vol. 106, pp. 466–478, 2015, doi: 10.1016/j.enconman.2015.09.058.

[35] C. Lythcke-Jørgensen and F. Haglind, "Design optimization of a polygeneration plant producing power, heat, and lignocellulosic ethanol," Energy Convers. Manag., vol. 91, pp. 353–366, 2015, doi: 10.1016/j.enconman.2014.12.028.

[36] L. Tock and F. Maréchal, "Thermo-environomic optimisation strategy for fuel decarbonisation process design and analysis," Comput. Chem. Eng., vol. 83, pp. 110–120, 2015, doi: 10.1016/j.compchemeng.2015.04.018.

[37] K. Jana and S. De, "Environmental impact of biomass based polygeneration – A case study through life cycle assessment," Bioresour. Technol., vol. 227, pp. 256–265, 2017, doi: 10.1016/j.biortech.2016.12.067.

[38] Y. Khojasteh Salkuyeh and T. A. Adams, "Integrated petroleum coke and natural gas polygeneration process with zero carbon emissions," Energy, vol. 91, pp. 479–490, 2015, doi: 10.1016/j.energy.2015.08.056.

[39] C. Lythcke-Jørgensen, F. Haglind, and L. R. Clausen, "Exergy analysis of a combined heat and power plant with integrated lignocellulosic ethanol production," Energy Convers. Manag., vol. 85, pp. 817–827, 2014, doi: 10.1016/j.enconman.2014.01.018.

[40] Y. Li, G. Zhang, Y. Yang, D. Zhai, K. Zhang, and G. Xu, "Thermodynamic analysis of a coal-based polygeneration system with partial gasification," Energy, vol. 72, pp. 201–214, 2014, doi: 10.1016/j.energy.2014.05.025.

[41] Q. Yi, J. Feng, and W. Y. Li, "Optimization and efficiency analysis of polygeneration system with coke-oven gas and coal gasified gas by Aspen Plus," Fuel, vol. 96, pp. 131–140, 2012, doi: 10.1016/j.fuel.2011.12.050.

[42] H. Song, F. Starfelt, L. Daianova, and J. Yan, "Influence of drying process on the biomass-based polygeneration system of bioethanol, power and heat," Appl. Energy, vol. 90, no. 1, pp. 32–37, 2012, doi: 10.1016/j.apenergy.2011.02.019.

[43] M. Samavati, R. Raza, and B. Zhu, "Design of a 5-kW advanced fuel cell polygeneration system," Wiley Interdiscip. Rev. Energy Environ., vol. 1, no. 2, pp. 173–180, 2012, doi: 10.1002/wene.6.

[44] F. Calise, M. D. D'Accadia, and L. Vanoli, "Design and dynamic simulation of a novel

solar trigeneration system based on hybrid photovoltaic/thermal collectors (PVT)," Energy Convers. Manag., vol. 60, pp. 214–225, 2012, doi: 10.1016/j.enconman.2012.01.025.

[45] F. Calise, A. Palombo, and L. Vanoli, "Design and dynamic simulation of a novel polygeneration system fed by vegetable oil and by solar energy," Energy Convers. Manag., vol. 60, no. x, pp. 204–213, 2012, doi: 10.1016/j.enconman.2012.02.014.

[46] D. Maraver, J. Uche, and J. Royo, "Assessment of high temperature organic Rankine cycle engine for polygeneration with MED desalination: A preliminary approach," Energy Convers. Manag., vol. 53, no. 1, pp. 108–117, 2012, doi: 10.1016/j.enconman.2011.08.013.

[47] P. Ahmadi, M. A. Rosen, and I. Dincer, "Multi-objective exergy-based optimization of a polygeneration energy system using an evolutionary algorithm," Energy, vol. 46, no. 1, pp. 21–31, 2012, doi: 10.1016/j.energy.2012.02.005.

[48] D. Djuric Ilic, E. Dotzauer, L. Trygg, and G. Broman, "Integration of biofuel production into district heating - Part I: An evaluation of biofuel production costs using four types of biofuel production plants as case studies," J. Clean. Prod., vol. 69, pp. 176–187, 2014, doi: 10.1016/j.jclepro.2014.01.035.

[49] Z. Li, P. Liu, F. He, M. Wang, and E. N. Pistikopoulos, "Simulation and exergoeconomic analysis of a dual-gas sourced polygeneration process with integrated methanol/DME/DMC catalytic synthesis," Comput. Chem. Eng., vol. 35, no. 9, pp. 1857–1862, 2011, doi: 10.1016/j.compchemeng.2011.01.015.

[50] L. F. Pellegrini and S. de Oliveira Junior, "Combined production of sugar, ethanol and electricity: Thermoeconomic and environmental analysis and optimization," Energy, vol. 36, no. 6, pp. 3704–3715, 2011, doi: 10.1016/j.energy.2010.08.011.

[51] C. Rubio-Maya, J. Uche-Marcuello, A. Martínez-Gracia, and A. A. Bayod-Rújula, "Design optimization of a polygeneration plant fuelled by natural gas and renewable energy sources," Appl. Energy, vol. 88, no. 2, pp. 449–457, 2011, doi: 10.1016/j.apenergy.2010.07.009.

[52] M. J. De Kam, R. Vance Morey, and D. G. Tiffany, "Biomass Integrated Gasification Combined Cycle for heat and power at ethanol plants," Energy Convers. Manag., vol. 50, no. 7, pp. 1682–1690, 2009, doi: 10.1016/j.enconman.2009.03.031.

[53] L. Gao, H. Li, B. Chen, H. Jin, R. Lin, and H. Hong, "Proposal of a natural gas-based polygeneration system for power and methanol production," Energy, vol. 33, no. 2, pp. 206–212, 2008, doi: 10.1016/j.energy.2007.10.011.

[54] A. K. Hossain, R. Thorpe, P. Vasudevan, P. K. Sen, R. E. Critoph, and P. A. Davies,

"Omnigen: Providing electricity, food preparation, cold storage and pure water using a variety of local fuels," Renew. Energy, vol. 49, pp. 197–202, 2013, doi: 10.1016/j.renene.2012.01.032.

[55] Z. Ma, Y. Zhang, Q. Zhang, Y. Qu, J. Zhou, and H. Qin, "Design and experimental investigation of a 190 kWe biomass fixed bed gasification and polygeneration pilot plant using a double air stage downdraft approach," Energy, vol. 46, no. 1, pp. 140–147, 2012, doi: 10.1016/j.energy.2012.09.008.

[56] R. Paleta, A. Pina, and C. A. Santos Silva, "Polygeneration Energy Container: Designing and Testing Energy Services for Remote Developing Communities," IEEE Trans. Sustain. Energy, vol. 5, no. 4, pp. 1348–1355, 2014, doi: 10.1109/TSTE.2014.2308017.

[57] M. L. Ferrari, A. Traverso, and A. F. Massardo, "Smart polygeneration grids: Experimental performance curves of different prime movers," Appl. Energy, vol. 162, pp. 622–630, 2016, doi: 10.1016/j.apenergy.2015.10.144.

[58] J. Ortiga, J.C. Bruno. and A. Coronas, "Operational experience of the polygeneration plant in Parc de l'Alba (Spain): Start-up and first results,"," 2011 Int. Conf. Util. Exhib. Power Energy Syst. Issues Prospect. Asia (ICUE), 2011, pp. 1-5, doi: doi: 10.1109/ICUEPES.2011.6497757.

[59] I. Rossi, L. Banta, A. Cuneo, M. L. Ferrari, A. N. Traverso, and A. Traverso, "Real-time management solutions for a smart polygeneration microgrid," Energy Convers. Manag., vol. 112, pp. 11–20, 2016, doi: 10.1016/j.enconman.2015.12.026.

[60] S. Ali, K. Sørensen, and M. P. Nielsen, "Modeling a novel combined solid oxide electrolysis cell (SOEC) - Biomass gasification renewable methanol production system," Renew. Energy, vol. 154, pp. 1025–1034, 2020, doi: 10.1016/j.renene.2019.12.108.

[61] M. A. Adnan, Q. Xiong, O. Muraza, and M. M. Hossain, "Gasification of wet microalgae to produce H2-rich syngas and electricity: A thermodynamic study considering exergy analysis," Renew. Energy, vol. 147, pp. 2195–2205, 2020, doi: 10.1016/j.renene.2019.10.027.

[62] A. A. Olajire, "CO2 capture and separation technologies for end-of-pipe applications - A review," Energy, vol. 35, no. 6, pp. 2610–2628, 2010, doi: 10.1016/j.energy.2010.02.030.

[63] A. Mukhtar et al., "CO2 capturing, thermo-kinetic principles, synthesis and amine functionalization of covalent organic polymers for CO2 separation from natural gas: A review," J. Nat. Gas Sci. Eng., vol. 77, no. February, p. 103203, 2020, doi: 10.1016/j.jngse.2020.103203.

[64] R. Østergaard, L. Røngaard, T. Pape, J. Ahrenfeldt, and U. Birk, "Flexible TwoStage biomass gasifier designs for polygeneration operation," Energy, vol. 166, pp. 939–950, 2019, doi: 10.1016/j.energy.2018.10.144.

[65] S. A. Grigoriev, V. N. Fateev, D. G. Bessarabov, and P. Millet, "Current status, research trends, and challenges in water electrolysis science and technology," Int. J. Hydrogen Energy, vol. 45, no. 49, pp. 26036–26058, Oct. 2020, doi: 10.1016/j.ijhydene.2020.03.109.

[66] Y. Pang, S. Shen, and Y. Chen, "High Temperature Steam Gasification of Corn Straw Pellets in Downdraft Gasifier: Preparation of Hydrogen-Rich Gas," Waste and Biomass Valorization, vol. 10, no. 5, pp. 1333–1341, May 2019, doi: 10.1007/s12649-017-0143-3.

[67] F. Calise, G. de Notaristefani di Vastogirardi, M. Dentice d'Accadia, and M. Vicidomini, "Simulation of polygeneration systems," Energy, vol. 163, pp. 290–337, 2018, doi: 10.1016/j.energy.2018.08.052.

[68] P. Kumar, M. Varkolu, S. Mailaram, A. Kunamalla, and S. K. Maity, Biorefinery polyutilization systems: Production of green transportation fuels from biomass. Elsevier Inc., 2018.

[69] M. Asadullah, "Barriers of commercial power generation using biomass gasification gas: A review," Renew. Sustain. Energy Rev., vol. 29, pp. 201–215, 2014, doi: 10.1016/j.rser.2013.08.074.

[70] J. Hrbek, "Status report on thermal biomass gasification in countries participating in IEA Bioenergy Task 33," 2016. [Online]. Available: http://www.ieatask33.org/content/publications/Status_report%5Cnhttp://www.ieatask33.org/app/webroot/files/file/2016/Status_report.pdf.

[71] C. Srinivasakannan and N. Balasubramanian, "The significance of indirectly heated gasifiers for the generation of medium calorific value syngas through biomass gasification," Energy Sources, Part A Recover. Util. Environ. Eff., vol. 32, no. 17, pp. 1579–1586, 2010, doi: 10.1080/15567030903076768.

[72] E. Balu, U. Lee, and J. N. Chung, "High temperature steam gasification of woody biomass - A combined experimental and mathematical modeling approach," Int. J. Hydrogen Energy, vol. 40, no. 41, pp. 14104–14115, 2015, doi: 10.1016/j.ijhydene.2015.08.085.

[73] H. J. Cho and E. N. Wang, "Bubble nucleation, growth, and departure: A new, dynamic understanding," Int. J. Heat Mass Transf., vol. 145, p. 118803, 2019, doi: 10.1016/j.ijheatmasstransfer.2019.118803.

[74] P. Chandran, S. Bakshi, and D. Chatterjee, "Study on the characteristics of hydrogen bubble formation and its transport during electrolysis of water," Chem. Eng. Sci., vol. 138, pp. 99–109, 2015, doi: 10.1016/j.ces.2015.07.041.

[75] H. Matsushima, Y. Fukunaka, and K. Kuribayashi, "Water electrolysis under microgravity. Part II. Description of gas bubble evolution phenomena," Electrochim. Acta, vol. 51, no. 20, pp. 4190–4198, 2006, doi: 10.1016/j.electacta.2005.11.046.

[76] P. Basu, Biomass Gasification and Pyrolysis. Burlington, USA: Elsevier Inc., 2010.

[77] M. Milhé, L. Van De Steene, M. Haube, J. M. Commandré, W. F. Fassinou, and G. Flamant, "Autothermal and allothermal pyrolysis in a continuous fixed bed reactor," J. Anal. Appl. Pyrolysis, vol. 103, pp. 102–111, 2013, doi: 10.1016/j.jaap.2013.03.011.

[78] G. Cheng et al., "Allothermal gasification of biomass using micron size biomass as external heat source," Bioresour. Technol., vol. 107, pp. 471–475, 2012, doi: 10.1016/j.biortech.2011.12.074.

[79] M. Hu et al., "A novel pilot-scale production of fuel gas by allothermal biomass gasification using biomass micron fuel (BMF) as external heat source," Clean Technol. Environ. Policy, vol. 18, no. 3, pp. 743–751, 2016, doi: 10.1007/s10098-015-1038-2.

[80] D. D. A. de Fátima Palhares, L. G. M. Vieira, and J. J. R. Damasceno, "Hydrogen production by a low-cost electrolyzer developed through the combination of alkaline water electrolysis and solar energy use," Int. J. Hydrogen Energy, vol. 43, no. 9, pp. 4265–4275, 2018, doi: 10.1016/j.ijhydene.2018.01.051.

[81] P. Olivier, C. Bourasseau, and P. B. Bouamama, "Low-temperature electrolysis system modelling: A review," Renewable and Sustainable Energy Reviews. 2017, doi: 10.1016/j.rser.2017.03.099.

[82] A. A. P. Susastriawan, H. Saptoadi, and Purnomo, "Small-scale downdraft gasifiers for biomass gasification: A review," Renew. Sustain. Energy Rev., vol. 76, no. March, pp. 989–1003, 2017, doi: 10.1016/j.rser.2017.03.112.

Chapter2 MODELING APPROACH FOR INTEGRATION OF POLYGENERATION SYSTEMS IN DISTRICT ENERGY NETWORKS

Summary: This chapter develops models integrated to analyze polygeneration systems in very low-temperature district energy networks. Firstly, we describe the process modeling of the polygeneration plant. Finally, the last block includes the six sub-systems models: (i) syngas production unit (ii) electrolysis unit; (iii) gas turbine; (iv) heat pumps; (v) hydrogen storage tank and (vi) compression unit.

2.1 PROCESS MODELING OF THE POLYGENERATION PLANT

The principles applied for modeling the main plant processes are presented here following static regime. In this section a model is developed for a biomass gasification polygeneration plant that simultaneously produces heat, cold, electricity and hydrogen. The polygeneration unit is composed of five sub-systems (figure 2-1): syngas production unit, heat recovery unit, gas clean-up unit, gas utilization unit, and compression and store gas unit and other specific units: (i) heat pump (ii) electrolyzer unit; (iii) gas turbine; (iv) heat exchangers.

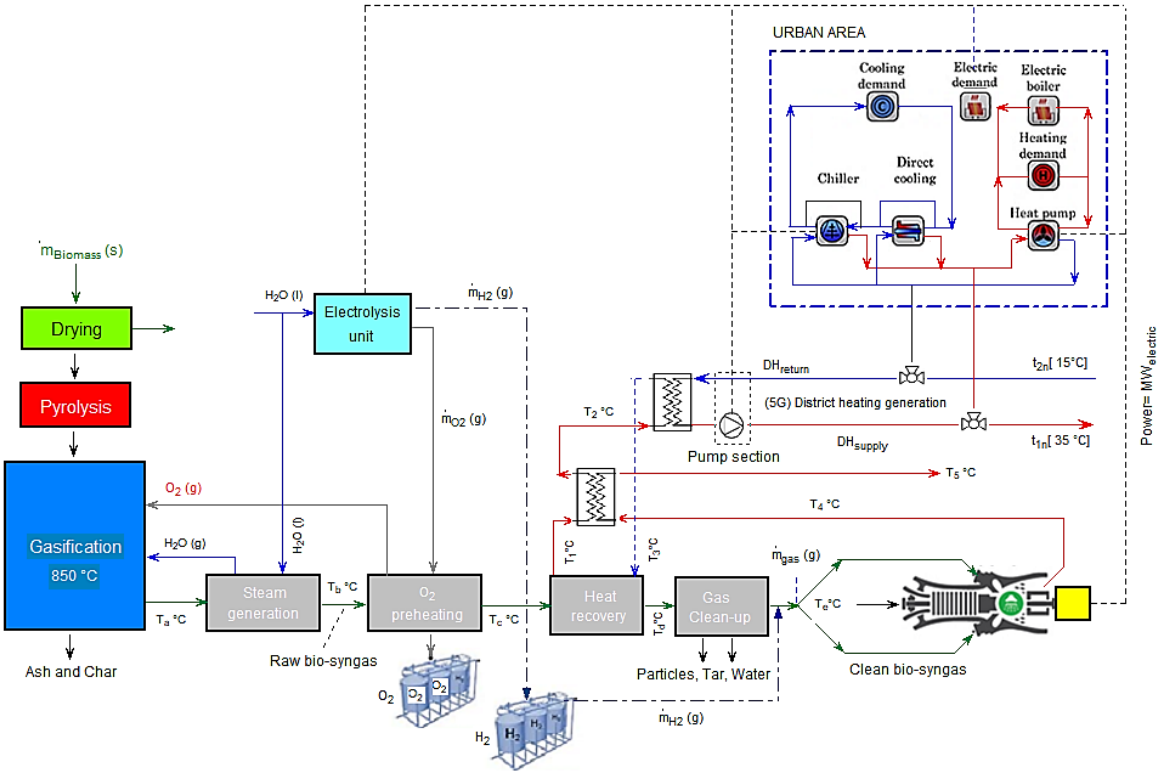

Figure 2-1 Schematic representation of the polygeneration plant concept for syngas upgrading in district energy networks of 5th generation

2.1.1 **GASIFICATION UNIT**

Usually, the air is selected as the gasifying agent because it is the most economical option and does not require an air separation unit to provide the oxygen in the gasifier [1]. This option is not cost-effective, even at small scales. Therefore, integrating an electrolyzer unit to contribute the oxygen necessary to the gasification process solves the problem previously mentioned. A downdraft gasifier with indirect heating (allothermal) is operated with the combustion of one fraction of syn gas generated. Likewise, oxygen or steam can also increase the LHV of syngas and be selected as an oxidizing agent. The technological advantages of this type of gasifier are related to the simplicity of operation and maintenance. Downdraft configuration allows obtaining a gas of low tar content, and indirect heating allows obtaining a gas with a higher calorific value by not having a combustion zone inside it. Finally, water vapor and oxygen are oxidizing agents due to their high reactivity and the availability and calorific value of the gas obtained. The biomass gasification model is presented in detail in chapter 3 and experimentally supported by chapter 4.

2.1.2 **ELECTROLYSIS UNIT**

Water electrolysis (WE) powered by renewable sources is one option to produce hydrogen, which is generated by passing an electric current through a conductive substance (electrolyte) to conduct a non-spontaneous reaction. The reaction of interest is the decomposition of water into hydrogen and oxygen, which is endothermic and requires energy input to be carried out. Precisely, water electrolysis can provide the O_2 as the gasifying agent, while H_2 is directly sent to the syngas stream to improve the heating value of syngas generated. Likewise, a water electrolyzer consists of a series of electrochemical cells composed of: (i) electrolyte (ionic conductor), (ii) electrodes (anode and cathode) where oxidation and reduction reactions occur, (iii) supply system of electricity and auxiliary systems for supply and collection of reagents and products [2][3].

The decomposition of water into hydrogen and oxygen can be achieved by passing an electric current (DC) between two electrodes separated by an aqueous electrolyte with good ionic conductivity. The total reaction for splitting water is:

$$H_2O\,(l) + \text{Electric energy} \Rightarrow H_2(g) + 1/2\ O_2(g) \qquad (1)$$

For this reaction to occur a minimum electric voltage must be applied to the two electrodes. This minimum voltage, or reversible voltage, can be determined from Gibbs energy for water splitting [4][5]. In an alkaline electrolyzer the electrolyte is usually aqueous potassium hydroxide (KOH), where the potassium ion K+ and hydroxide ion OH^- take care of the ionic transport. The anodic and cathodic reactions taking place here are:

$$\text{Anode:} \quad OH^-(aq) \Rightarrow 1/2\ O_2(g) + H_2O\ (l) + 2e^- \qquad (2)$$

$$\text{Cathode:} \quad 2\ H_2O\ (l) + 2e^- \Rightarrow H_2\ (g) + 2\ OH^-(aq) \qquad (3)$$

In an alkaline solution the electrodes must be resistant to corrosion, and must have good electric conductivity and catalytic properties, as well as good structural integrity, while the diaphragm should have low electrical resistance. This can, for instance, be achieved by using anodes based on nickel, cobalt, and iron (Ni, Co, Fe), cathodes based on nickel with a platinum activated carbon catalyst (Ni, C-Pt), and nickel oxide (NiO) diaphragms [4][6] [7].

2.1.2.1. ELECTROCHEMICAL MODEL

The electrode kinetics of an electrolyzer cell can be modeled using empirical current-voltage (I-U) relationships. Several empirical I-U models for electrolyzers have been suggested [8][9][10]. In order to properly model the I-U curve for a given temperature, overvoltage and ohmic resistance are taken into account, as proposed in [11].

- **Current-Voltage characteristic (per cell)**

$$U_{cell} = U_{rev}\ r^* \frac{I_{ely}}{Area} + s^*\ \log\left(\frac{s^* I_{ely}}{Area} + 1\right) \qquad (4)$$

With:

$$r^* = r_1 + r_2 T_{ely} \qquad (5)$$

$$s^* = s_1 + s_2 T_{ely} + s_3 {T_{ely}}^2 \qquad (6)$$

$$t^* = t_1 + \frac{t_2}{T_{ely}} + \frac{t_3}{{T_{ely}}^2} \qquad (7)$$

Table 2-1: I-U curve parameters (taken from [11])

r_1	$8.05\ e-5\ \Omega\ m^2$	Ohmic resistance
r_2	$-2.5\ e-7\ \Omega\ m^2 \circ C^{-1}$	Ohmic resistance
$s_{1,2,3}$	$0.185\ V$	Overvoltage on electrodes
t_1	$-1.002\ A^{-1}m^2$	Overvoltage on electrodes
t_2	$8.424\ A^{-1}m^2\ °C$	Overvoltage on electrodes
t_3	$247.3\ A^{-1}\ m^2 \circ C^2$	Overvoltage on electrodes
I_{ely}	Current applied in electrolyzer	A
Area	Area per cell in electrolyzer	m^2
T_{ely}	Temperature of the electrolyzer	°C

- **Faraday efficiency**

The Faraday efficiency is defined as the ratio between the actual and theoretical maximum amount of hydrogen produced in the electrolyzer. Since the Faraday efficiency comprises the parasitic current losses along the gas ducts, it is often called the current efficiency. The parasitic currents increase with decreasing current densities due to an increasing share of electrolyte and therefore also a lower electrical resistance [10]. Furthermore, the parasitic current in a cell is linear to the cell potential [11]. Hence, the fraction of parasitic currents to total current increases with decreasing current densities. An increase in temperature leads to a lower resistance, more parasitic current losses, and lower Faraday efficiencies. An empirical expression that accurately depicts these phenomena for a given temperature is:

$$\eta_F = \left(\frac{I_{density}^{\ 2}}{f_1 + I_{density}^{\ 2}}\right) f_2 \qquad (8)$$

With:

$$I_{density} = \frac{I}{Area} \qquad (9)$$

Table 2-2: : Faraday efficiency parameters (taken from [11])

T	80	40	60	80	°C	
f_1	250	150	200	250	mA^2cm^{-4}	Faraday efficiency
f_2	0.96	0.990	0.985	0.980	0….1	Faraday efficiency

- **Hydrogen production**

According to Faraday's law, the production rate of hydrogen in an electrolyzer cell is directly proportional to the transfer rate of electrons at the electrodes, which in turn is equivalent to the electrical current in the external circuit. Hence, the total hydrogen production rate in an electrolyzer, which consists of several cells connected in series, can be expressed as:

$$\dot{m}_{H_2} = \eta_F N_{cells} \frac{I_{ely}}{F} \qquad (10)$$

With: N_{cells} indicate cell number in the pack system; F indicate Faraday constant

- **Oxygen production**

The oxygen production rate is simply found from stoichiometry (Eq. 3), which on a molar basis is:

$$\dot{m}_{O_2} = \quad 0.5\ \dot{m}_{H_2} \qquad (11)$$

- **Energy efficiency**

The generation of heat in an electrolyzer is mainly due to electrical inefficiencies. The energy efficiency can be calculated from the thermoneutral voltage ($U_{tn} = 1.482\ V$) and the cell voltage (U_{cell}):

$$\eta_e = \frac{U_{tn}}{U_{cell}} \qquad (12)$$

For a given temperature, an increase in hydrogen production (i.e., an increase in current density) increases the cell voltage, which consequently decreases the energy efficiency.

2.1.2.2. THERMODYNAMIC MODEL

Thermodynamics provides a framework for describing reaction equilibrium and thermal effects in electrochemical reactors. It also gives a basis for the definition of the driving forces for transport phenomena in electrolytes and leads to the description of the properties of the electrolyte solutions [12][13][14][15]. Below is a description of the thermodynamics of the low-temperature hydrogen-oxygen electrochemical reactions used in the electrolyzer model. The following assumptions can be made about the water splitting reaction: (a) Hydrogen and air (or oxygen) are ideal gases, (b) water is an incompressible fluid, and (c) the gas and liquid phases are separate. Based on these assumptions the change in enthalpy ΔH,

Entropy ΔS and Gibbs Energy ΔG of the water splitting reaction can be calculated with reference to pure hydrogen (H_2), oxygen (O_2), and water (H_2O) at a standard temperature and pressure (25°C and 1 atm). The total change in enthalpy for splitting water is the enthalpy difference between the products (H_2 and O_2) and the reactants (H_2O). The same applies for the total change in entropy. The change in Gibbs energy is expressed by:

$$\Delta G = \Delta H - \Delta S T_{ely} \qquad (13)$$

At standard conditions (25 °C and 1 atm) the splitting of water is a non-spontaneous reaction, which means that the change in Gibbs energy is positive. The standard Gibbs energy for water splitting is $\Delta G^0 = 237\ \mathrm{kJ\ mol^{-1}}$. For an electrochemical process operating at constant pressure and temperature the maximum possible useful work (i.e., the reversible work) is equal to the change in Gibbs energy ΔG. Faraday's law relates the electrical energy (emf) needed to split water to the chemical conversion rate in molar quantities. The emf for a reversible electrochemical process, or the reversible cell voltage, is expressed by:

$$U_{rev} = \frac{\Delta G}{nF} \qquad (14)$$

The total amount of energy needed in water electrolysis is equivalent to the change in enthalpy ΔH. From Error! Reference source not found. it is seen that ΔG includes the thermal irreversibility TΔS, which for an eversible process is equal to the heat demand. The standard enthalpy for splitting water is $\Delta H^0 = 286\ \mathrm{kJ\ mol^{-1}}$. The total energy demand ΔH is related to the thermoneutral cell voltage:

$$U_{tn} = \frac{\Delta H}{nF} \qquad (15)$$

At standard conditions $U_{rev} = 1.229\ \mathrm{V}$ and $U_{tn} = 1.482\ \mathrm{V}$, but these will change with temperature and pressure. In the applicable temperature range U_{rev} decreases slightly with increasing temperature (U_{rev} @ 80°C, 1 bar = 1.184 V), while U_{tn} remains almost constant (U_{tn} @ 80°C, 1 bar = 1.473 V). Increasing pressure increases Urev slightly (U_{rev} @ 25°C, 30 bar = 1.295 V), while U_{tn} remains constant.

- **Overall energy balance**

$$C_T dT dt_{ely} = \dot{Q}_{gen} - \dot{Q}_{loss} - \dot{Q}_{cw} \qquad (16)$$

The first term on the right-hand side is the internal heat generation (Eq. 17), he second term the total heat loss to the ambient (Eq. 18), and the third term the auxiliary cooling demand (Eq. 19). The overall thermal capacity C_T and resistance R_T for the electrolyzer, and the UA-product for the cooling water heat exchanger are the constants. Finally, It should be noted that the thermal model presented here is on a per stack basis and UA is given as a function of electrolyzer current:

- **Generated thermal energy**

$$\dot{Q}_{gen} = N_{cells} I_{ely} (U_{cell} - U_{tn}) \qquad (17)$$

- **Heat losses to ambient**

$$\dot{Q}_{lcss} = \frac{1}{R_T} \left(T_{ely} - T_{amb} \right) \qquad (18)$$

- **Auxiliar cooling requirements**

$$\dot{Q}_{cw} = C_{P_{H_2O}} \left(T_{cw,out} - T_{cw,in} \right) \qquad (19)$$

- **Transfer coefficient**

$$UA_{hx} = h_1 + h_2 I_{ely} \qquad (20)$$

2.1.3 **GAS TURBINE**

The gas turbine (GT) cycle is commonly used to produce electrical power and useful heat recovering waste heat. Compared to the Rankine cycle, the gas turbine cycle offers the advantages of quick startup and shutdown. Gas turbine power plants are often started remotely when there is a need for electrical power above the base load level. The gas turbine cycle is characterized by a huge power-to-weight ratio, which is a primary advantage of these cycles in many cases. GT technology consists of the combustion of previously compressed gaseous fuels in an internal combustion chamber and the subsequent expansion of the combustion gases in a turbine. When a gasification unit, gas cleaning unit and a heat recovery steam generator (HRSG) are integrated with the GT, this system is called Biomass Integrated Gasification Combined Cycle (BIGCC). By contrast, Microturbines are down-scaled versions of GT, being more suitable for small-scale applications. Accordingly, microturbines can be used in places with low biomass production rates, such as Mediterranean forests. The electric output of these devices ranges from a few kWe up to 500 kWe [16] although some authors limit this output to 250 kWe [17][18]. In microturbines, the compressor and the turbine have a solidary shaft, so fewer maintenance requirements are necessary due to their simplicity [16][18]. Their performance is quite good even with biomass-based fuels. Better efficiencies can be achieved than

with diesel fuel [16] or with ICE technology, although being less commercially proven [18].

The gas turbine cycle is shown schematically in figure 2-6. The basic cycle is often called the Brayton cycle. Outdoor air at state 1 is drawn into a compressor and compressed to a higher pressure at state 2. The pressure ratio at state 2 to the pressure at state 1 is called the pressure ratio PR [-], and it is an important design parameter for this cycle. The compressed air at state 2 enters a recuperator and combustion chamber where it is mixed with fuel and combusted. The combustion process is assumed to occur at nearly constant pressure. In this work, we assume that the energy provided by the fuel combustion can be expressed in terms of the heat of combustion of fuel (HC), which is the energy released per unit mass of fuel. Likewise, we assume that the properties of the combustion products are the same as the properties of pure air. The ratio of the mass flow rate of air to the mass flow rate of fuel is referred to as the air-fuel ratio (AF). High air-fuel ratios are used in the combustion process to control the temperature of the combustion products entering the turbine at state 4 and avoid damage to the blades. Higher turbine inlet temperatures lead to higher cycle efficiency. However, the fatigue strength of the turbine blades that are continuously exposed to the high-temperature exhaust products dictates a maximum temperature of approximately 1200 °C although higher temperatures could be achieved using special techniques and materials.

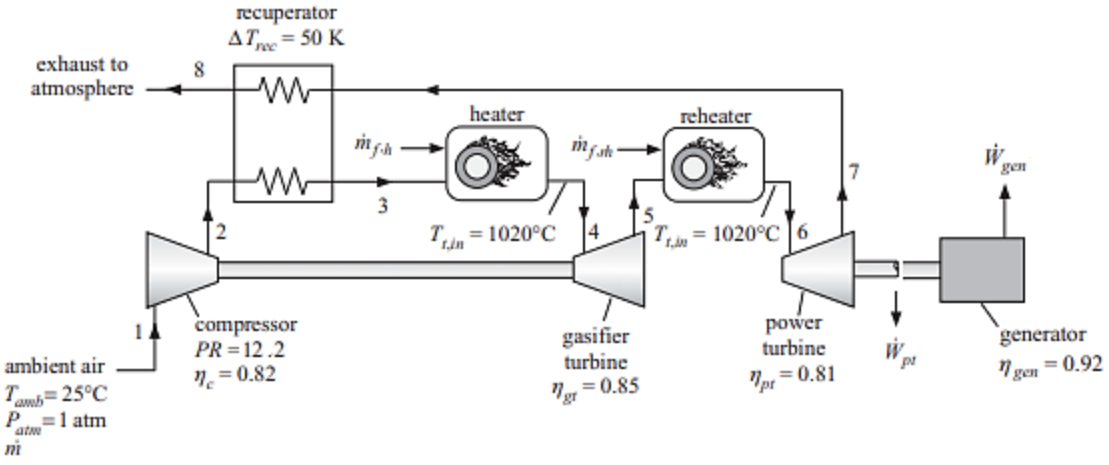

Figure 2-2: Gas turbine engine with reheat and recuperation, adapt from [19][20][21]

The high pressure and high-temperature combustion gas entering the turbine at state 4 expand in a turbine that produces shaft power sufficient to drive the compressor. If the gas turbine power cycle is operating correctly, it is unnecessary to expand the gas to atmospheric pressure in the gasifier turbine ($P_6 > P_7$). Therefore, the gas can subsequently be expanded in a power turbine that produces

some net useful power. Depending on the application, the output power may be used to provide mechanical power (rotor) o electrical power using a generator.

Usually, some modifications are made to the gas turbine cycle to improve the efficiencies. Firstly, the reheat modification leads to higher turbine output power by pushing the low-pressure portion of the expansion process into a region of higher specific volume (increase in the specific volume of the working fluid with increased temperature). Secondly, the recuperation modification includes taking advantage of a large fraction of the energy obtained from combustion in the basic gas turbine cycle. In a recuperated gas turbine cycle, a heat exchanger referred to as a recuperator or regenerator is used to accomplish the heat transfer. The air leaving the compressor at state 2 is heated in the recuperator to a temperature T_7 that is somewhat less than the turbine exit temperature. Thus, the energy required by the combustor is substantially reduced relative to the un-recuperated gas turbine engine, which increases the efficiency of the cycle. The model of gas turbine shown in figure 6-6 is developed in order to illustrate the proper method of analysis as well as to explore some of the feature and behaviors of the cycle. In order to specify the gas turbine cycle, it is necessary to set the ambient temperature and atmospheric pressure (T_{amb} and P_{atm}), the pressure ratio (PR) and the air-fuel ratio (AF). We will assume that the fuel is syngas generated by biomass gasification with a heat of combustion HC. The performance parameters include the efficiency of the compressor (η_c) as well as the efficiencies of the gasifier and power turbines η_{gt} and η_{pt}, respectively).

2.1.4 **HEAT PUMP SIMULATION**

Vapor compression heat pumps and refrigeration systems have been studied through a series of simulation models; these have been classified into three domains: i) Simulation by functional fit, ii) Simulation by deterministic models, and iii) Simulation by mixed models [22][23]. First, functional fit models treat the system as a black box and fit the performance of the system to one or a few equations; then, the simulation by deterministic models are based on the application of laws of thermodynamics and the fundamentals of heat and mass transfer to each of the components and the relationship of each of the components with the study system; finally, mixed models use both criteria (simulation by functional fit and deterministic models) for each element, each of the fundamental equations that describe the components of the system can have one or more parameters, which are estimated simultaneously; Once the parameters have been estimated, the heat pump model can be used as part of a simulation of multiple component systems [24].

Simulation by functional fit allows to predict entirely or part of the performance of the equipment. Basic equations that govern the operation in a steady state are obtained by applying the physical laws to the systems (mass and energy balance). Internal variables are eliminated using variables with functional relation of performance data of the systems. The functional relationships of the components are given by polynomial adjustment of constant coefficients obtained from the regression of experimental data. The first proposed functional fit model is shown in Figure 5. It is assumed that the system is controlled to maintain a specific water supply temperature through the compressor capacity; the inputs to the component are the temperatures and total flow rates of evaporator and condenser water.

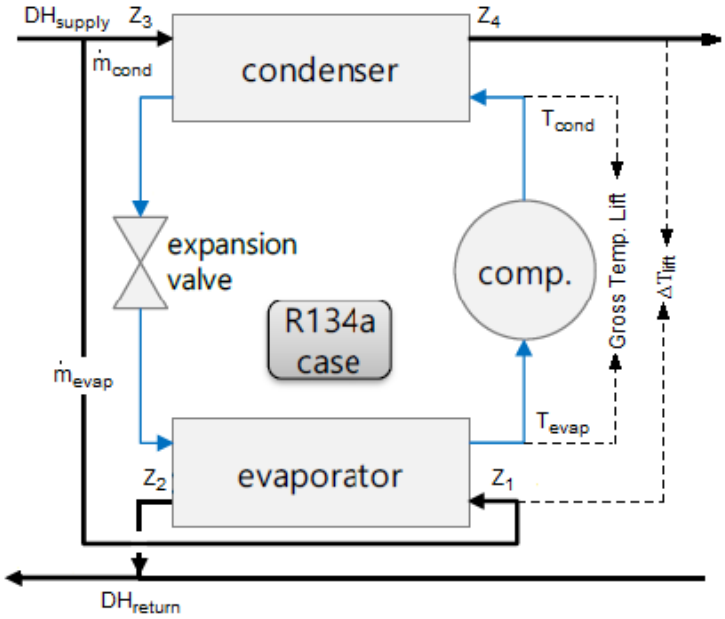

Figure 2-3: Heat pump connection in direct use of energy from the DEN supply of the high-temperature stream to evaporate the refrigerant (HRT)

EVAPORATOR

$$\mathrm{QE} = \text{Evaporator cooling load}, \qquad (\mathrm{kW})$$

$$\mathrm{Z_1} = \mathrm{T_{\_source}}, \text{in} \qquad °\mathrm{C}$$

$$Z_3 = \mathrm{T_{\_sink}}, \text{in} \qquad °\mathrm{C}$$

$$\mathrm{QE} = \mathrm{B_1 Z_1} + \mathrm{B_2 Z_3} + \mathrm{B_3 Z_1 Z_3} + \mathrm{B_4 {Z_1}^2} + \mathrm{B_5 {Z_3}^2} + \mathrm{B_6} \qquad (21)$$

COMPRESSOR

$$P = \text{Compressor power}, \qquad (kW)$$

$$Z_1 = T_{\_source}, \text{in} \qquad °C$$

$$Z_3 = T_{\_sink}, \text{in} \qquad °C$$

$$P = B_7 Z_1 + B_8 Z_3 + B_9 Z_1 Z_3 + B_{10} {Z_1}^2 + B_{11} {Z_3}^2 + B_{12} \quad (22)$$

ENERGY BALANCE IN EVAPORATOR AND CONDENSER

$$\dot{m}_e = \text{mass flow of water in hte evaporator } \frac{kg}{s}$$

$$C_P = \text{specific heat of water } \frac{kJ}{kg * K}$$

$$QC = \text{rate of heat released in the condenser}, \qquad kW$$

$$\dot{m}_c = \text{mass flow of water in the condenser } \frac{kg}{s}$$

$$Z_2 = T_{\_source}, \text{out} \qquad °C$$

$$Z_4 = T_{\_sink}, \text{out} \qquad °C$$

TO SOLVE THE SYSTEM, WE MUST DEFINE:

$$\text{Input data: } Z_1, Z_3, \dot{m}_{evap} \text{ y } \dot{m}_{cond}$$

$$\text{Output data : } QE, P, QC, Z_2, Z_4 \text{ y } COP$$

$$COP = \frac{QC}{P} \qquad (23)$$

$$QE = QC - P \quad (24)$$

$$T_{\_source,out} = T_{-source,in} - \frac{QE}{\dot{m}_e Cp_{source}} \quad (25)$$

$$T_{\_sink,out} = T_{\_sink,in} - \frac{QC}{\dot{m}_c Cp_{sink}} \qquad (26)$$

2.1.5 HYDROGEN STORAGE TANK

The hydrogen is generated by electrolysis and is stored in tanks for future use—one hydrogen tank design use N_{tank} heavy-wall steel fuel cylinders. The tanks are cylindrical with a height of H_{tank} and an internal diameter of D_{tank}. However, the tanks are expensive and heavy. Therefore, storage stations will receive hydrogen at pressure $P_{supply} = 300\ bar$ and ambient temperature, T_{supply}=$T_{amb} = 25\ °C$.

The tanks station has $T_{inicial} = T_{amb}$ and initial pressure $P_{inicial} = 60\ bar$. The tanks are connected, and the fill valve is opened for $t_{fill} = 4\ minutes$, at which time the valve is closed. The mass flow rate through the fill valve has been found to scale with the square root of the pressure difference between the supply and fuel tank according to:

$$\dot{m} = C_{valve}\sqrt{(P_{supply} - P)} \qquad (27)$$

Where P is the instantaneous pressure in the tank and $\dot{m}$ is the instantaneous mass flow rate. Measurements on the valve set used for the fuel tanks indicate that the valve coefficient is $C_{valve} = 2{,}68\ x\ 10^{-6}\ \frac{kg}{s}\ Pa^{0,5}$ [25]. The heat transfer rate to the hydrogen in the tanks from the tank walls is given by:

$$\dot{Q} = h_{conv} * A_s(T_{wall} - T) \qquad (28)$$

Where $h_{conv} = 40\ W/m^2\ K$ is the convective heat transfer coefficient between the hydrogen in the fuel tanks and the cylinder wall and A_s is the internal surface area of the tank walls (T_{wall}) remains at T_{amb} during the entire filling process.

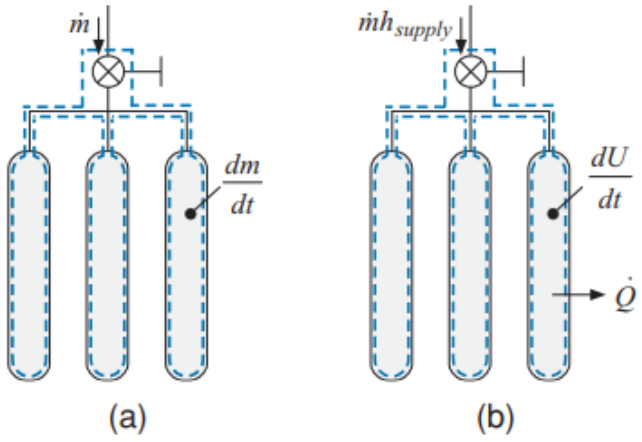

Figure 2-4: (a) Mass balance and (b) energy balance, adapt from [26]

The volume of a single tank is determined according to:

$$V_{tank} = \pi \frac{H_{tank} {D_{tank}}^2}{4} \qquad (29)$$

The initial state of the hydrogen in the tank is fixed by the temperature and pressure. Therefore, the specific volume and specific internal energy ($v_{initial}$ and u_{ini}) can be calculated. The initial mass and internal energy are calculated according to:

$$m_{ini} = \frac{N_{tank}\, V_{tank}}{v_{initial}} \qquad (30)$$

$$U_{ini} = u_{ini}\ m_{ini} \qquad (31)$$

The specific volume and specific internal energy correspond to the specified values of m and U:

$$v = \frac{N_{tank}\, V_{tank}}{m} \qquad (32)$$

$$U = \frac{U}{m} \qquad (33)$$

The mass flow rate into the tank is determined from equation (34). A mass balance on the system is indicated in figure 7.

$$\dot{m} = \frac{d_m}{d_t} \qquad (34)$$

The specific enthalpy of the entering hydrogen (h_{supply}) is fixed by the temperature and pressure in the reservoir. Likewise, the internal surface is of the N_{tank} cylindrical tanks is calculated:

$$A_s = N_{tank} \left(2\pi \frac{{D_{tank}}^2}{4} + \pi\, D_{tank}\, H_{tank} \right) \qquad (35)$$

Finally, an energy balance on the system is indicated in figure 2-4.

$$\dot{m} h_{supply} = \dot{Q} + \frac{dU}{dt} \qquad (36)$$

$$m_{fuel} = m - m_{ini} \qquad (37)$$

2.1.6 **COMPRESSION UNIT**

The compression work W_{comp} (in kW) is calculated using equation (38).

$$W_{comp} = \frac{\gamma}{\gamma - 1} . \frac{\eta_{gas} Z . R . T_{in}}{\eta_{isen} . \eta_{mec}} . \left(\frac{P_{out}^{\frac{\gamma-1}{\gamma}}}{P_{in}} - 1 \right) \qquad (38)$$

Where, γ is the heat capacity ratio; $\dot{\eta}_{gas}$ is the flow rate of gas ($\mathrm{mol.s^{-1}}$); Z is the compressibility factor; R is the gas constant ($\mathrm{kJ.mol^{-1}.K^{-1}}$); T_{in} is the inlet temperature; η_{isen} is the isentropic efficiency; η_{mec} is the mechanical efficiency; P_{out} is the outlet pressure (bar) and P_{in} is the inlet pressure (bar).

2.2 **REFERENCES**

[1] H. Zhang, L. Wang, M. Pérez-Fortes, J. Van herle, F. Maréchal, and U. Desideri, “Techno-economic optimization of biomass-to-methanol with solid-oxide electrolyzer,” *Appl. Energy*, vol. 258, no. May 2019, p. 114071, 2020, doi: 10.1016/j.apenergy.2019.114071.

[2] M. David, C. Ocampo-Martínez, and R. Sánchez-Peña, “Advances in alkaline water electrolyzers: A review,” *J. Energy Storage*, vol. 23, no. January, pp. 392–403, 2019, doi: 10.1016/j.est.2019.03.001.

[3] FuelCellToday, “Water Electrolysis & Renewable Energy Systems,” 2013. doi: 10.1017/CBO9781107415324.004.

[4] K. Zeng and D. Zhang, “Recent progress in alkaline water electrolysis for hydrogen production and applications,” *Prog. Energy Combust. Sci.*, vol. 36, no. 3, pp. 307–326, 2010, doi: 10.1016/j.pecs.2009.11.002.

[5] Y. Petrov, J. P. Schosger, Z. Stoynov, and F. De Bruijn, “Hydrogen evolution on nickel electrode in synthetic tap water - Alkaline solution,” *Int. J. Hydrogen Energy*, vol. 36, no. 20, pp. 12715–12724, 2011, doi: 10.1016/j.ijhydene.2011.07.049.

[6] S. Niaz, T. Manzoor, and A. H. Pandith, “Hydrogen storage: Materials, methods and perspectives,” *Renewable and Sustainable Energy Reviews*. 2015, doi: 10.1016/j.rser.2015.05.011.

[7] M. Fatouh, M. H. Shedid, and S. Elshokary, “Effect of operating and geometric parameters on hydrogen production from an alkali electrolyzer,” *Int. J. Power Eng. Energy*, vol. 4, no. October, pp. 395–399, 2013.

[8] H. J. Cho and E. N. Wang, “Bubble nucleation, growth, and departure: A new, dynamic understanding,” *Int. J. Heat Mass Transf.*, vol. 145, p. 118803, 2019, doi: 10.1016/j.ijheatmasstransfer.2019.118803.

[9] Y. Wang, X. Hu, Z. Cao, and L. Guo, “Investigations on bubble growth mechanism during photoelectrochemical and electrochemical conversions,” *Colloids Surfaces A Physicochem. Eng. Asp.*, vol. 505, pp. 86–92, 2016, doi: 10.1016/j.colsurfa.2016.01.004.

[10] P. Chandran, S. Bakshi, and D. Chatterjee, “Study on the characteristics of hydrogen bubble formation and its transport during electrolysis of water,” *Chem. Eng. Sci.*, vol. 138, pp. 99–109, 2015, doi: 10.1016/j.ces.2015.07.041.

[11] Ø. Ulleberg, “Modeling of advanced alkaline electrolyzers:a system simulation approach,” *Int. J. Hydrogen Energy*, vol. 28, pp. 21–33, 2003, doi: 10.1016/S0360-

3199(02)00033-2.

[12] D. D. A. de Fátima Palhares, L. G. M. Vieira, and J. J. R. Damasceno, “Hydrogen production by a low-cost electrolyzer developed through the combination of alkaline water electrolysis and solar energy use,” *Int. J. Hydrogen Energy*, vol. 43, no. 9, pp. 4265–4275, 2018, doi: 10.1016/j.ijhydene.2018.01.051.

[13] P. M. Diéguez, A. Ursúa, P. Sanchis, C. Sopena, E. Guelbenzu, and L. M. Gandía, “Thermal performance of a commercial alkaline water electrolyzer: Experimental study and mathematical modeling,” *Int. J. Hydrogen Energy*, 2008, doi: 10.1016/j.ijhydene.2008.09.051.

[14] N. Nagai, M. Takeuchi, T. Kimura, and T. Oka, “Existence of optimum space between electrodes on hydrogen production by water electrolysis,” *Int. J. Hydrogen Energy*, 2003, doi: 10.1016/S0360-3199(02)00027-7.

[15] J. Milewski, G. Guandalini, and S. Campanari, “Modeling an alkaline electrolysis cell through reduced-order and loss-estimate approaches,” *J. Power Sources*, 2014, doi: 10.1016/j.jpowsour.2014.06.138.

[16] H. I. Onovwiona and V. I. Ugursal, “Residential cogeneration systems: review of the current technology,” *Renew. Sustain. Energy Rev.*, vol. 10, no. 5, pp. 389–431, Oct. 2006, doi: 10.1016/J.RSER.2004.07.005.

[17] E. Monteiro, N. A. Moreira, and S. Ferreira, “Planning of micro-combined heat and power systems in the Portuguese scenario,” *Appl. Energy*, vol. 86, no. 3, pp. 290–298, 2009, doi: 10.1016/j.apenergy.2008.04.010.

[18] E. Bocci, M. Sisinni, M. Moneti, L. Vecchione, A. Di Carlo, and M. Villarini, “State of art of small scale biomass gasification power systems: A review of the different typologies,” *Energy Procedia*, vol. 45, pp. 247–256, 2014, doi: 10.1016/j.egypro.2014.01.027.

[19] L. Magistri, P. Costamagma, A. F. Massardo, C. Rodgers, and C. F. MacDonald, “A hybrid system based on a personal turbine (5 kW) and a solid oxide fuel cell stack: A flexible and high efficiency energy concept for the distributed power market,” *J. Eng. Gas Turbines Power*, vol. 124, no. 4, pp. 850–857, 2002, doi: 10.1115/1.1473825.

[20] S. Katulić, M. Čehil, and D. R. Schneider, “Thermodynamic efficiency improvement of combined cycle power plant’s bottom cycle based on organic working fluids,” *Energy*, vol. 147, pp. 36–50, 2018, doi: 10.1016/j.energy.2018.01.033.

[21] F. J. Brooks, “GE Gas Turbine Performance Characteristics.”

[22] H. JIN, “Parameter Estimation BAsed Models of Water Source Heat Pumps,” 2002.

[23] A. R. Mazhar, S. Liu, and A. Shukla, “A state of art review on the district heating systems,” *Renew. Sustain. Energy Rev.*, vol. 96, no. September 2017, pp. 420–439, 2018, doi: 10.1016/j.rser.2018.08.005.

[24] P. A. Østergaard and A. N. Andersen, “Booster heat pumps and central heat pumps in district heating,” *Appl. Energy*, vol. 184, pp. 1374–1388, 2016, doi: 10.1016/j.apenergy.2016.02.144.

[25] Y. A. Cengel, “Fluid Mechamics: Fundamentals and Application,” , p. 342, 2006.

[26] A. Nakano, T. Maeda, H. Ito, T. Motyka, J. M. Perez-Berrios, and S. Greenway, “Experimental study on a metal hydride tank for the totalized hydrogen energy utilization system,” *Energy Procedia*, vol. 29, pp. 463–468, 2012, doi: 10.1016/j.egypro.2012.09.054.

Chapter3 THERMODYNAMIC EQUILIBRIUM MODEL OF A DOWNDRAFT GASIFIER.

Summary: The main contribution of the present chapter consists of developing a rigorous but straightforward gasification model for designing and simulating a biomass gasification plant using the equation solver program Engineering Equation Solver (EES). The model includes some modifications for adaptation to real processes, in which only a partial approach to chemical equilibrium is achieved. The model developed, which has been validated with own and other authors' experimental data, provides the opportunity to evaluate different gasification processes and variations in fuel and operating conditions. The data was obtained to confirm a variation of less than 10% when comparing the proposed model's compositions with the experimental results reported in the literature. The model has also been used to evaluate the influence of temperature and the oxidizing agents in the syngas' hydrogen production and Lower heating value (LHV). Comparing the three oxidizing agents, steam showed a higher capacity to generate hydrogen than air + steam and air by 52% and 63%, respectively. Likewise, a higher capacity to generate syngas with superior LHV than air + steam and air by 44 % and 51%, respectively.

3.1 INTRODUCTION

Biomass can be transformed into solid, liquid, or gaseous fuels through physicochemical conversion processes (extraction and transesterification), biochemicals (alcoholic fermentation, anaerobic digestion, and aerobic digestion), and thermochemical (torrefaction, pyrolysis, gasification, and liquefaction)[1][2]. Despite the widespread use of biomass, this is not yet fully exploited and is awaiting improved conversion methods to produce solid, liquid, and gaseous energy for commercial purposes [2][3]. Biomass gasification has, in the short term, more significant commercial potential than other thermochemical processes (liquefaction, pyrolysis, and combustion), due to its greater flexibility in terms of energy application for power generation and raw materials for industrial chemicals, to its greater efficiency as it can be integrated into combined gasification and to its potential for low environmental impact [4][5][6].

The gasification conversion process is defined as partial thermal oxidation; the use of an oxidizing agent is essential for the gasification process; it reacts with the carbonized product of pyrolysis and converts heavier hydrocarbons into gases with low molecular weight, such as CO, CO_2, CH_4 and H_2 and minor quantities of char, ash,

and several condensable compounds (tars and oils) [7]. Of oxidizing agents, gasification with air is the most widely used, part of the processed biomass is burned with the oxygen present, and the surplus is reduced; the process generates a gas of low calorific value between $4-7\ \mathrm{MJ/Nm^3}$ [8]. When using water vapor or oxygen, one obtains a gas with a calorific value between $10-18 \text{ and } 12-28\ \mathrm{MJ/Nm^3}$ respectively [9][10]. Additionally, when using hydrogen as an oxidizing agent, a gas is obtained with an approximate calorific value of $40\ \mathrm{MJ/Nm^3}$ [7]. Finally, the reactors used for gasification are classified based on their disposition and the type of heating used; within the classification by disposition are the gasifiers entrained bed, fluidized bed, moving bed, and fixed bed. Moreover, according to the type of equipment heating, they can be classified into direct (autothermal) and indirect (allothermal) heating gasifiers [11][12].

Design and operation of gasifiers require an understanding of essential parameters like biomass characteristics (composition, moisture content, and size) and process parameters (equivalence ratio, gasification temperature, and feeding rate) prior to designing a gasifier to improve the performance of the gasifier in terms of quality of produced gas and gasification efficiency [13][14][15]. Operating parameters such as temperature and pressure in the reactor, feed rate, and reaction agent greatly influence the gasification process [16]. Any changes in the operating parameters have a considerable effect on the final composition of the gas and, therefore, on the process's performance [17]. It is also observed that differences in raw materials, inherent to their composition and thermochemical properties, affect the gasification process, showing an interrelated behavior between process parameters, raw material, and yield. Therefore, the task of experimentation to find the optimal operating conditions for a gasifier that uses a specific raw material becomes a process that requires much time and high investment costs. Under these conditions, mathematical models have become an important tool to study the gasifier's behavior to optimize its design and operation without performing the physical experimentation of equipment and processes.

Mathematical models are developed to represent the physical and chemical phenomena within a gasifier [17]. An excellent mathematical model allows the real operation to be reproduced with an acceptable degree of deviation [18]. An excellent mathematical model can: (i) find the optimal operating conditions or design parameters for the manufacture of a gasifier;(ii) identify areas of dangerous operation; (iii) provide information on extreme operating conditions (high pressure, high temperature) where experiments are difficult to perform; (iv) provide information on a greater breadth of operating condition than can be obtained

experimentally; (v) improve interpretation of experimental results and behavior analysis abnormal in a gasifier, and (vi) allow scaling in size of a gasifier, which allows the successful work of one size to another and varying the type of biomass used. Therefore, The mathematical models of the gasification process can be classified in (i) thermodynamic equilibrium; (ii) kinetic model; (iii) computational fluid dynamics (CFD); (iv) artificial neural network (ANNs), and (v) ASPEN Plus models [17].

The thermodynamic equilibrium model allows predicting the maximum yield achievable of the desired product for a reaction system [19], that is, if, when isolated from its environment, it does not undergo observable macroscopic changes. The yield and composition of the products in this condition are determined by the equilibrium constants and the minimization of Gibbs' free energy [17]. The system is considered in its most stable composition in chemical equilibrium, indicating that its entropy is maximized while Gibbs' free energy is minimized [17][20]. Although chemical equilibrium cannot be achieved in a gasifier, equilibrium models reasonably predict the final composition and control process parameters such as temperature and pressure [21].

Many researchers have used the thermodynamic equilibrium model to predict gas composition in the gasification process. Puig-Arnavat et al. [22], Niladri et al. [23], Dutta et al. [24], and Mendiburu et al. [25] carried out studies of the gasification process making use of the thermodynamic equilibrium determined utilizing equilibrium constants, the results obtained were compared with studies carried out by other authors, establishing that the results obtained numerically are between 20-30 % of deviation compared with the results obtained experimentally.

Despite frequent use in the simulation of gasification processes, the shortcomings found in the thermodynamic equilibrium model to accurately predict the final composition of the gases, using finite reaction times and including the effect that the gasifier geometry has on the final composition of the gas generated, reveals the need to use kinetic models to evaluate and predict with greater accuracy the gasifier behavior [26]. Therefore, the kinetic model allows predicting gases' performance, their final composition, in a finite residence time, in a finite volume, and at a specific temperature inside the gasifier [27]. On the other hand, this involves parameters such as reaction rate, residence times, surface velocity, diffusion rate within the reactor, length, and the need for a more intensive computational resource [17]. Budhathoki [27] and Khan et al. [26] have carried out studies using kinetic models to improve gas composition prediction; their work reports approximately 90% accuracy in predicting gas composition.

Computational fluid dynamics (CFD) models play an essential role in modeling entrained flow, fluidized bed, moving bed, and fixed bed gasifiers [28]. CFD models involve solving equations of conservation of mass, species conservation, and energy conservation in a defined region. A CFD code for gasification typically includes a set of sub-models for the sequence of operations such as the vaporization of biomass particles, their pyrolysis, side reactions in pyrolysis, and carbon oxidation, the solution of these equations can be achieved with commercial software such as ANSYS, FLUENT, and COMSOL and not commercial like C ++ or Fortran [29] [30]. Antonopoulos et al. [31] and Sivakumar et al. [32] have analyzed gasification products' reaction agent flow, temperature distribution, and concentration using CFD code for biomass gasification.

Neural network analysis is a relatively new simulation tool for gasifier modeling [17]; it works by mimicking the functioning of the human brain, which uses the experience of previous experiments to predict how the gasifier will behave under certain conditions. Neural networks of a gasifier require an extensive experimental database that is used as input parameters in the neural network model. Due to their non-analytical, non-equilibrium behavior, neural network models have many limitations in terms of dynamic modeling, despite its accuracy in predicting composition, neural network modeling is currently not a viable option for new ones, due to the scarce experimental data available [17][27], for technologies such as biomass gasification. Mikulandric et al. [33] have worked on the neural network analysis of biomass gasification; their work concludes that it is possible to achieve the gasification process parameters with reasonable precision when comparing with numerical results of biomass gasification plants in operation.

The kinetic and thermodynamic equilibrium models do not provide precise results because they are limited to a small number of species and reactions with clearly defined mechanisms [23][25]. Furthermore, for more complex systems, the reaction mechanisms and the species produced often require a more extensive study and incorporation of empirical correlations based on experimental studies to increase the models' precision [17][34]. The importance of equilibrium models is that they are simple to solve and are capable of predicting the composition of the synthesis gas with considerable precision [22][34][35].

Although the equilibrium approach is relatively easy to implement and converges quickly, it has inherent thermodynamic limitations because thermodynamic equilibrium is not fully achieved during relatively low operating temperatures (exit temperature of gases formed from 750 to 1000 ° C). [20][21][25]. Therefore, the equilibrium approach does not give a true representation of the process during low-

temperature operations. Despite the limitations mentioned, the equilibrium models allow a practical description of the gasification processes. It can be highlighted from the results obtained in the literature, that the operating limits, the relationship between the different operating parameters, and the composition of the gases produced can be defined. Although equilibrium models are simple, they can describe gasification processes with good 80-90 % approximation, such as those in downdraft gasifiers [27][29].

This study proposes developing a rigorous but straightforward gasification model for designing and simulating biomass gasification plants using the equation solver program Engineering Equation Solver (EES). The model includes some modifications for adaptation to real processes (tar composition, temperature gradient along the height of the gasifier, and the update of equilibrium constants used) in which only a partial approach to chemical equilibrium is achieved. Elemental mass balance and energy balance are included in the model, predicting exit gas temperature, gas composition, and gasification performance.

3.2 **MATERIAL AND METHODS**

This chapter aims to develop a rigorous but straightforward gasification model for designing and simulating a biomass gasification plant. Based on thermodynamic equilibrium calculations, this model includes some modifications for adaptation to real processes, in which only a partial chemical equilibrium is achieved. The molecular form of biomass, the generalized gasification reactions, elemental balance, typical tar values, additional independent chemical reactions, the equilibrium constant, heat balance, and calculation procedure are explained and developed.

3.2.1 FORMULATION OF THE MODEL

The biomass used can be expressed in the molecular form $CH_xO_yN_z$ where the subscripts x, y, z is determined from the last analysis of the biomass to be gasified (Eq. 1).

$$x = \frac{w_H}{PM_H} \;\; ; \;\; y = \frac{w_O}{PM_O} \;\; ; \;\; z = \frac{w_N}{PM_N} \qquad (1)$$

The generalized gasification reaction can be represented as [21][23][36]

$$CH_xO_yN_z + w\,H_2O + m(O_2 + 3.76N_2) = n_{H_2}H_2 + n_{CO}CO + n_{CO_2}CO_2 + n_{H_2O}H_2O + n_{CH_4}CH_4 + \left(\frac{z}{2} + 3.76m\right)N_2 + n_{tar}CH_pO_q \quad (2)$$

Where $n_{H_2}, n_{CO}, n_{CO_2}, n_{H_2O}, n_{CH_4}, n_{N_2}$ and n_{tar} are the number of moles of $H_2, CO, CO_2, H_2O, CH_4, N_2$ and tars respectively, w is the humidity associated with the biomass plus the additional water (w) to achieve the water vapor/biomass ratios, CH_pO_q represents the typical composition of tars [34][37].

The elemental balance of the global gasification reaction (Eq. 2) leads to the following equations.

Carbon balance:

$$n_{CO} + n_{CO_2} + n_{CH_4} + n_{tar} - 1 = 0 \quad (3)$$

Hydrogen balance:

$$2n_{H_2} + 2n_{H_2O} + 4n_{CH_4} + pn_{tar} - x - 2w = 0 \quad (4)$$

Oxygen balance:

$$n_{CO} + 2n_{CO_2} + n_{H_2O} + qn_{tar} - w - 2m - y = 0 \quad (5)$$

The tar s are a mixture of several hydrocarbons and aromatic rings generated from the primary decomposition reactions in the pyrolysis phase [38][39], predict the composition of the tars present in the generated gas using any numerical technique is very difficult to achieve, due to the number and complex mathematical handling of the reactions that favor the formation of tars [25][40]. For this reason, in most models of thermodynamic equilibrium, the formation of tars is not considered [25] [41][42][43]. Due to this difficulty and to predict the composition of the gases of the gasification process, including the formation of tars; in the present model of thermodynamic equilibrium, the composition of the tars as well as their molar fraction (n_{tar}) in the gasification gas products are considered an input parameter in the model [40].

The yield and composition of tars present in the gases generated depend on the gasification temperature, type of reactor, and raw material. Typical values of tars reported by various authors [38][40][44] indicate that the levels of tars in the gases generated in updraft and downdraft gasifiers are $1\,gr/Nm^3$ and $50\ gr/Nm^3$, respectively. For fluidized bed gasifiers, the characteristic tar levels are $10\ gr/Nm^3$

and for drag flow reactors less than $0{,}5\ \mathrm{gr/Nm^3}$. Table 3-1 summarizes the information mentioned.

Table 3-1: Typical values of tars in different types of biomass gasifiers [38][40][44]

Gasifier type	The average concentration of tars in generated gas, $\mathrm{gr/Nm^3}$
Updraft	< 1
Fluidized bed	10
Downdraft	50
Entrained bed	< 0,5

From the literature review, several authors report typical levels of tars in updraft stream gasifiers that work with water vapor as a reaction agent and wood as raw material, ranging from $1-2\ \mathrm{gr/Nm^3}$. An average concentration of tars in the gases generated 2% tars as a percentage of fed biomass [38][40]. Likewise, Barman et al. [23] and Tinaut et al. [45] report 4.5% (percentage by mass fed) as maximum tar content. Experimental results obtained by Milne et al. [40] and Galvagno et al. [46] report $\mathrm{C_nH_pO_q}$ as the representative formula for the composition of tars. It was used to perform a comparative analysis between stoichiometric models and experimental results using different residues (wood) and water vapor as an oxidizing agent.

Iovane et al. [47] reports 1.9% by volume of $\mathrm{C_2H_6}$ in the gasification with the steam of palm kernel in a rotary kiln. Likewise Galvagno et al.[46] reported 1% by volume of $\mathrm{C_2H_6}$. In the gas generated in the gasification of wood with steam in a fixed-bed gasifier with parallel currents and Gómez et al. [48] report 1% by volume of $\mathrm{C_2H_4}$ in gas generated in gasification with palm kernel shell and water vapor in a fixed-bed gasifier. According to the results reported in the bibliographic review of the present study, 4.5% is considered as the average value of the tar yield as a percentage of biomass fed and considers the corresponding molar value ($\mathrm{n_{tar}}$) as an input parameter in the model of balance. The representative formula for tars used has the following composition $\mathrm{C_6H_{6,2}O_{0,2}}$.This value represents the volatile condensable matter used by Tinaut et al. [45] in biomass gasification in a fixed-bed gasifier.

Several authors have shown that under gasification conditions, the only species present are $\mathrm{CO, CO_2, H_2O, CH_4, H_2}$tars and solid carbon C [38][18], when this system of components is considered and applying the phase rule [18][49], there would be four independent chemical reactions. For the case raised in this work where the

composition and molar fraction of the tars generated are known, it is also assumed that the solid carbon does exist in a state of equilibrium (defined by a percentage %). The species system is reduced to a homogeneous system that is composed of $CO, CO_2, H_2O, CH_4, H_2$ in such a way, two additional independent chemical reactions are necessary to solve equations 3, 4, and 5.

Three reaction systems are used when solid carbon is considered in the products of the gasification process [18]:

Water-gas shift reaction: $CO + H_2O = CO_2 + H_2$

$$K_1 = \frac{(n_{CO_2})(n_{H_2})}{(n_{CO})(n_{H_2O})} \qquad (6)$$

Where the equilibrium constant K_1 is evaluated from the following relation (Eq. 7) [46], where T is in K.

$$K_1 = e^{\left\{\frac{4000}{T} - 3{,}5\right\}} \qquad (7)$$

Methane formation reaction: $C + 2H_2 = CH_4$

$$K_2 = \frac{(n_{CH_4})(n_{total})}{(n_{H_2})^2} \qquad (8)$$

The equilibrium constant K_2 is evaluated from the following relation [50], where T is in K.

$$K_2 = e^{\left\{\frac{10000}{T} - 12{,}2\right\}} \qquad (9)$$

Due to the difference in design in parallel stream gasifiers, the composition of the gases generated by this equipment will be different. Many authors have modified the equilibrium models, including experimental results, to improve the precision in predicting the composition of the gases generated. Works reported by Barman et al. [23], Jarungthammachote et al. [50], and Jayah et al. [51] consider equations 3, 4, 5, 6, and 8 in their model. During the validation of the experimental results of Jayah et al. [51], it was observed that to validate their model with the experimental results, more quantity of reaction agent had to be considered. The meaning of this observation is that to satisfy the percentage of moles of methane, more quantity of reaction agent was required. That is why, to take this condition into account in the proposed model, the methane reforming reaction is incorporated into the model, excluding the carbon balance (Eq.3). Even if carbon balance is excluded, a compliance check is performed on the implemented code.

Methane Reforming Reaction: $CH_4 + H_2O = CO + 3H_2$

$$K_3 = \frac{(n_{CO})(n_{H_2}{}^3)}{(n_{CH_4})(n_{H_2O})(n_{total}{}^2)} \quad (10)$$

The equilibrium constant K_3 is expressed as:

$$K_3 = 1.198x\,10^{13}\, e^{\frac{-26830}{T}} \quad (11)$$

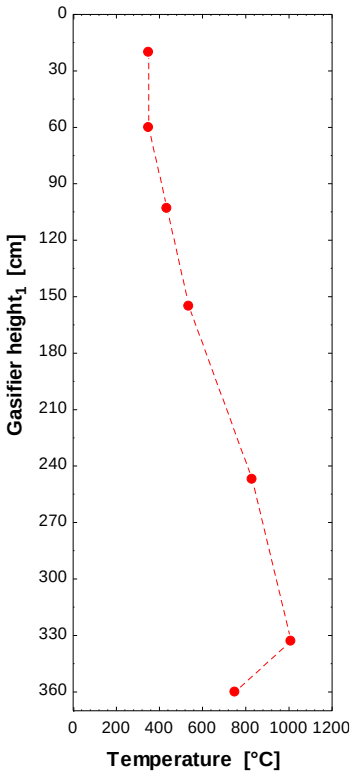

Figure 3-1: Temperature gradient along the height of the downdraft gasifier.

The heat balance was then incorporated into the model, using validated results of the gasification temperature along the gasifier. The size of the gasifier was built using a unitary temperature gradient (shown in figure 3-1), and the heat loss across the gasifier was defined by the user fixing a percentage of the dry biomass flow product entering the system (kg/h) and its LHV (kJ/kg). The streams' kinetic and potential energy changes were neglected, and the steady-state, steady flow energy equation was applied. When the temperature in the gasification zone was T_i and the temperature at the inlet to the gasifier was assumed to be 298 K (25 °C), the enthalpy balance is shown in Eq. 12-14

$$H_{reactant} + Q_{in} = H_{products} + Q_{out} \quad (12)$$

$$H_{reactant} = h^{\circ}_{f\,biomass} + w\left[h^{\circ}_{f\,moisture} + \int_{298}^{T_i} C_{p\,moisture} * dT_i\right] \quad (13)$$

$$H_{products} = \sum_{products} n_i \left[h^{\circ}_{fi} + \int_{298}^{T_i} C_{pi} * dT_i\right] + n_{tar} * h^{\circ}_{ftar} \quad (14)$$

The Q_{in} and Q_{out} are estimated by the user as a percentage of biomass energy input to the system using experimental data. The specific heat (C_p) was assumed as a function of temperature as shown in Eq. (15-16) below Jarungthammachote et al. [50]. T is in Kelvin and C_p is in $kJ/kmol.K$.

$$C_p = a + b.T_i + c.T_i{}^2 + d.T_i{}^3 \quad (15)$$

$$\int_{298}^{T_i} C_p\,(T_i) * dT_i = \left[a.T_i + b.\frac{T_i^{\,2}}{2} + c.\frac{T_i^{\,3}}{3} + d.\frac{T_i^{\,4}}{4}\right]_{298}^{T_i} \qquad (16)$$

Where a,b,c,d are the values of the coefficients and are given in table 3-2 used by Jarungthammachote et al. [50].

Table 3-2: Coefficients for specific heat for the empirical equation (Taken from [50][52])

Gas species	a	b	c	d	Temperature range (K)
H_2	29.11	$-0.1916\ x10^{-2}$	$0.4003\ x10^{-5}$	$-0.8704\ x10^{-9}$	273-1800
CO	28.16	$0.1675\ x10^{-2}$	$0.5372\ x10^{-5}$	$-2.222\ x10^{-9}$	273-1800
CO_2	22.26	$5.981\ x10^{-2}$	$-3.501\ x10^{-5}$	$-7.469\ x10^{-9}$	273-1800
$H_2O(steam)$	32.24	$0.1923\ x10^{-2}$	$1.055\ x10^{-5}$	$-3.595\ x10^{-9}$	273-1800
CH_4	19.89	$5.204\ x10^{-2}$	$1.269\ x10^{-5}$	$-11.01\ x10^{-9}$	273-1800
N_2	28.90	$-0.1571\ x10^{-2}$	$0.8081\ x10^{-5}$	$-2.973\ x10^{-9}$	273-1800

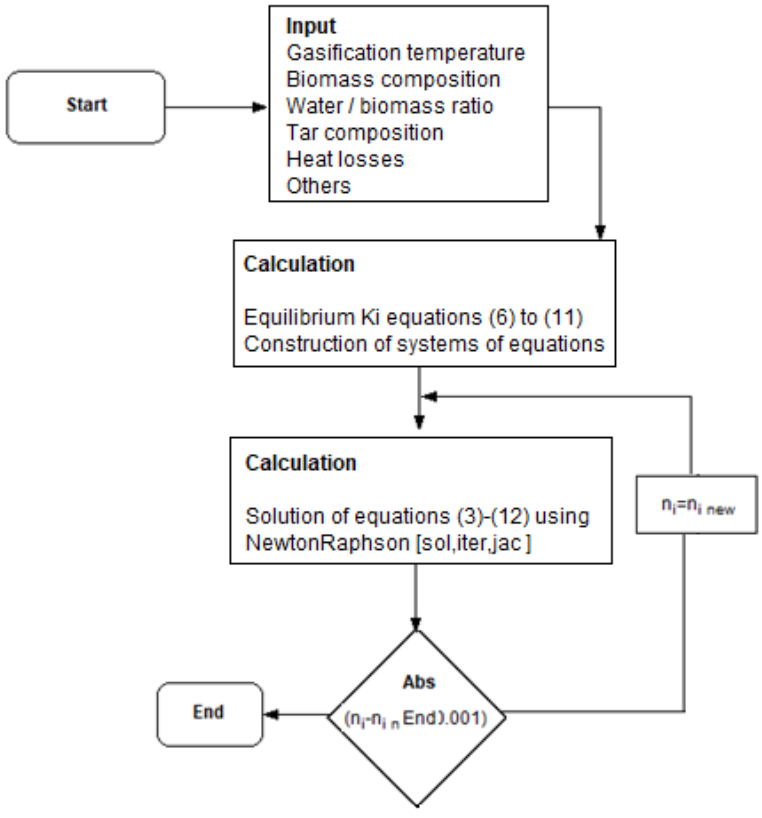

Figure 3-2: Resolution diagram of the developed model.

The calculation procedure (figure 3-2) begins with the entry of the gasification temperature, biomass composition, the water/biomass ratio, tar composition, heat losses in the gasification unit (the user estimates these heat losses as a percentage of biomass energy input to the system),; with these values, are calculate the equilibrium constants K_1, K_2 and K_3, once the equilibrium constants are defined, the non-linear system of equations is constructed that will be solved by the Newton-Raphson method. The results are used to calculate the percentages per volume of dry gas of each component. Utilizing this iterative method (figure 3-2), the gasification temperature increases, and the gas composition values are obtained for each gasification temperature considered.

3.3 **RESULT AND DISCUSSION**

3.3.1 VALIDATION OF THE MODEL

The previously described equilibrium model is used to predict the gas composition in biomass gasification using the equation-solving program "Engineering Equation Solver" (EES). EES allows for numerical solutions of algebraic equations, linear and non-linear differential equations, using already built-in thermodynamic functions with high-quality fluid property data and numerical integration.

The gasification model is composed of a system of equations, including the generalized gasification reaction (Eq. 2), with the elemental balance of the global reaction (Eq. 3-11), and inclusion of tars formation and composition. Likewise, the heat balance was incorporated with the use of experimental temperature profiles and the specific heat (C_p) coefficients of empirical equations used in previous works Puig-Arnavat et al. [22], Balu et al. [52], and Jarungthammachote et al. [50]. The model developed includes a communication interface (figure 3-3) with the user that allows defining the inputs (mass flows, fuel data from the ultimate analysis of the biomass, temperatures, percentage of ash, and heat losses) to adjust the model to experimental conditions.

Tables 3-3, 3-4, 3-5 and figure 3-3 summarize the type of fuel and gasifier, oxidizing agent, fuel data, temperatures, heat losses, and char defined to validate the model. The equilibrium model was used to predict the gas composition for the gasification of various biomass and oxidizing agents (air, air + steam, and steam). Figure 3-4 compares the results obtained in the equilibrium model used, with the experimental results reported by Jayah et al. [51], Erlich et al. [54], Trninić et al. [53], Ngamchompoo et al. [55], Pang et al. [57], and Balu et al. [52]. The compositions

obtained are on a vol % dry basis; the gasification temperature and the oxidizing agent/biomass ratio used are shown in Tables 3-3 and 3-5. The data was obtained and confirm a less than 10% variation when comparing the proposed model's compositions with the reported experimental results. Therefore, it is verified that the proposed equilibrium model reproduces the real operation with an acceptable degree of deviation.

Table 3-3: Identification and mass flow description in a modified equilibrium model

Ref.	**Type of fuel**	**Type of gasifier**	**Oxidizing agent**	**Dry biomass (kg/h)**	**Steam (kg/h)**	**% O_2**
[51][53]	Rubberwood	Downdraft	Air	18.6	0	21
[54]	Sugarcane bagasse	Downdraft	Air	2.7-3.5	0	21
[54]	Empty fruit bunch	Downdraft	Air	2-3.3	0	21
[53]	Sawdust	Downdraft	Air	15	0	21
[55]	Eucalyptus wood	Downdraft	Air + Steam	15	1.5	21
[56]	Coconut Shell	Downdraft	Air+ Stream	15	2.7	21
Own	Palm kernel shell	Downdraft	Steam	57.1	48.53	0
[57]	Corn stalk	Downdraft	Steam	1.25	0.45-1.20	0
[52]	Wood	Downdraft	Steam	1	2.5	0

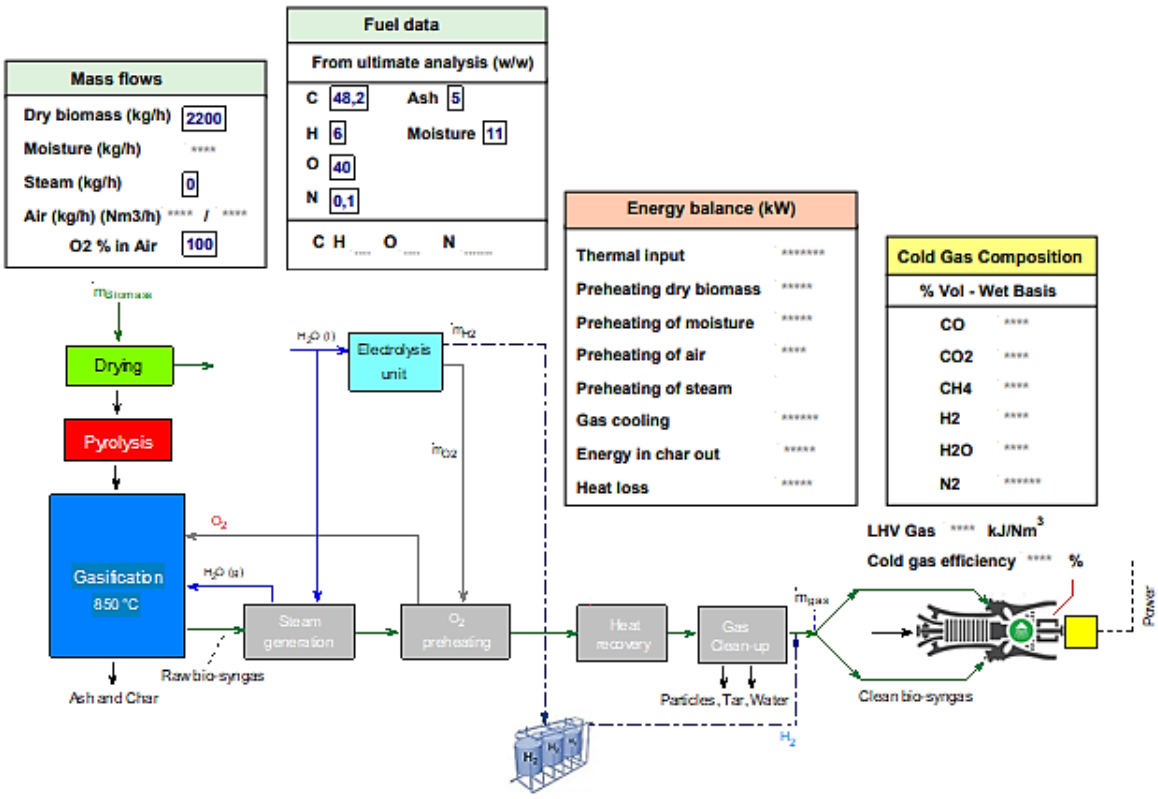

Figure 3-3: Schematic of the modified equilibrium model, developed in EES software

Table 3-4: Fuel data from ultimate analysis

Ref	Type of fuel	C (%)	H (%)	O (%)	N (%)	Ash (%)	Moisture (%)
[51][53]	Rubber wood	50.6	6.5	42	0.2	0.7	18.5
[54]	Sugarcane bagasse	48.2	6.1	44.3	0.3	1.1	9.7
[54]	Empty fruit bunch	47.2	6	38.2	0.6	7.9	11
[53]	Sawdust	52	6.07	41.55	0.25	0.1	15
[55]	Eucalyptus wood	45.69	4.65	50.32	0	4.56	11.33
[56]	Coconut Shell	50.2	5.4	43.4	0.94	12.44	8.55
Own	Palm kernel shell	48.2	6.0	40	0.1	5	11
[57]	Corn stalk	47.8	6.3	44.12	0.36	1.36	6.21
[52]	Wood	1	1.5	0.67	0.1	2	7

Table 3-5: Gasifier operating conditions of the experiments used for model validation

Ref	Type Of fuel	Inlet Temperatures (°C)					Heat loss	Other
		Biomass	Steam	Air	Gas (outlet)	Gasification	% Thermal input	Char (%)
[51][53]	Rubber wood	70	0	600	150	750	15	3.76
[54]	Sugarcane bagasse	70	0	300	150	900	6.5	1
[54]	Empty fruit bunch	70	0	450	50	725	15.5	1
[53]	Sawdust	70	0	400	50	950	10	1
[55]	Eucalyptus wood	100	450	450	50	850	10	1
[56]	Coconut Shell	100	400	400	50	950	2	1
Own	Palm kernel shell	180	600	0	70	850	5	10
[57]	Corn stalk	150	500	0	80	850	7	10
[52]	Wood	200	1000	0	100	900	10	5

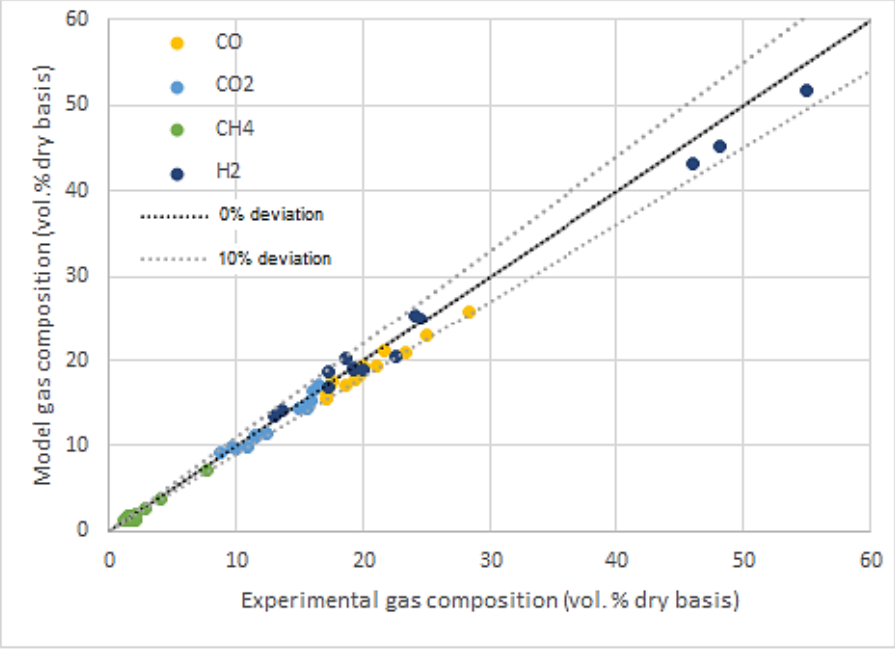

Figure 3-4: Comparison of predicted results from the modified equilibrium model to experimental data from Jayah et al. [51], Erlich et al. [54], Trninić et al. [53], Ngamchompoo et al. [55], Pang et al. [57], and Balu et al. [52]

3.3.2 SYNGAS COMPOSITION AND HEATING VALUES

The previously described equilibrium model is used to predict the composition of gases and the calorific value in biomass gasification with air, air + water vapor, and only water vapor as a gasifying agent. The results obtained are presented in figures 3-5 and 3-6, the thermodynamic equilibrium model was evaluated at 850 °C, and oxidizing agent/biomass ratios of 0.3 to 1.2 respectively. To explain the results obtained in figure 3-5 and 3-6, the following set of reactions was selected as representative of the biomass gasification process:

$$C + CO_2 \leftrightarrow 2CO \quad \Delta H = +172\ \text{kJ/mol} \tag{17}$$

$$C + H_2O \leftrightarrow CO + H_2 \quad \Delta H = +131\ \text{kJ/mol} \tag{18}$$

$$C + 2H_2 \leftrightarrow CH_4 \quad \Delta H = -74.8\ \text{kJ/mol} \tag{19}$$

$$CO + H_2O \leftrightarrow CO_2 + H_2 \quad \Delta H = -41.2\ \text{kJ/mol} \tag{20}$$

$$CH_4 + H_2O \leftrightarrow CO + 3H_2 \quad \Delta H = +206\ \text{kJ/mol} \tag{21}$$

The only homogeneous reactions are the shift reaction equation (20) and steam-reforming reaction equation (21); the other presented reactions are classified as heterogeneous (17-19). The speed with which the char (consisting mainly of carbon) gasifies depends mainly on its reactivity and the gasification medium reaction potential. Since the gasification process is carried out in the absence of oxygen and water vapor as the oxidizing agent, the predominant reaction is the water-gas or steam reaction equation (18), followed by the shift reaction equation (20). When the gasifying medium is air or oxygen, the Boudouard reaction equation (17), hydrogasification equation (19), and the steam-reforming reaction equation (21) are dominant [7][20]. Based on the above, the relative order of the heterogeneous reaction rates can be summarized as: $R_{C+O_2} \gg R_{C+H_2O} \gg R_{C+CO_2} \gg R_{C+H_2}$ [7]. Likewise, the homogeneous reaction equation (20) is responsible for increasing the hydrogen content in the gasification products at the expense of carbon monoxide, the shift reaction is slightly exothermic, and under equilibrium conditions, the yield of the products decreases slowly with temperature [7][58].

Researchers like Cheng et al. [59] demonstrated the existence of a relative impact in the composition of the gasification products (CO, CO_2, CH_4 and H_2) of 42% due to the biomass characteristics, 21 % of gasification temperature, 10% of particle size, 10 % of the inner diameter of the gasifier, 9 % of the height of gasifier, and 8% of equivalence ratio. For the correct analysis of the equilibrium model results, it is essential to remember that the equilibrium of the reactions is characterized by the equilibrium constant (Eq. 7, 9, and 11). Therefore, a high value for the equilibrium

constant indicates that the reaction favors the formation of products, and a low value for the equilibrium constant favors reactants [60].

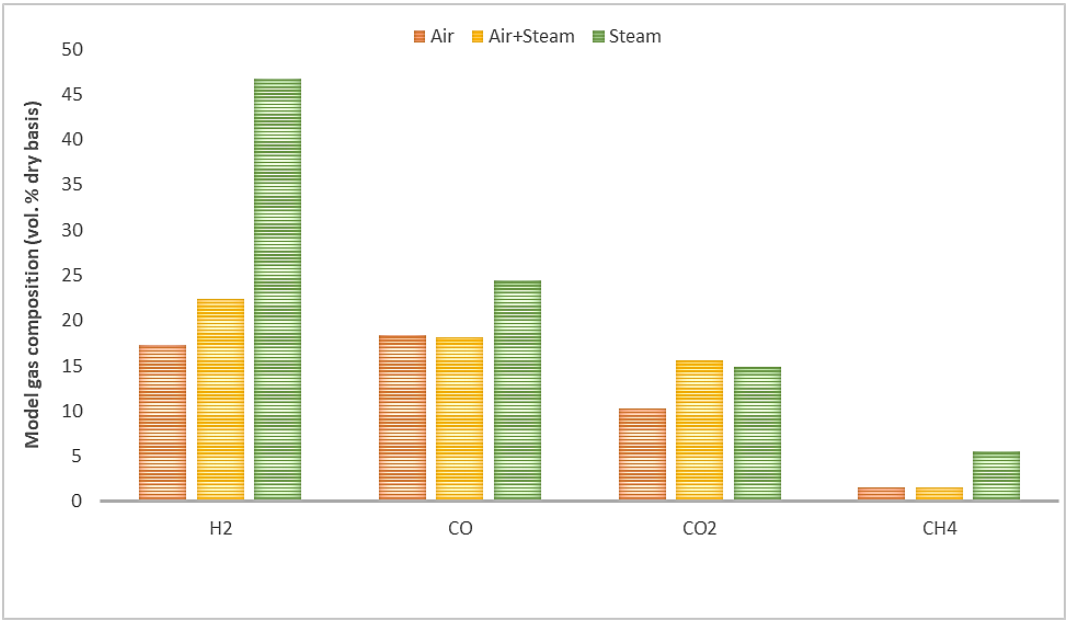

Figure 3-5: Comparison of model gas composition between air, air + steam, and steam gasification

When analyzing figures 3-5 and 3-6 and the information in tables 3-3 – 3-5, it is observed that increasing the temperature favors the formation of carbon monoxide and hydrogen—likewise, the decrease in temperature in the formation of carbon dioxide and methane. The results agree that as the temperature increases, the constants K_1, and K_2 (eq. 7 and 9) decrease under equilibrium conditions favors the formation of reactants. Therefore, it is observed that in the case of water vapor as the oxidizing agent, it influences the gas composition; increasing the water vapor/biomass ratio necessarily promotes hydrogen gas formation at the expense of carbon monoxide in gasification. This change in the concentration of H_2 and CO is due to the high activity of the water-gas displacement reaction (eq. 18) within this temperature range. Likewise, both the formation of the products CO of the water-gas displacement reaction (eq. 20) and H_2 of the methane formation reaction (eq. 21) are favored.

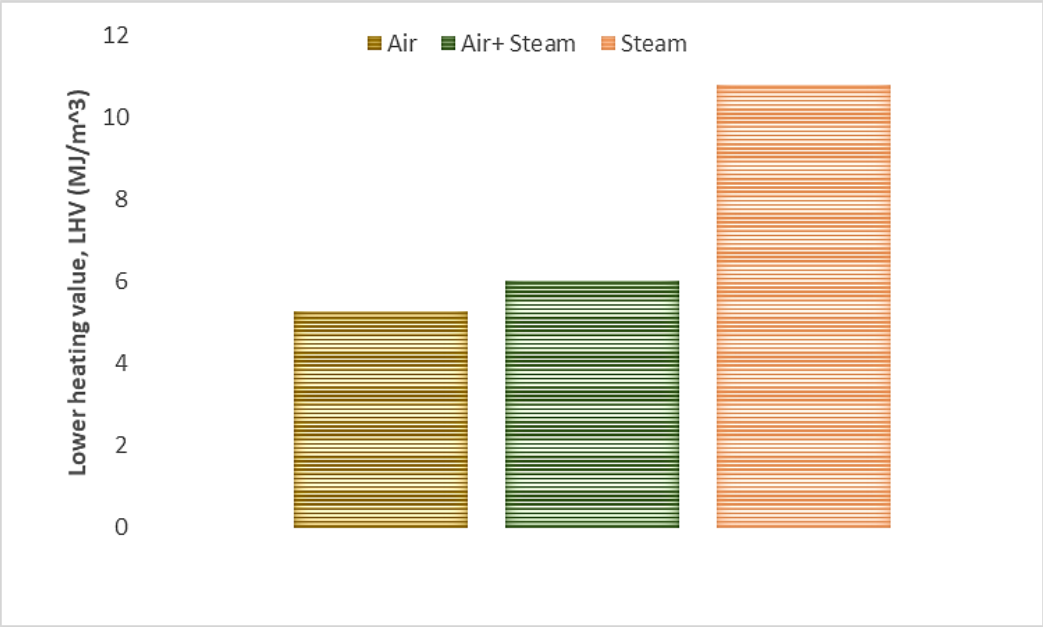

Figure 3-6: Comparison of Lower heating value (LHV) between air+ air + steam and steam gasification

Finally, for a gasification temperature of $850\,℃$ and steam as an oxidizing agent, hydrogen increased in the gas composition by 52% compared to air + steam and 63% higher than air as an oxidizing agent. CO increased 26% more than air + steam and 25% higher than air as an oxidizing agent for the same conditions. CO2 production increased slightly by 5% more than air + steam and 25% higher than air as an oxidizing agent. Likewise, the CH_4 production increased by 72% more than air + steam and 71% higher than air as an oxidizing agent. Finally, when more steam is supplied than biomass in the gasification zone, the remaining char and methane are transformed into H_2 and CO. On the other hand, CO is reduced due to the homogeneous water-gas displacement reaction promoted by steam. Therefore, the increase in water vapor significantly promotes the formation of H_2 at the expense of the decrease in CH_4, $\text{and}\ CO$ which translates into a decrease in lower calorific value (LHV). Thus, LHV of the resulting gas presented an increase of 44% compared to air + steam and 51% higher than with air as an oxidizing agent (figure 3-6).

3.4 **CONCLUSIONS**

This study presents a numerical model capable of simulating the gasification process in a downdraft gasifier and will use in chapter 6 to analyze the integration of gasifier + electrolyzer + turbine + DENN in polygeneration systems. The equilibrium model

was used to predict the gas composition in the gasification of various biomass and oxidizing agents (air, air + steam, and steam). Likewise, the model is implemented in the "Engineering Equation Solver (EES)" equation solving program and includes a communication interface with the user that allows defining the inputs (mass flow rates, fuel data from the final analysis of the biomass, temperatures, ash percentage, and heat losses) to adjust the model to experimental conditions. The proposed equilibrium model is validated using real data and reproduces the real operation with a 10 % of deviation and allows predicting, analyzing, and comparing gasification processes with different oxidizing agents (air, air + steam, and steam) to estimate the trend in the composition of the gas, calorific value, and energy balance.

The numerical run indicated that temperature is the most crucial factor in the gasification process; low temperatures favor CO production, and high temperatures the production of H_2. Additionally, the concentration of CO_2 and CH_4 increase when temperatures decrease. These results are explained by the fact that at temperatures of 850 $^{\circ}C$, the heterogeneous water-gas reactions and the homogeneous water-gas displacement reaction (equations 20 and 21) favored the greater formation of H_2 at the expense of CO and CH_4.

Finally, when comparing the three oxidizing agents, steam showed a higher capacity to generate hydrogen than air + steam and air by 52% and 63%, respectively. Likewise, a higher capacity to generate higher LHV than air + steam and air by 44 % and 51%, respectively.

3.5 REFERENCES

[1] H. Balat and E. Kirtay, “Hydrogen from biomass - Present scenario and future prospects,” Int. J. Hydrogen Energy, vol. 35, no. 14, pp. 7416–7426, 2010, doi: 10.1016/j.ijhydene.2010.04.137.

[2] J. S. Tumuluru, Biomass Preprocessing and Pretreatments for Production of Biofuels. 2018.

[3] I. Hannula, “Hydrogen production via thermal gasification of biomass in near-to-medium term Hydrogen production via thermal gasification of biomass in near-to-medium term,” 2009. [Online]. Available: http://www.vtt.fi/publications/index.jsp.

[4] A. Indarto, Syngas Production, Applications and environmental impact. 2554.

[5] I. Dincer, “Green methods for hydrogen production,” Int. J. Hydrogen Energy, vol. 37, no. 2, pp. 1954–1971, 2012, doi: 10.1016/j.ijhydene.2011.03.173.

[6] S. Heidenreich and P. Ugo, “New concepts in biomass gasi fi cation,” Prog. Energy Combust. Sci., vol. 46, pp. 72–95, 2015, doi: 10.1016/j.pecs.2014.06.002.

[7] P. Basu, Biomass Gasification and Pyrolysis. Burlington, USA: Elsevier Inc., 2010.
[8] P. Plis and R. K. Wilk, “Theoretical and experimental investigation of biomass gasification process in a fixed bed gasifier,” Energy, vol. 36, no. 6, pp. 3838–3845, 2011, doi: 10.1016/j.energy.2010.08.039.
[9] Y. Ueki, T. Torigoe, H. Ono, R. Yoshiie, J. H. Kihedu, and I. Naruse, “Gasification characteristics of woody biomass in the packed bed reactor,” Proc. Combust. Inst., vol. 33, no. 2, pp. 1795–1800, 2011, doi: 10.1016/j.proci.2010.07.080.
[10] Y. H. Li et al., “A novel dual-bed for steam gasification of biomass,” Biomass Convers. Biorefinery, vol. 8, no. 2, pp. 357–367, 2018, doi: 10.1007/s13399-017-0288-0.
[11] J. Hrbek, “Status report on thermal biomass gasification in countries participating in IEA Bioenergy Task 33,” 2016. [Online]. Available: http://www.ieatask33.org/content/publications/Status_report%5Cnhttp://www.ieatask33.org/app/webroot/files/file/2016/Status_report.pdf.
[12] M. Milhé, L. Van De Steene, M. Haube, J. M. Commandré, W. F. Fassinou, and G. Flamant, “Autothermal and allothermal pyrolysis in a continuous fixed bed reactor,” J. Anal. Appl. Pyrolysis, vol. 103, pp. 102–111, 2013, doi: 10.1016/j.jaap.2013.03.011.
[13] P. J. Woolcock and R. C. Brown, “A review of cleaning technologies for biomass-derived syngas,” Biomass and Bioenergy, vol. 52, pp. 54–84, 2013, doi: 10.1016/j.biombioe.2013.02.036.
[14] S. M. Atnaw, S. A. Sulaiman, and S. Yusup, “Syngas production from downdraft gasification of oil palm fronds,” Energy, vol. 61, pp. 491–501, 2013, doi: 10.1016/j.energy.2013.09.039.
[15] M. Asadullah, “Barriers of commercial power generation using biomass gasification gas: A review,” Renew. Sustain. Energy Rev., vol. 29, pp. 201–215, 2014, doi: 10.1016/j.rser.2013.08.074.
[16] F. Guo, Y. Dong, L. Dong, and C. Guo, “Effect of design and operating parameters on the gasification process of biomass in a downdraft fixed bed: An experimental study,” Int. J. Hydrogen Energy, vol. 39, no. 11, pp. 5625–5633, 2014, doi: 10.1016/j.ijhydene.2014.01.130.
[17] T. K. Patra and P. N. Sheth, “Biomass gasification models for downdraft gasifier: A state-of-the-art review,” Renew. Sustain. Energy Rev., vol. 50, pp. 583–593, 2015, doi: 10.1016/j.rser.2015.05.012.
[18] M. Vaezi, M. Passandideh-Fard, M. Moghiman, and M. Charmchi, “Gasification of heavy fuel oils: A thermochemical equilibrium approach,” Fuel, vol. 90, pp. 1–8, 2011, doi: 10.1016/j.fuel.2010.10.011.
[19] X. Li, J. R. Grace, A. P. Watkinson, C. J. Lim, and A. Ergu, “Equilibrium modeling of gasification : a free energy minimization approach and its application to a circulating fluidized bed coal gasifier,” Fuel, vol. 80, pp. 1–13, 2001.
[20] C. Franco, F. Pinto, I. Gulyurtlu, and I. Cabrita, “The study of reactions influencing the biomass steam gasification process,” FUEL, vol. 82, pp. 1–8, 2003.

[21] H. Luo, “Modelling of Biomass Combustion and Gasification : from Particle-scale to Reactor-scale Hao Luo,” 2019.
[22] M. Puig-Arnavat, J. C. Bruno, and A. Coronas, “Modified thermodynamic equilibrium model for biomass gasification: A study of the influence of operating conditions,” Energy and Fuels, vol. 26, no. 2, pp. 1385–1394, 2012, doi: 10.1021/ef2019462.
[23] N. S. Barman, S. Ghosh, and S. De, “Gasification of biomass in a fixed bed downdraft gasifier a realistic model including tar,” Bioresour. Technol., vol. 107, pp. 1–7, 2012, doi: 10.1016/j.biortech.2011.12.124.
[24] P. Dutta, V. Pandey, A. Das, S. Sen, and D. Baruah, “Down Draft Gasification Modelling and Experimentation of Some Indigenous Biomass for Thermal Applications,” Energy Procedia, vol. 54, pp. 1–14, 2014, doi: 10.1016/j.egypro.2014.07.246.
[25] A. Mendiburu, J. Carvalho, and C. Coronado, “Thermochemical equilibrium modeling of biomass downdraft gasifier: Stoichiometric models,” Energy, vol. 66, pp. 1–13, 2014, doi: 10.1016/j.energy.2013.11.022.
[26] Z. Khan, A. Inayat, S. Yusup, and M. Ahmad, “Kinetic parameters determination using optimization approach in integrated catalytic adsorption steam gasification for hydrogen production,” Int. J. Hydrogen Energy, vol. 40, pp. 1–9, 2015, doi: 10.1016/j.ijhydene.2015.05.069.
[27] R. Budhathoki, “Three zone modeling of Downdraft biomass Gasification : Equilibrium and finite Kinetic Approach,” University of Jyväskylä, 2013.
[28] J. F. Vélez, F. Chejne, C. F. Valdés, E. J. Emery, and C. A. Londoño, “Co-gasification of Colombian coal and biomass in fluidized bed : An experimental study,” Fuel, vol. 88, no. 3, pp. 424–430, 2009, doi: 10.1016/j.fuel.2008.10.018.
[29] E. Biagini, F. Barontini, and L. Tognotti, “Development of a bi-equilibrium model for biomass gasification in a downdraft bed reactor,” Bioresour. Technol., vol. 201, pp. 156–165, 2016, doi: 10.1016/j.biortech.2015.11.057.
[30] H. Ishaq, S. Islam, I. Dincer, and B. S. Yilbas, “Development and performance investigation of a biomass gasification based integrated system with thermoelectric generators,” J. Clean. Prod., vol. 256, p. 120625, 2020, doi: 10.1016/j.jclepro.2020.120625.
[31] I. S. Antonopoulos, A. Karagiannidis, A. Gkouletsos, and G. Perkoulidis, “Modelling of a downdraft gasifier fed by agricultural residues.,” Waste Manag., vol. 32, pp. 1–9, 2012, doi: 10.1016/j.wasman.2011.12.015.
[32] S. Sivakumar, K. Pitchandi, and E. Natarajan, “Design and Analysis Of Down Draft Biomass Gasifier using Computational Fluid Dynamics,” India.
[33] R. Mikulandrić, D. Lončar, D. Böhning, R. Böhme, and M. Beckmann, “Artificial neural network modelling approach for a biomass gasification process in fixed bed gasifiers,” Energy Convers. Manag., vol. 87, pp. 1–14, 2014, doi: 10.1016/j.enconman.2014.03.036.
[34] A. Gagliano, F. Nocera, F. Patania, M. Bruno, and D. G. Castaldo, “A robust numerical model for characterizing the syngas composition in a downdraft gasification process,” Comptes Rendus Chim., vol. 19, no. 4, pp. 441–449, 2016, doi: 10.1016/j.crci.2015.09.019.

[35] P. Baggio, M. Baratieri, L. Fiori, M. Grigiante, D. Avi, and P. Tosi, “Experimental and modeling analysis of a batch gasification / pyrolysis reactor,” Energy Convers. Manag., vol. 50, no. 6, pp. 1426–1435, 2009, doi: 10.1016/j.enconman.2009.03.004.

[36] M. Puig-Arnavat, J. C. Bruno, and A. Coronas, “Review and analysis of biomass gasification models,” Renew. Sustain. Energy Rev., vol. 14, no. 9, pp. 2841–2851, 2010, doi: 10.1016/j.rser.2010.07.030.

[37] G. Ravenni, “Application of biomass char to tar conversion and producer gas upgrading to syngas,” 2018.

[38] J. Fjellerup, B. Gøbel, J. Ahrenfeldt, and U. Henriksen, Formation , Decomposition and Cracking of Biomass Tars in Gasification. Denmark: Technical University of Denmark, 2005.

[39] A. Molino, S. Chianese, and D. Musmarra, “Biomass gasification technology: The state of the art overview,” J. Energy Chem., vol. 25, no. 1, pp. 10–25, 2016, doi: 10.1016/j.jechem.2015.11.005.

[40] T. A. Milne and R. J. Evans, “Biomass Gasifier Tars : Their Nature , Formation , and Conversion,” Natl. Renew. Energy Laboratoy, pp. 1–204, 1998.

[41] M. V. Ramanan, E. Lakshmanan, R. Sethumadhavan, and S. Renganarayanan, “Performance prediction and validation of equilibrium modeling for gasification of cashew nut shell char,” Brazilian J. Chem. Eng., vol. 25, pp. 1–17, 2008.

[42] C. Koroneos and S. Lykidou, “Equilibrium modeling for a downdraft biomass gasifier for cotton stalks biomass in comparison with experimental data,” J. Chem. Eng. Mater. Sci., vol. 2, pp. 1–8, 2011.

[43] J. Ratnadhariya and S. Channiwala, “Three zone equilibrium and kinetic free modeling of biomass gasifier – a novel approach,” Renew. Energy, vol. 34, pp. 1–9, 2009, doi: 10.1016/j.renene.2008.08.001.

[44] K. Patil, P. Bhoi, R. Huhnke, and D. Bellmer, “Biomass downdraft gasifier with internal cyclonic combustion chamber: design, construction, and experimental results.,” Bioresour. Technol., vol. 102, pp. 1–5, 2011, doi: 10.1016/j.biortech.2011.03.033.

[45] F. V Tinaut, A. Melgar, J. F. Pérez, and A. Horrillo, “Effect of biomass particle size and air superficial velocity on the gasification process in a downdraft fixed bed gasifier. An experimental and modelling study,” Fuel Process. Technol., vol. 89, pp. 1–14, 2008, doi: 10.1016/j.fuproc.2008.04.010.

[46] S. Galvagno et al., “Steam gasification of tyre waste, poplar, and refuse-derived fuel: A comparative analysis,” Waste Manag., vol. 29, pp. 1–12, 2009, doi: 10.1016/j.wasman.2008.06.003.

[47] P. Iovane, A. Donatelli, and A. Molino, “Influence of feeding ratio on steam gasification of palm shells in a rotary kiln pilot plant. Experimental and numerical investigations,” Biomass and Bioenergy, vol. 56, pp. 1–9, 2013, doi: 10.1016/j.biombioe.2013.05.025.

[48] A. Gómez, S. Rincón, and W. Wiest, “Transformación termoquímica de la biomasa residual del proceso de extracción del aceite de palma : tecnologías y perspectivas Thermochemical Transformation of the Residual Biomass from the Palm Oil Extraction Process : Technologies and Prospects,” Palmas,

vol. 25, pp. 1–10, 2004.

[49] M. J. MORAN and H. N. SHAPIRO, Fundamentos de Termodinámica Técnica, 2004th ed. Editorial Reverté, S.A, 2004.

[50] S. Jarungthammachote and A. Dutta, “Thermodynamic equilibrium model and second law analysis of a downdraft waste gasifier,” Energy, vol. 32, pp. 1–10, 2007, doi: 10.1016/j.energy.2007.01.010.

[51] T. Jayah, L. Aye, R. Fuller, and D. Stewart, “Computer simulation of a downdraft wood gasifier for tea drying,” Biomass and Bioenergy, vol. 25, pp. 1–11, 2003, doi: 10.1016/S0961-9534(03)00037-0.

[52] E. Balu, U. Lee, and J. N. Chung, “High temperature steam gasification of woody biomass - A combined experimental and mathematical modeling approach,” Int. J. Hydrogen Energy, vol. 40, no. 41, pp. 14104–14115, 2015, doi: 10.1016/j.ijhydene.2015.08.085.

[53] M. Trninić, D. Stojiljković, N. Manić, Ø. Skreiberg, L. Wang, and A. Jovović, “A mathematical model of biomass downdraft gasification with an integrated pyrolysis model,” Fuel, vol. 265, no. December 2019, p. 116867, 2020, doi: 10.1016/j.fuel.2019.116867.

[54] C. Erlich and T. H. Fransson, “Downdraft gasification of pellets made of wood , palm-oil residues respective bagasse : Experimental study,” Appl. Energy, vol. 88, no. 3, pp. 899–908, 2011, doi: 10.1016/j.apenergy.2010.08.028.

[55] W. Ngamchompoo and K. Triratanasirichai, “Experimental investigation of high temperature air and steam biomass gasification in a fixed-bed downdraft gasifier,” Energy Sources, Part A Recover. Util. Environ. Eff., vol. 39, no. 8, pp. 733–740, Apr. 2017, doi: 10.1080/15567036.2013.783657.

[56] R. Alipour Moghadam, S. Yusup, W. Azlina, S. Nehzati, and A. Tavasoli, “Investigation on syngas production via biomass conversion through the integration of pyrolysis and air-steam gasification processes,” Energy Convers. Manag., vol. 87, pp. 670–675, 2014, doi: 10.1016/j.enconman.2014.07.065.

[57] Y. Pang, S. Shen, and Y. Chen, “High Temperature Steam Gasification of Corn Straw Pellets in Downdraft Gasifier: Preparation of Hydrogen-Rich Gas,” Waste and Biomass Valorization, vol. 10, no. 5, pp. 1333–1341, May 2019, doi: 10.1007/s12649-017-0143-3.

[58] P. Parthasarathy and K. S. Narayanan, “Hydrogen production from steam gasification of biomass: Influence of process parameters on hydrogen yield - A review,” Renew. Energy, vol. 66, pp. 1–10, 2014, doi: 10.1016/j.renene.2013.12.025 Review.

[59] G. Cheng et al., “Allothermal gasification of biomass using micron size biomass as external heat source,” Bioresour. Technol., vol. 107, pp. 471–475, 2012, doi: 10.1016/j.biortech.2011.12.074.

[60] R. Sonia, G. Alexáder, and K. Wolfgang, Gasificación de biomasa residual de procesamiento agroindustrial Gasificación de carbonizados. Kassel: Kassel University, 2011.

Chapter4 HYDROGEN-RICH SYNGAS PRODUCTION FROM BIOMASS ON A DOWNDRAFT ALLOTHERMAL GASIFIER USING STEAM AS A GASIFYING AGENT

Summary: The main contribution of the present chapter consists of the investigation of the steam gasification of palm kernel shells (PKS) for hydrogen-rich N_2-free syngas production in a pilot-scale atmospheric downdraft allothermal gasifier. The feedstock material characterization, description of the gasifier design, auxiliary systems, operating conditions, and evaluation of the operating methodology for obtaining fuel gas are presented. The gasification equipment was tested under gasification temperatures between $800 \text{ and } 950\ ^{\circ}C$ and steam-biomass mass ratios between 0,2 and 1,2. The maximum H_2 generation is achieved with a gasification temperature of $850\ ^{\circ}C$, steam/biomass ratio of $0{,}85$, particle sizes of 2 - 3 mm, and biomass feed of $57{,}1\ kg/h$. The volume fraction of $H_2 + CO$ can reach 80,4 %, and maximum cold gas efficiency of 80 % with an average lower calorific value of $11{,}5\ MJ/Nm^3$. This experimental data will use to improve the mathematical model (developed in chapter 3) and increase the capacity to predict the gas composition in the gasification of various biomass and oxidizing agents (air, air + steam, steam, and oxygen). Finally, this improved model will allow better theoretical/simulation analysis in waste-based flexible energy plants to test the polygeneration concept on the Dominion Bridge area in Lachine-Est in Montreal.

4.1 INTRODUCTION

The transformation to future fully renewable energy systems poses a challenge since it implies substantial infrastructure changes to existing transport energy [1]. networks that is, the electricity grid, the gas network, and district energynetworks. All these networks face the common challenge of facilitating distributed activities that involve interaction with consumers and bidirectional flowss [2][3]. Essentially, all networks will benefit from modern information, control, and optimization technologies as an integrated part of the networks at all levels [4]. For the cities of the future to become independent from fossil fuels, in the first place, they need to rationalize their production and energy consumption in large, and implemente combined plants of heat and power in efficient buildings [5][6]. Similarly, public transport must be expanded, and energy optimization in buildings must reduce heating consumption [6][7][8][9].

Hydrogen is emerging as an alternative carrier of energy [10]. It can play a key role in the energy sector's decarbonization if produced by zero or low emissions

sources in future cities [11]. There is a strong need to identify reliable, affordable, abundant, and clean sources for H_2 production [12]. Hydrogen can be made from widely available primary energy sources, including coal, natural gas, ammonia, methane, biomass, wind, water, and wastes [13]. Indeed, biomass can be transformed into solid, liquid, or gaseous fuels through physicochemical conversion processes (extraction and transesterification), biochemicals (alcoholic fermentation, anaerobic digestion, and aerobic digestion), and thermochemical (torrefaction, pyrolysis, gasification, and liquefaction) conversion processes [14][15]. Despite the widespread use of biomass, this is not yet fully exploited and is awaiting improved conversion methods to produce solid, liquid, and gaseous energy for commercial purposes [15][16]. Biomass gasification has, in the short term, more significant commercial potential than other thermochemical processes (liquefaction, pyrolysis, and combustion), due to its greater flexibility in terms of energy application for power generation and raw materials for industrial chemicals, to its greater efficiency as it can be integrated into combined gasification and to its potential for low environmental impact [17][18][19].

Torrefaction and pyrolysis are the thermal degradations of biomass generated prior to the other thermochemical transformation processes and generate solid (carbonized), liquid (bio-oils), and gas mixture products [19][20][21]. Likewise, the permanence of their solid and volatile phase in reaction zones at high temperatures allows their transformation to a fraction of permanent gases (gasification). The use of an oxidizing agent is essential for the gasification process; it reacts with the carbonized product of pyrolysis and converts heavier hydrocarbons into gases with low molecular weight, such as $CO, CO_2, CH_4 \text{ and } H_2$ [22]. Among oxidizing agents, gasification with air is the most widely used, part of the processed biomass is burned with the oxygen present, and the surplus is reduced; the process generates a gas of low calorific value between $4 - 7\ \mathrm{MJ/Nm^3}$ [23]. When using steam or oxygen, one obtains a gas with a calorific value between $10 - 18 \text{ and } 12 - 28\ \mathrm{MJ/Nm^3}$ respectively [24][25]. When using hydrogen as an oxidizing agent, a gas is obtained with an approximate calorific value of $40\ \mathrm{MJ/Nm^3}$ [15]. Finally, the reactors used for gasification are classified based on their disposition and the type of heating used; within the classification by disposition are the gasifiers entrained bed, fluidized bed, moving bed, and fixed bed (table 4-1). Moreover, according to the type of equipment heating, they can be classified into direct (autothermal) and indirect (allothermal) heating gasifiers [26][27].

First, the entrained bed is the most successful and widely used type of gasifier for large-scale gasification of coal, petroleum coke, and refinery residues [28]. Typical

characteristics found for entrainment flow gasifiers are high exhaust gas temperatures, very low tar content in the generated gas, construction problems due to the requirement of materials that resist high temperatures, and production ranges from $80\ \mathrm{MW}$ to $1000\ \mathrm{MW}$ [22]. Secondly, fluidized bed gasifiers facilitate a good mixture between the carbonized material and the oxidizing agent used; this is due to the carbonized material being suspended in a bed at high temperatures, allowing high reaction rates that encourage the volatile formation phase [15]. Typical characteristics found for fluidized bed gasifiers are high reaction rates, high flue gas temperatures, low tar content in the generated gas, and production ranges from $2\ \mathrm{MW}$ to $100\ \mathrm{MW}$ [29]. Finally, within the fixed and moving bed gasifiers are the parallel current gasifiers (downdraft), where the solid and the gas move in the same downward direction, and the countercurrent gasifiers (updraft) where the solid and the gas move in the opposite direction, the solid in the downward direction, and the gas in the upward direction [30]. Typical characteristics found for gasifiers in parallel streams are the relative ease of construction and high outlet gas temperatures; a relatively clean tar gas is generated, and production ranges from $10\ \mathrm{kW}$ to $2\ \mathrm{MW}$ [22]. The typical characteristics found for gasifiers in countercurrents are the robust construction that can be achieved in the equipment, the low temperature of the outlet gas, a gas with high tar content is generated, and production ranges from $2\ \mathrm{MW}$ to $20\ \mathrm{MW}$ [31].

Table 4-1: Comparison of characteristics of gasifier technology (taken from [22][23][30])

Parameters	Entrained bed	Fluidized bed	Fixed/Moving bed
Feed size	< 0.15 mm	< 6 mm	< 51 mm
Tolerance to fine particles	Excellent	Good	Limited
Tolerance to coarse particles	Poor	Good	Very good
Gas exit temperature	$> 1260\ ℃$	$800 - 1000\ ℃$	$450 - 700\ ℃$
Feedstock tolerance	High	Low rank	Low rank
Oxidant requirements	High	Moderate	Low
Reaction zone temperature	$1990\ ℃$	$800 - 1000\ ℃$	$1100\ ℃$
Steam requirement	High	Moderate	Low
Nature of ash produced	Slagging	Dry	Dry
Cold-gas efficiency	80 %	89%	80%
Application	Large capacities	Medium-sized units	Small capacities
Problem areas	Raw-gas cooling	Carbon conversion	Tar production and utilization of fine particles

Design and operation of gasifiers require an understanding of essential parameters like biomass characteristics (composition, moisture content, and size) and process parameters (steam-fuel ratio, gasification temperature, and feeding rate) prior to designing a gasifier in order to improve the performance of the gasifier in terms of quality of produced gas (volume fraction of H_2) and gasification efficiency [32][33][34]. Many experimental works have been conducted to optimize the quality of produced gas and gasification efficiency, modifying the gasifier's basic design [35][36][37]. Researchers like Cheng et al. [38] demonstrated the existence of a relative impact in 42% of biomass characteristics, 21 % of gasification temperature, 10% of particle size, 10 % of the inner diameter of the gasifier, 9 % of the height of gasifier, and 8% of equivalence ratio with the gasification products (CO, CO_2, CH_4 and H_2). Likewise, Susastriawan et al. [39] presented a literature review on the design improvement of downdraft gasifiers and their performance effect. Based on this work, the improvements are performed on (i) the feeding system, (ii) the steam supply system, (iii) produced recirculating gas system, and (iv) the discharge system. The feeding system is improved with the use of pneumatic, screw, and belt conveyors. The utilization of single-stage and atmospheric water steam supply is enhanced with the use of multi-stage and heated steam supply systems, respectively. The recirculating system is employed to heat the produced gas for water steam heating and biomass drying.

Finally, the discharge system that includes the grate and ash disposal system is improved using a shaking, vibrating, rotating, or reciprocating grate. Ash and char are disposed of from the ash pit by a screw or pneumatic conveyor. Despite these solutions, biomass generally contains reactive ashes, which can be readily converted to new mineral species during the thermochemical conversion process [10]. Agricultural biomass as a PKS contains high contents of alkali and alkaline earth metals (AAEMs) and a considerable amount of silica, which can readily result in the formation of sticky molten alkali silicates at low temperatures [40][41][42][43]. As a result, biomass ash is easy to melt and volatilize. Molten ash may stick to bed particles or to heat transfer surfaces, resulting in severe ash agglomeration and deposition problems [40][41][42]. Specifically, the relatively high temperature in downdraft gasifiers can significantly increase the risk of ash agglomeration or fusion during gasification, which can further result in severe ash-related problems due to ash melting and slag formation inside the downdraft gasifier. In contrast, the ash agglomeration degree of slag formation tendency of downdraft gasifiers is much higher than that of updraft gasifiers [43]. Therefore, for extensive future application of the downdraft fixed-bed gasification technology,

it is important to understand the migration and transformation behaviors of ashes and tars from the downdraft gasification of biomass [37][43][44].

One of the significant advantages of allothermal gasification is producing medium-heating value gas without needing expensive nitrogen separation technology. Few experimental studies have been made using indirect (allothermal) heating downdraft gasifiers and steam as an oxidizing agent [22][27][38][43][45][46]. Most studies at laboratory or pilot scale used electric heaters or fossil fuel to supply heat for the gasification process [47]. According to the previous literature review, none of the allothermal concepts seems to provide optimal heat integration while operating in a continuous manner and getting the most out of the biomass energetic content [22][27][38][43][45][46]. In our opinion, major advances towards the ideal gasifier can be made by combining better heat exchange performances at the surface. Despite its very attractive approach, in situ transfer of heat through a separating wall has clearly not met the expectations, mainly due to poor heat exchange performances at the surface (insufficient contacting area and/or low heat transfer coefficient). However, rare is the publication's recognition that the exchange is too low relative to the volume of the chamber, or to the amount of material being heated [37]. In the proposed concept, we suggest increasing the heat exchange surface-to-volume ratio by introducing a new configuration in the reactor and integrating baffles in charge of obstructing the passage of combustion gases from the burners; in such a way that the minimum residence time of the gases is guaranteed, which allows the effective heat transfer to the biomass. Likewise, prove the new geometries and distributions in the body reactor. For example, use concentric tubes, the internal tube through which the gases generated are evacuated allows and promoting tar cracking by forcing the gas generated to pass through areas of high temperatures (twice), thus reducing the percentage of tars and allowing the generation of a greater volume of gas (specifical hydrogen) without use catalysts systems.

Pang et al. [48] evaluated an indirect heating (allothermal) biomass gasification system. The biomass pellets were used as raw material for preparing hydrogen-rich gas in a downdraft gasifier. The gas composition and the effects of some parameters such as temperature and flow rate on product gas composition were investigated using a laboratory-scale fixed-bed gasifier. The experimental results show that the higher the temperature, the higher the $\mathrm{H_2 + CO}$ content. However, the higher the amount of steam, the lower $\mathrm{H_2 + CO}$ content. Another influencing factor is gasification temperature. When the gasification reaction temperature is higher than $750\,^{\circ}\mathrm{C}$, the volume fraction of $\mathrm{H_2}$ in the product, gas is higher than

$50\ \%$ and has little effect on temperature, the variation range is less than $3\ \%$, and the maximum value is $56{,}7\%$. The volume fraction of CO is up to $43{,}42\%$, and the $H_2 + CO$ can reach $94{,}62\%$. Finally, the steam/biomass (S/B) relation is another essential factor in water steam gasification. H_2 and CO_2 were increased with the increase of $\frac{S}{B}$, while CO decreased. The volume fraction of H_2, CO_2, CO and $H_2 + CO$ were $51{,}2$ to $56{,}70\ \%$, $4{,}63$ to $13{,}59\%$, $28{,}35 - 40{,}21\%$ and $84{,}13 - 92{,}43\%$, respectively. Similarly, Balu et al. [49] investigated the characteristics of woody biomass conversion to syngas using a high temperature ($877 - 1000\ ℃$) water steam allothermal gasification process. The results indicate that the syngas from pine wood as the feedstock contains relatively higher H_2 concentrations ($42 - 50\ \%$), volume fractions between $11 - 20\ \%$ of CO_2, 17 – 20% of CO and 3 – $5\ \%$ of CH_4; and the heating values of the syngas reach $9 - 10\ MJ/Nm^3$. Finally, Hu et al. [45] investigated a novel pilot-scale allothermal biomass gasification system integrating steam gasification, thermal cracking, and catalytic reforming with biomass molded fuel (BMF) with its low cost and high combustion temperature could be a potential ideal fuel in the future to substitute electricity/fossil energy as the heat source for the gasification process. The effect of catalysts on product yields and gas composition (gasification temperature of $846\ ℃$) were evaluated. The results indicate that the gasification process without catalyst generates syngas with a volume fraction of $33{,}91\ \%\ H_2$, $25{,}73\ \%\ CO$, $21{,}83\ \%\ CO_2$, $8{,}14\ \%\ CH_4$, and a low heating value of $11{,}61 - 12{,}81\ MJ/Nm^3$. In contrast, gasification with catalyst (Calcined MD and NiO/MD catalyst) generates syngas with an average volume fraction of 40,23 to 46,31 $\%\ H_2$, 18,42 to 26,9 $\%\ CO$, 16,99 to 25,36 $\%\ CO_2$, 6,41 to 8,11 $\%\ CH_4$, and a low heating value of $11{,}61 - 12{,}81\ MJ/Nm^3$.

To continue advancing in the appropriation of gasification technology to develop, optimize and implement this technology for the alternative use of residual biomass from many of our industries of waste (wood, brick, solid urban waste, coal, and agro-industrial)[34], further studies on relationships of various operating parameters on the gasification systems. Specifically, the implementation of large-scale biomass gasification remains challenging in many aspects, such as the interdependence of several issues that must be considered (gasification temperature, reactor design, tar yields, oxidizing agent, N_2-free syngas, ash deposits, and agglomeration problems) in point to optimize the syngas production. It is crucial to generate experimental data as those given in this work to support the large-scale implementation of downdraft allothermal gasifiers to produce hydrogen-rich syngas [26][47][49]. Thus, this work will use a downdraft gasifier at a pilot laboratory scale; with indirect heating (allothermal) through the combustion

of gases and steam as an oxidizing agent. The technological advantages of this type of gasifier are related to the simplicity of operation and maintenance. Downdraft configuration allows obtaining a gas of low tar content, and indirect heating allows obtaining a gas with a higher calorific value by not having a combustion zone inside it. Finally, water vapor is an oxidizing agent due to its availability and increase in the calorific value of the gas obtained due to its high reactivity.

4.2 MATERIAL AND METHODS

Experimental tests are carried out with an indirect (allothermal) heating downdraft gasifier and steam as an oxidizing agent. The feedstock material characterization, description of the gasifier design, auxiliary systems, operating conditions, and evaluation of the operating methodology for obtaining fuel gas are presented next.

4.2.1 FEEDSTOCK MATERIAL CHARACTERIZATION

Each type of biomass has specific properties that determine its performance as a fuel. The most important properties related to thermal conversion are moisture content, ash content, volatile matter content, proximate analysis, calorific value, and bulk density. Properties are presented on a wet basis, ash-free basis, or moisture and ash-free basis.

In the proximate analysis, the moisture is determined using the procedure described by the DIN 51718 standard for fossil fuels or the DIN EN 14774-4 standard for biomass fuels reaching a temperature of 105 ± 2 ° C. Samples of 1 g ± 0.1 g weighed with a precision of 0.1 mg are ground to a particle size of less than 1 mm. The determination of the volatile matter content is carried out according to the procedure indicated in the DIN 51720 standard for fossil fuels or the DIN 15148 standard for biomass fuels, which is similar. For this test, 1 ± 0.1 g is weighed with a precision of 0.1 mg and grain size less than 0.2 mm and dried according to DIN 51718. The ash content is determined utilizing the DIN 51719 used for fuels solids such as peat, lignites, coke, charcoal, and mineral.

In the ultimate analysis, the carbon, hydrogen, and nitrogen content is determined and the oxygen content is determined by difference. The sulfur content in biomass is assumed to be negligible. A Perkin Elmer brand elemental analyzer, model 2400 is used, supplemented with a Sartorius M500P microbalance and EAGER information analysis software. The equipment burns the sample at $1023\,^{\circ}C$ followed by a

reduction of the gases formed towards N_2, CO_2, H_2O, and SO_2 and detected by a thermal conductivity detector following the ASTM 5373 standard.

Palm kernel shell (PKS) was utilized as the feedstock (figure 4-1), considering that near 15000×10^3 tonnes/year are produced every year as a waste of the palm oil transformation process worldwide [50].

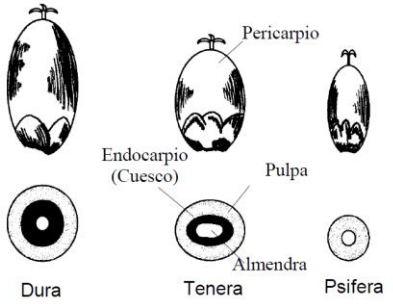

Figure 4-1: Palm kernel shell (PKS) types

The high carbon element in PKS shows its potential to be used as solid fuel feedstock for steam generation to produce electricity [51]. Based on the proximate and ultimate analysis of PKS feedstock shown in table 4-2, PKS contains the most significant volatile matter despite a moderate amount of fixed carbon. The fuel moisture and ash content are low, but the heating value is relatively high, making it a good feedstock source compared to other palm biomass for power generation in the industry. Therefore, this work aims to determine the energy potential of oil palm shells when transformed through the gasification process.

Table 4-2: Properties for palm kernel shell (PKS) [52][53]

Proximate analysis (wt% dry basis)		**Ultima analysis (wt% dry basis)**		**Lignocellulosic content (wt% dry basis)**		**LHV (MJ/kg)**	**HHV (MJ/kg)**
Moisture content	5-11	C	45-55	Holocellulose-cellulose	25-40	16.14	22.22
Volatile matter	65-79	H	5-7	Alpha-cellulose-hemicellulose	15-20		
Fixed carbon	15-20	O	30-45	Lignin	35-45		
Ash	2-5	N	0.05-2.00				
		S	0.05-0.20				

4.2.2 **DESCRIPTION OF THE GASIFIER DESIGN AND AUXILIAR SYSTEMS**

The initial gasification scheme implemented is shown in figure 4-1; it is composed of a reactor (4) where the thermal decomposition of the biomass is carried out, a feeding system (2) (3), an indirect heating system (6) that provides the heat necessary for the thermal decomposition of biomass to take place, of a stripping gas regulation system (1), of an oxidizing agent dosing system (7), of a measurement system of temperature (5) and pressure (9), a data acquisition system (20) and (21), a gas cooling system and tar condensation (10) (11) (12) (13), a gas suction pump (14), an oxygen meter (17), a gas sample extraction point (18), and combustion of gases system (19).

4.2.3 **FEEDING SYSTEM**

The feeding system (2) and (3) consists of a $150\,\mathrm{kg}$ capacity hopper and $3-100\,\mathrm{kg/h}$ feeding range, built in 304 stainless steel and provided with a sight glass to verify the system's correct dosage and operation when working at high temperatures ($>500\,^{\circ}\mathrm{C}$). Likewise, the system consists of an endless screw made of 304 stainless steels with a length of $950\,\mathrm{mm}$, nominal diameter, and pitch of $25.4\,\mathrm{mm}$, coupled to a 0.5 Hp SEW-EURODRIVE type AC gearmotor.

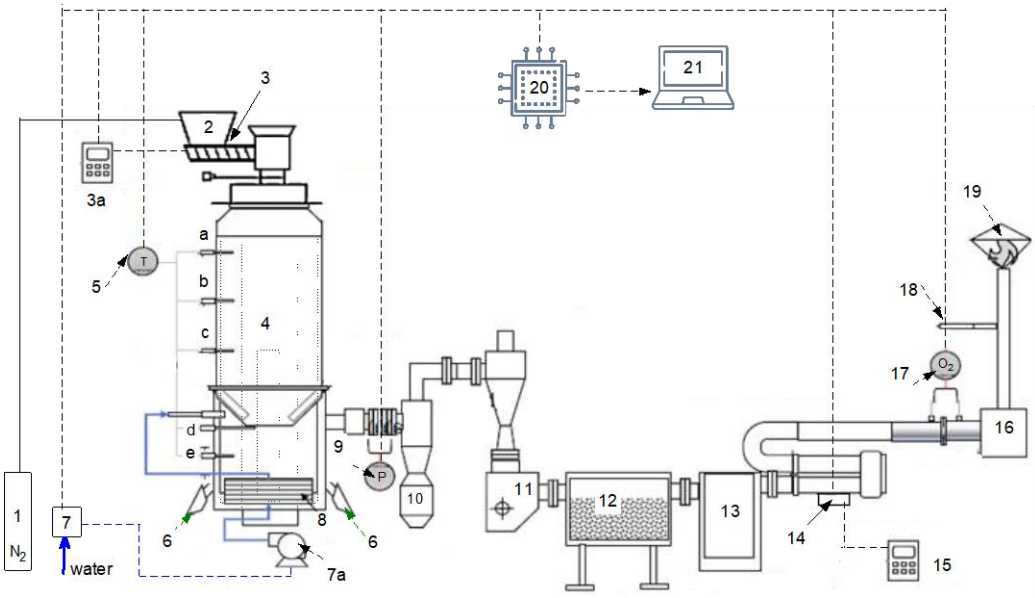

Figure 4-2: Schematic of pilot-scale downdraft bed gasification system: (1) stripping gas regulation system N_2; (2) hopper; (3) screw feeder; (3a) variable frequency driver; (4) downdraft reactor; (5) temperature sensor system; (6) indirect heating system; (7) oxidizing agent dosing system; (7a) peristaltic pump (8) heat recovery system ; (9) pressure sensor; (10) cyclone; (11) heat exchanger; (12) storage of condensate tank; (13)

auxiliary filter; (14) suction pump; (15) variable frequency driver; (16) flowmeter; (17) oxygen sensor; (18) gas sample extraction point; (19) combustion of gases system; (20) acquisition data system and (21) portable computer equipment.

4.2.4 **DESCRIPTION OF THE REACTOR**

The reactor's body (4) comprises three concentric tubes of 310 S stainless steel. First, an inner tube of 88.97 mm in internal diameter and 2100 mm in length through which the gases generated are evacuated. Second, an intermediate tube with an internal diameter of 224 mm and a length of 3600 mm, where the biomass from the feeding system (2) and (3) is stored internally and where the different thermal decomposition processes are carried out. On the outside, there are baffles in charge of obstructing the passage of combustion gases from the burners; in such a way that the minimum residence time of the gases is guaranteed, which allows the effective heat transfer to the biomass. Finally, the outer part of the reactor comprises a 431 mm and 3600 mm tube in length, concentric to the intermediate and internal tubes mentioned above. When installed, they form an annular space through which the combustion gases from the burners circulate. In the upper-right part, the gas outlet line to the chimney is located. Likewise, in the lower part of it, the burner connection ducts are located opposite each other and are displaced concerning the tube's axial to create an ascending vortex with the combustion gases.

4.2.5 **GAS CLEANING SYSTEM**

The condensate collection system is in charge of cooling and separating condensable substances present in the syngas. It is composed of a cyclone (10) and a concentric tube heat exchanger (11). As a complementary system for the storage of condensates, a $0{,}05\ \mathrm{m}^3$ tank (12) is in charge of storing the condensates generated during a long-term experimental run. Finally, the gas is conducted through an additional filter (13) to condense the gas tars and protect the suction pump (14).

4.2.6 **AUXILIARY SYSTEMS**

They are the gasification system devices that do not act in the processing of the raw material but are essential for the correct execution of the process. Firstly, (i) temperature sensor systems; built with four (4) multipoint type K thermoelements located in four evaluation positions (1030 mm, 1550 mm, 2470mm, and 3330 mm),

where the origin is established in the upper part of the gasifier body. Secondly, (ii) the indirect heating system; includes two (2) gas burners; from the Joannes brand, reference JM3, with a thermal power ranging from 11.9 to 37.7 kW. Thirdly, (iii) the oxidizing agent dosing system; a peristaltic pump, Masterflex brand, model 7518-10 is used. Finally, a Univac brand diaphragm pump model MPKC 2403 T for dry applications, oil-free, with ultimate suction pressure P <10 kPa, pumping speed of $18 - 20\ \mathrm{m^3/h}$ TGF600 thermal mass flow meters for syngas with range $0.25 - 25\ \mathrm{Nm^3/h}$, and a computer with an Agilent brand data acquisition card HP34970A.

4.3 **EXPERIMENTAL PROCEDURE**

Before, during, and after completing each gasification experience, a verification protocol of the correct functioning of the components has the objective of guaranteeing the correct development of the tests and ensuring that conditions are maintained with adequate security for personnel. It should be noted that the procedure described here may present different modifications depending on the type of fuel to be gasified, as well as depending on the type of gasifying agent used.

4.3.1 **TIGHTNESS TEST**

This is a test that is carried out to verify the tightness in each of the systems and subsystems of the gasification equipment, industrial nitrogen is injected, and leaks are evaluated with a maximum gauge pressure of 100 kPa. This evaluation is carried out in parts; checking for leaks in the reactor body (lower and upper flange), feed hopper, gas outlet ducts, heat exchangers, condensate collection system, suction pump, and connection lines.

4.3.2 **GASIFICATION TEST**

Firstly, the process is started by loading the feed hopper (2) with a palm kernel shell. The flow meter is regulated to dose during the experiment $0.3\ \mathrm{m^3/h}$ of nitrogen as entrainment gas (1), for 10 minutes, it is verified that the oxygen meter (17) indicates 0 %. Second, the data acquisition system (20 and 21) is turned on, and the temperature and pressure values in the reactor are monitored using the sensors (5) and (9); When the 0% condition has been reached in the oxygen meter (17), heating is started employing the burners (6) at a constant flow of $2.5\ \mathrm{m^3/h}$ of natural gas. Thirdly, during the heating phase, when the thermoelements located at 1030 mm register temperatures of $200\ ^{\circ}\mathrm{C}$, an intermittent feeding cycle is started (every 2 minutes, the level control system is turned on and it works at a low rate

of feeding for 10 seconds), which guarantees that the feeding system (3) does not get stuck due to the thermal decomposition of the biomass stored in the endless screw.

When operating temperatures have been reached (stable temperatures of approximately $1000\ ^{\circ}\mathrm{C}$ measured in the thermoelement located at 3330 mm), one of the burners is turned off in order to stabilize temperatures close to $850\ ^{\circ}\mathrm{C}$. Then, the oxidizing agent dosing is started utilizing the peristaltic pump (7), the system is expected to stabilize (due to the dosing of water vapor in the reactor, the pressure increases slightly between 5 - 10 kPa); The pressure regulation in the system is carried out utilizing the needle valve installed in the suction pump (14), the measured pressure values are displayed and stored through the Agilent Benchlink Data Logger 3 software interface (20 and 21) in order to maintain the operating of the equipment close to atmospheric pressure. Once the equipment has been stabilized, after starting the oxidizing agent's feeding (7), the level control is activated, and the biomass feeding begins. As the syngas is generated in the reactor body (4), the gas is conducted through the gas outlet ducts to the cyclone (9), heat exchangers (11), and a $0.05\ \mathrm{m}^3$ tank (12). At the outlet of (12), the syngas enters a safety filter (13) in order to retain possible tars that have not been condensed in the cooling system (10), (11), and (12). Finally, the gas generated is counted by the gas meter (16), and a gas sample (18) is collected for subsequent analysis by Intuvo 9000 GC chromatography system for subsequent burning in (19) before being evacuated to the environment.

4.3.3 **EXPERIMENTAL PLAN**

The experimental plan includes evaluating the modified gasification system's operating conditions and evaluating the operating methodology for obtaining fuel gas from palm kernel shells.

In the gasification of biomass, the temperature is the second most important parameter controlling the gas composition, tar concentration, reaction rate, and ash build-up. Therefore, it needs to be highly controlled. Low-temperature gasification is attributed to high tar content and low CO and H_2 content in the product gas. On the other hand, high-temperature gasification leads to a desired high yield of CO and H_2 while reducing the tar content. However, two significant problems limit high-temperature gasification above $1000^{\circ}\mathrm{C}$. (i) The stringent reactor material specification requirement and (2) the ash melting, mainly when high ash-containing biomass is used. Therefore, numerous studies have been conducted to investigate

the gas composition, tar concentration, and other requirements within the temperature range of $750 - 900\ ℃$.

Another critical parameter for an allothermal gasifier is the steam-to-carbon (S/C) molar ratio. Its parameter contributes mainly to hydrogen generation, and the quantity of steam depends on fuel feed rate and carbon mass fraction in the fuel. Likewise, both H_2 and CO increases with an increasing S/C ratio for a given temperature. In order to obtain a gas with a calorific value between $10 - 20\ \mathrm{MJ/Nm^3}$ steam is used as the oxidizing agent with a relation S/B of more than 0.75.

Finally, the palm extractor plant supplies palm kernel shells with a particle size between 15 - 25 mm. To homogenize the variety of sizes, the palm kernel shell is ground in a blade mill whose working power is 1.1 kW, to which a No. 4 mesh (4.76 mm opening) is incorporated, ranging from a six mesh (3.35 mm) to 10 mesh (2.00 mm).

4.3.4 **PERFORMANCE OF BIOMASS GASIFIER**

Several parameters could characterize the performance of biomass gasifiers. Here, we will review two such parameters: yields and syngas composition, which directly influences the heating value of the gas and gasification efficiency.

To measure the energy content of the fuel gas mixture, the lower calorific value was calculated using the expression:

$$\mathrm{LHV_{syngas}} = \sum_{i=1}^{n} x_i \,.\, \mathrm{LHV_i} \qquad (1)$$

Where $\mathrm{LHV_{syngas}}$ is the lower calorific value of the fuel gas mixture, x_i and $\mathrm{LHV_{syngas}}$ are the mole fraction and the lower calorific value of each of the gas mixture components obtained from palm kernel shell gasification. Table 4-3 shows the lower calorific value (LHV) at standard conditions for each compound that is part of the gas mixture and used to determine the lower calorific value in each of the presented gasification experiments.

Table 4-3: Lower calorific value (LHV) of the main combustible gases generated in the biomass gasification [14][15][22]

Components	$\mathrm{LHV\ (Mj/Nm^3)}$
H_2	10.78
CO	12.63
CO_2	0

CH_4	35.88

The calculation of the efficiency of biomass gasification can be determined from equation (2). To compare the gasification efficiencies, most authors consider the cold efficiency value as the best option to avoid the uncertainty related to the calculations of the sensible heat of generated gas from the reactor.

$$\eta = \frac{\dot{m}_{cold\_syngas} \cdot LHV_{cold\_syngas}}{\dot{m}_{biomass} \cdot LHV_{biomass}} \quad (2)$$

where $\dot{m}_{cold\ syngas}$ is the mass amount of product gas (kg); LHV_{syngas} is the lower calorific value of the fuel gas mixture (MJ/Nm^3), and finally, $\dot{m}_{biomass}$ and $LHV_{biomass}$ are biomass feedstock (kg) and the lower calorific valor (MJ/kg) of the biomass used.

The material balance is evaluated experimentally. To determine the biomass flow previously fed, the weighing was carried out before and after the feeding hopper figure 4-1. After the end of the experiment, the equipment was allowed to cool, and the ashes were evacuated and weighed.

The condensable products accumulated in the condensates collection system were removed and weighed. After weighing them, the ASTM D95-05 standard was applied to determine the amount of water present in the tars employing the xylene distillation process. The procedure consists of preparing a 50 ml sample of condensates, the sample is mixed with xylene, and the temperature is increased. The steam generated is passed through a cooling system, and the condensate is deposited in a calibrated volume burette; a mixture is achieved in which the water is separated from the xylene due to the difference in density. Calculating the water volume present in the mixture, the fraction of water in the condensate is found based on the initial weight. Also, fuel gas was counted by TGF600 thermal mass flow meters for syngas with a range of $0.25 - 25\ Nm^3/h$.

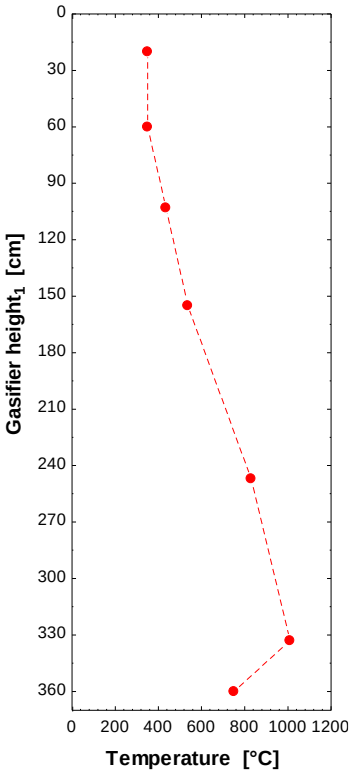

Figure 4-3 Temperature gradient along the height of the downdraft gasifier.

4.4 RESULT AND DISCUSSION

4.4.1 TEMPERATURE AND PRESSURE DISTRIBUTION IN THE GASIFIER

The temperature distribution has a significant effect on the gasification products' production and is an essential factor in evaluating the gasifier's performance. The gasification temperature is dominated mainly by the amount of water flowing into the gasifier and the biomass feed rate. Based on the maximum temperature values from points analyzed, a temperature gradients profile along the height of the allothermal downdraft gasifier is illustrated in figure 4-2.

Figure 4-3 shows the axial temperature distribution in the gasifier under a typical operating condition with water as a gasifying agent. As shown in fig, thermocouples and pressure transmitters located at four different positions continuously monitored the temperatures and pressures. 3. $\mathrm{T}_{103\mathrm{cm}}$ and $\mathrm{T}_{155\,\mathrm{cm}}$ are pyrolysis temperature, $\mathrm{T}_{247\mathrm{cm}}$, and $\mathrm{T}_{333\,\mathrm{cm}}$ are reduction zone temperatures.

From figure 4-3, one can see that the time required to reach a steady state is 65 minutes for the test described in the experimental procedure. During the experiment, five phases are presented successively. In the first phase, the reactor is heated up to $1000\,℃$ by the combustion gases from the two burners for 30 minutes without feeding biomass. In the second phase, the feeding of the water flow begins; consequently, there is an increase of 103 mbar (10 kPa) in pressure due to the generation of an atmosphere rich in water vapor in the reactor, parallel to the feeding of the water flow, one of the burners is turned off to reach stable temperatures close to $850\,℃$. The third phase activates the biomass feeding system intermittently to avoid jamming of the endless screw due to the biomass's thermal decomposition; the feed generates syngas that causes an increase of 1030 mbar (103 kPa) in pressure and a decrease in temperature in the system.

In the fourth phase, thermal stabilization is achieved in the reactor with the oxidizing agents and continuous biomass feeding. In the stable zone, there is a maximum radial temperature of $\Delta\mathrm{T}_{\mathrm{radial}} = 6℃$ in thermoelements located at 103 cm and maximum axial temperature of $\Delta\mathrm{T}_{\mathrm{axial}} = 300\,℃$ between the thermoelements located at 103 cm and 333 cm (figure 2-3). In the 100 minutes of thermal stabilization, ten samples of gas are extracted (60, 80, 90, 100, 105, 120, 125, 130, 135, and 150 minutes after the heating is started employing the burners) to be able to know how the composition of gases varies as the equipment stabilizes. Finally, in the fifth phase, the biomass feeding is suspended, and two gas samples are taken

(at 160 and 170 minutes) to know the composition of the gas as the remaining char is consumed.

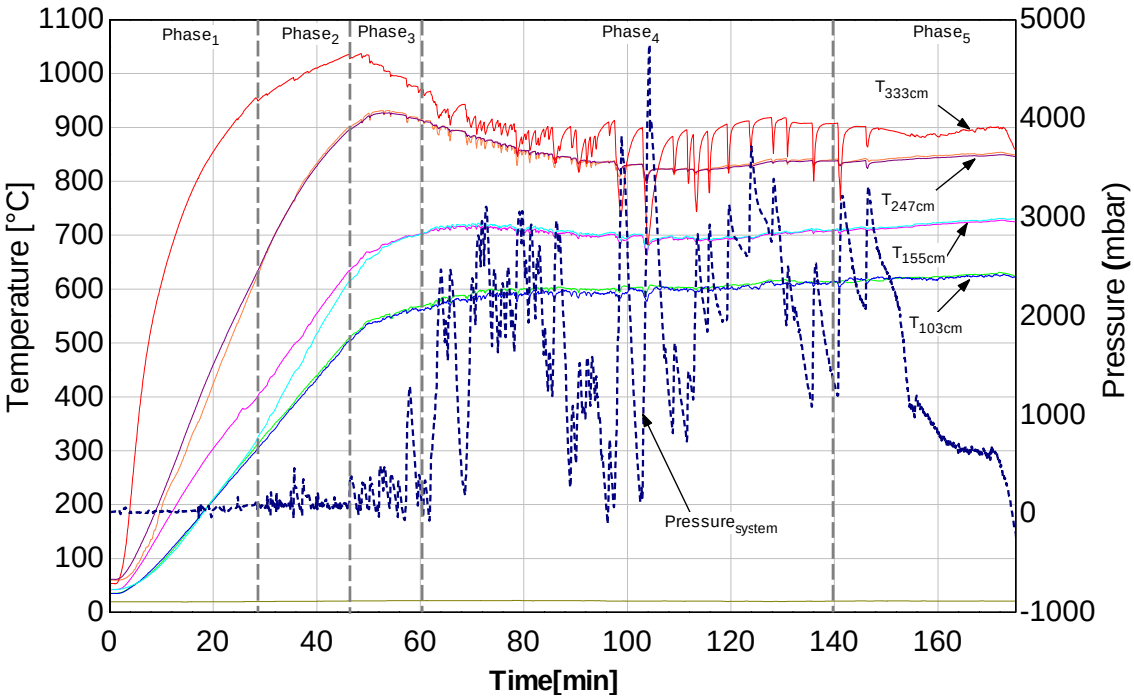

Figure 4-4: Temperature and pressure distributions of the gasifier during the warm-up and stable operational phases.

4.4.2 **SYNGAS COMPOSITION**

Figure 4-4 shows the volumetric composition profile of the syngas generated. From the analysis of the gases generated, it is possible to obtain critical information on the chemical reactions involved and temperature in the palm kernel shell gasification process. In effect, this variable affects the gasification process performance due to the endothermic nature of the main reactions. Likewise, the steam/biomass ratio (S/B) influences the performance of the gas and its calorific value. An increase or decrease in the S/B ratio in the reactor favors or disfavors the steam reforming reactions, resulting in an increase or decrease in gas yield, hydrogen yield, and calorific value of the gas generated.

To explain the results obtained in figure 4-4, the following set of reactions was selected as representative of the palm kernel shells carbonization gasification process:

$$C + CO_2 \leftrightarrow 2CO \quad \Delta H = +172 \text{ kJ/mol} \tag{3}$$

$$C + H_2O \leftrightarrow CO + H_2 \quad \Delta H = +131 \text{ kJ/mol} \tag{4}$$

$$C + 2H_2 \leftrightarrow CH_4 \quad \Delta H = -74.8\ kJ/mol \tag{5}$$

$$CO + H_2O \leftrightarrow CO_2 + H_2 \quad \Delta H = -41.2\ kJ/mol \tag{6}$$

$$CH_4 + H_2O \leftrightarrow CO + 3H_2 \quad \Delta H = +206\ kJ/mol \tag{7}$$

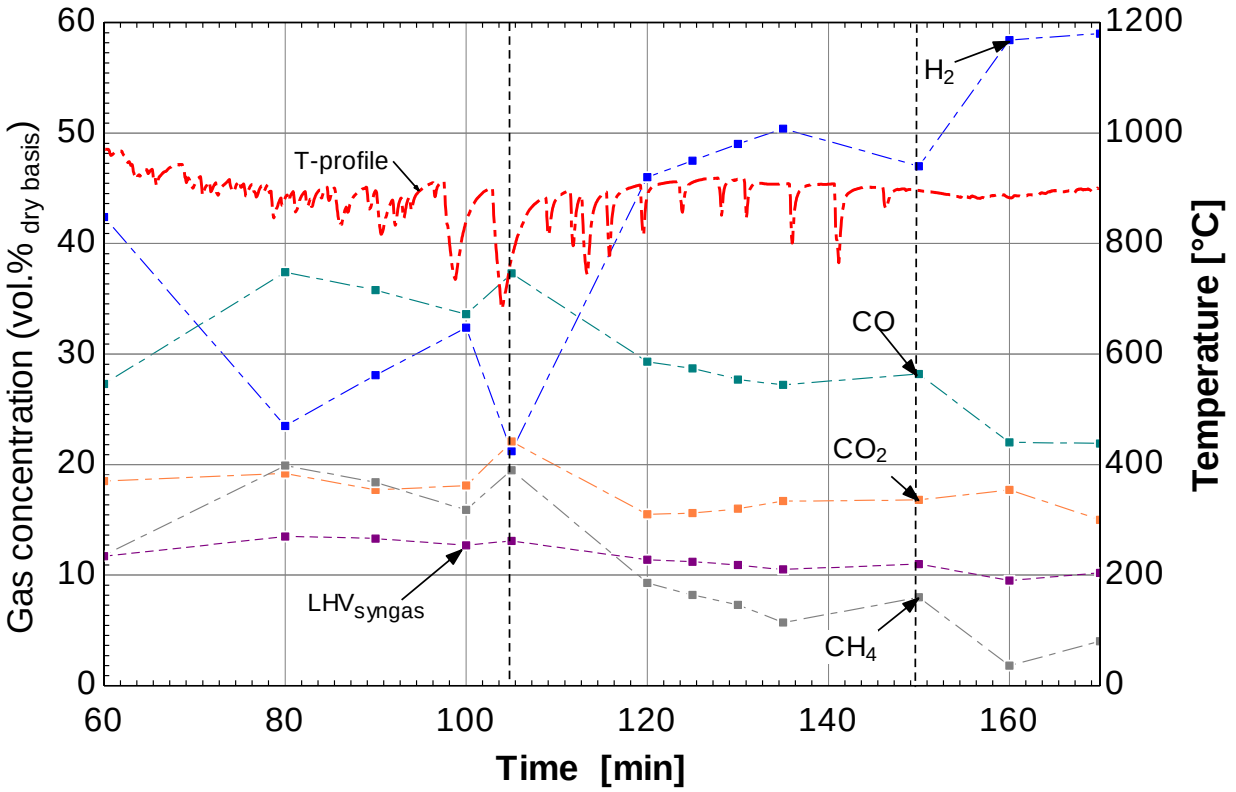

Figure 4-5: Gas composition profile

The only homogeneous reactions are the shift reaction equation (6) and steam-reforming reaction equation (7); the other reactions present are classified as heterogeneous. The speed with which the char (consisting mainly of carbon) gasifies depends mainly on its reactivity and the gasification medium reaction potential. Since the gasification process is carried out in the absence of oxygen and water vapor as the oxidizing agent, the predominant reaction is the water-gas or steam reaction equation (4), followed by the shift reaction equation (6). Finally, the Boudouard reaction equation (3), hydrogasification equation (5), and the steam-reforming reaction equation (7). Based on the above, the relative order of the heterogeneous reaction rates can be summarized as: $R_{C+H_2O} \gg R_{C+CO_2} \gg R_{C+H_2}$ [22]. Likewise, the homogeneous reaction equation (6) is responsible for increasing the hydrogen content in the gasification products at the expense of carbon monoxide.

For the stable state indicated in figure 4-3, the effect of temperature on the composition of the gases generated is shown in figure 4-4. For example, when the raw material feed starts, the equipment is at temperatures higher than $900\ ℃$

measured by the thermoelement located 333 cm from the upper gasifier cover, due to the endothermic condition of the predominant reaction equation (4), there is a drop in temperature and subsequent recovery of the equipment in search of its equilibrium condition. The gas samples were taken in this phase at 60, 80, 90, 100, and 105 minutes to corroborate the effect of temperature and reactivity on the gas composition; low temperatures favor carbon monoxide production high temperatures the production of hydrogen.

As can be seen in figure 4-4, the H_2 content decreases when the temperature falls from 927 to 835 $℃$ and 860 to 785 $℃$ and increases when there is an increase in temperature from 835 to 845 $℃$ and 845 to 860 $℃$. On the contrary, the CO content increases when the temperature falls from 927 to 835 $℃$ and 860 to 785 $℃$. Likewise, it decreases when there is an increase in temperature from 835 to 845 $℃$ and 845 to 860 $℃$. This change in the concentration of H_2 and furthermore, CO is due to the high activity of the water-gas displacement reaction within this temperature range.

Similar trends have been observed in the gasification of biomass with water vapor [27][38][45][49][54][55]. Additionally, the concentration of CO_2 and CH_4 increase when temperatures fall from 927 to 835 $℃$ and 860 to 785 $℃$. Likewise, they decrease when there is an increase in temperatures from $835 \text{ to } 845\ ℃$ and $845 \text{ to } 860\ ℃$. The low concentrations of CH_4 reveal that the methane formation reaction shows less activity in gasification at the working temperatures.

The gas formed for the stable condition is composed of 48.2 % H_2, 28.2% CO, 15.9 % CO_2 and 7.6 % CH_4 by volume fraction and a lower calorific value of 11,5 MJ/Nm^3. These results are explained by the fact that at temperatures of 850 $℃$, the heterogeneous water-gas reactions and the homogeneous water-gas displacement reaction (equations 3 and 5) favored the greater formation of H_2 at the expense of CO and CH_4.

The gas formed at the end of the experiment is mainly composed of 58.7 % H_2, 21.95 % CO, 13.35 % CO_2 and 2.9 % CH_4 in volume fraction and a lower calorific value of 10,5 MJ/Nm^3. It is evident that in this phase, the interruption of the continuous feeding of biomass, even maintaining the same water vapor dosage, generates an increase in the S/B ratio. For low S/B, carbon monoxide and methane are favored [22][38]. When more steam is supplied than biomass in the finishing zone, the remaining char and methane are transformed into H_2 and CO. On the other hand, CO is reduced due to the homogeneous water-gas displacement reaction promoted by steam. Therefore, the increase in water vapor significantly

promotes the formation of H_2 at the expense of the decrease in CH_4, and CO which translates into a decrease in lower calorific value (figure 4-4).

4.4.3 PERFORMANCE OF THE GASIFICATION SYSTEM

The performance of the gasifier is measured in terms of the quality and quantity of gas produced. The mass balance result is presented in figure 4-5. Mass balances vary between 80% and 90%. The deviation from 100% in mass balance reflects the cumulative effect of practical difficulties in quantifying all tars and solid residues at the end of experiments—likewise, possible errors in measurements of all inputs and outputs.

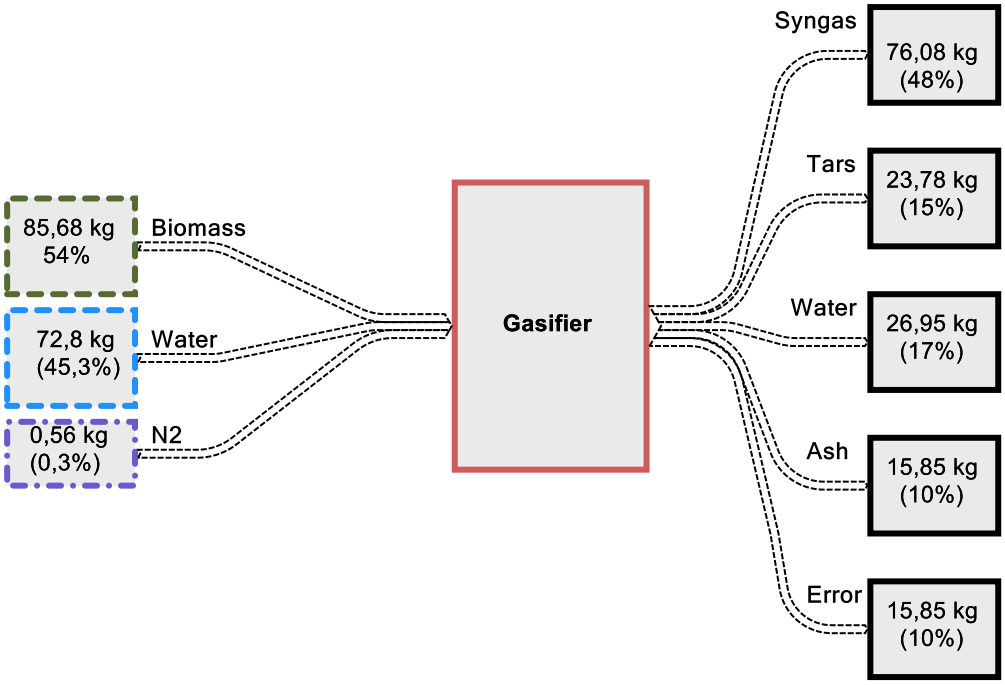

Figure 4-6: Mass balance analysis.

One of the ways to express the efficiency of the gasification process is through the cold gas efficiency (equation 2); this equation relates the energy present in the gas formed and the energy present in the biomass fed and is implemented when it is of interest to use the gas generated in power applications.

$$m_{biomass} + m_{water} = m_{syngas} + m_{tars} + m_{water} + m_{ash} + error \quad (8)$$

According to figure 4-5, the material balance for the gasification process can be represented by equation (8). Calculation of the weight of the gases is done based

on the volume measured during the experimental run, and the density of the mixture is shown in table 4-4.

Table 4-4: Syngas density experimental test [14][15][22]

Components	Steady-state average syngas composition (Vol.%)	Individual component density (kg/m^3)
H_2	48,2	0.0899
CO	28,2	1.145
CO_2	15,9	1.842
CH_4	7,6	0.667

Table 4-5 shows the lower calorific value of the natural gas used for the reactor's indirect heating utilizing the two burners used in the experimental test.

Table 4-5: The lower calorific value of natural gas used for indirect heating [14][15][22]

Component	Natural gas composition (vol.%)	LHV (MJ/Nm^3)
CH_4	98	35.88
C_2H_6	0,25	64.34
C_3H_8	0,06	99.09
C_4H_{10}	0,01	122.91

Table 4-6 shows the summary of the performance of the gasification equipment under operating conditions. First, the gasification temperature, particle size, feed rate, and water vapor/biomass molar ratio are displayed; second, the composition of the gas generated, the calorific value, and the gasification efficiency; finally, natural gas consumption for indirect heating, the energy generated and required to keep the zone stable in the experimental run.

Table 4-6: Summary of performance of the gasification equipment under operating conditions

Reactor Temperature (°C)	850
Particle size (mm)	2-3
Fuel feed rate (kg/h)	57.1
Steam/Biomass ratio	0.85
Syngas composition (vol.%)	
H_2	48.2
CO	28.2
CO_2	15.9
CH_4	7.6
LHV (MJ/Nm^3)	11.5
Cold gas efficiency $(\%)$	80
Consumption of natural gas (Nm^3)	6.25
Syngas generation (Nm^3)	95.4
$Q_{required}$ (MJ)	221.25
$Q_{generated}$ (MJ)	885

4.4.4 **COMPARISON STUDY**

4.4.4.1. PRODUCT GAS COMPOSITION AND HYDROGEN YIELD

Figure 4-6 illustrates the comparison of gas composition with data from the literature. In the present study, maximum H_2 composition of 48,22 vol% was observed. Pang et al. [48], Balu et al. [49], Hu et al. [45], and Acevedo-Páez et al.[56] studied steam gasification of palm kernel shells and similar biomass without catalyst in a fixed bed and reported 55 vol%, 45 vol%, 33,91 vol%, and 37,3 vol% H_2 content, respectively. Hu et al. [45] reported 46,31 vol% H_2 content in catalytic (NiO/MD catalyst) steam gasification in allothermal biomass gasification. The little differences are mainly due to the raw material, temperature gasification, and relation steam/biomass used. The lowest CH_4 and CO content in the steam gasification system was due to enhance the activity of steam methane reforming and water gas shift reaction. The application of steam gasification promotes higher H_2 rich gas with negligible N_2 content in the product gas without the use of catalytic system.

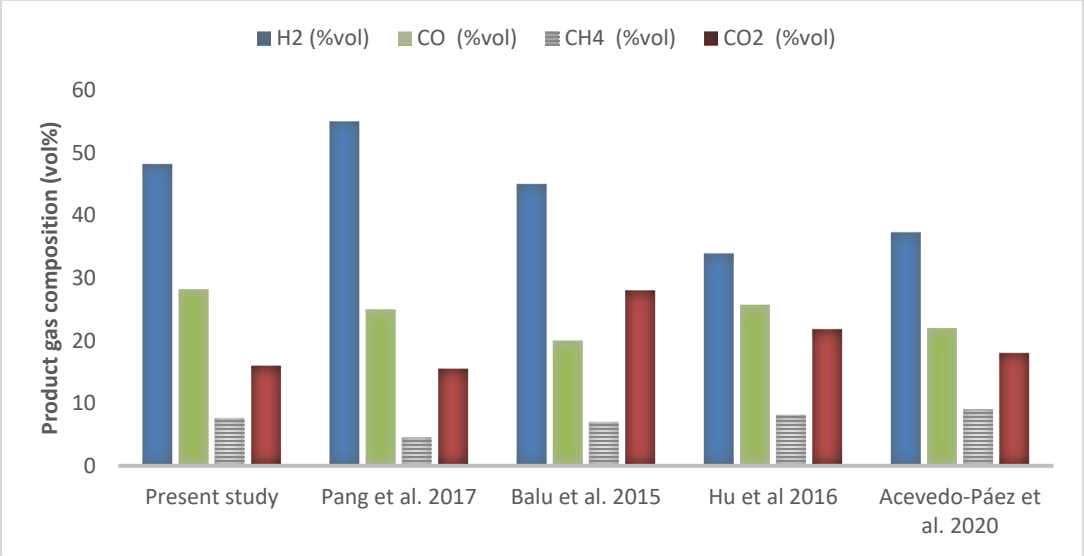

Figure 4-7: Comparative study of syngas composition (vol%) in allothermal gasification process.

4.4.4.2. GASIFICATION EFFICIENCY AND SYNGAS HEATING VALUES

Figure 4-7 compares the cold gas efficiency and syngas heating values reported by other researchers. Comparing the efficiency obtained in the present study with similar works reported by other researchers. In the present study, the maximum cold gas efficiency of 80 % was observed at a steam/biomass (S/B) ratio of 0,85 and a temperature of 850 °C. Balu et al. [49] observed lower cold gas efficiency of 70% at a similar S/B ratio and a temperature of 877 °C in a downdraft gasifier. However, the high efficiency (91,6 %) produced in Pang et al. [48] work was due to operating conditions and pelletizing of corn straw 2 in the steam gasification in an allothermal downdraft gasifier. Likewise, figure 4-7 illustrates the comparison of $\mathrm{LHV_{gas}}$ in the literature. Lower heating values of $9\ \mathrm{MJ/Nm^3}$ reported by Balu et al. [49] were due to the S/B ratio at a similar temperature 877 °C of steam gasification. An increase or decrease in the S/B ratio in the reactor favors or disfavors the steam reforming reactions, resulting in an increase or decrease in gas yield, hydrogen yield, and calorific value of the gas generated. A good heating value generated by Hu et al. [45] was due to the low S/B ratio used (S/B=0,17) at a gasification temperature of 846 °C used in the allothermal downdraft gasifier utilizing pine sawdust as the feedstock. The comparative study showed that the biomass was successfully gasified to produce hydrogen-rich syngas with high-temperature steam in a downdraft gasifier. When more steam is supplied than biomass in the finishing zone, the remaining char and methane are transformed into $\mathrm{H_2}$ and CO. On the

other hand, CO is reduced due to the homogeneous water-gas displacement reaction promoted by steam. Therefore, the increase in water vapor significantly promotes the formation of H_2 at the expense of the decrease in CH_4, $\text{and } CO$ which translates into a decrease in lower calorific value (figure 4-4).

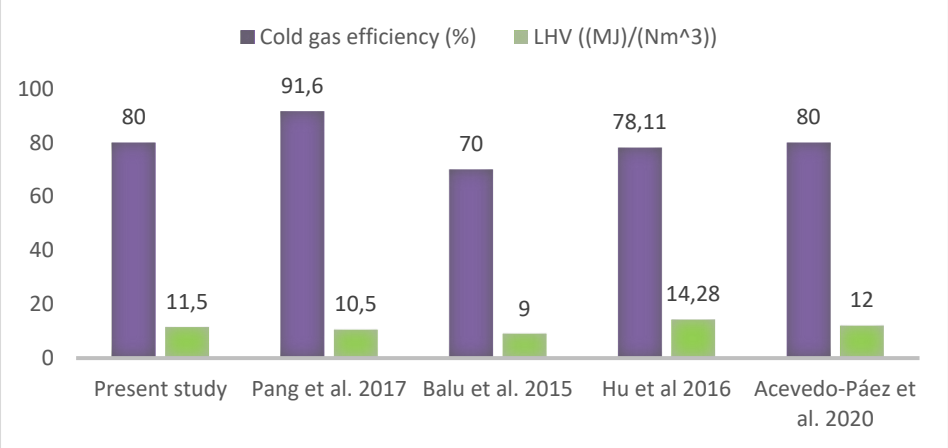

Figure 4-8: Comparison of gasification efficiency and syngas heating values

4.5 **CONCLUSIONS**

An N_2-free hydrogen-rich syngas yield was obtained from palm kernel shells (PKS) steam gasification in downdraft allothermal gasifier reactors. In this equipment, the temperature, biomass feeding rate, water concentration, and internal configuration of the equipment were adjusted for the correct experimental execution. Special attention was paid to instrumentation to access information such as temperature, gas composition, and pressure throughout the equipment. On the other hand, increasing the heat exchange surface-to-volume ratio by introducing a new configuration in the reactor and integrating baffles in charge of obstructing the passage of combustion gases from the burners, in such a way that the minimum residence time of the gases is guaranteed, which allows the effective heat transfer to the biomass reduced the tar generation, appearance ash deposits, and agglomeration problems.

The gasification equipment was tested under gasification temperatures between $800 \text{ and } 950$ ℃ and steam-biomass mass ratios between 0,2 and 1,2. The reliability of both the equipment and the operating methodology was confirmed by obtaining N_2-free syngas. Likewise, it was shown that the steady-state could be reached during the experiments in a downdraft allothermal gasifier with a maximum generation of $95.4\ \text{Nm}^3$ of fuel gas with a syngas volume fraction of $48.2\ \%\ H_2$, $28.2\ \%\ CO$, $15.9\ \%\ CO_2$, $7.6\ \%CH_4$ and average lower calorific value of $11.5\ \text{MJ/Nm}^3$.

The experimental run indicated that temperature is the most crucial factor in the gasification process; low temperatures favor CO production, and high temperatures the production of H_2. Additionally, the concentration of CO_2 and CH_4 increase when temperatures decrease. These results are explained by the fact that at temperatures of 850 °C, the heterogeneous water-gas reactions and the homogeneous water-gas displacement reaction (equations 6 and 7) favored the greater formation of H_2 at the expense of CO and CH_4.

Finally, in chapter 7, we will use the temperature profile and other information will be used to improve the capacity to prediction of the syngas composition using the model developed in chapter 3. Likewise, the Downdraft configuration allows obtaining a gas of low tar content, and indirect heating operated with the combustion of one fraction of syn gas generated allows obtaining a gas with a higher calorific value by not having a combustion zone inside it.

4.6 REFERENCES

[1] I. Dincer and C. Acar, "Smart energy solutions with hydrogen options," Int. J. Hydrogen Energy, vol. 43, no. 18, pp. 8579–8599, 2018, doi: 10.1016/j.ijhydene.2018.03.120.

[2] G. Prinsloo, A. Mammoli, and R. Dobson, "Discrete cogeneration optimization with storage capacity decision support for dynamic hybrid solar combined heat and power systems in isolated rural villages," Energy, vol. 116, pp. 1051–1064, 2016, doi: 10.1016/j.energy.2016.10.026.

[3] Thr¨an D. Smart bioenergy, Technologies and concepts for a more flexible bioenergy provision in future energy systems. Cham, Heidelberg ua: Springer. Online verfügbar unter https://link.springer.com/book/10.1007% 2F978-3-319-16193-8

[4] D. Patteeuw and L. Helsen, "Combined design and control optimization of residential heating systems in a smart-grid context," Energy Build., vol. 133, pp. 640–657, 2016, doi: 10.1016/j.enbuild.2016.09.030.

[5] C. Finck, R. Li, R. Kramer, and W. Zeiler, "Quantifying demand flexibility of power-to-heat and thermal energy storage in the control of building heating systems," Appl. Energy, vol. 209, no. July 2017, pp. 409–425, 2018, doi: 10.1016/j.apenergy.2017.11.036.

[6] K. Jana, A. Ray, M. M. Majoumerd, M. Assadi, and S. De, "Polygeneration as a future sustainable energy solution – A comprehensive review," Appl. Energy, vol. 202, pp. 88–111, 2017, doi: 10.1016/j.apenergy.2017.05.129.

[7] M. Hatti and E. Systems, Lecture Notes in Networks and Systems 62 Renewable Energy for Smart and Sustainable Cities. 2020.

[8] N. Lamaison, S. Collette, M. Vallée, and R. Bavière, "Storage influence in a combined

biomass and power-to-heat district heating production plant," Energy, vol. 186, 2019, doi: 10.1016/j.energy.2019.07.044.

[9] A. Bloess, W. P. Schill, and A. Zerrahn, "Power-to-heat for renewable energy integration: A review of technologies, modeling approaches, and flexibility potentials," Appl. Energy, vol. 212, no. August 2017, pp. 1611–1626, 2018, doi: 10.1016/j.apenergy.2017.12.073.

[10] Natural Resources Canada (NRCan), "Hydrogen strategy for Canada Seizing the Opportunities for Hydrogen," 2020.

[11] K. Mazloomi and C. Gomes, "Hydrogen as an energy carrier: Prospects and challenges," Renew. Sustain. Energy Rev., vol. 16, no. 5, pp. 3024–3033, 2012, doi: 10.1016/j.rser.2012.02.028.

[12] R. P. Menon, M. Paolone, and F. Maréchal, "Study of optimal design of polygeneration systems in optimal control strategies," Energy, vol. 55, pp. 134–141, 2013, doi: 10.1016/j.energy.2013.03.070.

[13] O. Bičáková and P. Straka, "Production of hydrogen from renewable resources and its effectiveness," Int. J. Hydrogen Energy, vol. 37, no. 16, pp. 11563–11578, 2012, doi: 10.1016/j.ijhydene.2012.05.047.

[14] H. Balat and E. Kirtay, "Hydrogen from biomass - Present scenario and future prospects," Int. J. Hydrogen Energy, vol. 35, no. 14, pp. 7416–7426, 2010, doi: 10.1016/j.ijhydene.2010.04.137.

[15] J. S. Tumuluru, Biomass Preprocessing and Pretreatments for Production of Biofuels. 2018.

[16] I. Hannula, "Hydrogen production via thermal gasification of biomass in near-to-medium term Hydrogen production via thermal gasification of biomass in near-to-medium term," 2009. [Online]. Available: http://www.vtt.fi/publications/index.jsp.

[17] A. Indarto, J. Palgunadi, Syngas Production, Applications and environmental impact. 2554.

[18] I. Dincer, "Green methods for hydrogen production," Int. J. Hydrogen Energy, vol. 37, no. 2, pp. 1954–1971, 2012, doi: 10.1016/j.ijhydene.2011.03.173.

[19] S. Heidenreich and P. Ugo, "New concepts in biomass gasi fi cation," Prog. Energy Combust. Sci., vol. 46, pp. 72–95, 2015, doi: 10.1016/j.pecs.2014.06.002.

[20] A. A. P. Susastriawan and H. Saptoadi, "Small-scale downdraft gasi fi ers for biomass gasi fi cation : A review," vol. 76, no. March, pp. 989–1003, 2017, doi: 10.1016/j.rser.2017.03.112.

[21] Prabir Basu, Biomass Gasification and Pyrolysis Practical Design and Theory. .

[22] P. Basu, Biomass Gasification and Pyrolysis. Burlington, USA: Elsevier Inc., 2010.

[23] P. Plis and R. K. Wilk, "Theoretical and experimental investigation of biomass gasification process in a fixed bed gasifier," Energy, vol. 36, no. 6, pp. 3838–3845, 2011, doi: 10.1016/j.energy.2010.08.039.

[24] Y. Ueki, T. Torigoe, H. Ono, R. Yoshiie, J. H. Kihedu, and I. Naruse, "Gasification

characteristics of woody biomass in the packed bed reactor," Proc. Combust. Inst., vol. 33, no. 2, pp. 1795–1800, 2011, doi: 10.1016/j.proci.2010.07.080.

[25] Y. H. Li et al., "A novel dual-bed for steam gasification of biomass," Biomass Convers. Biorefinery, vol. 8, no. 2, pp. 357–367, 2018, doi: 10.1007/s13399-017-0288-0.

[26] J. Hrbek, "Status report on thermal biomass gasification in countries participating in IEA Bioenergy Task 33," 2016. [Online]. Available: http://www.ieatask33.org/content/publications/Status_report%5Cnhttp://www.ieatask33.org/app/webroot/files/file/2016/Status_report.pdf.

[27] M. Milhé, L. Van De Steene, M. Haube, J. M. Commandré, W. F. Fassinou, and G. Flamant, "Autothermal and allothermal pyrolysis in a continuous fixed bed reactor," J. Anal. Appl. Pyrolysis, vol. 103, pp. 102–111, 2013, doi: 10.1016/j.jaap.2013.03.011.

[28] N. A. Samiran, M. N. M. Jaafar, J.-H. Ng, S. S. Lam, and C. T. Chong, "Progress in biomass gasification technique – With focus on Malaysian palm biomass for syngas production," Renew. Sustain. Energy Rev., vol. 62, pp. 1047–1062, 2016, doi: 10.1016/j.rser.2016.04.049.

[29] G. Mirmoshtaghi, H. Li, E. Thorin, and E. Dahlquist, "Evaluation of different biomass gasification modeling approaches for fluidized bed gasifiers," Biomass and Bioenergy, vol. 91, pp. 69–82, 2016, doi: 10.1016/j.biombioe.2016.05.002.

[30] J. A. Ruiz, M. C. Juárez, M. P. Morales, P. Muñoz, and M. A. Mendívil, "Biomass gasification for electricity generation: Review of current technology barriers," Renew. Sustain. Energy Rev., vol. 18, pp. 174–183, 2013, doi: 10.1016/j.rser.2012.10.021.

[31] L. Van de steene, J. . Tagutchou, F. Mermoud, E. Martin, and S. Salvador, "A new experimental Continuous Fixed Bed Reactor to characterise wood char gasification," Fuel, vol. 89, pp. 1–10, 2010, doi: 10.1016/j.fuel.2010.03.035.

[32] P. J. Woolcock and R. C. Brown, "A review of cleaning technologies for biomass-derived syngas," Biomass and Bioenergy, vol. 52, pp. 54–84, 2013, doi: 10.1016/j.biombioe.2013.02.036.

[33] S. M. Atnaw, S. A. Sulaiman, and S. Yusup, "Syngas production from downdraft gasification of oil palm fronds," Energy, vol. 61, pp. 491–501, 2013, doi: 10.1016/j.energy.2013.09.039.

[34] M. Asadullah, "Barriers of commercial power generation using biomass gasification gas: A review," Renew. Sustain. Energy Rev., vol. 29, pp. 201–215, 2014, doi: 10.1016/j.rser.2013.08.074.

[35] H. Ishaq and I. Dincer, "A new energy system based on biomass gasification for hydrogen and power production," Energy Reports, vol. 6, pp. 771–781, 2020, doi: 10.1016/j.egyr.2020.02.019.

[36] A. Molino, S. Chianese, and D. Musmarra, "Biomass gasification technology: The state of the art overview," J. Energy Chem., vol. 25, no. 1, pp. 10–25, 2016, doi: 10.1016/j.jechem.2015.11.005.

[37] I. Iliuta, A. Leclerc, and F. Larachi, "Allothermal steam gasification of biomass in cyclic multi-compartment bubbling fluidized-bed gasifier/combustor - New reactor concept," Bioresour. Technol., vol. 101, no. 9, pp. 3194–3208, 2010, doi: 10.1016/j.biortech.2009.12.023.

[38] G. Cheng et al., "Allothermal gasification of biomass using micron size biomass as external heat source," Bioresour. Technol., vol. 107, pp. 471–475, 2012, doi: 10.1016/j.biortech.2011.12.074.

[39] A. A. P. Susastriawan, H. Saptoadi, and Purnomo, "Small-scale downdraft gasifiers for biomass gasification: A review," Renew. Sustain. Energy Rev., vol. 76, no. March, pp. 989–1003, 2017, doi: 10.1016/j.rser.2017.03.112.

[40] X. Yao et al., "A comprehensive study on influence of operating parameters on agglomeration of ashes during biomass gasification in a laboratory-scale gasification system," Fuel, vol. 276, no. May, 2020, doi: 10.1016/j.fuel.2020.118083.

[41] X. Yao, Z. Zhao, J. Li, B. Zhang, H. Zhou, and K. Xu, "Experimental investigation of physicochemical and slagging characteristics of inorganic constituents in ash residues from gasification of different herbaceous biomass," Energy, vol. 198, p. 117367, 2020, doi: 10.1016/j.energy.2020.117367.

[42] X. Yao, Z. Zhao, S. Chen, H. Zhou, and K. Xu, "Migration and transformation behaviours of ash residues from a typical fixed-bed gasification station for biomass syngas production in China," Energy, vol. 201, p. 117646, 2020, doi: 10.1016/j.energy.2020.117646.

[43] A. Zubair Yahaya, M. Rao Somalu, A. Muchtar, S. Anwar Sulaiman, and W. Ramli Wan Daud, "Effects of temperature on the chemical composition of tars produced from the gasification of coconut and palm kernel shells using downdraft fixed-bed reactor," Fuel, vol. 265, no. December 2019, p. 116910, 2020, doi: 10.1016/j.fuel.2019.116910.

[44] Z. Khan, S. Yusup, M. M. Ahmad, and B. L. F. Chin, "Hydrogen production from palm kernel shell via integrated catalytic adsorption (ICA) steam gasification," Energy Convers. Manag., vol. 87, no. x, pp. 1224–1230, 2014, doi: 10.1016/j.enconman.2014.03.024.

[45] M. Hu et al., "A novel pilot-scale production of fuel gas by allothermal biomass gasification using biomass micron fuel (BMF) as external heat source," Clean Technol. Environ. Policy, vol. 18, no. 3, pp. 743–751, 2016, doi: 10.1007/s10098-015-1038-2.

[46] M. Shahabuddin, B. B. Krishna, T. Bhaskar, and G. Perkins, "Advances in the thermo-chemical production of hydrogen from biomass and residual wastes: Summary of recent techno-economic analyses," Bioresour. Technol., vol. 299, no. September 2019, p. 122557, 2020, doi: 10.1016/j.biortech.2019.122557.

[47] C. Srinivasakannan and N. Balasubramanian, "The significance of indirectly heated gasifiers for the generation of medium calorific value syngas through biomass

gasification," Energy Sources, Part A Recover. Util. Environ. Eff., vol. 32, no. 17, pp. 1579–1586, 2010, doi: 10.1080/15567030903076768.

[48] Y. Pang, S. Shen, and Y. Chen, "High Temperature Steam Gasification of Corn Straw Pellets in Downdraft Gasifier: Preparation of Hydrogen-Rich Gas," Waste and Biomass Valorization, vol. 10, no. 5, pp. 1333–1341, May 2019, doi: 10.1007/s12649-017-0143-3.

[49] E. Balu, U. Lee, and J. N. Chung, "High temperature steam gasification of woody biomass - A combined experimental and mathematical modeling approach," Int. J. Hydrogen Energy, vol. 40, no. 41, pp. 14104–14115, 2015, doi: 10.1016/j.ijhydene.2015.08.085.

[50] "Oilseeds: World Markets and Trade," 2021.

[51] S. K. Sansaniwal, K. Pal, M. A. Rosen, and S. K. Tyagi, "Recent advances in the development of biomass gasification technology: A comprehensive review," Renew. Sustain. Energy Rev., vol. 72, no. December 2016, pp. 363–384, 2017, doi: 10.1016/j.rser.2017.01.038.

[52] Y. Uemura, W. N. Omar, T. Tsutsui, and S. B. Yusup, "Torrefaction of oil palm wastes," Fuel, vol. 90, no. 8, pp. 2585–2591, 2011, doi: 10.1016/j.fuel.2011.03.021.

[53] J. Park, Y. Lee, and C. Ryu, "Reduction of primary tar vapor from biomass by hot char particles in fixed bed gasification," Biomass and Bioenergy, vol. 90, pp. 114–121, 2016, doi: 10.1016/j.biombioe.2016.04.001.

[54] C. M. van der Meijden, A. van der Drift, and B. J. Vreugdenhil, "Experimental results from the allothermal biomass gasifier Milena," 15th Eur. Biomass Conf., no. May, pp. 7–11, 2007.

[55] C. M. Van Der Meijden, W. Sierhuis, A. Van Der Drift, and B. J. Vreughdenhil, "Waste wood gasification in an allothermal gasifier," 19th Eur. Biomass Conf. Exhib., no. June, pp. 841–845, 2011.

[56] J. C. Acevedo-Páez, J. M. Durán, F. Posso, and E. Arenas, "Hydrogen production from palm kernel shell: Kinetic modeling and simulation," Int. J. Hydrogen Energy, vol. 45, no. 47, pp. 25689–25697, 2020, doi: 10.1016/j.ijhydene.2019.10.146.

Chapter5 THERMAL CHARACTERIZATION OF ALKALINE ELECTROLYSIS CELL FOR HYDROGEN PRODUCTION AT ATMOSPHERIC PRESSURE

Summary: The main contribution of the present chapter consists of the design and thermal characterization of an alkaline electrolysis cell for hydrogen generation at atmospheric pressure. The measurement of temperature in electrodes allows for improving the selection of the faraday efficiency coefficients that are a function of the temperature to improve the prediction capacity of the model for the production of hydrogen and the general balance of energy (Energy consumption per flow of hydrogen and oxygen generated). The experimental results will be used to create a mathematical model, analyze the electrolyzer unit and how its integration affects the consumption of syngas and biomass across the contribution of the oxygen necessary to the gasification process, solving the problem related to the necessity to include an air separation unit to provide the oxygen in the gasifier. Likewise, in order to find strategies to reduce manufacturing costs and increase efficiency, this research analyzes the distribution and variation of temperature on the surface of the electrodes while they are in operation, managing to set as these changes are related to thermoelectric phenomena, the presence of areas of higher activity for oxidation and reduction reactions in metals widely used in alkaline electrolysis, such as stainless steel.

5.1 INTRODUCTION

The production of hydrogen using renewable resources plays a crucial role in the sustainable transformation of the energy and mobility systems because it is a multi-use energy carrier that can be used directly for clean mobility in fuel-cell vehicles and internal combustion engines, as a storage for variable renewable energy sources, or as a starting point for the production of synthetic fuels [1][2][3]. Water electrolysis (WE) powered by renewable sources is one of the options to produce hydrogen, which is generated by passing an electric current through a conductive substance (electrolyte) to conduct a non-spontaneous reaction. The reaction of interest is the decomposition of water into hydrogen and oxygen, which is endothermic and requires energy input to be carried out. Precisely, a water electrolyzer consists of a series of electrochemical cells composed of: (i) electrolyte (ionic conductor), (ii) electrodes (anode and cathode) where oxidation and reduction reactions occur, (iii) supply system of electricity and auxiliary systems for supply and collection of reagents and products [4][5].

Rural areas with abundant renewable resources (solar and wind) can take advantage of the electrolysis of water to produce hydrogen to meet their lighting and heating needs in homes, the energy supply in communication stations, and the generation of small-scale electric light in the industry [6][7]. Likewise, specialized applications in the reduction of electricity peaks in integrated systems connected to or independent of the network [8]. Both photovoltaic (PV) energy and water electrolysis are well-known technologies. However, the coupling of both systems still presents some challenges. Dynamic loads, solar availability, compensations between the primary energy rate, load profiles, storage capacity, the coupling of PV-WE systems without maximum power point followers, power converters, operation, and efficiency AWE, as well as the cost reduction required to compete with conventional energy systems, are some of the most studied parameters [9][10].

There is a growing interest in electrolysis that has led to the development of various types of electrolyzers; the most common types includes solid oxide electrolyzer cells (SOEC), proton exchange membrane cells (PEM), and alkaline water electrolysis (AWE)[6]. SOEC cells are characterized by having a 90 % - efficiency and providing high thermal and chemical stability at reduced energy consumption; however, they have limitations associated with the rapid degradation of materials, short operating times, and high manufacturing costs [6]. PEM cells offer high efficiency (80%) and more compactness compared to alkaline type cells [11]; nevertheless, these require more expensive electrodes, polymeric membranes, and specialized components to resist corrosion. On the other hand, electrolyzers AWE are a mature technology, which offers great simplicity and moderate efficiency ranging from 59% to70% [11][12]. Nonetheless, their main drawbacks are electrolytic corrosion, gas permeation, and slow charge response that demand more work to meet the challenges of durability/reliability, greater efficiencies, and integration with renewable energy sources[13]. The technical specifications, power range, cost, and a lifetime of various types of electrolyzers are given in table 5-1.

Table 5-1: Technical parameters of various types of electrolyzers (taken from [4][14][15])

Specification	**Units**	**SOEC**	**PEM**	**Alkaline**
Technology maturity	-	Research & Development	Commercialization	Widespread commercialization
Cell temperature	°C	900-1000	50-80	60-80
Cell pressure	Bar	<30	<30	<30
Current density	$A\ cm^{-2}$	0.3-1.0	1.0-2.0	<0.45
Cell voltage	V	0.98-1.3	1.8–2.2	1.8–2.4

Voltage efficiency	%	81-86	67-82	59-70
Specific system energy consumption	$\mathrm{kWh\ Nm^{-3}}$	2.5-3.5	4.4-5.0	4.2-4.8
Minimum partial load	%	-	0-10	10-40
Cell area	$\mathrm{m^2}$	<0.06	<0.13	3-3.6
Hydrogen production per stack	$\mathrm{Nm^3h^{-1}}$	<10	<400	<1400
Stack lifetime	kh	8-20	60-100	55-120
System lifetime	year	-	10-20	20-30
Hydrogen purity	%	-	99.999	>99.8
Cold start-up time	Min	>60	<15	15
Investment costs	$\mathrm{\$\ kW^{-1}}$	>2200	1500-2300	900-1700

Electrolyzers are energy transformation devices. Therefore, their operation must be simple, efficient, and low-cost. AWE cells offer the advantages of being simple. Also, this technology has been in development for several years and has been industrially tested [11][16][9]. Recently, researchers have examined the effects of operating parameters on hydrogen production in AWE cells and photovoltaic-hydrogen ($\mathrm{PV-H_2}$) systems. Therefore, the impact of the composition, size and electrode surface, concentration and type of electrolyte used, system temperatures, working pressure, space between electrodes, current density and type connection to the grid are the most evaluated configuration and operation parameters [10][17][18][19][20].

Noble metals such as gold, silver, platinum, and palladium, are ideal materials for water electrolysis, but their high costs make them unaffordable for this type of application. For this reason, metals commonly used for water electrolysis include copper, titanium, aluminum, galvanized steel, and stainless steel [11][21]. Fatouh et al. [22] developed an AWE to experimentally assess the effect of the geometry and material of the electrodes on hydrogen production. The researchers propose a series of tests with 5%-45% KOH electrolytes and temperatures between 40°C-70°C. The highest hydrogen production was obtained with a solid cylinder, above 11% as compared to a finned cylinder and 5% higher than with a screw geometry cylinder. When evaluating the performance of five materials, aluminum showed a

higher hydrogen production when compared to stainless steel, titanium, copper and galvanized steel by 9%, 16%, 17%, and 18%, respectively.

However, when evaluating three essential properties in the life of electrodes - (i) mechanical resistance, (ii) corrosion resistance, and (iii) high-temperature resistance- stainless steel exhibited better performance than aluminum by 68%, 35%, and 57% respectively [23][24][25]. Consequently, the electrodes used in low-cost electrolysis applications are made of chromium-nickel alloys such as stainless steel [4][10][26]. Olivares-Ramírez et al. [19] studied the hydrogen evolution reaction in different stainless-steel electrodes in alkaline solutions (NaOH and KOH). They confirmed that the best material to be used in alkaline media as a cathode electrode due to a higher nickel content is 316 stainless steels. Similar results were obtained by Lavorante et al. [26] and Zeng et al.[27] ; They studied the modification of the surface in 316 L stainless steel electrodes, the mechanized electrodes with straight-parallel topology presented the best yields for an increase in the active area of the electrodes which allowed to increase the current density by an average of 50%.

As it is well known, the acids and bases that are used to change the non-conductive nature of pure water have a great effect on the quality of the ionic conductivity of an electrolyte [10][28]. On the other hand, the corrosive nature of these materials limits the use of acidic and alkaline electrolytes that are highly concentrated in industrial electrolyzers. This problem is due to the adverse effects on the life of the electrodes and other system components [29]. Taking into account the difficulties mentioned above, the solutions of KOH and NaOH in water between 20% - 40% are the most used [11][30]. Several studies have revealed that at temperatures of 80°C the electrical conductivity of the KOH solution is 19% higher than that of the NaOH solution [31]. For instance, most studies in the field of alkaline electrolysis have focused on the effect of the system temperature and its relationship with the temperature reached by electrolyte [10][32][33][34]. Indeed, the thermocouples used in experimental tests have focused on temperature measurement in: (i) external cell surfaces; (ii) hydrogen outlet pipes; (iii) electrolyte inlet pipes; (iv) temperature environment and (v) temperature inside the cell where the electrolyte is contained [35][36]. Despite the extensive research carried out, current knowledge about the distribution and variation of temperature in the electrodes surface while they are in operation is still limited [4][10][20][37]. Likewise, how these changes are related to thermoelectric phenomena, the presence of areas of

higher activity for oxidation and reduction reactions in metals widely used in alkaline electrolysis such as stainless steel [38][39][40].

Previous studies show that the reaction potential for the division of the water molecule gets reduced as the temperature increases [41][42]. This division potential is due to the thermodynamic properties of the water molecule, reaction capacity, and ionic conductivity increase of an electrolyte with the temperature rise [19][28]. Consequently, high temperatures (60-100 °C) improve the efficiency of the electrolyzers, while increasing the operating pressure does not achieve a considerable improvement (> 3%) on the electrolyzer performance [17][28]. On the other hand, experimental data shows that the space between electrodes is strongly related to ohmic losses and fluid dynamics within electrolysis cells [42][43]. Thus, greater distances between electrodes require a higher voltage in the cell, with the necessity for an even higher voltage to ensure the operating current rises to maintain the generation hydrogen rate [22][28]. In consequence, there is an optimal space between electrodes that depends on the current density and other experimental conditions (electrode geometry, system temperature, and gas separation membrane). Finally, a deeper understanding of the complex electrochemical and physical interfacial phenomena that occur in a three-phase zone during bubble evolution may contribute to an improved design strategy for industrial water electrolysis systems [39][42][44].

Researchers, like Nagai et al. [33] demonstrated the existence of an optimal space between 1-3 mm that favors greater water electrolysis efficiency for current densities of $0.5\ \mathrm{A/cm^2}$, 50x100 mm stainless steel sheets, system temperatures of 60 °C and absence of gas separation membrane. Likewise, Amores et al. [45] developed a new mathematical model that includes the effect of electrolyte concentration and distance between electrodes, based on the modification of the Ulleberg equation. The simulation results were validated with experimental data of electrolysis cell tested with a gap between electrodes of 10, 4 and 1.5 mm, current density $0.35\ \mathrm{A/cm^2}$, Cathodes made of 316 stainless steel of 10x20 mm, system temperature of 60 °C, and the presence of gas separation diaphragm. The results that set a distance greater than 1 mm between electrodes generates an increase in bubble growth. Finally, Lavorante et al. [26] evaluated the performance of 316 stainless steel electrodes in the electrolysis cell, with two different configurations of the distance between electrodes (6.1 and 5.3 mm) a current density of $0.30\ \mathrm{A/cm^2}$ system temperature of 70 °C and the presence of gas separation diaphragm. The reported results show that the 6.1 mm configuration presented the best

performance for all the systems under study due to the decrease in the vacuum fraction as the distance between electrodes increased.

Several studies have been developed to calculate the size and optimal operation of photovoltaic (PV) powered AWE systems directly and indirectly coupled to optimize energy transfer [10][7]. Palhares et al. [10] evaluated an AWE system to produce hydrogen using photovoltaic panels as a source of energy for the electrolytic reaction and thus contributed to the exploration of renewable energy sources. The researchers used a cylindrical electrolytic cell made of acrylic, 304 stainless steel electrodes, sodium hydroxide (NaOH) as an electrolyte, and a gas separator plate connected to a 20 W photovoltaic panel exposed to an average irradiance of $800\,\mathrm{Wm^{-2}} \pm 60\,\mathrm{Wm^{-2}}$ and average hydrogen production of $5 \times 10^{-4}\,\mathrm{Nm^3/h}$. Similarly, Kovac et al.[9] evaluated an AWE system for hydrogen production through water electrolysis using a 960 W solar power plant exposed to an average irradiance of $550\,\mathrm{Wm^{-2}} \pm 30\,\mathrm{Wm^{-2}}$. The researchers manufactured a bipolar alkaline electrolyzer with porous nickel-based electrodes immersed in a 25% KOH electrolyte solution and a gas separation membrane and average hydrogen production of $1.27 \times 10^{-2}\,\mathrm{Nm^3/h}$.

The literature review revealed that the hydrogen production of an alkaline electrolyzer has not been fully explored under different operating environments [4][46]. Specifically, the challenges of reducing energy consumption, cost, and maintenance persist. At the same time, an increase in reliability, durability, and safety is required by integrating renewable energy [4][21]. In this chapter, an experimental study on the production of hydrogen at atmospheric pressure has been carried out using photovoltaic solar panels as a source of energy for the electrolytic reaction. The research consists of analyzing the effect of the applied electrical power, electrode, and membrane distance on the thermal behavior and hydrogen production efficiencies in an alkaline electrolysis cell made of stainless-steel sheets, immersed in 40% w/w KOH electrolytic solution, and low-cost polymer membrane with the goal of exploring new energy vectors from renewable sources.

5.2 MATERIAL AND METHODS

In the present work, experimental tests are carried out with an alkaline electrolysis cell in order to study the effect of electrode/membrane distance on hydrogen production. The calculation of the electrical power consumed, the efficiency of the cell, and the distribution of temperatures on the electrodes are evaluated in a generation system using solar energy to supply the electric power to the electrodes.

The method used for hydrogen production is illustrated in figure 5-1. The main elements that comprise it are described below. a) Polycrystalline solar panel with dimensions 1008 × 992 × 35 mm, maximum power of 130 W, 22.10 V in open circuit, 8.15 A of short-circuit current and performance of 14.7%. b) 12/24 V charge controller with automatic work detection, pulse width modulation (PWM) charge control, and 20 A nominal current for deep cycle battery. c) AGM 12V and 155 Ah deep cycle battery with a gas regulation valve. d) 40 A Bipolar Breaker. e) 12V / 40 A constant current pulse width modulator (CCPWM). The electrical connection of the components mentioned above is made with 16/18 AWG electrical conductors.

The system for generation, collection, and measurement of gases consists of the following elements: f) bipolar design alkaline electrolysis cell; g) oxygen receiver made of translucent acrylic of Φ135 mm × 150 mm; h) two electrolyte containers (KOH) responsible for feeding the alkaline electrolysis cell and serving as primary bubbles of the hydrogen generated and manufactured in translucent acrylic of Φ74 mm × 250 mm. Finally, i) adaptation of the pneumatic tank for gas separation developed by Stephen Hales whose principle of operation is to keep the gas isolated inside a container partially filled with water so that it does not mix with the gases that make up the air. During the experimental process a graduated cylinder of Φ74 mm × 230 mm that is used is submerged in a translucent acrylic box of 150 × 200 × 400 mm filled with water. The entire hydraulic circuit is manufactured with couplings and hoses made of plastic material resistant to high temperatures and high concentrations of electrolyte.

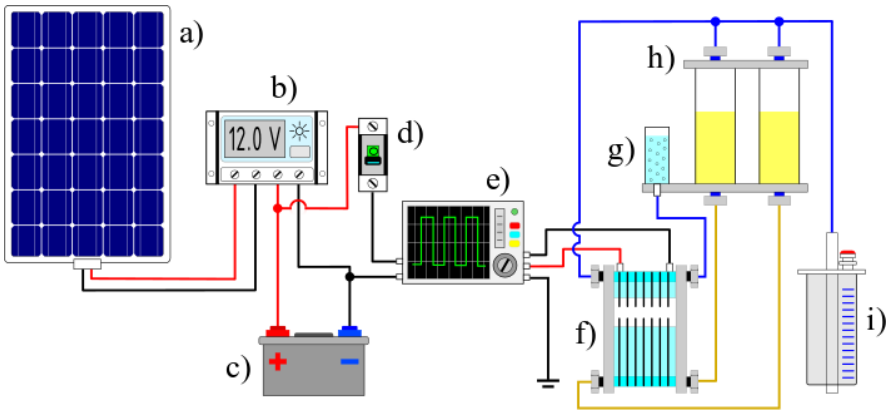

Figure 5-1: Representative diagram of the system used for hydrogen production: a) polycrystalline solar panel SolarEdge®; b) charge regulator Epever®; c) AGM deep cycle battery Mteck® ; d) bipolar breaker ABB®; e) constant current pulse width modulator

PowMr®, f) alkaline electrolysis cell TECHME®; g) oxygen receptor; h) KOH electrolyte containers and i) adaptation of the pneumatic tank.

Figure 5-2 shows the alkaline electrolysis cell of the bipolar design. It is composed of: a) two translucent acrylic plates of 200×200×8 mm, b) four neoprene seals of 200×200×1 mm, c) two 316 L stainless steel sheets with dimensions 200×200×1.9 mm (anode and cathode) modified by mechanical polishing with sandpapers P400 to increase the electrode surface area [238] and d) a membrane made of 200×200×0.12 mm polyester fiber. The electrodes and separator are immersed in a 40% aqueous solution of KOH w/w. Likewise, the cell is equipped with K-type temperature sensors and data acquisition systems.

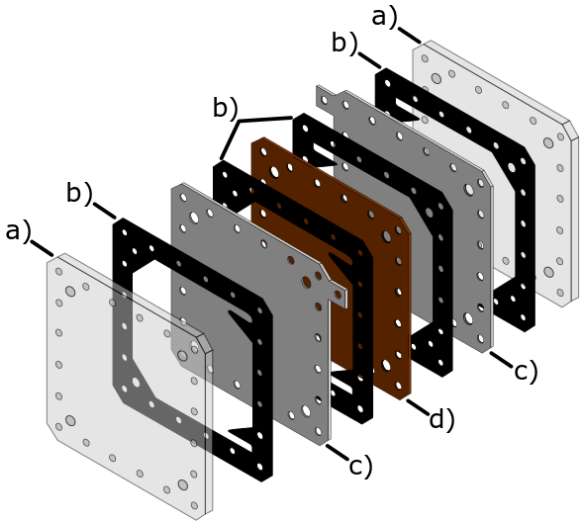

Figure 5-2: Alkaline electrolysis cell: a) 2 translucent acrylic plates, b) 4 neoprene seals, c) 2 stainless steel sheets (anode and cathode) and d) polyester fiber membrane

Figure 5-3 represents the tools used for measuring temperatures at different points on the anode and cathode. Five evaluation positions are considered as listed in Table 5-2, where the origin is established in the lower-left corner of each plate. The temperature measurement system consists of an OMEGA HH309A type K digital thermometer, Xplorer GLX type K temperature sensor, and a portable computer. The data acquisition system is carried out with the help of the Testlink SE-309 software.

Table 5-2: Position of the temperature sensors on the anode and cathode plates

Temperature indicator	**Anode**		**Cathode**	
	x (mm)	**y (mm)**	**x (mm)**	**y (mm)**

T_1	50	50	150	50
T_2	150	50	50	50
T_3	100	100	100	100
T_4	50	150	150	150
T_5	150	150	50	150

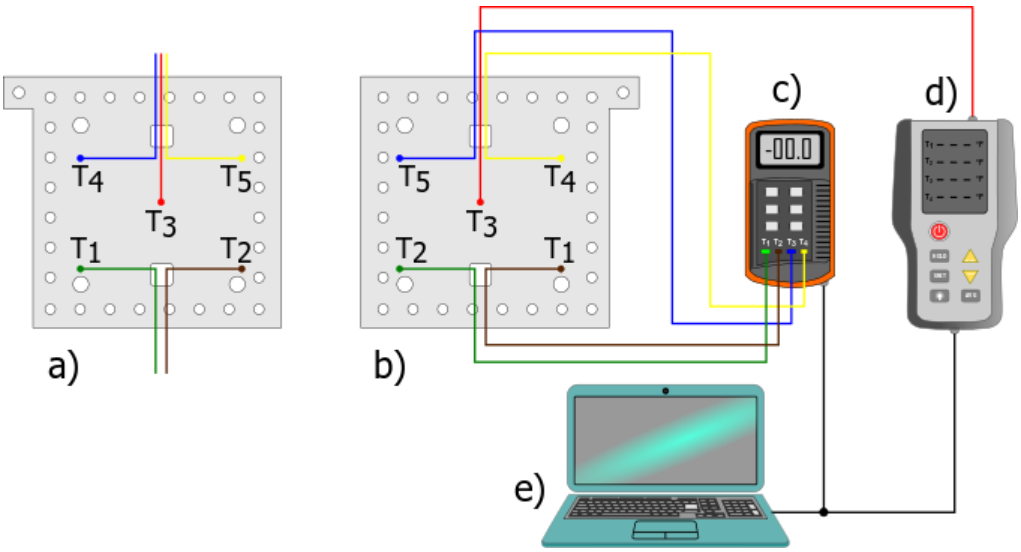

Figure 5-3: Schematic diagram of the electrode temperature measurement system. The components are labeled as follows: a) positive plate (anode); b) negative plate (cathode); c) OMEGA HH309A type K digital thermometer; d) Xplorer GLX type K temperature sensor; e) portable computer equipment.

It is important to note that the design of the alkaline electrolysis cell allows a simple replacement of the components (acrylic plate, electrodes, membrane, and gaskets). This makes it possible to modify the space between electrodes by using different neoprene seals. This feature gives the alkaline electrolysis system the great versatility that makes it suitable for the simulation and testing of prototypes or components on a medium and small scale. Figure 5-4 shows two different configurations of the alkaline electrolysis cell evaluated experimentally.

Figure 5-4: Alkaline electrolysis cells used in experimental tests

5.3 **EXPERIMENTAL CONFIGURATION**

The system with photovoltaic generation and electrolyzer was tested experimentally to produce hydrogen in remote outdoor areas in Bogotá-Colombia city. The procedure used for each configuration is described below: 40% KOH electrolyte w/w is supplied to the containers, see Figure 1- h). A hermeticity test is performed to rule out the presence of electrolyte leaks on each of the hydraulic lines and the electrolysis cell. A digital multimeter is used to verify electrical continuity in the lines laid from the solar panel, Figure 1- a) to the electrolysis cell, Figure 1- f). Next, the constant current pulse width modulator is turned on. This item is configured to work at 2 A and 12 V for 30 minutes. Subsequently, with the help of a gas meter, it is verified that there are no leaks in the lines that connect the gas collection and measurement system, Figure 1- g) -i). Once a specific operating time has been reached, the passage of hydrogen is enabled for measurement within the designed pneumatic tank system. Finally, the Testlink SE-309 software environment is configured to display and record the temperatures of each of the thermal sensors installed on the electrodes.

Experimental tests are developed by evaluating three different spaces between the electrode and the membrane (17, 11 and 3 mm). For each configuration, the system behavior for six current conditions (5, 10, 15, 20, 25 and 30 A) is studied. For each current condition, replicated three times, the temperature distribution in the anode and cathode, the power consumed, the efficiency of the cell and the hydrogen flow

are evaluated. The calculation of the efficiency of the electrolyzer, $\eta_{electrolyzer}$ and the efficiency of the system, η_{system}, can be determined from equations (1) and (2) [253][254][255].

$$\eta_{electrolyzer} = \frac{Q * LHV_{H_2}}{V * I} \% \quad (1)$$

$$\eta_{system} = PV_{efficiency} * \eta_{electrolyzer} \quad (2)$$

where the equations depend on the ratio of the hydrogen flow Q, the lower heating value of hydrogen LHV_{H_2}, the voltage load V, the current load I, and performance of polycrystalline solar panel $PV_{efficiency}$.

5.4 RESULT AND DISCUSSION

5.4.1 HYDROGEN FLOW RATE BY ALKALINE ELECTROLYSIS CELL

The amount of hydrogen generated by the alkaline electrolysis cell showed variations for different distances between electrodes and applied current. The experimental results of the hydrogen flow rate for the various electric currents considered are presented in Figure 5-5; from these results it can be concluded that increasing the current of the electrolyzer increases the flow rate of generated hydrogen. The present experimental work showed a 74% increase in hydrogen flow by increasing the current from 5 to 30 amps for the three distances between proposed electrodes. It can also be observed that the hydrogen flow rate increases continuously until reaching a maximum value of $2.6\ x10^{-2} Nm^3/h$ for a current of 30 A and a distance between electrodes of 3mm. When analyzing the three distances between the electrodes evaluated, it is established that for the 3 mm configuration there is higher hydrogen production, specifically around 21-35% higher gas generation than for the 11 and 17 mm configurations evaluated between 5- 30 amperes; the same behavior is observed when comparing the results obtained with experimental data from other researchers, Yilani et al. [3], Nagai et al. [33] and Amores et al. [50]. Likewise, it is concluded that with an electrode space between 1-3 mm [50][40], there is a higher gas generation, which is why a smaller distance between electrodes allows the electrolyte chamber to decrease, while the general conductivity increases. Additionally, there is a reduction in the vacuum fraction between the electrodes, which results in a decreased electrical resistance following the Ohms law [51] (that implies that in order to reduce voltage drop at the same

current density, either conductivity of electrolyte needs to be increased, or the electrode spacing needs to be decreased), an increased growth rate of the bubbles and, consequently, in a higher generation of hydrogen.

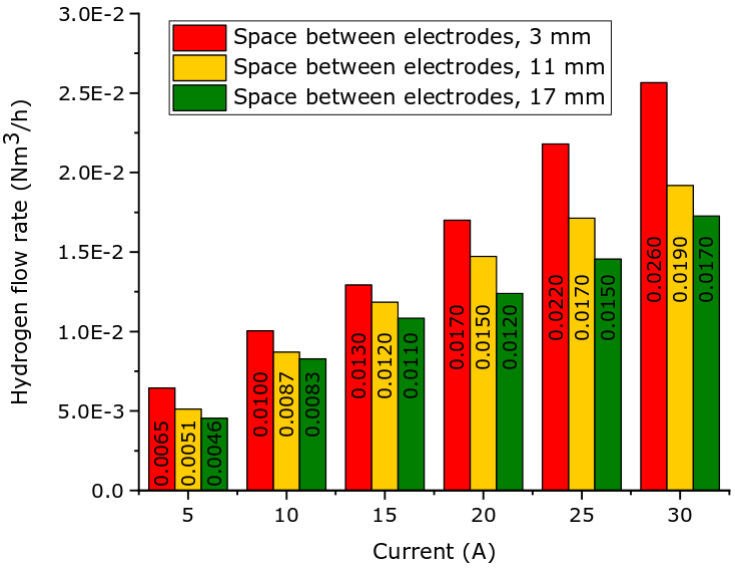

Figure 5-5: Experimental results of the H_2 flow rate with the direct current source.

5.4.2 **ENERGY EFFICIENCY**

The behavior of the efficiency of the cell, as well as the efficiency of the system, are shown in figure 5-6. It is observed that the highest yields were achieved with the 3mm configuration, followed by the 11mm configuration and finally the 17mm configuration. The electrolyzer reaches a maximum performance of 31% at 5 A and a minimum performance of 25% at 30 A with a 3mm electrode gap, see Figure 6 (a). On the other hand, the efficiency of the system reaches a maximum efficiency of 4.6% at 5 A and a minimum efficiency of 3.6% at 20 A with this same electrode configuration, see Figure 6 (b). When comparing these results with those reported in the literature [10][48][52], it is observed that the system efficiency values are quite similar [3]. However, the electrolyzer efficiency values show appreciable differences [3]. First, these differences are due to the type of a membrane used as it obstructs the increasing circulation of bubbles [32][38][53]. This generates an increase in the vacuum fraction and the electrical resistance between electrodes. Besides, cell overvoltage (12 V) increases ohmic losses; therefore, a decrease in cell efficiency is generated [3].

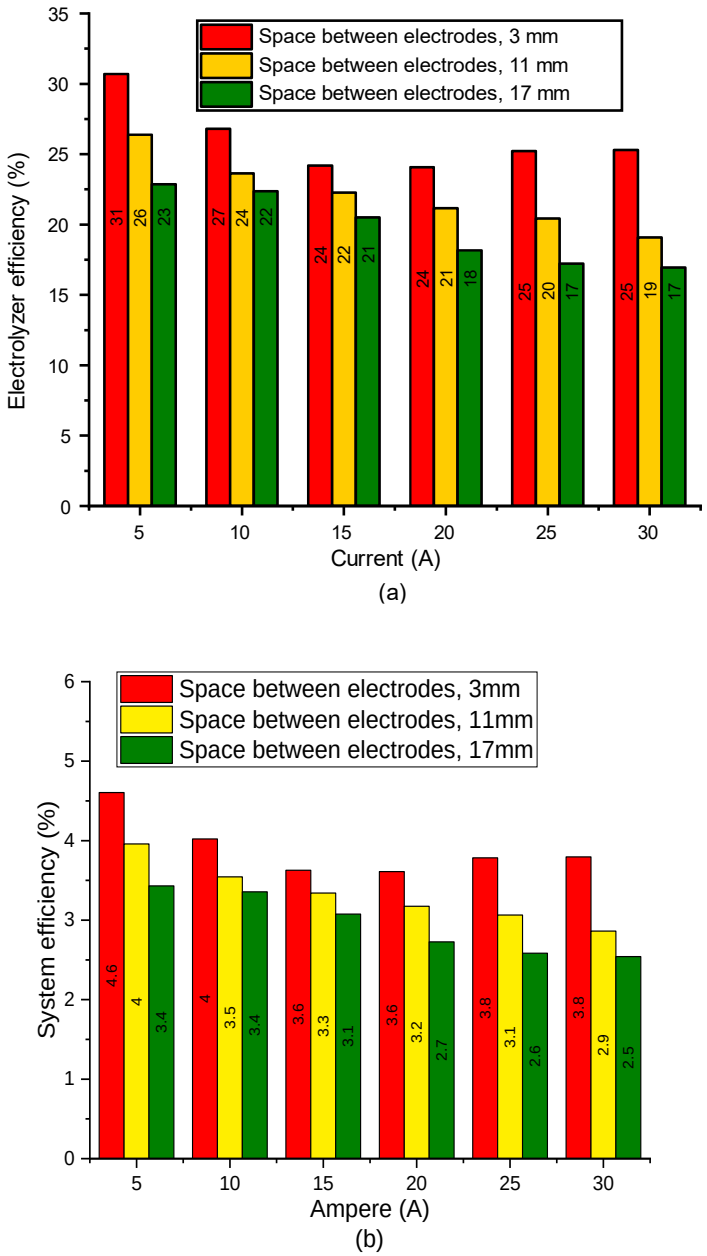

Figure 5-6: (a) Electrolyzer efficiency and (b) system efficiency measured

5.4.3 **DISTRIBUTION AND VARIATION OF TEMPERATURE IN ELECTRODES**

The temperature distribution on the electrodes (see Figure 3) is determined with the help of the Testlink SE-309 software. As mentioned earlier, the behavior for distances between electrodes of 3, 11 and 17 mm is analyzed for six current conditions (5, 10, 15, 20, 25 and 30 A). The results generated by each temperature sensor at the anode and cathode show the following trends. For the positive plate

(anode): (i) temperature increase, (ii) temperature decrease zones, (iii) constant temperature zone, and (iv) periods between 10 and 20 seconds for temperature stabilization when modifying the current condition in the electrolysis cell. Similarly, the negative plate (cathode) has (i) a zone with temperature decrease, (ii) a zone with temperature increase, (iii) constant temperature, and (iv) a period between 10 and 15 seconds to stabilize the temperatures when changing the current condition in the electrolysis cell.

Figure 5-7 shows the temperature distribution for the 3 mm configuration on the anode (Figure 7 (a)), the temperature sensor T4 registers a temperature increase ΔT = 209°C when passing from a current of 0 to 30 A. On the other hand, the thermal sensors T1, T2 and T5 register a decrease in temperature ΔT = -77 ° C, ΔT = -139°C and ΔT = -27°C, respectively. As for the T3 sensor, it exhibits a constant temperature of 31 ° C. By contrast, at the cathode (Figure 7 (b)), the T4 sensor registers a temperature decrease ΔT = -214°C when passing from a current condition of 0 to 20 A. Sensors T1, T2 and T5, show temperature increases of ΔT = 125°C, ΔT = 69°C and ΔT = 15°C, respectively, when passing from a current of 0 to 30 A. The temperature sensor T3 remains constant with an average temperature of 29°C.

Figure 5-8 shows the temperature distribution for the electrodes evaluated in the 11 mm separation configuration. For the anode (Figure 8 (a)), the T4 sensor records an increase in temperature (ΔT = 208°C) when passing from a current condition of 0 to 30 A. Sensors T1, T2 and T5 show a decrease in temperature of ΔT = -61°C, ΔT = -131°C and ΔT = -30°C, respectively. The thermal sensor T3 remains constant, with an average temperature of 27 ° C for the different current conditions tested. By contrast, the cathode sensor T4 (Figure 8 (b)) has a temperature decrease of ΔT = -220°C for current variations from 0 to 20 A. On this same plate, the thermal sensors T1, T2 and T5 show a temperature rise ΔT = 115°C, ΔT = 60°C and ΔT = 34°C, respectively, for current conditions from 0 to 30 A. Thermometer T3 remains constant with an average temperature of 25°C.

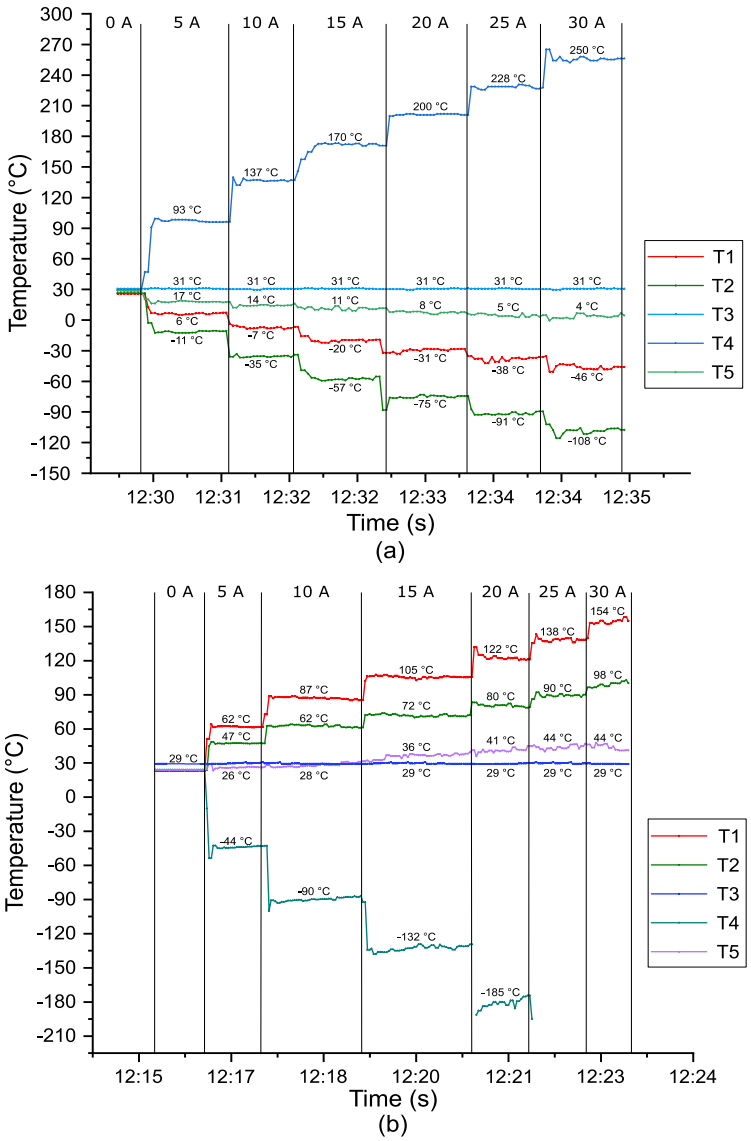

Figure 5-7: Temperature distribution for the distance between electrodes of 3 mm: (a) anode and (b) cathode.

Finally, figure 5-9 shows the temperature distribution for the electrodes evaluated in the 17 mm configuration. In the first instance, for the anode, the thermal sensor T4 registers a temperature increase of ΔT = 183°C, considering a current variation of 0 to 30 A. The group of sensors T1, T2 and T5 show a temperature decrease of ΔT = -50°C, ΔT = -109°C and ΔT = -37°C, respectively. On the other hand, the T3 sensor remains constant, with an average temperature of 24°C. As for the temperature distribution over the cathode, the T4 sensor records a temperature decrease of ΔT = -189°C for a current variation of 0 to 20 A. The group of sensors T1, T2 and T5 show a temperature increase of ΔT = 108°C, ΔT = 58°C and ΔT =

42°C, respectively for a current condition of 0 to 30 A. The thermal sensor T3 remains constant with an average temperature of 24°C.

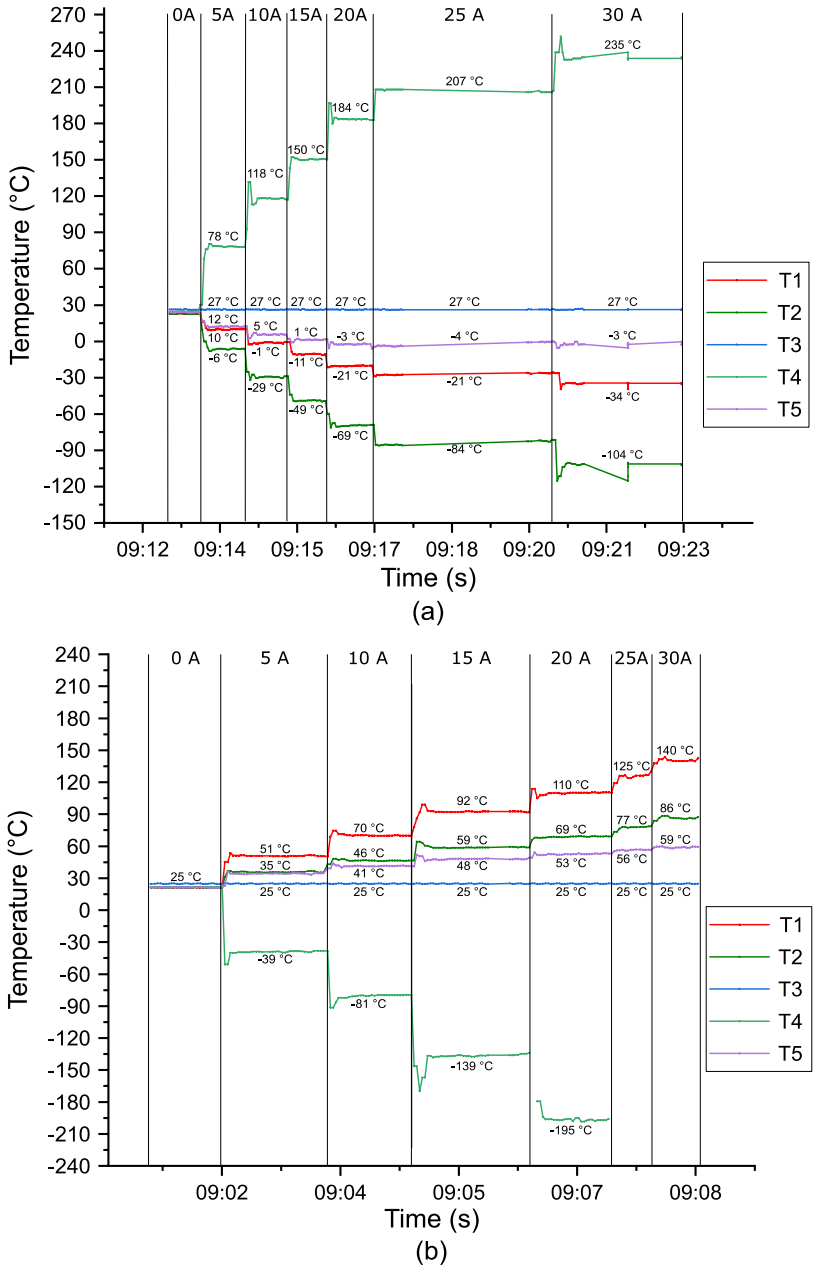

Figure 5-8: Temperature distribution for 11 mm electrode distance: (a) anode and (b) cathode.

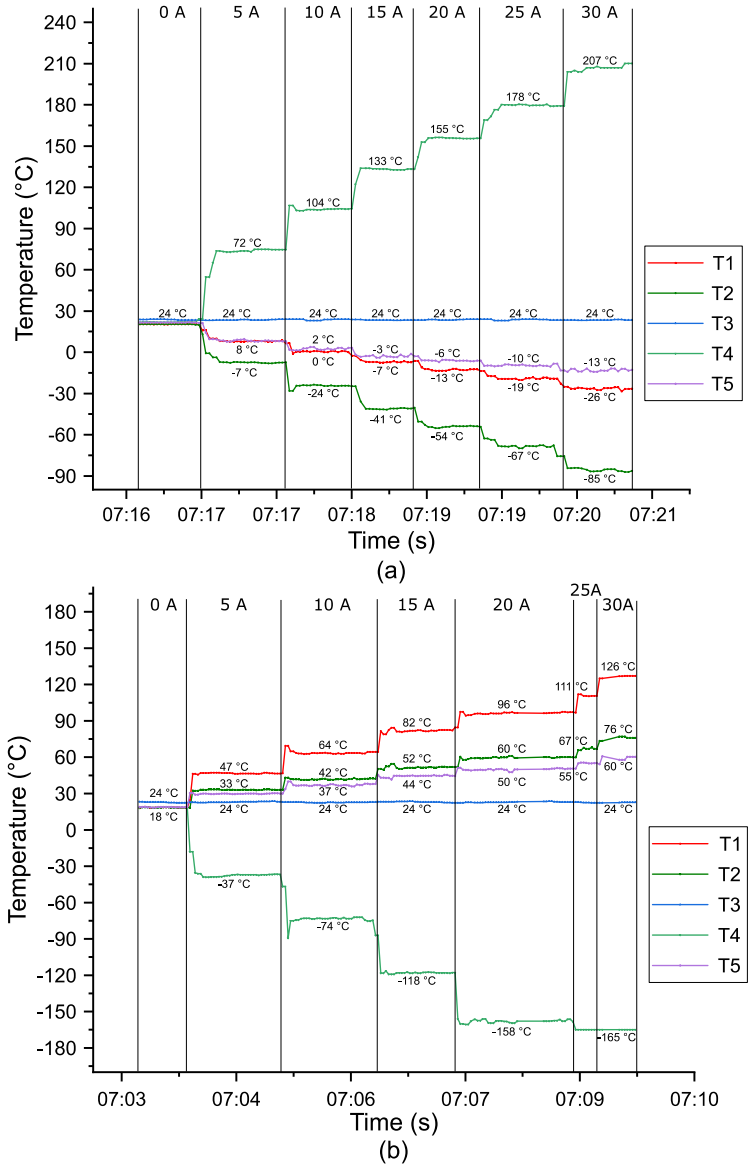

Figure 5-9: Temperature distribution for the distance between 17 mm electrodes: (a) anode and (b) cathode.

The interpretation of the results of figures 5-7-5-9 as follows; In all the case studies it is interesting to observe the following: for the anode, the thermal sensor T4 always registers the highest temperature point while the thermal sensor T2 registers the lowest temperature point. However, for the cathode, the thermal sensor T1 always registers the highest temperature point while the thermal sensor T4 registers the lowest temperature point out of the ten evaluated points. Consequently, the maximum decrease in temperature for the anode in the thermal sensor T4 is ΔT = 43°C and the maximum increase in temperature in the thermal sensor T2 is ΔT = 23°C when modifying the distance between electrodes of 3 to 17 mm. Similarly, the

maximum decrease in temperature for the cathode in the thermal sensor T1 is ΔT =29°C, and the maximum increase in temperature for the thermal sensor T4 is ΔT = 38°C.

5.4.4 INTERACTION BETWEEN THE ELECTRICAL AND THERMAL PHENOMENA IN ELECTRODES

The interaction between the electrical and thermal phenomena has been known since the 19th century. Since then, it has become common knowledge that thermoelectric interaction includes the effects of Joule, Seebeck, Peltier, and Thomson. To explain and justify the results obtained in Figures 7-9, the effects mentioned above must be understood [54]. First, the Joule effect relates to the heating of a conductive material through which the current flows. The Seebeck effect states that, in a circuit formed by different conductors, whose welded joints are in different temperature media, there is a potential difference. This difference is a function of the nature of the conductors and the temperature difference. By contrast, the Peltier effect consists of the cooling or heating of a junction between two different conductors when an electric current pass through it and depends exclusively on the composition and temperature of the junction. Finally, the Thomson effect deals only with elements of the same material or conductor; it does not consider thermocouples, unlike the Peltier effect and the Seebeck effect. Thus, the Thomson effect relates to the absorption or release of heat by an electric conductor with temperature gradients through which an electric current circulates.

Within the Thomson phenomenon, there are two manifestations: positive and negative Thomson effect. In the positive Thomson effect, the hot end acquires a high potential (+), and the cold end shows a low potential (-). Heat is generated when the current passes from the hottest end to the coldest end. Heat is absorbed when the current passes from the coldest end to the hottest end. The metals that show the positive Thomson effect are copper, antimony, cadmium, zinc, etc. Finally, in the negative Thomson effect, the hot end has a low potential (-), and the cold end has a high potential (+). Heat is generated when the current passes from the coldest end to the hottest end. On the other hand, heat is absorbed when the current flows from the hottest end to the coldest end. The metals that show the negative Thomson effect are iron, cobalt, bismuth, mercury, nickel, among others.

The results shown in Figures 5-7 to 5-9 match the negative Joule-Thomson effects described above. In the same way, one presents the phenomena of oxidation and reduction in the electrodes submerged in an electrolytic solution when conducting

the electric current. In other words, the metal that has a positive net charge (anode) attracts negative ions from the electrolyte solution. When negative ions touch the surface, it results in the process of oxidation or loss of electrons and at the same time, the oxidation state increases; this is how these electrons migrate from the bottom of the sheet (points of higher generation of bubbles), leaving a cold point, following what is described as the Thomson effect. According to this effect, there are areas of lower temperature in the electrode geometry, which indicates a higher oxidation activity [20][42]. These electrons are concentrated in the area near the thermal sensor T4, where the electrical connection for the anode is located, and consequently, there is an increase in temperature.

On the other hand, the negatively charged metal (cathode) attracts positive ions from the electrolyte solution. When the positive ions touch the surface, there is a reduction process or gain of electrons upon receiving the charge that releases the anode. So, the particles migrate from the top of the electrode to the bottom, leaving a cold end in the area near the thermal sensor T4 where the electrical connection for the cathode is located. Consequently, an accumulation of electrons is generated at the bottom of the cathode [42]. This increases its temperature following the Thomson effect. Therefore, there are areas of higher temperature in the electrode geometry that indicate greater reduction activity.

5.4.5 **GAS BUBBLE DYNAMICS IN ELECTRODES**

Previous studies have pointed out the importance of bubble dynamics and interfacial phenomena in the triphasic zone, where the electrolyte, gas bubble, and electrode surface come into contact [39][41][42]. Understanding the dynamics of bubbles evolving from the electrode surface in the electrolytic transformation is the key to interpreting the relationship between the process variables (optimal spacing between electrodes, contact surface, current density, temperature, and electrolyte used) and energy losses in AWE cells [42].

Firstly, the gas bubble evolution includes: (i) boiling or desorption process and (ii) electrolyte gas bubble formation (nucleation, growth, and departure). In nucleation, the dissolved gas is generated in molecular form by electrochemical reactions (electrode-electrolyte); The generated vapor bubbles are trapped and accumulated on the surface of the electrode to form a supersaturation layer with dissolved gas molecules [20][44][55][56]. In our experimental observations, we validate this behavior by observing an increase in temperature in the area of the T4 sensor (Fig 7-9) where the concentration of electrons near the electrical connection used for

the anode occurs. On the other hand, the negatively charged electrode (cathode) attracts positive ions from the electrolytic solution, when the positive ions touch the surface; there is a process of reduction or gain of electrons when receiving the charge released by the anode. For this reason, the electrons migrate from the top of the electrode to the bottom, leaving a cold end near the thermal sensor T4 (Fig 5-7;5-9) where the electrical connection for the cathode is located. Our experimental observations validate this behavior by observing an increase in temperature in the area of the T1 sensor (Fig 5-7 to 5-9), where an accumulation of electrons is generated at the bottom of the cathode following what is described by the Joule-Thomson effect. Therefore, there are specific areas on the cathode with higher temperatures that indicate greater reduction activity.

Secondly, in growth due to the convex curvature of the vapor bubbles trapped in the cavities, the vapor pressure within the bubbles is higher than the surrounding liquid. Although the surrounding fluid is at saturation temperature, its equilibrium vapor pressure would not match the vapor pressure within the trapped bubble. However, if the liquid were to overheat enough, its equilibrium vapor pressure would be higher than the vapor pressure of the bubble, causing the bubble to grow [39][55][56]. In this phase, the interfacial tension force and the drag force are presented as the most important forces in the analysis of the balance of forces in the dynamics of gas bubbles in the area of triphasic contact between the electrolyte, gas bubble, and the electrode surface. According to the theory and experimentation presented by Zhang et al. [20], the trend of increasing critical diameters with increasing current density can be explained by the increased interfacial tension at higher electrode potentials [20][39]. However, the authors find a decrease in the critical diameter of the gas bubbles; these results attribute it to the high current density that generates two possible conditions: (i) local heating and generation of temperature gradients on the electrode surface due to a high ohmic loss, (ii) higher gas formation, the premature depart of bubbles from the bottom of the electrodes and greater natural convection or micro convection of the electrolyte, caused by a high current density that generated temperature gradients on the electrode surface and upward movement of gas bubbles produced in the electrolyte.

Finally, we have the detachment and exit of the bubble. The presence of the captured supersaturation layer on the electrode surface induces monophasic free-convention phenomena (due to the concentration gradient of gases dissolved in the aqueous electrolyte); the growth of the bubble pushes the liquid in a radial direction. It will eventually get detached from the nucleation site to slide along the heating wall as the separation forces overcome the surface tension force. When

bubbles break off the electrode surface, they begin to move upward, dragging the electrolyte and buoyancy and inducing a gas-liquid pumping effect that improves the speed of mass transfer to the electrode surface [39][41][44].

The vacuum fraction of the total electrode area inactive due to bubble formation is an essential parameter in understanding the energy losses in AWE cells [20][42]. Recent research has demonstrated that bubble coverage shows a complex dependence on different parameters such as gas flow rate, surface roughness, bubble residence time, bubble volume leaving the electrode, and electrode wall temperature [20][55][57]. However, at present, it is not known what additional parameters are active and what affects the overall efficiency of the electrolysis process [39][41][58]. Likewise, there is no stable mathematical relationship to predict the value of the vacuum fraction that considers the variation in the distribution of wall temperatures in electrodes [43][59]. Such a relationship would be desirable for practical application and improvement in electrode design for industrial water electrolysis systems [11].

From our experimental observations, we can validate that at high current densities, the Joule-Thomson effects present on the electrodes generate two simultaneous phenomena: (i) temperature gradients on the surface of the electrodes and (ii) specific areas on the surface of the electrodes where oxidation-reduction reactions are favored and therefore, a greater generation of bubbles takes place. Alike, the results of the present work explain the differences in the prediction of mathematical models and experimental results presented by other authors. Zhang et al. [20], Cho et al. [39], and Wang et al.[41] Also, they allow us to broaden the understanding, optimization, and development of new designs for industrial water electrolysis systems where non-uniform bubble outlets are observed and to improve mathematical models of bubble growth dynamics where the surface temperature of the electrodes is not isothermal in water electrolysis relevant to different applications.

5.5 CONCLUSIONS

This chapter discusses the performance of an alkaline electrolysis cell for the application of remote area hydrogen using photovoltaic panels. Maximum efficiencies of 31% were achieved for the alkaline electrolysis cell and 4.6 % for the entire system including a 360 W solar panel.

The distribution of temperatures on the electrodes was determined, identifying the interaction between the electrical and thermal phenomena present in the anode and cathode. From the analysis of the data, it became evident that the Joule-Thomson effect dominates. This explains the existence of temperature gradients on the electrode surface and areas of higher activity for oxidation and reduction reactions in metals such as stainless steel with measured temperature differences in the anode of $\Delta T = 209°C$ and $\Delta T = -139°C$. Temperature differences in the cathode of $\Delta T = 125°C$ and $\Delta T = -214°C$ were measured.

The gas bubble formation was analyzed, and it could be shown that in nucleation the generated vapor bubbles are trapped and accumulated on the surface of the electrode to form a supersaturation layer with dissolved gas molecules due to a high current density and surface roughness on electrodes. These conditions generated temperature gradients and specific areas on the surface of the electrodes where oxidation-reduction reactions are favored and therefore, a greater generation of bubbles take place. The growth and departure of the bubble depending on the balance of forces in the area triphasic contact between the electrolyte, gas bubble, and the electrode surface influenced by the high current density and temperature gradients. These conditions described and explained by the Joule-Thomson effect generate higher gas formation, premature depart of bubbles from the bottom of the electrodes and greater natural convection or micro concentration of the electrolyte. These results are useful to improve the efficiency of alkaline electrolysis cells by managing and modifying temperature profiles.

Finally, in chapter 7, we will use the measurement of temperature in electrodes for improving the selection of the faraday efficiency coefficients that are a function of the temperature to improve the prediction capacity of the model for the production of hydrogen and the general balance of energy (Energy consumption per flow of hydrogen and oxygen generated) and analyze the electrolyzer unit and how its integration affects the consumption of syngas and biomass across the contribution of the oxygen necessary to the gasification process, solving the problem related to the necessity to include an air separation unit to provide the oxygen in the gasifier.

5.6 **REFERENCES**

[1] J. J. Brey, A. F. Carazo, and R. Brey, "Exploring the marketability of fuel cell electric vehicles in terms of infrastructure and hydrogen costs in Spain," Renewable and Sustainable Energy Reviews. 2018, doi: 10.1016/j.rser.2017.10.042.

[2] T. Tsujimura and Y. Suzuki, "The utilization of hydrogen in hydrogen/diesel dual fuel

engine," Int. J. Hydrogen Energy, vol. 42, no. 19, pp. 14019–14029, 2017, doi: 10.1016/j.ijhydene.2017.01.152.

[3] A. Yilanci, I. Dincer, and H. K. Ozturk, "A review on solar-hydrogen/fuel cell hybrid energy systems for stationary applications," Prog. Energy Combust. Sci., vol. 35, no. 3, pp. 231–244, 2009, doi: 10.1016/j.pecs.2008.07.004.

[4] M. David, C. Ocampo-Martínez, and R. Sánchez-Peña, "Advances in alkaline water electrolyzers: A review," J. Energy Storage, vol. 23, no. January, pp. 392–403, 2019, doi: 10.1016/j.est.2019.03.001.

[5] FuelCellToday, "Water Electrolysis & Renewable Energy Systems," 2013. doi: 10.1017/CBO9781107415324.004.

[6] J. Chi and H. Yu, "Water electrolysis based on renewable energy for hydrogen production," Cuihua Xuebao/Chinese J. Catal., vol. 39, no. 3, pp. 390–394, 2018, doi: 10.1016/S1872-2067(17)62949-8.

[7] F. Gutiérrez-Martín, A. B. Calcerrada, A. de Lucas-Consuegra, and F. Dorado, "Hydrogen storage for off-grid power supply based on solar PV and electrochemical reforming of ethanol-water solutions," Renew. Energy, vol. 147, pp. 639–649, 2020, doi: 10.1016/j.renene.2019.09.034.

[8] A. Mohammadi and M. Mehrpooya, "A comprehensive review on coupling different types of electrolyzer to renewable energy sources," Energy, vol. 158, pp. 632–655, 2018, doi: 10.1016/j.energy.2018.06.073.

[9] A. Kovač, D. Marciuš, and L. Budin, "Solar hydrogen production via alkaline water electrolysis," Int. J. Hydrogen Energy, vol. 44, no. 20, pp. 9841–9848, 2019, doi: 10.1016/j.ijhydene.2018.11.007.

[10] D. D. A. de Fátima Palhares, L. G. M. Vieira, and J. J. R. Damasceno, "Hydrogen production by a low-cost electrolyzer developed through the combination of alkaline water electrolysis and solar energy use," Int. J. Hydrogen Energy, vol. 43, no. 9, pp. 4265–4275, 2018, doi: 10.1016/j.ijhydene.2018.01.051.

[11] K. Zeng and D. Zhang, "Recent progress in alkaline water electrolysis for hydrogen production and applications," Prog. Energy Combust. Sci., vol. 36, no. 3, pp. 307–326, 2010, doi: 10.1016/j.pecs.2009.11.002.

[12] K. C. Sandeep et al., "Experimental studies and modeling of advanced alkaline water electrolyser with porous nickel electrodes for hydrogen production," Int. J. Hydrogen Energy, vol. 42, no. 17, pp. 12094–12103, Apr. 2017, doi: 10.1016/j.ijhydene.2017.03.154.

[13] R. Garc??a-Valverde, N. Espinosa, and A. Urbina, "Optimized method for photovoltaic-water electrolyser direct coupling," Int. J. Hydrogen Energy, vol. 36, no. 17, pp. 10574–10586, 2011, doi: 10.1016/j.ijhydene.2011.05.179.

[14] C. Ziems, D. Tannert, and H. J. Krautz, "Project presentation: Design and installation of advanced high pressure alkaline electrolyzer-prototypes," Energy Procedia, vol. 29, pp. 744–753, 2012, doi: 10.1016/j.egypro.2012.09.087.

[15] I. Dincer and C. Acar, "Review and evaluation of hydrogen production methods for better sustainability," Int. J. Hydrogen Energy, vol. 40, no. 34, pp. 11094–11111, 2014, doi: 10.1016/j.ijhydene.2014.12.035.

[16] J. Koponen, "Review of water electrolysis technologies and design of renewable hydrogen production systems."

[17] F. ezzahra Chakik, M. Kaddami, and M. Mikou, "Effect of operating parameters on hydrogen production by electrolysis of water," Int. J. Hydrogen Energy, 2017, doi: 10.1016/j.ijhydene.2017.07.015.

[18] R. Bhattacharyya, A. Misra, and K. C. Sandeep, "Photovoltaic solar energy conversion for hydrogen production by alkaline water electrolysis: Conceptual design and analysis," Energy Convers. Manag., vol. 133, pp. 1–13, 2017, doi: 10.1016/j.enconman.2016.11.057.

[19] J. M. Olivares-Ramírez, M. L. Campos-Cornelio, J. Uribe Godínez, E. Borja-Arco, and R. H. Castellanos, "Studies on the hydrogen evolution reaction on different stainless steels," Int. J. Hydrogen Energy, vol. 32, no. 15 SPEC. ISS., pp. 3170–3173, 2007, doi: 10.1016/j.ijhydene.2006.03.017.

[20] D. Zhang and K. Zeng, "Evaluating the behavior of electrolytic gas bubbles and their effect on the cell voltage in alkaline water electrolysis," Ind. Eng. Chem. Res., vol. 51, no. 42, pp. 13825–13832, 2012, doi: 10.1021/ie301029e.

[21] S. Niaz, T. Manzoor, and A. H. Pandith, "Hydrogen storage: Materials, methods and perspectives," Renewable and Sustainable Energy Reviews. 2015, doi: 10.1016/j.rser.2015.05.011.

[22] M. Fatouh, M. H. Shedid, and S. Elshokary, "Effect of operating and geometric parameters on hydrogen production from an alkali electrolyzer," Int. J. Power Eng. Energy, vol. 4, no. October, pp. 395–399, 2013.

[23] F. Moureaux, P. Stevens, G. Toussaint, and M. Chatenet, "Timely-activated 316L stainless steel: A low cost, durable and active electrode for oxygen evolution reaction in concentrated alkaline environments," Appl. Catal. B Environ., vol. 258, no. July, p. 117963, 2019, doi: 10.1016/j.apcatb.2019.117963.

[24] L. B. Coelho et al., "Mechanical and corrosion characterization of industrially treated 316L stainless steel surfaces," Surf. Coatings Technol., vol. 382, no. November 2019, p. 125175, 2020, doi: 10.1016/j.surfcoat.2019.125175.

[25] A. P. Manso, F. F. Marzo, X. Garicano, C. Alegre, A. Lozano, and F. Barreras, "Corrosion behavior of tantalum coatings on AISI 316L stainless steel substrate for bipolar plates of PEM fuel cells," Int. J. Hydrogen Energy, no. xxxx, 2020, doi: 10.1016/j.ijhydene.2019.12.157.

[26] M. J. Lavorante and J. I. Franco, "Performance of stainless steel 316L electrodes with modified surface to be use in alkaline water electrolyzers," Int. J. Hydrogen Energy, 2016, doi: 10.1016/j.ijhydene.2016.02.096.

[27] K. Zeng and D. Zhang, "Evaluating the effect of surface modifications on Ni based

electrodes for alkaline water electrolysis," Fuel, vol. 116, pp. 692–698, 2014, doi: 10.1016/j.fuel.2013.08.070.

[28] S. K. Mazloomi and N. Sulaiman, "Influencing factors of water electrolysis electrical efficiency," Renew. Sustain. Energy Rev., vol. 16, no. 6, pp. 4257–4263, 2012, doi: 10.1016/j.rser.2012.03.052.

[29] P. Millet, F. Andolfatto, and R. Durand, "Design and performance of a solid polymer electrolyte water electrolyzer," Int. J. Hydrogen Energy, vol. 21, no. 2, pp. 87–93, 1996, doi: 10.1016/0360-3199(95)00005-4.

[30] Y. Petrov, J. P. Schosger, Z. Stoynov, and F. De Bruijn, "Hydrogen evolution on nickel electrode in synthetic tap water - Alkaline solution," Int. J. Hydrogen Energy, vol. 36, no. 20, pp. 12715–12724, 2011, doi: 10.1016/j.ijhydene.2011.07.049.

[31] R. J. Gilliam, J. W. Graydon, D. W. Kirk, and S. J. Thorpe, "A review of specific conductivities of potassium hydroxide solutions for various concentrations and temperatures," Int. J. Hydrogen Energy, vol. 32, no. 3, pp. 359–364, 2007, doi: 10.1016/j.ijhydene.2006.10.062.

[32] P. M. Diéguez, A. Ursúa, P. Sanchis, C. Sopena, E. Guelbenzu, and L. M. Gandía, "Thermal performance of a commercial alkaline water electrolyzer: Experimental study and mathematical modeling," Int. J. Hydrogen Energy, 2008, doi: 10.1016/j.ijhydene.2008.09.051.

[33] N. Nagai, M. Takeuchi, T. Kimura, and T. Oka, "Existence of optimum space between electrodes on hydrogen production by water electrolysis," Int. J. Hydrogen Energy, 2003, doi: 10.1016/S0360-3199(02)00027-7.

[34] J. Milewski, G. Guandalini, and S. Campanari, "Modeling an alkaline electrolysis cell through reduced-order and loss-estimate approaches," J. Power Sources, 2014, doi: 10.1016/j.jpowsour.2014.06.138.

[35] M. Sánchez, E. Amores, L. Rodríguez, and C. Clemente-Jul, "Semi-empirical model and experimental validation for the performance evaluation of a 15 kW alkaline water electrolyzer," Int. J. Hydrogen Energy, vol. 43, no. 45, pp. 20332–20345, 2018, doi: 10.1016/j.ijhydene.2018.09.029.

[36] R. Bock et al., "Measuring the thermal conductivity of membrane and porous transport layer in proton and anion exchange membrane water electrolyzers for temperature distribution modeling," Int. J. Hydrogen Energy, vol. 45, no. 2, pp. 1236–1254, 2020, doi: 10.1016/j.ijhydene.2019.01.013.

[37] P. Olivier, C. Bourasseau, and P. B. Bouamama, "Low-temperature electrolysis system modelling: A review," Renewable and Sustainable Energy Reviews. 2017, doi: 10.1016/j.rser.2017.03.099.

[38] J. H. Kim, J. N. Lee, C. Y. Yoo, K. B. Lee, and W. M. Lee, "Low-cost and energy-efficient asymmetric nickel electrode for alkaline water electrolysis," Int. J. Hydrogen Energy, vol. 40, no. 34, pp. 10720–10725, 2015, doi: 10.1016/j.ijhydene.2015.07.025.

[39] H. J. Cho and E. N. Wang, "Bubble nucleation, growth, and departure: A new,

dynamic understanding," Int. J. Heat Mass Transf., vol. 145, p. 118803, 2019, doi: 10.1016/j.ijheatmasstransfer.2019.118803.

[40] R. Phillips, A. Edwards, B. Rome, D. R. Jones, and C. W. Dunnill, "Minimising the ohmic resistance of an alkaline electrolysis cell through effective cell design," Int. J. Hydrogen Energy, 2017, doi: 10.1016/j.ijhydene.2017.07.184.

[41] Y. Wang, X. Hu, Z. Cao, and L. Guo, "Investigations on bubble growth mechanism during photoelectrochemical and electrochemical conversions," Colloids Surfaces A Physicochem. Eng. Asp., vol. 505, pp. 86–92, 2016, doi: 10.1016/j.colsurfa.2016.01.004.

[42] P. Chandran, S. Bakshi, and D. Chatterjee, "Study on the characteristics of hydrogen bubble formation and its transport during electrolysis of water," Chem. Eng. Sci., vol. 138, pp. 99–109, 2015, doi: 10.1016/j.ces.2015.07.041.

[43] H. Vogt and R. J. Balzer, "The bubble coverage of gas-evolving electrodes in stagnant electrolytes," Electrochim. Acta, vol. 50, no. 10, pp. 2073–2079, 2005, doi: 10.1016/j.electacta.2004.09.025.

[44] H. Matsushima, Y. Fukunaka, and K. Kuribayashi, "Water electrolysis under microgravity. Part II. Description of gas bubble evolution phenomena," Electrochim. Acta, vol. 51, no. 20, pp. 4190–4198, 2006, doi: 10.1016/j.electacta.2005.11.046.

[45] E. Amores, J. Rodríguez, and C. Carreras, "Influence of operation parameters in the modeling of alkaline water electrolyzers for hydrogen production," 2014, doi: 10.1016/j.ijhydene.2014.07.001.

[46] S. Marini et al., "Advanced alkaline water electrolysis," Electrochim. Acta, 2012, doi: 10.1016/j.electacta.2012.05.011.

[47] A. Yilanci, I. Dincer, and H. K. Ozturk, "A review on solar-hydrogen/fuel cell hybrid energy systems for stationary applications," Prog. Energy Combust. Sci., vol. 35, no. 3, pp. 231–244, 2009, doi: 10.1016/j.pecs.2008.07.004.

[48] T. L. Gibson and N. A. Kelly, "Predicting efficiency of solar powered hydrogen generation using photovoltaic-electrolysis devices," Int. J. Hydrogen Energy, vol. 35, no. 3, pp. 900–911, 2010, doi: 10.1016/j.ijhydene.2009.11.074.

[49] C. Ghenai and M. Bettayeb, "Modelling and performance analysis of a stand-alone hybrid solar PV/Fuel Cell/Diesel Generator power system for university building," Energy, vol. 171, pp. 180–189, 2019, doi: 10.1016/j.energy.2019.01.019.

[50] E. Amores, J. Rodr??guez, and C. Carreras, "Influence of operation parameters in the modeling of alkaline water electrolyzers for hydrogen production," Int. J. Hydrogen Energy, vol. 39, no. 25, pp. 13063–13078, 2014, doi: 10.1016/j.ijhydene.2014.07.001.

[51] R. Phillips and C. W. Dunnill, "Zero gap alkaline electrolysis cell design for renewable energy storage as hydrogen gas," RSC Adv., vol. 6, no. 102, pp. 100643–100651, 2016, doi: 10.1039/c6ra22242k.

[52] M. Felgenhauer and T. Hamacher, "State-of-the-art of commercial electrolyzers and on-site hydrogen generation for logistic vehicles in South Carolina," Int. J. Hydrogen

Energy, vol. 40, no. 5, pp. 2084–2090, 2015, doi: 10.1016/j.ijhydene.2014.12.043.

[53] I. M. Sakr, A. M. Abdelsalam, and W. A. El-Askary, "Effect of electrodes separator-type on hydrogen production using solar energy," Energy, 2017, doi: 10.1016/j.energy.2017.09.019.

[54] A. S. Tijani, D. Barr, and A. H. A. Rahim, Computational Modelling of the Flow Field of An Electrolyzer System using CFD, vol. 79. Elsevier B.V., 2015.

[55] D. Chen, L. M. Pan, and S. Ren, "Prediction of bubble detachment diameter in flow boiling based on force analysis," Nucl. Eng. Des., vol. 243, pp. 263–271, 2012, doi: 10.1016/j.nucengdes.2011.11.022.

[56] H. Vogt, "On the gas-evolution efficiency of electrodes i - Theoretical," Electrochim. Acta, vol. 56, no. 3, pp. 1409–1416, 2011, doi: 10.1016/j.electacta.2010.08.101.

[57] H. Matsushima, D. Kiuchi, Y. Fukunaka, and K. Kuribayashi, "Single bubble growth during water electrolysis under microgravity," Electrochem. commun., vol. 11, no. 8, pp. 1721–1723, 2009, doi: 10.1016/j.elecom.2009.07.009.

[58] P. Haug, B. Kreitz, M. Koj, and T. Turek, "Process modelling of an alkaline water electrolyzer," Int. J. Hydrogen Energy, vol. 42, no. 24, pp. 15689–15707, 2017, doi: 10.1016/j.ijhydene.2017.05.031.

[59] H. Vogt, "On the gas-evolution efficiency of electrodes. II - Numerical analysis," Electrochim. Acta, vol. 56, no. 5, pp. 2404–2410, 2011, doi: 10.1016/j.electacta.2010.11.004.

Chapter6 REVIEW ON THE INTEGRATION OF HIGH-TEMPERATURE HEAT PUMPS IN DISTRICT ENERGY NETWORKS

Summary: The most efficient way to use the heat generated in the developed gasifier/electrolyzer hybrid plant is the transport of these heat through a low-temperature DEN (District Energy Networks) using heat pumps. This solution provides significant environmental and performance improvements, being an innovative and profitable solution for decarbonizing different sectors. This work reviews different district energy networks and the integration of high-temperature commercial heat pumps on the Dominion Bridge area in Lachine-Est in Montreal in the final case study in the next chapter. Likewise, it describes placement options and connection modes of a heat pump unit in DEN networks, identifying new generic configurations of heat pumps and how they can be integrated into DEN systems.

6.1 INTRODUCTION

Today our power generation systems mainly run on fossil fuels derived from crude oil; we also use them to heat our houses [1]. The vast quantities of energy that we need and use generate high levels of carbon dioxide (CO_2) and thus contribute to ever-rising greenhouse gas emissions [1][2][3]. The Paris Agreement aims at zero carbon and climate-neutral society as the largest and most influential political project in urban areas [1][4]. To make cities and their critical facilities truly resilient and zero carbon, we need strategies to find practical ways to incorporate and take advantage of renewable energy sources. Although some countries use renewables and waste to generate industrial process heating and solar thermal and geothermal systems for space heating and cooling, most heating needs (50 % of the total primary energy consumption in Europe) are still met by fossil fuels [5][6][7]. Consequently, there is a significant potential for decarbonization and air quality improvement offered by alternatives that have not yet been fully integrated and explored, such as Power-to Heat, DEN networks, and heat pumps [1][8][9][10].

Power-to-Heat (PtH) is the conversion of electrical power into heating and cooling; the technology increases the flexibility of the district heating sector by coupling power and heat networks through the use of heat pumps, electric boilers, or thermal storage systems [1][2][11][12]. Besides the increased flexibility, other benefits of converting biomass, solar, and wind power to heat include transforming the power sector, reducing the variable renewable energy, increasing the load shifting, and providing grid services via aggregators. Furthermore, PtH mass

installations and applications may be facilitated thanks to the favorable energy market environment with government regulators providing economic incentives for renewable energy use in buildings and industry [2][3].

Some key indicators that illustrate the current status of PtH solutions are as follows: i) four key markets (Canada, China, the United States, and Europe) have committed to implementing the PtH concept by 2030 [2][3]; ii) use of heat pumps from water, air, and land sources to heat spaces and domestic water in residential and commercial facilities[13]; iii) relatively low-temperature application (≤100 °C) of heat pumps for capturing waste in the pulp and paper, food and beverages, textiles, automotive, and chemicals industries [2][14]; iv) a 12 % increase of global heat pumps sales between 2017-2019, with 80% of household heat pump installations in China, Japan, and the United States; v) Power-to-heat expansion in Europe and China[2]. For instance, China will eliminate coal-fired boilers for water heating, subsidizing consumers to switch to electricity-based heat pumps [2][15]. Likewise, as part of its USD 2.1 billion efforts to curb emissions, Canada's government will be modernizing government-owned heating and cooling plants in the National Capital Region [2][3]. In summary, power-to-heat technologies can cost-effectively contribute to fossil fuel substitution, renewable energy integration, and decarbonization. In this context, integrated CHP, HPs, and passive thermal storage technologies emerge as particularly favorable options[14].

District energy systems play a crucial role in the energy transition towards a low-carbon economy, acting as a backbone towards efficient local energy systems [1][16][17]. District energysystems have emerged as a best practice approach for providing a local, affordable, and low-carbon energy supply [3][18]. They represent a mechanism that develops synergies between the production and supply of heat, cooling, domestic water, and electricity using renewable energy sources, such as biomass, wind, and solar, in the electricity system, using large-scale heat pumps, combined heat, and power (CHP), boilers and thermal storage [19]. Several authors have recently defined nine (9) key success factors that lead to high-quality, efficient, and sustainable DH service [13]. They could be split into four (4) external and five (5) internal factors [7][13][20]. Firstly, external factors include: i) adequate national policy and regulatory framework; ii) direct/indirect financial support; iii) focused local policy coherent with urban planning; and iv) alignment of interests/ cooperation maturity. Finally, internal factors include: v) availability and relevance of local resources; vi) comprehensive project development; vii) price competitiveness against alternative energy solutions, viii) flexible heat and cold production, and ix) a combination of technical and non-technical innovations.

Heat pumps present immense contributions to a sustainable and low-carbon energy future by converting electric power into efficient heating or cooling [21][22][23]. The integration of heat pumps into DEN provides significant environmental and performance improvements, being an innovative and profitable solution for different decarbonizing sectors [3]. Currently, heat pumps are still not a particularly standard technology in European district heating systems [24]. At the same time, companies in the district heating sector aim to reduce carbon emissions in the generation of heat, and high-temperature heat pumps provide interesting features for their integration into DEN using various heat sources [25]. Small DEN systems present the most significant potential for HPs use, significantly reducing fossil fuels [7][26], while, in medium and large systems with efficient CHP production, the HP potential is lower [1]. For example, by reducing the fraction of thermal units available for electricity production (CHP plants), the possibility that CHPs will not be able to satisfy the heat demand required by large cities increases [27]. One possible alternative is the conversion of electricity into heat, which at the same time, can help maintain the balance between electricity supply and demand. However, the optimal size of HPs for DEN systems depends widely on the system and its characteristics and external factors, such as electricity and fuel prices and other economic inputs [28]. E.g., Mahmoudi et al. [29] made an experimental thermodynamic analysis using Temperature - entropy cycles in two commercial heat pump types (variable-speed and fixed-speed compression systems) fully powered with photovoltaic (PV). The results reveal that the variable-speed compression system shows up to 400 % higher efficiencies under partial loads. In addition, the variable-speed compression air-conditioner provides 64 % and 88% of the heat and cold of the fixed-speed counterpart, respectively. About the economic evaluation, the variable-speed compression provides 50 % and 16 % extra cooling and heating compared to fixed-speed. Likewise, available waste heat sources, heat requirements, and HP technology naturally affect the potential of HPs, being one of the reasons why there are no uniform criteria for the potential of HPs integrated into DEN systems [16][24][30].

Various configurations are possible while integrating both CHP and heat pumps [24][26]. By combining these two technologies, better performance of the combined system is achieved, as opposed to their individual operation[31]. The improvement in system performance is obtained by imposing more significant operating constraints on the heat pump unit. Integrated systems (CHP + HP) have a better performance compared with CHP without heat pumps operating at the same temperature level [32][33]. Only a few works discuss the optimal and basic integration of heat pumps in district energysystems: Mazhar et al.[5], Volkova et

al.[34], Rhein et al.[35] Moreover, Mateu-Royo et al. [17] studied four different district heating (DH) systems and how they can incorporate low-temperature distributed renewable heat sources into centralized and distributed configurations. Pieper et al.[32], Sommer et al. [36] and Roh et al. [37] made other essential studies [37], where they compare the overall system performance of hourly temperature variations of different heat sources, influenced by the seasonal coefficient of performance (SCOP) of HPs when supplying district heating in centralized and distributed systems. In contrast, Ommen et al. [31][38] investigated the operational performance of five configurations of heat pumps and their optimal integration into a DH network. The analysis focuses on four key performance factors (coefficient of performance (COP), coefficient of system performance (COSP), volumetric heating capacity (VHC), and cost of fuel and investigated for different DH network temperatures, assuming that a CHP plant supplies the heating network and electric motors operate the HP. Finally, Sayegh et al. [22] studied the criteria for the appropriate selection of HPs system, which included heat source, heat pump technology, and heat requirements. They also included eight different connection and operation modes and heat sources available for heat pumps in centralized and distributed configurations.

Several papers dealing with the integration of heat pumps into district energynetworks have been published [17][24][31][37][38]. Still, none of the documents put together all the possible heat pumps configurations in district energynetworks. The purpose of the current chapter is to present a review of configurations to integrate HPs into DEN networks. As seen in the following subsections, the chapter's structure is organized as follows: firstly, the definition and description of district heating networks are given. Secondly, the technical description of high-temperature heat pumps is presented. Finally, the heat pump unit's placement and connection modes in district heating networks are described and discussed.

6.2 DISTRICT ENERGY NETWORKS

District energy systems have been successfully implemented for years in an increasing number of cities worldwide [7]. These systems will play a fundamental role in the energy demand of the cities of the future. They will include a variety of technologies that seek to centralize the production of electricity, cooling, and heat for distribution to end-users to accelerate, distribute, and reduce primary energy consumption [16]. In this way, today, many urban areas are adopting district

energy systems to benefit from a diversity of supply and reduction in imports of fossil fuels, leading to fewer GHG emissions and a more significant share of renewable energies in the local energy mix [10].

The historical progression of district energy networks can be grouped into five large (5) generations [7][5]: the first generation (1G) was used between the years 1880-1930. It was characterized by the use of local heating steam with operating temperatures between 120-200 ° C generated through coal-waste steam production plants and storage systems that distributed energy from a centralized generation plant to various remote customers. Subsequently, the second generation (2G) used between 1930-1980 was differentiated from the first by incorporating pressurized hot water systems with working temperatures between 120-160 ° C generated through coal steam generation plants and combined power and heat generation systems (CHP). The third-generation (3G) district heating systems were incorporated between 1980-2020 with industrialized compact substations, measurement systems, monitoring and building construction with better thermal insulation that allowed lower operating temperatures (70-100 ° C) and integrating heat storage systems, use of waste heat from industrial processes, carbon-biomass CHP systems, and large-scale solar systems [39].

Today, many district heating systems require modernization to bring them to a reliable standard for the fourth and fifth-generation district energy networks (4G and 5G). These new categories are the natural progression of the third-generation (3G) district network and are defined as the future standard for district energy network systems in cities [40][41][42]. Distributing heat on efficient buildings with underfloor heating or low-temperature radiators allows further reducing temperatures (35-50 °C), resulting in less heat loss than previous generations and allowing them to be connected to modern power supply systems [43]. These networks can use a variety of heat sources, including low-grade waste heat, and allow consumers to supply heat to the grid (consumers known as "prosumers"= producers + consumers) using smart control and flexible energy supply utilizing available technologies, such as (i) CHP with mixed fuel or hybrid sources; (ii) renewable energy sources (RES); (iii) thermal energy storage and (iv) centralized heat pumps or heat pumps integrated at substation level [7][39]. Table 6-1 summarizes heat sources and technologies used in different district heating generations.

District networks are traditionally made up of many buildings and dwellings heated

by a central heat source (standard). The hot water passes through a network of double pipes (supply and return) distributed to the buildings for different applications. Conventional district heating systems are structured by three (3) systems [5][19][44]: (i) generation system, (ii) distribution system, and (iii) consumption system (figure 6-1). First, generation consists of a central energy production source and heat exchangers (HX) designed to transfer heat. Then, distribution is made up of a network of hot water distribution pipes. Finally, consumption includes space heating (SH), domestic hot water (DHW), and process heating (PH) services.

Table 6-1: Summary of heat sources and technologies used in different district heating generations [1][5][24]

Name	Range temperature (°C)	Pressure (MPa)	Heat carrier	Heat source		Integration technology possibilities	Advantages	Disadvantages
First-generation (1G)	120-200	≥ 1.6	Steam	Fossil Fuel (FF)	Oil	Solar	For industrial setups, only	High heat losses and exergetically inefficient
					Gas	Boiler		
					Coal	CHP		
Second-generation (2G)	120-160	1.6	Water	FF	Oil	Solar	Reliable operation, high flexibility, and existing infrastructure	Exergetically inefficient, unable to integrate low-grade renewable sources
					Gas	HPs		
					Coal	Boiler/CHP		
Third generation (3G)	70-100	1.0	Water	FF	Biomass	CHP/ HPs	Reliable operation, high flexibility, and existing infrastructure	The actual system used in the district heating network
				RES	Solar	Absorption HP/ solar collector		
				FF+RES	Geothermal	Geothermal Boiler		
Fourth generation (4G)	35-70	≤ 0.5	Water	FF	Air/ biomass	Mechanical HP	Low heat losses, integration of low-grade renewable heat sources, exergetically efficient	Emerging technology, substations are more expensive, individual domestic hot water is needed
				RES	Water/ solar	Thermal HP		
				FF+RES	Waste/ Geo-thermal	Solar/ wind		
Fifth	15-35	≤ 0.5	Water	FF	Air/ biomass	Mechanical HP	Allow recovering	Emerging technology,

generation (5G)	RES	Water/ solar	Thermal HP	low-temperature excess heat and include renewable. High modularity and flexibility	electricity costs for HPs, high pumping cost per unit of energy due to small operative ΔT
	FF+RES	Waste/ Geo-thermal	Solar/ wind		

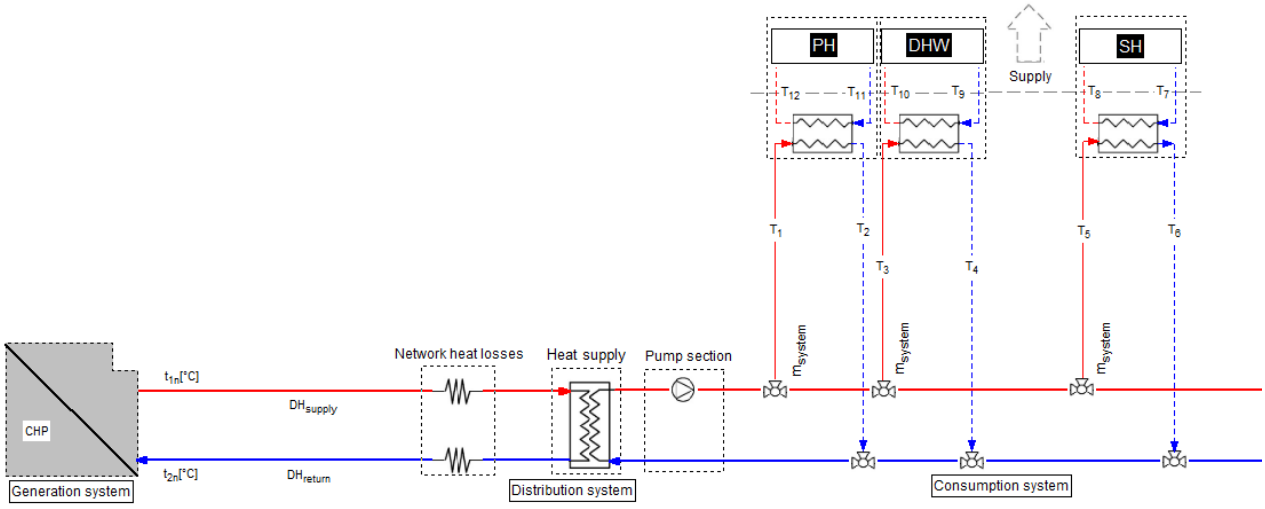

Figure 6-1 Structure of the operating principle of conventional heating system with compact substations with plate heat exchangers; process heating (PH), domestic hot water (DHW), and space heating (SH)

A key aspect of modernizing district heating systems (advanced) is the integration of new components to meet SH, DHW, and PH requirements for buildings and industries that address current environmental, climate and energy challenges and new energy efficiency requirements [10][18]. Therefore, new DEN generation systems could integrate renewable energy sources, heat pumps, and thermal energy storage. Then available local heat sources, renewable energy sources, including heat pumps, heat exchangers, and thermal energy storage, are incorporated into the network. Finally, consumer systems can incorporate renewable energy sources, including heat pumps and thermal energy storage (table 6-2).

Table 6-2: Comparison of standard and advanced district heating networks

Generation	Central heat source	
	Exchanger	

Standard	Distribution	Network
	Consumption	Exchanger
		Sink
Advanced	Generation	Central heat source
		Exchanger
		Thermal energy storage system
	Distribution	Network
		Local heat source
		Thermal energy storage system
	Consumption	Individual heat source
		Exchanger
		Sink
		Thermal energy storage system

6.3 HIGH-TEMPERATURE HEAT PUMPS

Heat pumps are reverse heat engines used to heat and cool residential, commercial, and industrial buildings. This technology offers coefficients of performance (COP) between 2 to more than 6 using low thermal quality air heat, water, geothermal energy, and waste. The use of heat pumps within district heating systems can increase the proportion of heat and electricity generated from renewable energy sources, contributing to the replacement of fossil fuel boilers, with its corresponding decrease in greenhouse gas emissions, and increased grid flexibility by balancing the excesses of renewable electricity avoiding the use of storage as a benefit in the design of future power systems [22]. The market potential for heat pumps is high, and this can create several social-economic benefits. However, the widespread diffusion of HP technologies faces several challenges, including technological (limitation of the electrical network due to intensive electrification of the heating sector), economic (high investment and installation cost), regulatory (lack of standards and mandatory policies), policy (uncertainty in policy and lack of clear heat decarbonization pathways and technology uptake), and public acceptance issues (unwarranted fear, misperception, misinformation, and previous experiences on the reliability of heat pumps).

A schematic diagram of a single-stage vapor compression heat pump with finite temperatures in the reservoirs is presented in figure 6-2. Any heat pump's operation point can be analyzed based on five variables [31][45]: i) the sink temperature of the leaving stream at the condenser $\mathbf{T_{sink}}$; ii) the temperature

lift $\mathbf{T_{lift}}$, between the input evaporator stream and the output stream of the condenser (iii) energy input to the compressor,(iv) and (v) the temperature gliding between the inlet and outlet in both heat exchangers $\Delta\mathbf{T_{sink,glide}}$ **and** $\Delta\mathbf{T_{source,glide}}$ [45]. Thus, it is possible to normalize the HP system's working point by defining these five variables and the adequate state point for both heat exchangers using properties of a pure refrigerant or the mixture of them as a working fluid with a high relative heat transfer [38] for condenser-evaporator in a single-stage heat pump system with finite temperatures of the reservoirs[45].

Commercial heat pumps based on vapor-compression are the most widely used with numerous industrial applications[2][14]. Several authors have classified HPs according to the temperature level at which they supply heat (table 6-4). In this way, they can be distinguished as follows: Conventional heat pumps (HP) with heat recovery temperatures $\mathbf{T_{source}}$ $[\mathbf{0\,°C \leq HP < 40°C}]$ and heat supply temperature $\mathbf{T_{sink}}$ $[0\,\mathbf{°C \leq HP < 80\,°C}]$ compatible with the fourth and fifth district heating generations' operating temperatures. High-temperature heat pumps (HTHP) with heat recovery temperatures $\mathbf{T_{source}}$ $\mathbf{40\,°C \leq HTHP < 60°C}$ and heat supply temperature $\mathbf{T_{sink}}$ $\mathbf{80\,°C \leq HTHP < 100°C}$ compatible with operating temperature of the third district heating generation; and finally, very high-temperature heat pumps (VHTHP) with heat recovery temperatures $\mathbf{T_{source}}$ $\mathbf{60\,°C \leq VHTHP < 120°C}$ and temperature heat supply $\mathbf{T_{sink}}$ $\mathbf{100\,°C \leq VHTHP < 160°C}$ compatible with the supply of industrial process heat [46].

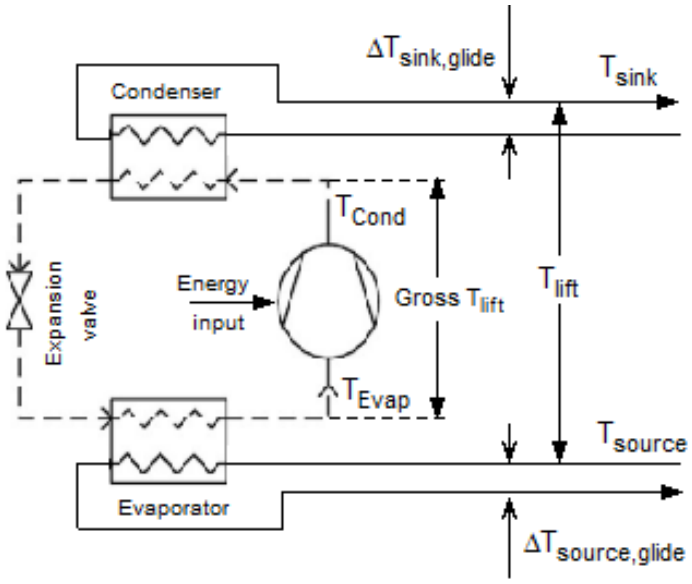

Figure 6-2: Schematic diagram of a single-stage heat pump system adapted from [31][38]

Nowadays, the manufacturers of HTHP can provide heat ($\mathbf{T_{sink}}$) at temperatures of at least 90 °C [46]. Out of these producers, only a few can supply temperature up to 120 °C; among the HPs of very high temperature, it is worth mentioning the Vicking's HeatBooster at 150 °C [47], Rank's HTHP at 140 °C [48], Ochsner at 130 °C [49], and finally, Kobelco SGH120 [50], Mayekawa Eco Sirocco [51], and Hybrid Energy Heat Pumps[52] with heating temperatures up to 120 ° C. The heating capacities of these commercial HTHPs vary from approximately 100 kW to 20 MW, with COP values ranging from 2.4 to 5.8 with a temperature lift increase of 100 to 40 K, respectively. In addition to this, the main refrigerants applied in commercial HTHPs are R245fa, R717, R718, R744, R134a, and R1234ze, with operational data varying between 40 and 60% of the maximum Lorenz efficiency according to the second law of thermodynamics (figure 6- 3)[46][47][48][49][50][51][52]. Generally, single-stage heat pump cycle concepts are applied. Cycle optimizations are achieved by implementing an internal heat exchanger (IHX) between the suction gas and the subcooling liquid, parallel compressors, economizer circuits with intermediate steam injection into the compressor, or two-stage cascades [45]. There are several types of heat pumps. They could be classified according to five technical characteristics (table 6-4).

Table 6-3: Development of temperature levels for compression heat pumps, HP: conventional heat pump, HTHP: high-temperature heat pump, VHTHP: very high-

temperature heat pump, and their compatibility with different district heating networks, adapted from Arpagaus et al. [46]

Heat pumps	Heat source temperature T_{source} (°C)	Heat sink temperature T_{sink} (°C)	Compatible District heating network
HP	$\mathbf{0\ °C \leq HT < 40°C}$	$0\ \mathbf{°C \leq HP < 80\ °C}$	Fourth generation (4G) Fifth generation (5G)
HTHP	$\mathbf{40\ °C \leq HTHP < 60°C}$	$\mathbf{80\ °C \leq HTHP < 100°C}$	Third generation (3G)
VHTHP	$6\mathbf{0\ °C \leq VHTHP < 120°C}$	$\mathbf{100\ °C \leq HTHP < 160°C}$	Second generation (2G) and process heat

The temperature glide of the heat source and the heat sink can vary significantly depending on the industrial application [53]. For small temperature glides, like those found in the drying and steam generation processes, the highest theoretical performance between the constant heat sources and sinks temperatures can be represented with an ideal Carnot heat pump cycle [54]. However, high-temperature networks like the ones studied here have higher temperature glides. Thus, the Lorenz cycle (figure 6-3) that considers the theoretical limit between a temperature glide on the heat source and sink sides using logarithmic mean temperatures is more appropriate [55].

Table 6-4: Classification of heat pumps by technical characteristics

Principle of Operation	Compressor type
	Absorption type
	Heat transformer
	Hybrids
Heat source	Renewable, geothermal
	Seas, rivers, air
	Sewage, waste heat
	District networks
	Multiple sources
Operating stages	Single stage
	Multi-stage
	Advanced settings
Temperature range at which to supply heat	40 °C – 160 °C
Heat dissipation carrier fluid	Air
	Water
	Mixed

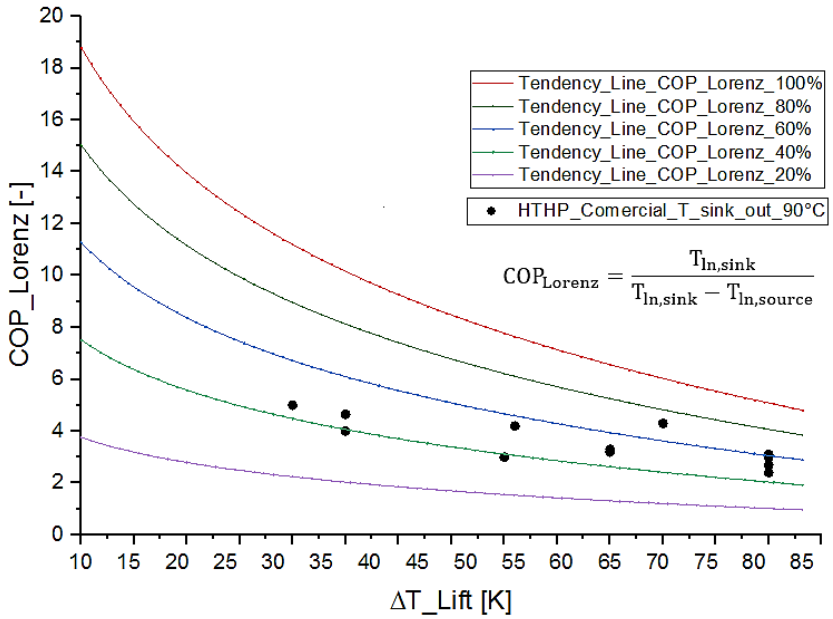

Figure 6-3: COP of various industrial HTHPs as a function of the temperature lift. data from literature [46]: Vicking's HeatBooster [47], Rank's HTHP [48], Ochsner [49], Kobelco SGH120 [50], Mayekawa Eco Sirocco [51], Hybrid Energy Heat Pump [52]

6.4 PLACEMENT AND CONNECTION MODES OF A HEAT PUMP UNIT IN A DISTRICT ENERGY NETWORK

The optimal integration of heat pumps into DEN networks depends mainly on the location, connection, and operation modes (table 6-5). Firstly, heat pump units can be installed in individual dwellings or as centralized heat production units in DH networks. They can be placed as a central, local, or individual heat source. Also, HP units can be connected to the DEN network in a single connection mode with one individual HP supplying the entire heating requirement of the DEN, in parallel connection modes when two or more HPs cooperate to receive the heat carrier fluid from the same suction manifold and discharge into a common discharge manifold for district heating supply. Finally, in serial connection modes, when two or more HPs cooperate to deliver its flow to the next, it increases the heat carrier fluid's energy and raises the district heating supply's temperature. In addition, each connection mode can be operated with a single heat source where the heat pump unit alone supplies heat to the district heating network. In a multi heat source system, the heat pump is the major heat source, and other alternatives (e.g., fossil fuels or renewable energy sources) are used to cover the peak heating requirements. Lastly, in multi-stage operation mode, each stage of the heat pump

units contributes to the district heating supply and depends on each other. The operation mode also includes a) direct use of energy from the DEN supply of the high-temperature stream to evaporate the refrigerant (HRT) and (b) use of energy from the DEN return low-temperature to evaporate the refrigerant (LRT).

Table 6-5: Options for the integration of heat pumps into district energy networks

	Location	Connection mode	Operation mode
Heat pumps in district energynetworks	Central	Single	Single heat source
	Local	Parallel	Multi heat source parallel
	Individual	Serial	Multi heat source serial
			Multi-stage heat pumps
			High returning temperature (HRT)
			Low returning temperature (LRT)

Central heat pumps (figure 6-4) are designed with a high thermal capacity of $\mathbf{2000\ kW \leq Qt \leq 20.000\ kW}$ and, therefore, with a high source thermal input requirement ($\mathbf{-5\ °C \leq T_{source} \leq 25\ °C}$) [32][56] to meet the demands of heating as a replacement unit for CHPs systems. They can operate under single or multiple heat source connection modes and serial, parallel, or multi-stage operating modes. Very high-temperature heat pumps working in a single heat source mode can supply heat to the district heating network. They can include other sources like fossil fuels or renewable energy sources to meet maximum heating requirements in multiple heat source modes.

Local heat pumps (figure 6-4) are designed with a medium thermal capacity of 100 kW $\leq \mathbf{Qt} \leq \mathbf{2000}$ kW; one or more local high-temperature heat pumps can be integrated into the DEN network, supplying stable or variable thermal capacity depending on the available heat sources. Local HPs can operate using single or multiple heat sources and parallel, series, or multi-stage connection modes. Incorporating HP units into the DEN network increases the system's flexibility and thermal capacity using different technologies and various local heat sources to cover the heating requirement. Specifically, the HPs placement option in advanced DEN let use one- or two-pipe systems capable of supplying both heating and cooling using heat pumps at the end-users, an achievement hitherto only feasible using a four-pipe system [57][58].

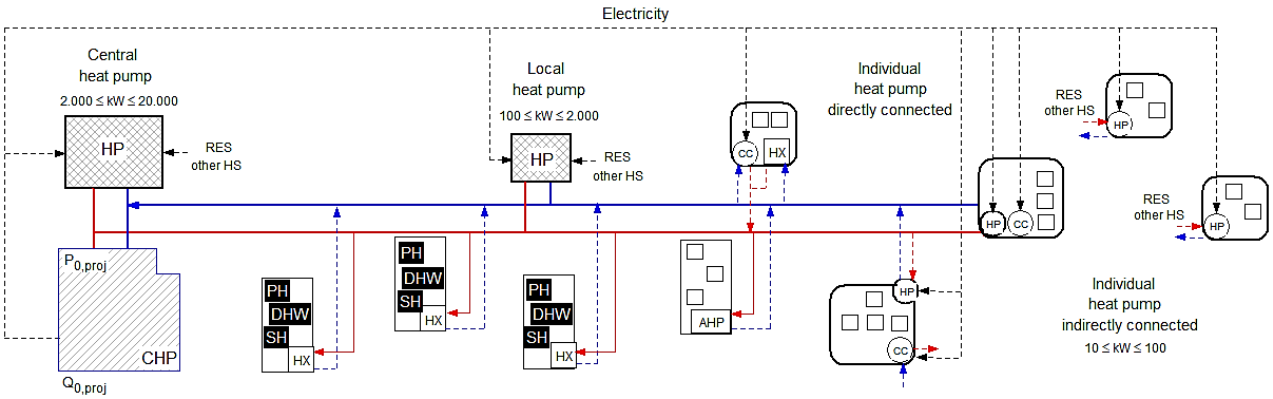

Figure 6-4: Heat pump placement options in advanced DH (DH- district heating, HX- heat exchanger, HP- heat pump, HS- heat sources, AHP- Absorption heat pump or Compression chiller (CC), RES (renewable energy sources)

Individual heat pumps can be connected directly to a network of pipes that connect buildings in a neighborhood and can be powered by CHP from centralized plants and working in a single or multi heat source connection (figure 6-4). This alternative has the option to use a warm, and cold pipe with a temperature difference of about $\mathbf{5-10\ K}$. Both pipes are operated at temperatures close to the surrounding ($\mathbf{10-35\ °C}$). Due to the low temperatures, the heating demands of buildings cannot be covered directly, and a heat pump is installed in each building to raise the temperature to the level required by the building's heating system. A heat pump takes water from the warm pipe and uses it as a heat source in heating mode. The cooled-down water from the evaporator of the heat pump is then discharged to the cold pipe. If the building has a cooling demand (fig 6-5), it can be cover by a compression chiller and a heat exchanger for direct cooling with the cold pipe in advanced district heating networks where the fluid from the cold pipe is warmed up in the building and discharged to the warm pipe.

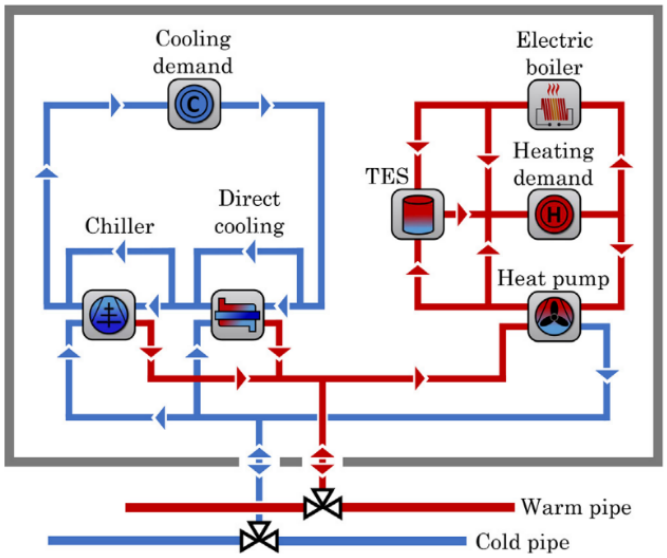

Figure 6-5: Energy systems (Base on [57]): Heating demands are covered by a water-to-water heat pump, electric boiler, and thermal energy storage (TES). Cooling demands are covered by a compression chiller and a heat exchange

For example, small-scale HPs ($\mathbf{10\ kW \leq Qt \leq 100\ kW}$) can use local renewable energy sources or DEN supply and return water lines as heat sources, as shown in figure 6-4. Similarly, individual HPs indirectly connected to DEN networks use local sources to supply the buildings with heat powered by CHP plant electricity. This placement favors the heat generation to meet the rising heating demands in the DEN network, so the electricity consumed by the HPs unit increases the CHP efficiency by utilizing extra renewable electricity (e.g., wind power) and can be stored as heat in domestic hot water tanks and space heating installations.

Previous studies like the ones by Mazhar et al. [5], Volkova et al. [34], and Rhein et al. [35] used practical measurements to analyze four different generations of district heating (DH) and how they are capable of incorporating low temperature distributed renewable heat sources into centralized and distributed configurations. These studies divided the DH grid into the generation zone, where one or more heat-producing facilities, with water as the medium of heat transfer, are connected to the transmission network of pipes covering the area up to the distribution grid, where the end-consumer finally uses it. The most common heat generation technologies addressed in papers [5][34][35] were CHP plants, waste heat, geothermal heat, solar thermal heat, conventional boilers, and heat pumps. Heat pumps in the articles [5][34][35] were analyzed at the node where the primary

heat of the DH grid was transferred to the second grid (substation connections); instead of using an indirect heat exchanger, the system operated with HPs whose driving force is the lift temperature difference between T_{supply} and T_{return}. Indeed, this configuration is interesting when the temperature of use is much higher than the temperature supplied by the DH.

Pieper et al.[32], Sommer et al. [36] and Roh et al. [37] used practical and theoretical studies, where they compared the overall system performance of hourly temperature variations of different heat sources, influenced by the seasonal coefficient of performance (SCOP) of HPs when supplying district heating into distributed configurations. The result shows that the maximum SCOP may be achieved for HPs based on a combination of different heat sources (groundwater, air, and seawater) compared with the use of only one heat source. The sensitivity analysis has shown that the system performance depends on the proportion of different heat sources, the climate region, the total installed HP capacity, and the building type supplied. For example, when the heat demand was included in the analysis, it was shown that an HP of the same capacity using seawater, air, and groundwater presented a reduction in COP by 11%, 15%, and 3% respectively, when it was compared using the arithmetic mean COP during the analysis time. Thus, delivering energy to booster heat pumps under different operating scenarios and enhancement measures produced a change in the overall flexibility according to the studies. The local measure, such as booster pumps (supplementary pumping systems located away from the main pumping stations), has more impact on flexibility enhancement but is only effective for a part of substations. Similarly, the ability of the renewable energy use and its later storage, combined with high-efficiency units could be used in the selection and operation configuration of HPs in DH systems.

Ommen et al. [31] used practical and theoretical studies to investigate the operational performance of five heat pump configurations and their optimal integration into a DH network. The analysis focuses on four key performance factors: (i) Coefficient of performance (COP), defined as the ratio of useful thermal energy produced to electricity consumed; (ii) Coefficient of system performance (COSP), defined as total heat extracted (includes losses) in relation to the total energy supplied (electricity consumption) to the heat pump; (iii) Volumetric heating capacity (VHC) defined as the ratio between the displacement rate volume flow of suction gas and the useful heating capacity of the heat pump, and (iv) cost of fuel calculated according to average yearly values defined by the geographic location of installation of the HP. This investigation was made for different DH network

temperatures, assuming that a CHP plant supplies the network and electric motors operate the HP. The results show that only two configurations are best suited for all the five considered cases in terms of COSP and fuel cost. Firstly, let us take the first configuration where the sink and source temperatures are T_{demand} and T_{source} respectively. This configuration is like commercially available heat pump installations in dwellings. The sink process stream is heated from the temperature of the source. The source's temperature glide corresponds to the heat capacity of the heat source's finite heat capacity. Indeed, this configuration does not require a DH network in order to operate, and the location of this heat pump type is decentralized as the heat is delivered directly to the consumer. The second configuration requires using other generation technologies to increase the temperature to that of the forward line, and the heat pump can be used to preheat the return line of a DH network before entering the CHP plant. Under this configuration, the temperature lift of the heat pump is the difference between DH_{return} and T_{source} generating a low-temperature lift and increasing COP of the HP.

Like Sayegh et al. [22], researchers studied the criteria for the appropriate selection of HPs system, which included heat source, heat pump technology, and heat requirements. The authors of the paper created an instrument that evaluates heat pump integration into residential district heating. They also presented HPs district heating scenarios regarding heat pump placement, connection, and operation modes based on available heat sources and heat requirement profiles and their environmental impact. At least four basic scenarios were analyzed: i) heat pumps placement into an existing network without significant changes; ii) heat pump placement into an expanded network; iii) deep refurbishment of the existing district heating, and iv) the design of a new district heating system supplied by a heat pump. Moreover, the given approach includes eight different connection and operation modes and heat sources available for heat pumps. This work's conclusions indicate that the choice of heat pump technology for its integration into district heating networks is complex and multicriterial. There is no consistent way of creating heat pump-based district heating. Besides, low-temperature district heating is now a feasible option and a practical application for current district heating networks.

Although heat pumps can be beneficial to DH networks, they are still marginalized. Identifying and describing different placement options and connection modes of a heat pump unit in DEN networks will help overcome the current unawareness. The opportunities and challenges identified from the literature review and commercial

heat pump suppliers can be summarized into eight categories. Firstly, the challenges are summarized into three areas (social, economic, and technical barriers). (i) The social includes the necessity of shifting policy and long-term strategies to have new system change (technology, and distribution system)—likewise, lack of confidence and specific funding to development HP. (ii) Economic aspects include price volatility (gas and oil), investment costs of HP in combination with DEN, and commercial availability of HP products. Finally, (iii) technical aspects include lack of knowledge related to integration and operation of HP in DEN, lack of availability of technical requirements, and heat sources (location and temperature). Secondly, the opportunities to use HP in DEN can be divided into five areas. (iv) usage of low-temperature alternative heat sources for direct feed-in. (v) use other alternative energy sources like waste heat and renewable energy. (vi) link to the power system through the balance of energy and demand-side management. (vii) reduces network temperatures and encourages decentralized HP in fourth and fifth-generation district energynetworks. Lastly, (viii) increasing transport capacities using the return line as the source and integrating HP as reinforcement systems.

Based on the five recognized types or generations of DH networks (table 6-1), the current state-of-the-art of high-temperature heat pumps (table 6-3), and the different options to integrate HPs into DH networks (table 6-5), twelve (12) possible heat pumps configurations have been identified. The configurations are termed with the initial letter of location, heat source used for evaporating the refrigerant, and the direction of sink level (e.g., the classification $\mathbf{C\_HP\_DH_r\_DH_s}$ corresponds to a Central heat pump, with DH return line as a heat source and DH supply as a sink). The configurations are classified and described in tables 6-6 and presented using schematic diagrams in table 2-8. Besides, was used the schematic diagram of a single-stage vapor compression heat pump (figure 6-2) to show the different network connections possible; and the conventional case without HP (figure 6-1) is used as a reference to describe the different connections available and the ones that have already been studied in the literature.

Table 6-6: Classification and description of possible heat pump configurations in district heating networks.

	Classification	Description	Source	Sink
1	$\mathbf{C\_HP\_T_s\_DH_s}$ Central heat pump, T_{source} low-grade heat and the DH supply used as a heat sink	In this configuration, the heat pump is placed at the central power station and utilizes low-grade heat as a heat source to evaporate the refrigerant. Likewise, the HP heat sink is used to provide heat to the return line's temperature and the DH supply line as a sink. Central HPs with a single heat source should have sufficient and flexible thermal capacity (T_{source} low-grade heat) to fulfill the heating	T_{source} low-grade heat	DH supply line

		requirement throughout the year entirely. Centralized HP can be alone or form a system with other equipment (CHP and boilers), thus achieving higher flexibility when electricity prices are low.		
2	**L_HP_DH$_s$_DH$_s$** Local heat pump, DH supply line as heat source Sink to DH supply	Locally placed, this heat pump configuration (named heat Split HP) can be used as a booster in DH and utilizes the DH network's supply line as the heat source to evaporate the refrigerant. Likewise, the sink process stream is heated from the supply line's temperature and the forward supply line as a sink. The temperature glide of the source corresponds to the difference between T_{supply} and T_{return}. The DH network's optimal temperature can be reached by combining this system with other heat production equipment to increase the temperature of the forward line of the DH network.	DH supply line	DH supply line
3	**L_HP_DH$_r$_DH$_s$** Local heat pump DH return line as a heat source Sink to DH supply	Locally placed, this heat pump configuration can be used as a booster in DH and utilizes the DH network's return line as the heat source to evaporate the refrigerant. Likewise, the sink process stream is heated from the return line's temperature and the forward supply line as a sink. The source temperature glide is the lowered temperature of the return line of the DH network, and the temperature glide of the sink is the difference between (T_{sink} -T_{source}). The DH network's optimal temperature can be reached by combining this system with other heat production equipment to increase the temperature of the forward line of the DH network.	DH return line	DH supply line
4	**L_HP_DH$_s$_DH$_s$_a** Local heat pump DH return line as a heat source Sink DH supply alternative	Locally placed, this heat pump configuration is an alternative option of **L_HP_DH$_s$_DH$_s$** Moreover, it can be used as a booster in DH. Its main difference is the use of the DH network's return line as the heat source to evaporate the refrigerant; the sink process stream is heated from the temperature of the supply line and the forward supply line as a sink. The source temperature glide is the lowered temperature of the return line of the DH network. The configuration requires the use of other heat sources to increase the forward line's optimal temperature.	DH supply line	DH supply line
5	**I_HP_DH$_s$_PH_DHW** Individual heat pump directly connected DH supply line as a heat source, heat sink connected to PH and DHW	The direct connection involves pipelines between the heat pump unit and the district heating network. This individual heat pump configuration can be used as a DH booster to cover SH and DHW demand. It can utilize the supply line of the DH network as the source to evaporate the refrigerant. Likewise, the sink process stream is heated from the supply line's temperature and network of pipes connecting PH and DHW as a high-temperature sink (≥90 °C). The temperature glide of the source corresponds to the difference between T_{supply} and T_{return}. This configuration requires a DH network in order to operate and can cover the SH demand directly. In addition, the location of this heat pump type is decentralized close to the consumer and replaces a connection substation.	DH supply line	SH and DHW
6	**I_HP_DH$_r$_T$_{demand}$** Individual heat pump directly connected DH return line as a heat source, Sink to T_{demand}	Utilizing the return line as the heat source to evaporate the refrigerant, directly connected to the DH network, this individual heat pump configuration can be used as a booster in DH to cover specific T_{demand}. The temperature lift is the difference between Tdemand and T_{return}. Moreover, the source temperature glide is the lowered temperature of the return line of the DH network. These configuration requires the use of other heat sources in order to increase the temperature of the forward line (T_{demand}). The location of this heat pump type is decentralized as the heat is delivered directly to the consumer.	DH return line	T_{demand}

7	**I_HP_DH$_s$_T$_{demand}$** Individual heat pump directly connected DH supply line as a heat source, Sink to T_{demand}	Decentralized HP that utilizes the supply line as the heat source to evaporate the refrigerant, directly connected to the DH network; this individual heat pump configuration can be used as a booster in DH to meet specific T_{demand}. The temperature lift is the difference between T_{demand} and T_{supply}. Moreover, the source temperature glide is the lowered temperature of the return line of the DH network. The configuration requires the use of other heat sources in order to increase the temperature of the forward line (T_{demand}).	DH supply line	T_{demand}
8	**I_HP_T$_s$_DH$_s$** Individual heat pump directly connected, T_{source} low-grade heat, DH return line as a heat source, Sink to DH supply	Directly connected to the DH network, this individual heat pump utilizes the T_{source} of the low-grade heat to evaporate the refrigerant. Likewise, the sink process stream is heated from the return line's temperature and the forward supply line as a sink. The temperature glide of the source corresponds to the heat capacity of the finite heat source. and the temperature glide of the sink is the difference between (T_{sink} -T_{source}). It is thus subject to optimization in each individual DH system considering the generation technologies. The configuration requires the use of other heat sources to increase the forward line's temperature.	T_{source} low-grade heat	DH supply line
9	**I_HP_T$_s$_DH$_s$-**a Individual heat pump directly connected T_{source} low-grade heat as a heat source, Sink to DH supply alternative	Directly connected to the DH network, this individual heat pump utilizes the T_{source} of the low-grade heat to evaporate the refrigerant. Likewise, the sink process stream is heated from the supply line's temperature and the supply line as a sink. The temperature glide of the source corresponds to the heat capacity of the finite heat source, and the temperature lift is the difference between (T_{sink} -T_{source}). It is thus subject to optimization in each individual DH system considering the generation technologies. The configuration requires the use of other heat sources to increase the forward line's temperature.	T_{source} low-grade heat	DH supply line
10	**I_HP_T$_s$_DH$_r$** Individual heat pump directly connected T_{source} low-grade heat as a heat source, Sink to DH return	Directly connected to the DH network, this individual heat pump utilizes the T_{source} of the low-grade heat to evaporate the refrigerant. Likewise, the sink process stream is heated from the return line's temperature and the return line as a sink to preheat a DH network's return line before entering the CHP plant. The temperature glide of the source corresponds to the heat capacity of the finite heat source, and the temperature lift of the heat pump is the difference between (T_{sink} -T_{source}). Thus, the temperature lift is significantly lower compared to configuration $8-$ **I_HP_T$_s$_DH$_s$**So it will increase the COP of the heat pump. Another implication of this configuration is the reduction of the CHP plant's electric efficiency due to the increased condensing pressure [138]. The configuration is subject to optimization and requires other heat sources to increase the forward line's temperature.	T_{source} low-grade heat	DH return line
11	**I_HP_T$_s$_DH$_r$-a** Individual heat pump directly connected T_{source} low-grade heat as a heat source Sink to DH return alternative	Directly connected to the DH network, this individual heat pump utilizes the T_{source} of the low-grade heat to evaporate the refrigerant. Likewise, it is an alternative option of **10** $-$ **I_HP_T$_s$_DH$_r$** with the principal difference that the sink process stream is heated from the supply line's temperature.	T_{source} low-grade heat	DH return line
12	**I_HP_T$_s$_T$_{demand}$** Individual heat pumps indirectly connected T_{source} low-grade heat as a heat source Sink to T_{demand}	Sink and source temperatures are T_{demand} and T_{source}, respectively. This configuration is similar to commercially available heat pump installations in dwellings. Using an individual heat pump in place of a heat exchanger in the building allows a decrease in the whole network's temperature, so the network becomes low-temperature district heating. This configuration does not require a DH network in	T_{source} low-grade heat	T_{demand}

	order to operate, but the CHP can power them. All heat pump units can be managed centrally and controlled as a part of a smart grid or district energy system. The CHP plant can increase the heat generation because the additional electricity generated can be consumed as driven energy in the individual heat pumps and stored in the form of heat in domestic hot water tanks, space heating, etc.

From the interpretation of tables 6-6, 6-7, and 6-8, it is clear that a change in supply temperature has a significant effect on power production compared to a corresponding change in return temperature. From our literature review, we can validate that six out of twelve heat pump configurations identified have been studied by Ommen et al. [31], two have been studied by Sayegh et al. [22] and Roh et al. [37] four configurations have not been studied so that these cases may be worth further investigation.

Ommen et al.[31] concluded that configurations $\mathbf{3-L\_HP\_DH_r\_DH_s}$, $\mathbf{4-L\_HP\_DH_s\_DH_s\_a}$, and $\mathbf{8-I\_HP\_T_s\_DH_s}$ may thus be disregarded in a system feeding a CHP plant, due to a more significant impact on power production and also higher condensation pressure in the heat pump compared to the $\mathbf{10-I\_HP\_T_s\_DH_r}$ configuration. However, the authors recommend these cases be further investigated if the primary production technology of heat is not sensitive to increased temperatures like in the systems where the DH network is fed by co-generation of electricity and heat from an internal combustion engine (ICE).

Likewise, Ommen et al.[31] concluded that configuration $\mathbf{12-I\_HP\_T_s\_T_{demand}}$ in terms of COSP has advantages at high DH network temperatures (3G). However, there are no conclusive results, and the authors explain that several arguments used can be questioned due to assumptions made for central and small capacity heat pumps. This comment agrees with Sayegh et al. [22], where the choice of heat pump technology for integration into district heating networks is complex and multicriterial. There is no consistent way to create heat pump-based district heating, and each case must be studied with its assumptions.

Sayegh et al. [22] and Roh et al. [37]also concluded that a decreased supply temperature in the DH system could improve power generation efficiency in the DH using a CHP system and decrease the rate of use of peak boilers. Likewise, they concluded that the direct use of energy from the DH supply of high-temperature stream to evaporate the refrigerant (HRT) generates higher COP for the booster HP than the use of energy from the DH returns low-temperature to evaporate the refrigerant (LRT).

Table 6-7: List of configurations included in the review, their classification, developer/publisher, options of integration into district heating, HP placement, type and connection mode, heat pump ΔT_{lift}, COP, and coefficient of system performance [18][21][26][31][32][51].

	Classification unit	Network generation type	Published Developed by	HP placement	HP type	Connection mode	Operation mode	ΔT_{lift} (K)	COP [-]	COSP [-]
1	$C\_HP\_T_s\_DH_s$	4G and 5G	Yes, by [19] [60]	Centralized combined with CHP	Compressor water-source	Single, series, and Parallel	Single heat source- LRT	70-80	2 - 6	3 - 4
2	$L\_HP\_DH_s\_DH_s$	3G, 4G, and 5G	New	Local combined with CHP	Compressor water-source	Single, series, and Parallel	Single heat source- HRT	60-80	2-6	-
3	$L\_HP\_DH_r\_DH_s$	3G, 4G, and 5G	Yes, by [31]	Local combined with CHP	Compressor water-source	Single	Single heat source- LRT	35-60	5-6	0.95
4	$L\_HP\_DH_s\_DH_s\_a$	3G, 4G, and 5G	Yes, by [31] [37]	Local combined with CHP	Compressor water-source	Single	Single heat source- LRT	35-60	2.5	0.94
5	$I\_HP\_DH_s\_PH\_DHW$	3G	Yes, by [37]	Individual	Compressor water-source	Single	Single heat source- LRT and HRT	60-70	2.7-4.5	7-9
6	$I\_HP\_DH_r\_T_{demand}$	3G, 4G, and 5G	Yes, by [31]	Individual	Compressor water-source	Single	Single heat source- LRT	35-60	6-8	0.95
7	$I\_HP\_DH_s\_T_{demand}$	3G, 4G, and 5G	New	Individual	Compressor water-source	Single, series, and Parallel	Single heat source- HRT	35-70	2-6	-
8	$I\_HP\_T_s\_DH_s$	3G, 4G, and 5G	Yes, by [31]	Individual	Compressor water-source	Single	Single heat source- LRT	35-60	3-4	3-4
9	$I\_HP\_T_s\_DH_s$-a	3G, 4G, and 5G	New	Individual	Compressor water-source	Single, series, and Parallel	Single heat source- HRT	35-70	2-6	-
10	$I\_HP\_T_s\_DH_r$	3G, 4G, and 5G	Yes, by [31]	Individual	Compressor water-source	Single	Single heat source Low heat from RES	35-60	3-6	3-5
11	$I\_HP\_T_s\_DH_r$-a	3G, 4G, and 5G	New	Individual	Compressor water-source	Single, series, and Parallel	Single heat source- HRT	35-70	2-6	-
12	$I\_HP\_T_s\_T_{demand}$	3G, 4G, and 5G	Yes, by [31]	Individual	Compressor water-source	Single	Single heat source Low heat from RES	35-60	4.5	4

Table 6-8: Twelve schematic diagrams of the identified configurations for the integration of heat pumps into DH networks.

Central heat pump
1 – C_HP_T_s_DH_s
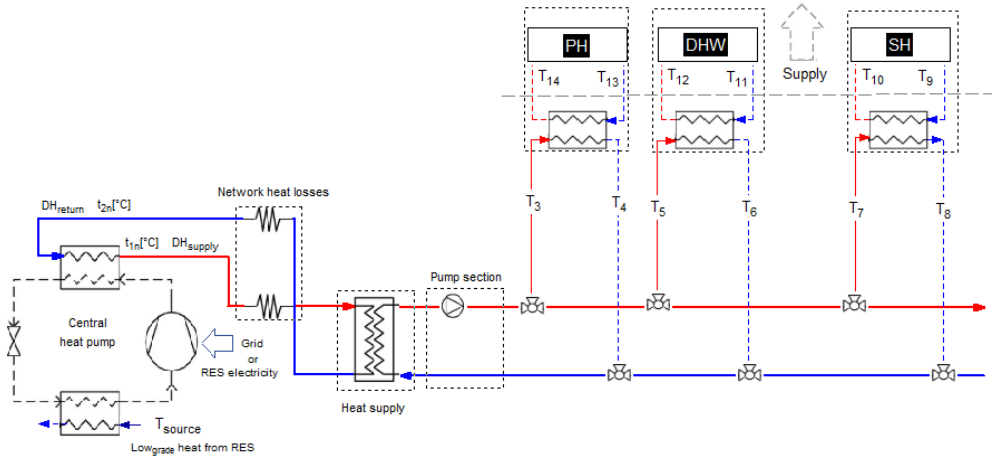
Local heat pump
2 – L_HP_DH_s_DH_s
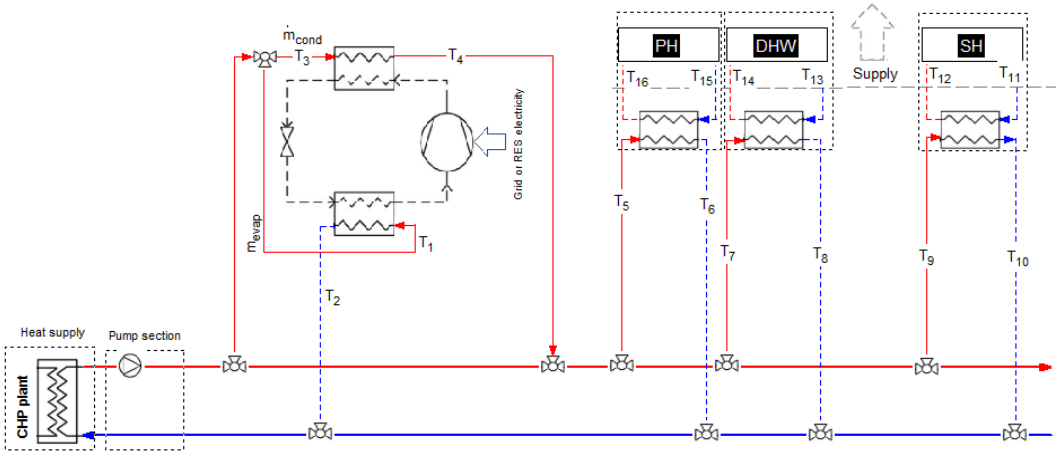
3 – L_HP_DH_r_DH_s

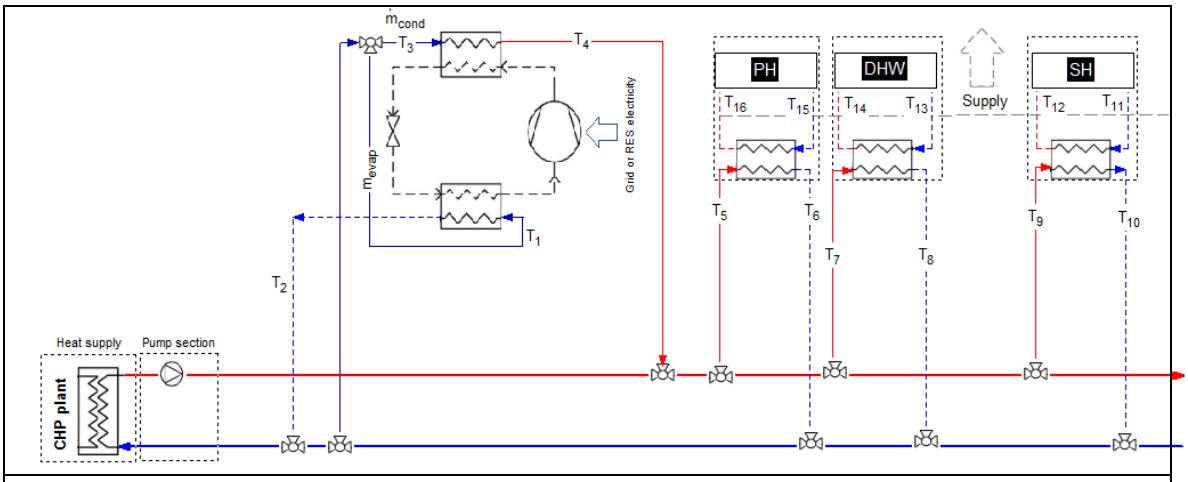

4 – L_HP_DH$_s$_DH$_s$_a

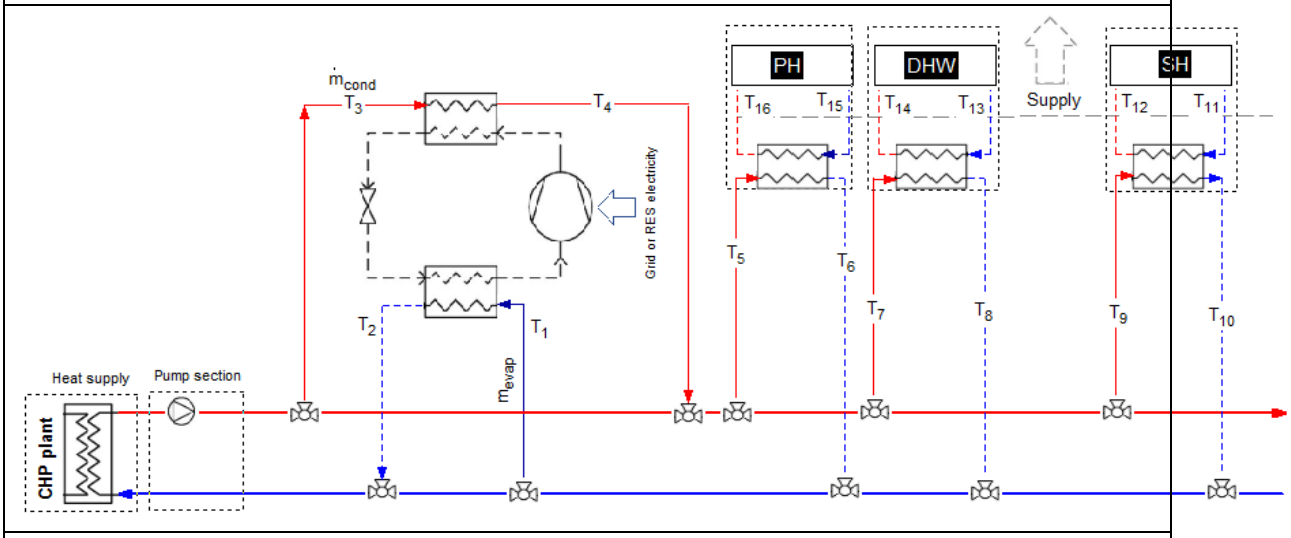

Individual heat pump directly connected

5 – I_HP_DH$_s$_SH_DHW

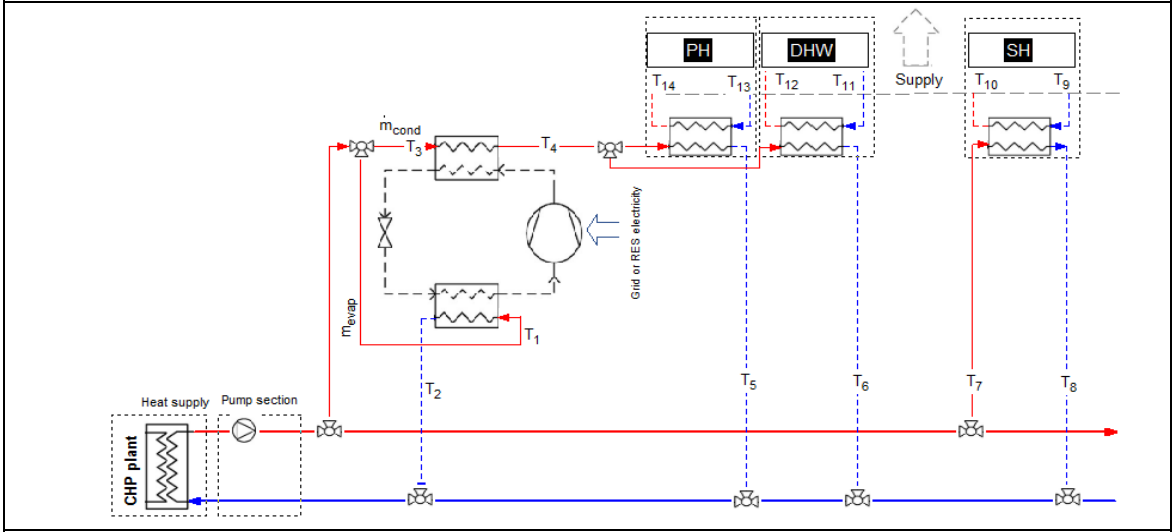

6 – I_HP_DH$_r$_T$_{demand}$

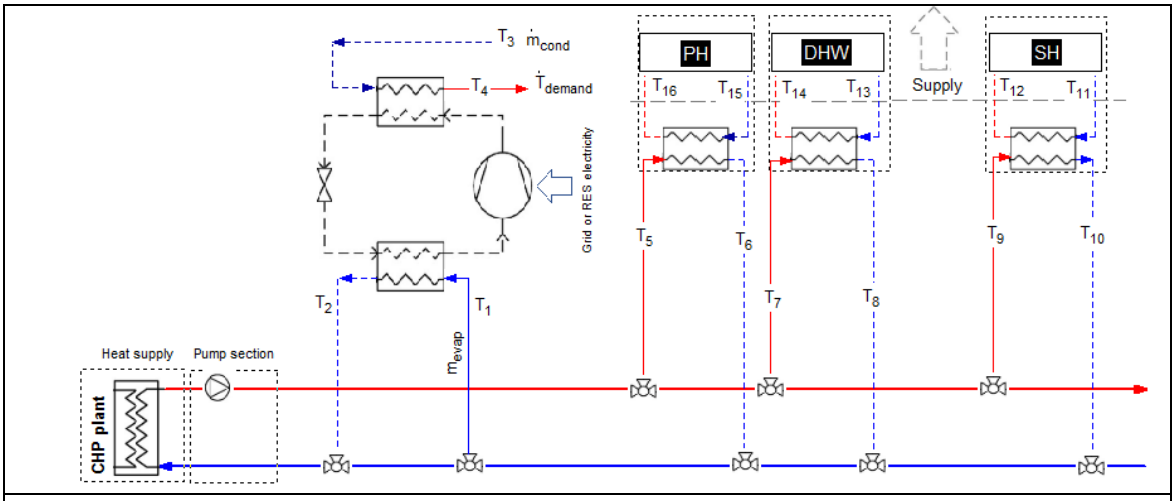

7 – I_HP_DH$_s$_T$_{demand}$

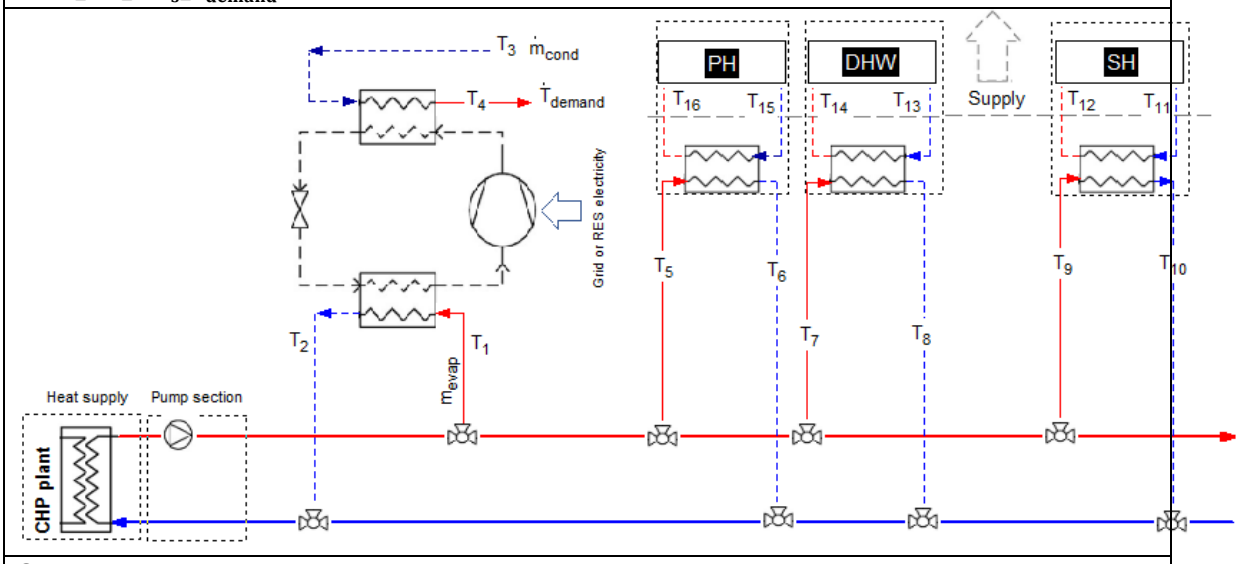

8 – I_HP_T$_s$_DH$_s$

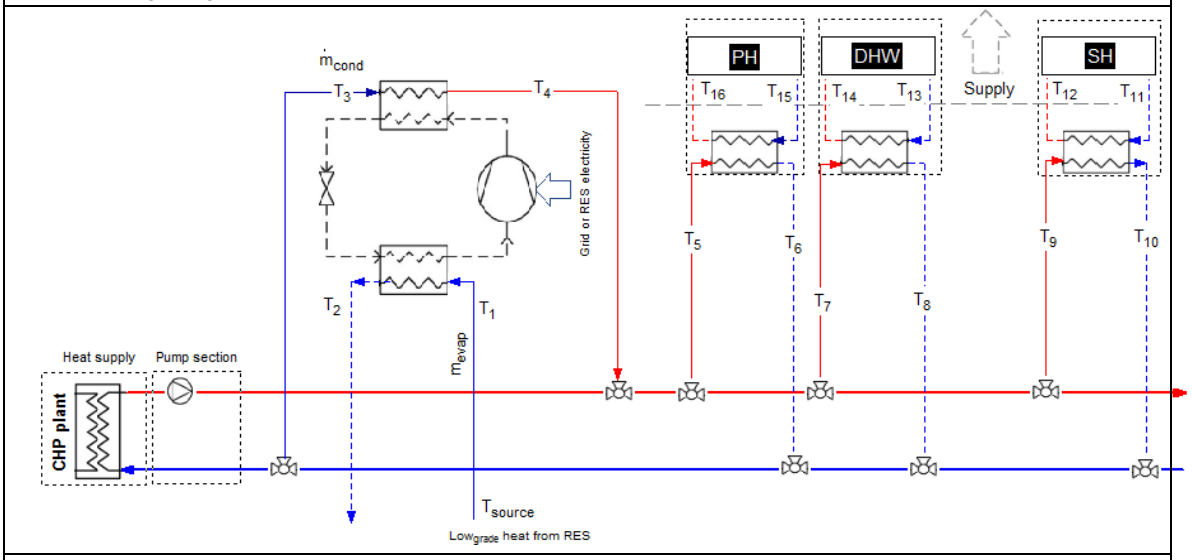

9 – I_HP_T$_s$_DH$_s$-a

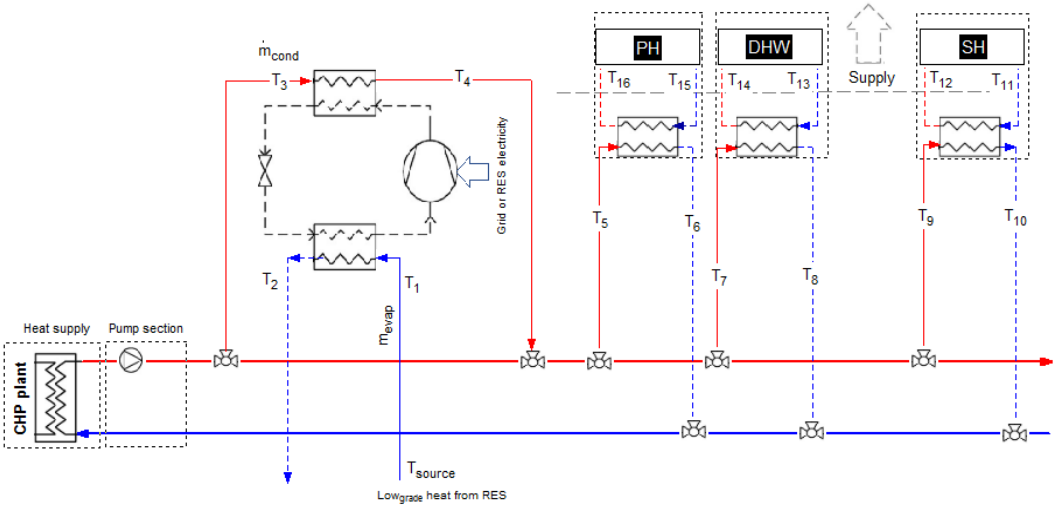

10 – I_HP_T_s_DH_r

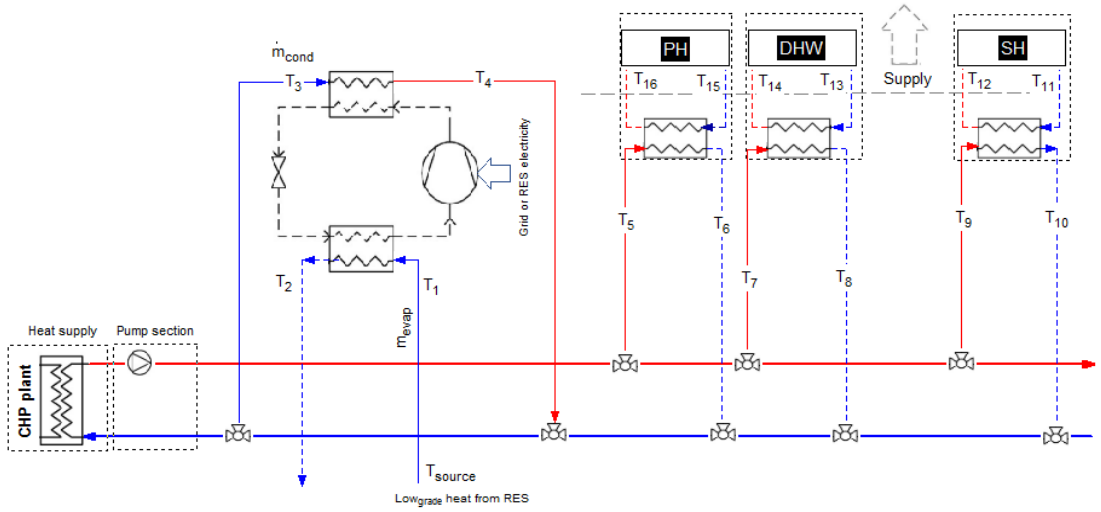

11 – I_HP_T_s_DH_r-a

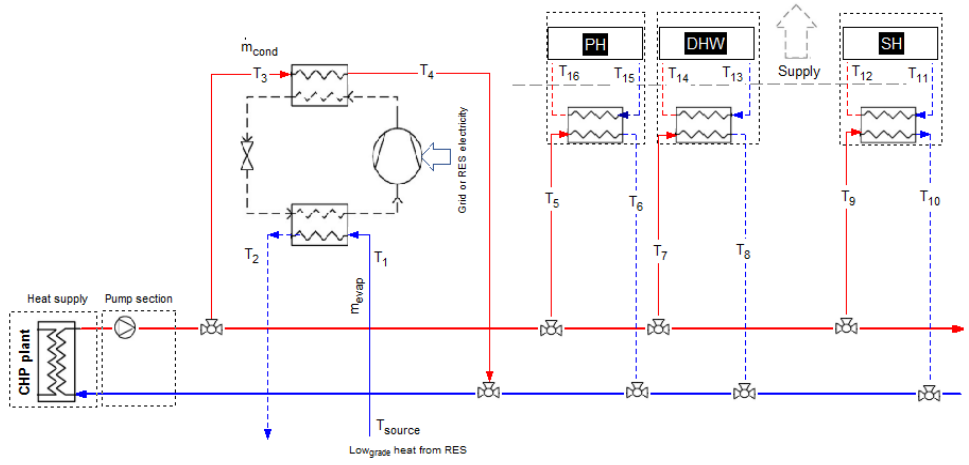

Individual heat pump indirectly connected

12 – I_HP_T_s_T_{demand}

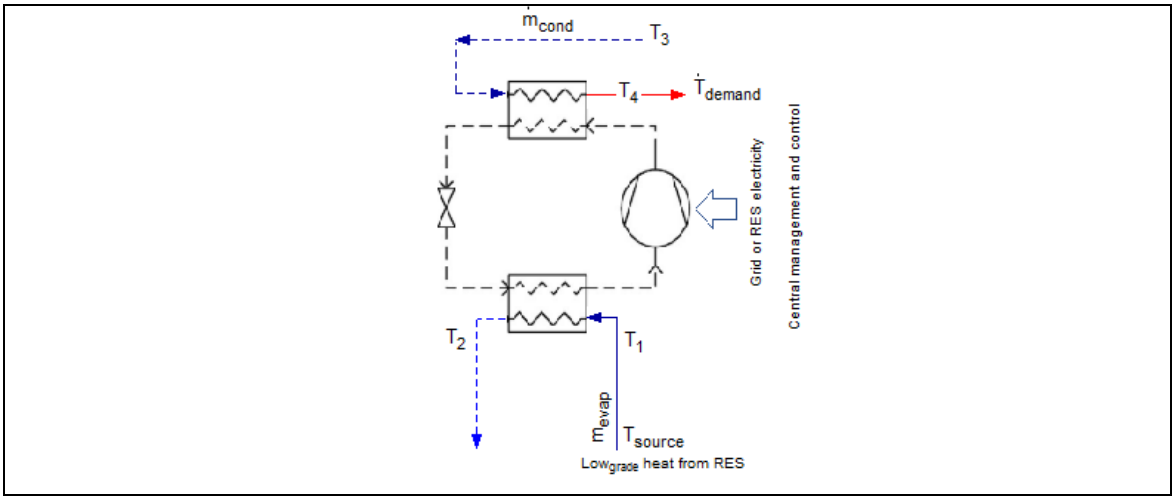

6.5 **CONCLUSIONS**

The present research aimed to examine power-to-heat technologies that can cost-effectively contribute to fossil fuel substitution, renewable energy integration, and decarbonization. In this context, integrating heat pumps into DEN systems provides significant environmental and performance improvements, being an innovative and profitable solution for different decarbonizing sectors. Specifically, small DH systems present the most significant potential for using HPs, significantly reducing the use of fossil fuels, while, in medium and large structures with efficient CHP production, the HP potential is lower. However, the optimal size of HPs for DH systems depends mainly on the system and its characteristics and external factors, such as electricity and fuel prices and other economic inputs. Likewise, available waste heat sources, heat requirements, and HP technology naturally affect the HP potential, being one reason why there are no single criteria for the potential of HPs in DH systems.

The DH literature identifies five generations of district heating networks. Additionally, several manufacturers can provide heat dissipation temperatures (T_{sink}) of at least 90 °C, with heating capacities varying from 20 kW to 20 MW with COP values ranging from 2.4 to 5.8, and with a temperature increase of 100 to 40 K. The experimental data of the operation of commercial heat pumps indicates that their efficiency oscillates between 40 and 60% of the maximum efficiency according to the second law of thermodynamics.

Twelve (12) possible heat pump configurations in DH networks have been identified, termed, and described. From our literature review, we could identify that eight of twelve heat pump configurations identified have been studied (table 6-7).

Even so, four of twelve heat pump configurations have not been studied (table 6-7), and the authors recommend these cases be further investigated. The analysis focused on two key performance factors chosen to indicate the performance from a system perspective and differences between system performance (COSP) and the heat pump component performance (COP). For example, three configurations $\mathbf{3-L\_HP\_DH_r\_DH_s}$,$\mathbf{4-L\_HP\_DH_s\_DH_s\_a}$, and $\mathbf{8-I\_HP\_T_s\_DH_s}$ do not perform well in a system feeding a CHP plant due to a more considerable impact on power production and higher condensation pressure in the heat pump than in the $\mathbf{10-I\_HP\_T_s\_DH_r}$ configuration. Likewise, configurations $\mathbf{10-I\_HP\_T_s\_DH_r}$ and $\mathbf{12-I\_HP\_T_s\_T_{demand}}$ have more advantages in terms of COSP at high DH network temperatures (3G).

The market potential for heat pumps is high, and this can create several social-economic benefits. However, the widespread diffusion of HP technologies faces several challenges, including technological (limitation of the electrical network due to intensive electrification of the heating sector), economic (high investment and installation cost), regulatory (lack of standards and mandatory policies), policy (uncertainty in policy and lack of clear heat decarbonization pathways and technology uptake), and public acceptance issues (unwarranted fear, misperception, misinformation, and previous experiences on the reliability of heat pumps). Thus, further work based on this classification will address the effect of district grid configuration, the difference between high-temperature supply lines and low-temperature returns lines on the thermal performance of a district heating system that integrates commercial high-temperature heat pumps using the twelve configurations identified.

Finally, in chapter 7, we will use the results of this chapter to analyze the connection of DEN in polygeneration systems (Gasifier + electrolyzer + gas turbine). Specifically, a district energy network of 5th generation.

Chapter7 CASE OF STUDY OF POLYGENERATION SYSTEM IN LACHINE-EST IN MONTREAL, CANADA

Summary: In Chapter 1 was provided background information and possible scenarios for polygeneration systems. Specifically, the integration of biomass gasification and renewable-energies-driven water electrolysis for hydrogen-rich syngas production. Chapter 2 proposes the modeling for the integrated polygeneration systems. With a more detailed gasification model for designing and simulating a biomass gasification plant using the equation solver program Engineering Equation Solver (EES) in chapter 3. The data an information to perform the simulation was gathered through two experimental analyses. One on the steam gasification of palm kernel shells (PKS) for hydrogen-rich N_2- free syngas production in a pilot-scale atmospheric downdraft allothermal gasifier and another one for characterization of an alkaline electrolysis cell for hydrogen generation at atmospheric pressure. The system was completed by the proposal of the use of heat pumps and energy transport networks to complete the whole system. Finally, in this chapter all previously developed models and experimental data are integrated to analyze polygeneration systems in very low-temperature district energy network in Lachine Est in Montreal, Canada.

7.1 LACHINE-EST AREA

The current study is based on the Dominion Bridge area in Lachine-Est in Montreal, Canada. Figure 7-1 shows the location of the case study and the newly proposed designs. Developers intend to design an eco-quartier with an energy-efficient and cost-effective energy system.

Figure 7-1: Study area: **(a)** and **(b)** location of the Lachine-Est quartier in the formal Dominion Bridge Area; **(c)** bird view of buildings distribution in the newly proposed design

Two scenarios have been considered for the energy system of the mentioned area (Fig. 7-2). Both scenarios share the same sets of buildings with the same characteristics, schedule, usage, and material. In the first scenario, the gasifier operates with air and/or steam as the gasifying agent. The resulting product gas is fed to heat recovery units, a clean-up section, and a turbine coupled with a chiller to generate power, heat, and cold in the Lachine-Est area. In contrast, in the second scenario and for the same demand conditions, the system is operated with the gasifier but with integrated electrolysis cells. The electrolyzer converts electricity and water into H_2 and O_2, water electrolysis is used to provide the O_2 as gasifying agent. At the same time, H_2 is directly sent to the syngas stream to improve the heating value of syngas generated that produces an N_2-free gas suited for biofuel synthesis, hydrogenpower, heating, and cooling production.

The first step will be to determine the energy demands according to the buildings' characteristics. The methodology used is explained in the next sections.

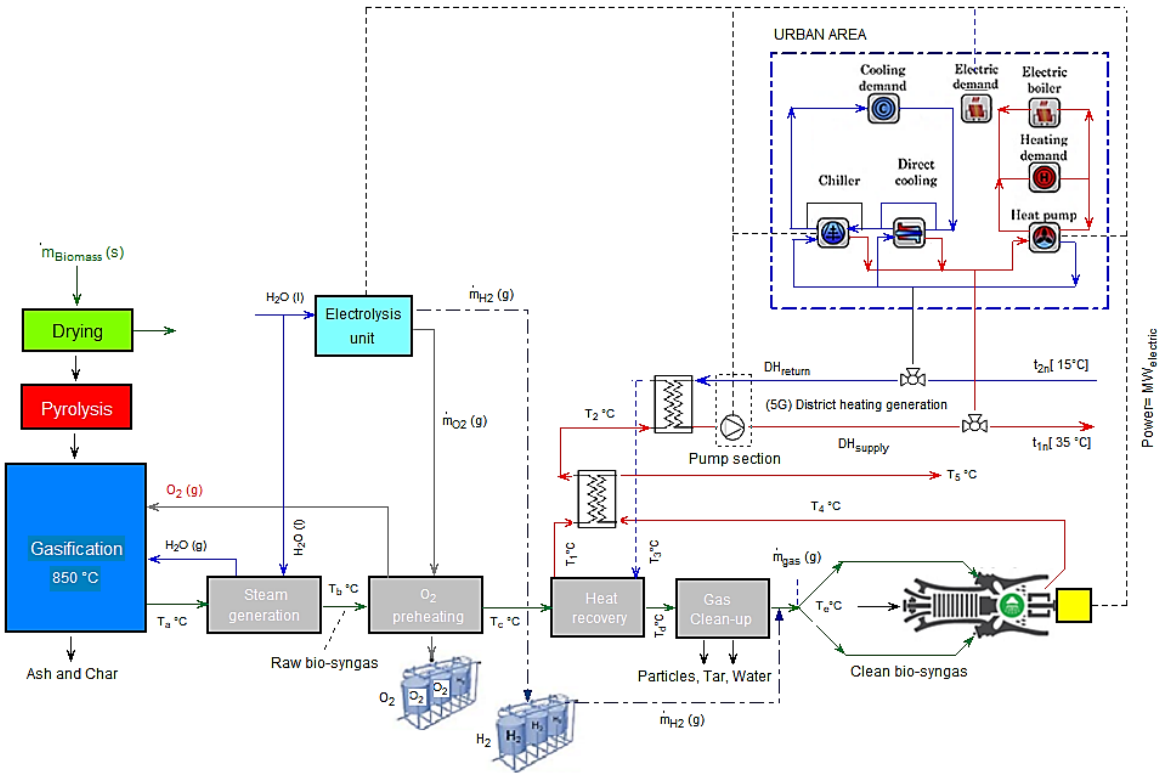

Figure 7-2: Schematic representation of the polygeneration plant concept for syngas upgrading in district energy networks of 5th generation

7.2 AUTOMATIC URBAN BUILDING ENERGY MODELING (AUBEM

This study uses a CityGML file of the new design integrated into a software workflow that performs the 3D building modeling process to obtain the energy demand. Structuring the detailed geometry data of buildings in the City Geography Markup Language (CityGML) format allows the information to be stored so that it is readable by computer programming. CityGML is a text-based format similar to the XML format, which uses hierarchical structures to store objects and attributes related to building geometries. The CityGML format can be read using programming languages such as Matlab and Python.

A Python code was written to perform the following tasks: (i) extracting the building coordinates and building characteristics (building use-type, year of construction, etc.) from CityGML format; (ii) merging the building surface coordinates with their related characteristics in the same list and organizing the data to be suitable for energy simulation software; (iii) assigning the building materials and constructions to each surface based on building use-types and surface types, whether they are walls, roof surfaces, or ground surfaces;(iv) reading and organizing the occupancy, electrical equipment, lighting, and ventilation schedule and assigning them to each building based on building usage; (v) feeding the data into EnergyPlus for energy demand calculation.

Figure 7-3 summarizes the proposed workflow for the AUBEM system. The CityGML file is read and analyzed through Python code to extract the ID, geometric and material information of each building to organize them following the defined hierarchical structure (building ID, building type, surface information).

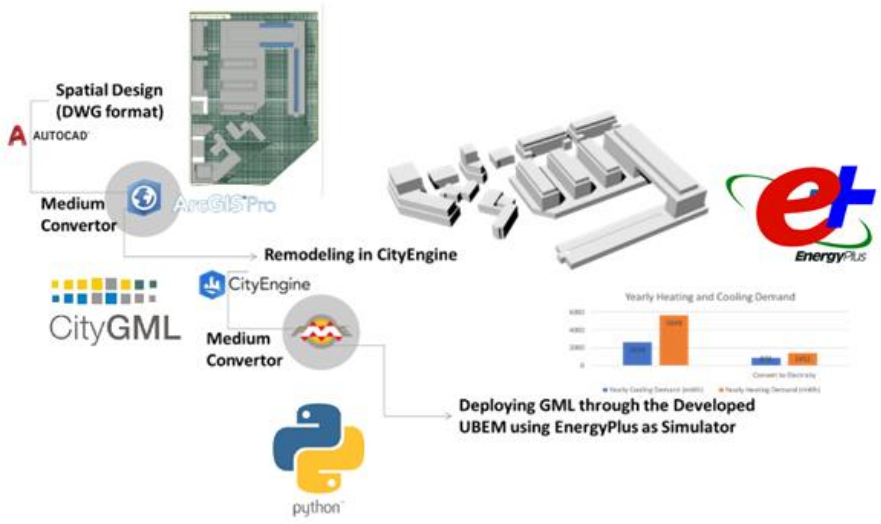

Figure 7-3: Automatic Urban Building Energy Modeling System

7.3 ENERGYPLUS FOR URBAN BUILDING ENERGY MODELING

EnergyPlus is a physics-based model that captures the whole dynamic of the building performance to provide a detailed analysis [1]. Due to the flexibility and accuracy of EnergyPlus, it is used for building energy demand calculations. EnergyPlus first defines the building zones and then creates 3D building models. Building IDs are used to name the zones. It is necessary to assign each building's surface to its related building zones. Therefore, each surface has a zone name defined based on the building ID and should be determined automatically before adding the surface coordinates into EnergyPlus.

The building materials and constructions are extracted from the National Renewable Energy Laboratory (NREL) website [2] and stored in a JavaScript Object Notation (JSON) format. Thus, the JSON format is parsed, the building constructions and materials are categorized based on the building use type, stored in a Python dictionary, and named NREL building construction archetypes. Finally, the building construction archetypes are assigned to each building's surface based on the building use (building use-types are extracted from CityGML).

The occupancy, electrical equipment, lighting, and ventilation schedules are extracted from the Department of Energy (DOE) building archetypes website [3] for a large office, secondary school, small office, and midrise apartment buildings. Since DOE has limited building archetypes, we had to consider the most similar building archetype for each building use-type in the Lachine district. The large office archetype is considered for the Civic Center building type, the secondary school for school, the large office for a commercial, the midrise apartment for a residential, and the small office for an office. The extracted archetypes are stored in a text file and read through Python to be assigned to each building.

In the last step, each surface, with all its related information, the building occupancy, electrical equipment, lighting, and ventilation schedules, is fed to the EnergyPlus to calculate the heating and cooling demands. EnergyPlus positions the surfaces in their specific location and connects them to form a 3D building urban model. Moreover, the building surfaces are categorized into three groups, walls, roof surfaces, and ground surfaces, and their related archetypes are assigned to

each group accordingly. The other required parameters for accurate building energy demand calculation, such as occupancy, electrical equipment, lighting, and ventilation schedules, change dynamically based on building use-types and are all automatically assigned to each building and are summarized in Table 1.

Table 7-1: EnergyPlus setting parameters for Urban Building Energy Modeling [4][5][6]

Parameters		**Settings**
Window-towall ratio		0,35
Constant heating set point		22 °C
Constant cooling set point		25 °C
Heating, ventilation and air conditioning (HVAC) templates		Ideal loads air system
Solar distribution	Full interior and exterior	
Shading calculation	**Calculation method**	**Average over days in Frecuency**
	Calculation frecuency	Every 20 days
	Maximum figures in shadow overlap calculations	15000
	Polygon clipping algorithm	SutherlandHodgman
	Sky diffuse modeling algorithm	Simple sky diffuse modeling
	External shading calculation method	Internal calculation
Surface convection algorithm inside	TARP	
Surface convection algorithm outside	DOE-2	
Heat balance algorithm	Conduction transfer function	
Solar model indicator	Winter design day	
	Summer design day	
Solar model indicator	ASHRAE clear sky	
Occupancy	**Number of people calculation method**	**People/Area**
	People per zone florr area	$0{,}05\ \text{people}/\text{m}^2$
Parameters	Settings	
Lighting	**Design level calculation method**	**Watts/Area**
	Watts per zone floor area	$10\ \text{W}/\text{m}^2$
Equipment	**Design level calculation method**	**Watts/Area**
	Watts per zone floor area	$5\ \text{W}/\text{m}^2$
Infiltration	**Design flow rate calculation method**	**Residential: Flow/Exterior Area and Commercial: Flow/ExteriorWall Area**
	Flow per exterior surface area	Residential: $0{,}0002\ \text{m}^3/\text{s} - \text{m}^2$
		Commercial: $0{,}0005\ \text{m}^3/\text{s} - \text{m}^2$
HVAC	**Outdoor air method**	**Flow/Area**
	Outdoor airflow rate per zone Floor area	$0{,}00043\ \text{m}^3/\text{s} - \text{m}^2$

7.4 PLACEMENT AND CONNECTION MODES OF BUILDINGS IN A DISTRICT HEATING AND COOLING NETWORK FOR LACHINE-EST AREA

Figure 7-4 shows the studied placement and connection modes of the buildings in the district energynetwork for the Lachine-Est area. The District network is made up of six buildings (A,B,C,D,E and F) heated by central heat source (gasification unit+electrolyzer+gas turbine (G), central heat pumps (H)) and local heat pump (I). The hot water passes through a network of double pipes (supply and return) distributed to the buildings for different applications. The district heating system is composed by three (3) systems: (i) generation system (polygeneration unit), (ii) distribution system, and (iii) consumption system (Figure 7.4). First, the generation system consists of a central energy production plant (using the polygeneration concept) and heat exchangers (HX). Then, distribution is made up of a network of hot water distribution pipes- fifth district heating generation (5G) with a supply and return temperature of 35 and 15°C. Finally, the consumption includes space heating (SH), domestic hot water (DHW), process heating (PH), and services supplied by compression chiller (CC), direct cooling (DC), and heat pumps (HP).

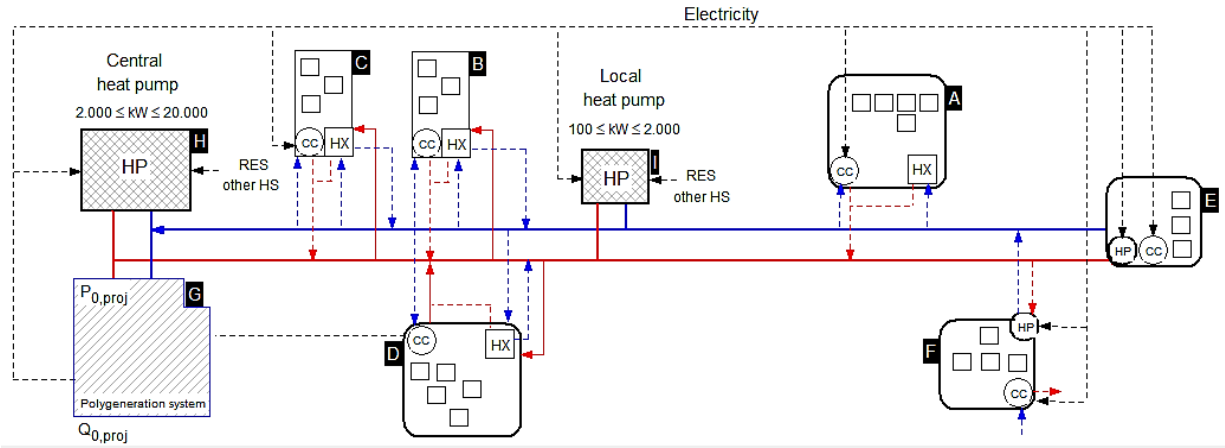

Figure 7-4: Configuration of buildings in district heating and cooling network for Lachine-Est Area: (A) - (F) Buildings; (G) Polygeneration system (gasifier + electrolyzer + turbine); (H) Central heat pump and (I) Local heat pump.

Individual heat pumps can be connected directly to a network of pipes that connect buildings in a neighborhood and can be powered by gasifiers from centralized plants and working in a single or multi heat source connection (figure 7-5). This alternative can use a warm and cold pipe with a temperature difference of about 5–10 K. Both pipes are operated at temperatures close to the surrounding (15–35 °C). Due to the low temperatures, the heating demands of buildings cannot be covered directly, and a heat pump is installed in each building to raise the temperature to the level required by the building's heating system. A heat pump takes water from the warm

pipe and uses it as a heat source in heating mode. In our case study, The cooled-down water from the evaporator of the heat pump is then discharged to the cold pipe. If the building has a cooling demand, it can be cover by a compression chiller and a heat exchanger for direct cooling with the cold pipe in advanced district heating networks where the fluid from the cold pipe is warmed up in the building and discharged to the warm pipe.

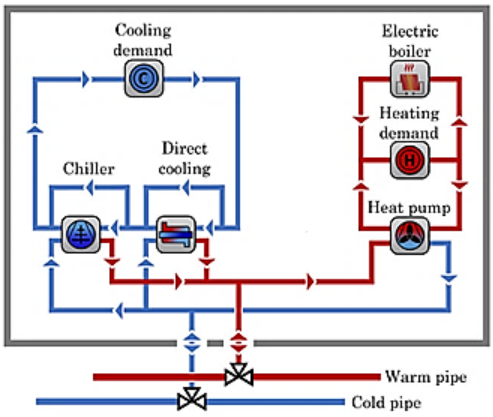

Figure 7-5: Energy systems (Base on [7]): Heating demands are covered by a water-to-water heat pump, electric boiler, cooling demands are covered by a compression chiller and a heat exchange.

7.5 **RESULTS AND DISCUSSION**

7.5.1 **ENERGY DEMAND RESULTS**

For the configuration of the buildings indicated in figure 7-4, the hourly heating and cooling demand is calculated. The maximum heating and cooling for each building throughout the year is shows in table 7-2. The annual energy demand for each building is summarized in table 7-3. The supply temperatures for domestic hot water and space heating - cooling are 50 °C and 15 °C, respectively.

Table 7-2: Maximum heating and cooling demand for buildings in Lachine-Est area

	Building A	Building B	Building C	Building D	Building E	Building F
Maximum heating load (kW)	5161,5	999,7	2331,4	2411,2	516,1	785,9
Maximum cooling load (kW)	4608,1	940,3	1902,3	1739,1	318,4	619,0
Total floor area m^2	136136	31056	54693	39410	11798	16908

Figure 7-6 shows the calculated heating and cooling demands of the buildings in the Lachine-Est area. Based on these results, the building A has the highest heating and cooling demand, due to its higher heated surface area. From figure 7-6, specific periods (3000-7000 hours) are detected where the demand for heating and cooling is simultaneous. Due to the high thermal inertia of the district network, we will use a warm and cold pipe with a temperature difference of about 5–10 K. Both pipes are operated at temperatures close to the surrounding (15-35 °C). Due to the low temperatures, the heating demands of buildings cannot be covered directly, and a local heat pump is installed in each building to raise the temperature to the level required by the building's heating system.

Table 7-3: Energy system model for buildings in Lachine-Est area

Output	Building A	Building B	Building C	Building D	Building E	Building F
Heating demand (kWh/yr)	1883178	414671	970676	1004891	346660	458603
Cooling demand (kWh/yr)	1681270	390032	792020	724787	213867	361211
Electricity demand (kWh/yr)	3564448	804704	1762696	1729678	560527	819814
Total floor area $(\mathbf{m^2})$	136136	31056	54693	39410	11798	16908

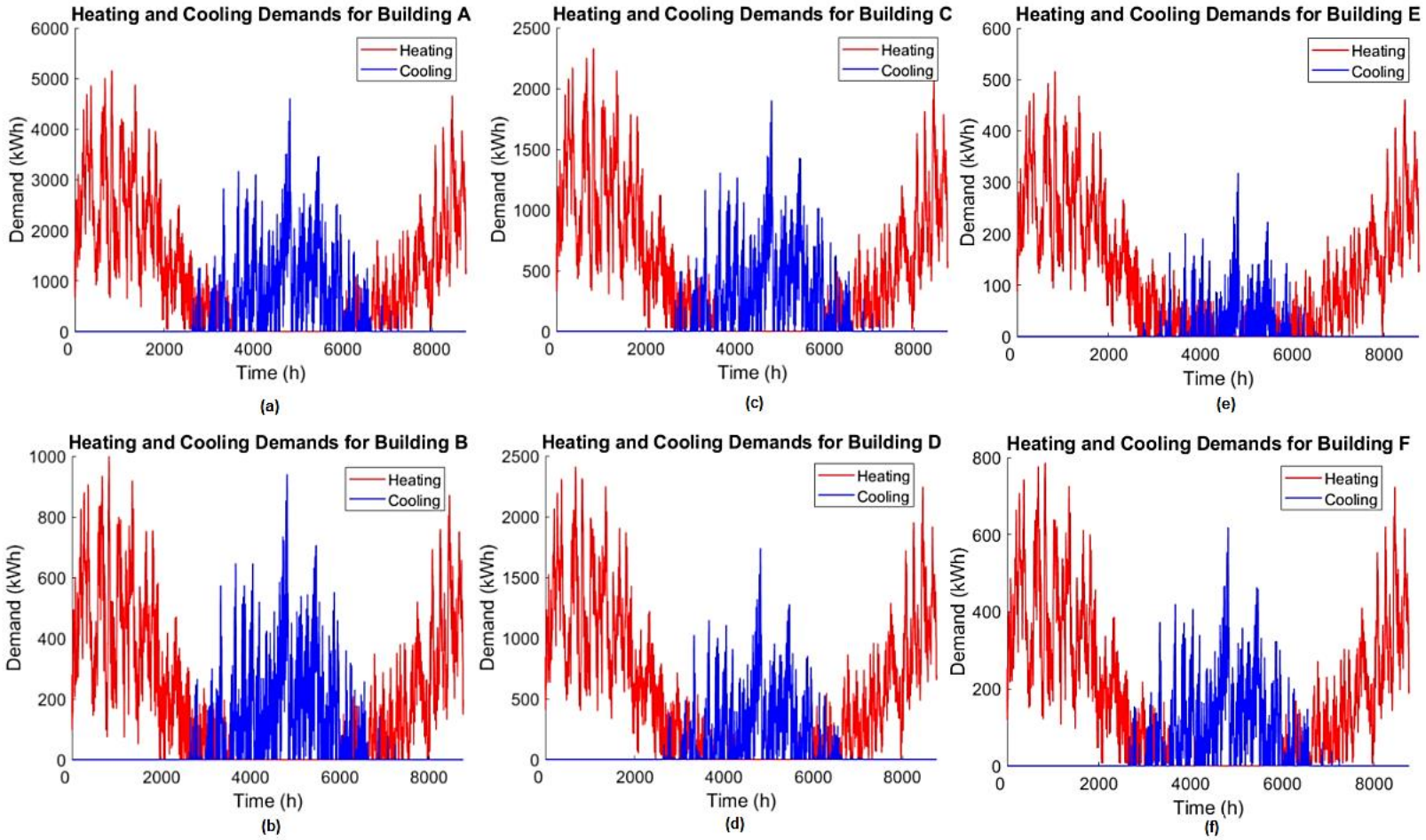

Figure 7-6: Heating and cooling demands for buildings in Lachine-Est area; **A**-commercial, **B**-residential, **C**-school, **D**-residential, **E**-residential, **F**-residential

7.5.2 **RESULT OF THE HEAT PUMPS MODEL**

Mathematical models were developed by functional adjustment for each heat pump configured as booster pumps or centralized stations to replace combined heat and power extraction (CHP) equipment. Two configurations were used: a) direct use of energy from the DHC supply of the high-temperature stream to evaporate the refrigerant (HRT) and (b) use of energy from the DHC return low-temperature to evaporate the refrigerant (LRT). The models used allowed to predict the coefficient performance of the equipment, temperatures in condensers and evaporators, mass flows, thermal capacity, and mechanical power. Then, graphs validation of the models was constructed with the reported COP against the calculated COP.

The range of heat pump models on the market with high heat capacities and sink temperatures has grown steadily. Over 20 heat pumps models from 13 manufacturers have been identified worldwide, which can supply at least a condensation temperature of 90 °C. In this work, three types of high-temperature heat pumps were selected, the Friotherm 50FY [8] with a capacity between 9 to 20 MW thought like centralized stations for the replacement of combined heat and power extraction (CHP). In contrast, the Hybrid heat pump [9] with a capacity between 0,8 to 2 MW and SABRO E Heat Pac HPX 704 [10] with 0,148 to 0,39 MW are configured as booster pumps. Figure 9 resumes the Condensation temperature vs. heat capacity of commercial high-temperature heat pumps modeled.

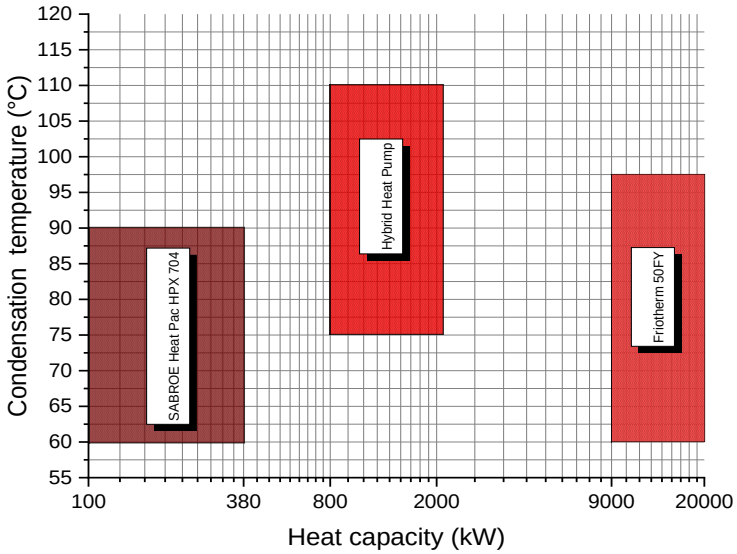

Figure 7-7: Condensation temperature vs. heat capacity of commercial high-temperature heat pumps [8] [9] [10]

The model calculates the heat flow rate at the evaporator and the electrical consumption of the compressor according to the parameters of the performance curves provided by the manufacturer. The curves are polynomial functions of the evaporating and condensing temperature with R-squared value of 0.9, as shown in equations (1), (2), (3), and (4). The schematics proposed for the HP booster in the DH system are shown in figure 7-8, the coefficients of the polynomials used in the simulation are indicated in Table 7-4, and the results indicate that direct use of energy from the DEN supply of the high-temperature stream to evaporate the refrigerant (HRT) increase in 25% the thermodynamic performance (COP) in comparison with the use of energy from the DEN return low-temperature to evaporate the refrigerant (LRT) .

$$QE = B_1 Z_1 + B_2 Z_3 + B_3 Z_1 Z_3 + B_4 {Z_1}^2 + B_5 {Z_3}^2 + B_6 \quad (1)$$

$$P = B_7 Z_1 + B_8 Z_3 + B_9 Z_1 Z_3 + B_{10} {Z_1}^2 + B_{11} {Z_3}^2 + B_{12} \quad (2)$$

$$COP = \frac{QC}{P} \quad (3)$$

$$QE = QC - P \quad (4)$$

Table 7-4: Coefficients of the polynomials of heat pumps

Industrial HTHPs available	B1/B7	B2/B8	B3/B9	B4/B10	B5/B11	B6/B12
Friotherm 50FY	-546.8/225.6	2667/-542.3	15.12/0.6226	-9.366/-5.29	20.56/4.831	97590/17774
Hybrid Heat Pump	-104.3/-41.95	208.2/58.01	-1.180/-0.16640	2.0860/0.53360	-1.8970/-0.55280	-1121/-32.33
SABROE Heat Pac HPX 704	-36.43/-13.44	11.33/5.686	-1.844/-1.023	3.024/1.418	0.3178/0.1798	153.6/44.6

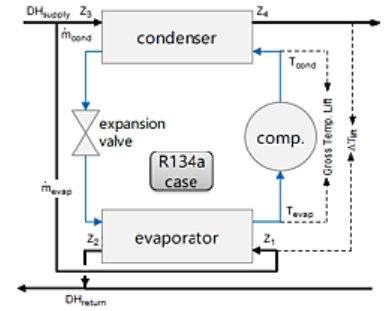

(a)

Z_1 (°C)	Z_2 (°C)	Z_3 (°C)	Z_4 (°C)	$\dot{m}_{cond}$ kg/sec	$\dot{m}_{evap}$ kg/sec	Q_c kW	Q_e kW	P_w kW	COP [-]
35	15	35	90	75.25	124.7	17342	10452	6890	2.52
40	20	40	90	53.17	68.89	11140	5773	5368	2.08
45	25	45	90	33.17	28.65	6255	2401	3854	1.62
48	30	48	90	22.47	13.34	3955	1006	2949	1.34
50	35	50	90	16.02	5.362	2685	337	2348	1.14

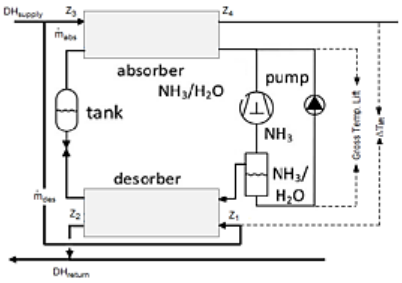

(b)

Z_1 (°C)	Z_2 (°C)	Z_3 (°C)	Z_4 (°C)	$\dot{m}_{abs}$ kg/sec	$\dot{m}_{des}$ kg/sec	Q_c kW	Q_e kW	P_w kW	COP [-]
30	15	30	90	4.391	13.07	1104	821.7	282.4	3.91
35	20	35	90	5.65	15.9	1302	999.1	302.4	4.31
40	25	40	90	6.916	18.07	1449	1136	313.1	4.63
45	30	45	90	8.21	19.62	1548	1233	314.5	4.92
50	35	50	90	9.529	20.53	1597	1290	306.7	5.21

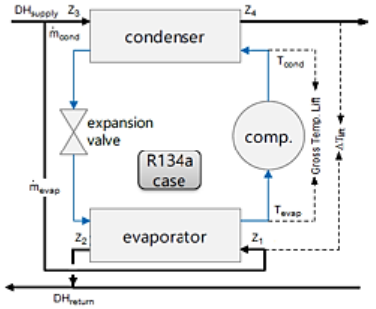

(c)

Z_1 (°C)	Z_2 (°C)	Z_3 (°C)	Z_4 (°C)	$\dot{m}_{cond}$ kg/sec	$\dot{m}_{evap}$ kg/sec	Q_c kW	Q_e kW	P_w kW	COP [-]
30	15	30	90	0.45	1.1	112	72	41.90	2.67
35	20	35	90	0.55	1.4	127	88	41.66	3.05
40	25	40	90	0.69	1.7	145	105.5	41.59	3.49
45	30	45	90	0.88	2.0	165.8	126.2	41.74	3.97
50	35	50	90	1.14	2.4	189.90	149.82	42.18	4.50

Figure 7-8: Cycle performance characteristic of simulated High-temperature heat pumps a) Friotherm 50FY; b) Hybrid heat pump, and c) Sabro E Heat Pac HPX 704.

7.5.3 **GAS TURBINE MODEL RESULTS**

First, the electrical, heating, and cooling demand for the Lachine area (Table 7-3) defines the selection criteria for the turbine to be used. Then, this power sets the fuel flow rate (syngas) necessary to operate, which in turn specifies the operating conditions of the gasification and electrolyzer unit to cover the energy (heat of combustion of fuel - HC) required to operate. Table 7-5 shows the output data obtained using the gas turbine model for the cycle simulation shown in figure 7-5.

Table 7-5: Result of variables in operation points of the analyzed cycle; PR=12[-]; HC=33 MJ/kg; Power =2,2 $MW_{electric}$

Point	$h_i[J/kg]$	$P_i[Pa]$	$s_i[J/kg-K]$	$T_i[K]$	$h_{s;i}[J/kg]$	$s_{s;i}[J/kg-K]$
1	29857	101325	5695	298.2		
2	675320	1,216E+06	5803	664.3	607505	5695
3	1,082E+06	1,216E+06	6289	1031		
4	1,459E+06	1,216E+06	6607	1353		
5	1,087E+06	325164	6672	1035	1,021E+06	6607
6	1,459E+06	325164	6985	1353		
7	1,140E+06	101325	7057	1081	1,065E+06	6985
8	741824	101325	6612	726.2		

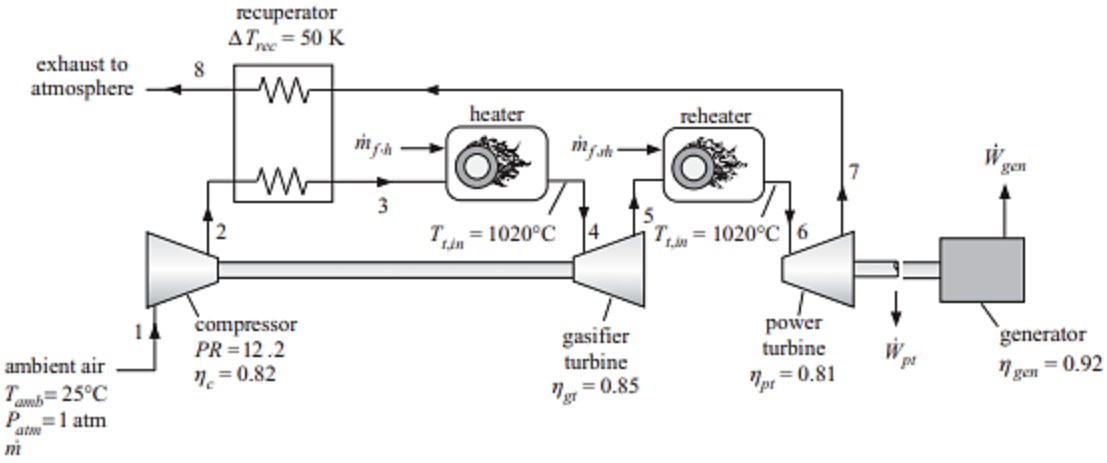

Figure 7-9: Gas turbine engine with reheat and recuperation, adapt from [11][12][13]

For a capacity of $2{,}2\ MW_e$ (extracted from table 7-3 of energy demand for the buildings in Lachine-Est area), the effect of pressure ratio (PR [-]) on the mass flow rate of fuel when we modified the heating content of the fuel (HC) is shown in figure 7-10. The mass flow consumed ($\dot{m}_{fuel}$ (kg/hr) increases when the pressure ratio increases from PR= 3-18 [-]. On the contrary, the $\dot{m}_{fuel}$ decrease when HC increases. The maximum mass flow generates at a PR 15 [-] and HC=20 MJ/kg. While a PR=3 [-] and HC=49 MJ/kg require the minimum mass flow.

Figures 7-11 show the overall efficiency as a function of pressure ratio (PR) and heat content of the fuel (HC); as can be seen, the efficiency is proportional to the increasing PR [-]. Although decreases for HC between 35-49 MJ/kg. For a fixed capacity (MW_e), the optimal integration (efficiency) increases with decreasing syngas heating value. As the heating value of the syngas decreases, a greater net system power output and efficiency are possible due to increased turbine mass flow; however, the gas turbine is more vulnerable to compressor surge, and the blade metal becomes increasingly overheated. As a result, the efficiency increased

as the syngas heating value decreased.Likewise, these models will define the properties of the syngas and natural gas used in the gas turbine to analyze the considered case study (table 7-6)

Table 7-6: Properties of the syngas and natural gas used later in the gas turbine of the considered case study

Component (mole fraction)	**Natural gas**	Air	Steam	Oxygen
$\mathbf{CH_4}(\%)$	91.33	1.1	7.6	1.2
$\mathbf{C_2H_6}(\%)$	5.36	-	-	-
$\mathbf{C_3H_8}(\%)$	2.14	-	-	-
$\mathbf{C_4H_{10}}(\%)$	0.95	-	-	-
$\mathbf{CO}\ (\%)$	-	22.56	28.2	28.75
$\mathbf{CO_2}(\%)$	-	8.053	15.9	2.04
$\mathbf{H_2}(\%)$	-	22.56	48.2	60.25
$\mathbf{H_2O}(\%)$	-	5.4	15.52	3.27
$\mathbf{N_2}(\%)$	0.22	37.41	3	2
$\mathbf{LHV}\ (\frac{\mathbf{kj}}{\mathbf{kg}})$	49303	6020	11050	24620

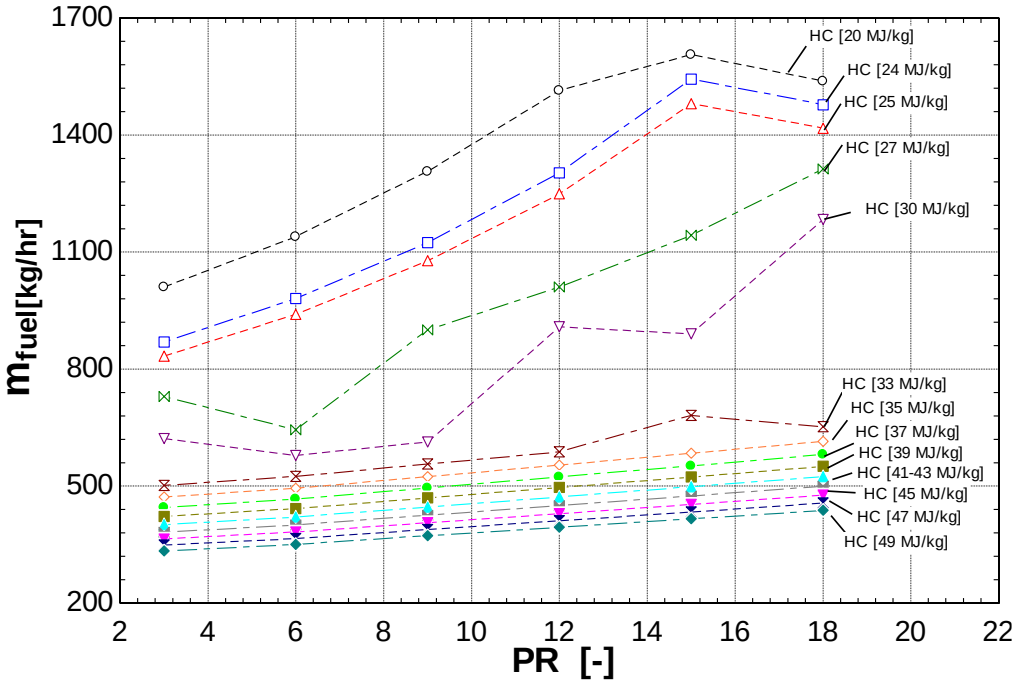

Figure 7-10: System mass flow as a function of the pressure ratio [-]. Also shown, the variation as a function of the heat content of the fuel (HC) for 2,2 MW_e of capacity.

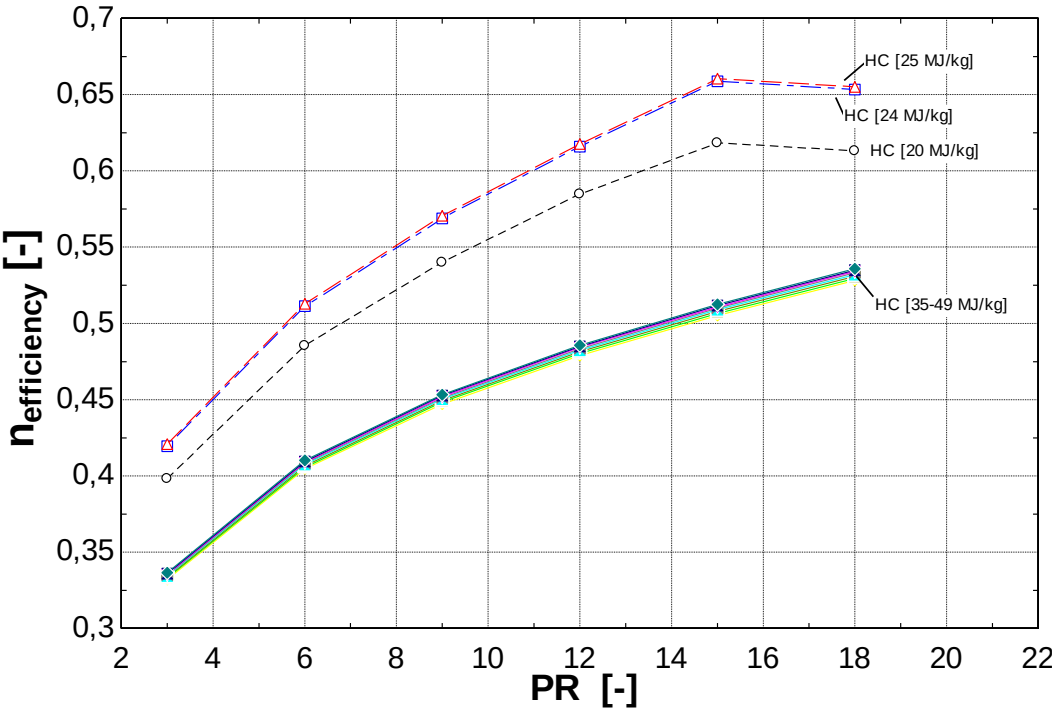

Figure 7-11: The overall efficiency of the gas turbine as a function of the lower heating value (HC) of the syngas and pressure ratio PR [-]

7.5.4 **INTEGRATION WITHIN A POLYGENERATION SYSTEM**

After the model , the gasifier, electrolyzer, and turbine models were integrated in a district heating network (figure 7-12). The biomass is fed, dried, pyrolyzed, and gasified to generate synthesis gas. A first option to valorize the residual heat is to use it to heat the oxidizing agent (air, water, oxygen) implemented in the gasification process. Also, the heat energy available in the gas is used as an energy source to supply the heat demand of the Lachine area. Finally, the gas is enriched with hydrogen to modify the heating content of fuel and fed to the turbine to generate the MW_e required to operate the refrigeration systems, electrolyzer, auxiliary heat pumps, and utility power consumption. The system was scaled up to the plant size (2-6 MW_e). The model assumptions and operation range are reported in tables 7-7 and 7-8 and figure 7-12 have been used in the scaled-up system model.

Also the integration within a polygeneration system include one (1) local heat pump with DH supply line as heat source Sink to DH supply ($\mathbf{L\_HP\_DH_s\_DH_s}$) where it is locally placed; this heat pump configuration (named heat Split HP) will be used as a booster in DH and utilizes the DH network's supply line as the heat source to evaporate the refrigerant. Likewise, the sink process stream is heated from the

supply line's temperature and the forward supply line as a sink. The temperature glide of the source corresponds to the difference between T_{supply} and T_{return}. The DH network's optimal temperature can be reached by combining this system with other heat production equipment to increase the temperature of the forward line of the DH network. Secondly, three (3) individual heat pumps are directly connected to the DH supply line as a heat source, a heat sink is connected to PH and DHW **(I_HP_DH$_s$_PH_DHW).** The direct connection involves pipelines between the heat pump unit and the district heating network. This individual heat pump configuration can be used as a DH booster to cover SH and DHW demand. It can utilize the supply line of the DH network as the source to evaporate the refrigerant. Likewise, the sink process stream is heated from the supply line's temperature, and a network of pipes connecting PH and DHW as a high-temperature sink (≥90 °C). The temperature glide of the source corresponds to the difference between T_{supply} and T_{return}. This configuration requires a DH network to operate and cover the SH demand directly. In addition, the location of this heat pump type is decentralized close to the consumer and replaces a connection substation.

Complete assessment of the whole polygeneration is essential [14]. Inputs and outputs of polygeneration are multiple [15][16]. Hence, designs and performance goals of polygeneration vary widely [14]. Due to its complex nature, the assessment procedure is not as straightforward as is the case for only power generation [17][18]. Objectives of assessment of polygeneration should be in line with the goal and scope of the energy system [14] [15][16] [17][18]. Presently, sustainability is assessed based on four indicators, i.e., technical, social, economic, and environmental [19].

In literature, different assessment procedures are reported (Thermodynamics 1st law, 2nd law; Techno-economic; Socio-economic; Environmental; and Multi-dimensional)[19]. The thermodynamic analysis is required to assess technical feasibility and possible improvements, and it is based on the 1st law and 2nd law of thermodynamics [20]. Likewise, thermodynamics establishes criteria for determining processes' efficiency, especially those where energy plays an important role. The restrictions imposed by the Second Principle (2nd law) allow us to know the different qualities of energy and raise the dilemma that when comparing the product obtained with the consumption or cost that has been necessary to get it, units of equal thermodynamic value or equivalents. Therefore, the need to define a new property, that is, the exergy, arises. It can be shown that two flows or systems are thermodynamically equivalent if and only if they have the same exergy[21].

Even so, the 1st law analysis techniques are widely used [20][22][23][24][25]. This law includes the quantity of energy but does not include the quality. One objective thermodynamic function of polygeneration design is to increase energy efficiency [26]. Plant efficiencies n_{plant} were determined using equation (5) that relates the ratio of the total energy content of hydrogen (present in the end-products). Likewise, helpful energy output (electrical-W_e, heat-Q_{heat}, and cold-Q_{cold}) to the sum of biomass's energy content and all electrical power requirements by the plant ($W_{electrolyzer} + W_{HP} + W_{comp} + W_{pumps}$).

$$\eta_{plant} = \frac{W_e + Q_{heat} + Q_{cold} + \dot{m}_{H_2} LHV_{H_2}}{\dot{m}_{biomass} LHV_{biomass} + W_{electrolyzer} + W_{HP} + W_{comp} + W_{pumps}} \quad (5)$$

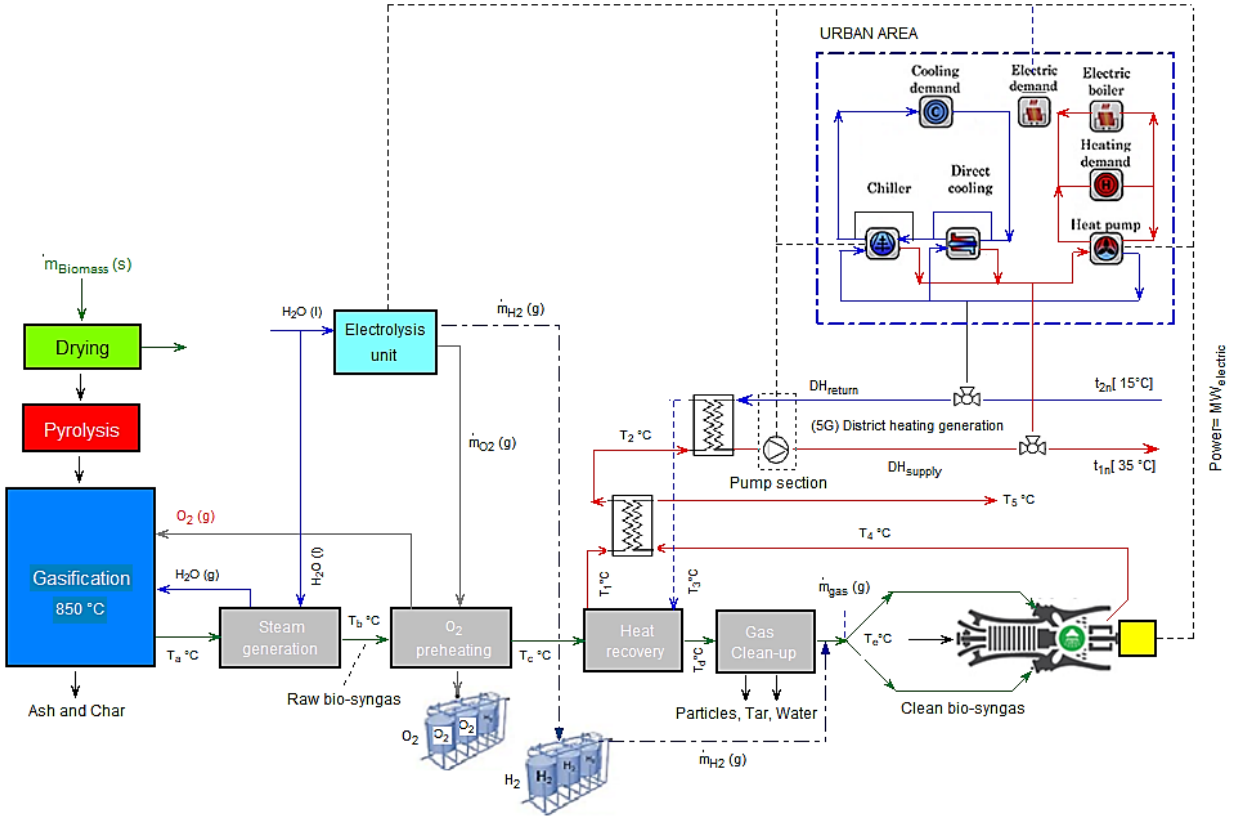

Figure 7-12: Schematic representation of the polygeneration plant concept for syngas upgrading in district energy networks of 5th generation.

The adjustment of the polygeneration system to cover the fixed demands of electricity, heat, and cooling in a typical year in the Lachine Est area was evaluated. Likewise, the ability to enrich the synthesis gas with a mixture of hydrogen produced by the electrolyzer was considered to modify the calorific value of the fuel and thus reduce the consumption of syngas and biomass fed to cover the demands set for

the Lachine Est area. The model's assumptions are summarized in table 7-8, and the results are shown in figures 7-13 to 7-15 and table 7-9.

The results include the demand for electricity, heating, and cooling for a typical year of the Lachine Est area. The operating conditions of the gas turbine are based on two design capacities of 2,2 MWe and 6 MWe, and specifically the calorific value and mass flow of the synthesis gas Once the properties of the biomass used in the gasification system are specified (table 7-8), the operating conditions of the gasifier are determined (temperature, volumetric composition of the gas, calorific value, efficiency, reaction agent used, and the mass flow of biomass) to obtain the amount of gas required by the generation system (gas turbine) to cover the demands set. Likewise, the energy balances in the gasifier are included (thermal input, preheating dry biomass, preheating of moisture, preheating of the air, preheating of steam, gas cooling, energy in char out, and heat losses). Finally, the percentage of additional hydrogen gas that must be mixed with the syngas generated by the gasification system to cover the demand for gas with the calorific power required by the generation system (gas turbine) to operate. Also, the plant efficiencies n_{plant} is calculated using equation (5). that relates the ratio of the total energy content of hydrogen (present in the end-products). Likewise, helpful energy output (electrical-W_e, heating-Q_{heat}, and cooling-Q_{cold}) to the sum of biomass's energy content and all electrical power requirements by the plant ($W_{electrolyzer} + W_{HP} + W_{comp} + W_{pumps}$).

Table 7-7: Model assumptions and operation ranges

Section	Specification	Value	Unit
Biomass feedstock (dry weight basis)	C	48	%
	O	44	%
	H	6	%
	N	0.1	%
	Initial wood moisture content	11	%
Gasifier	Type	Downdraft	[-]
	Capacity	3-10	MW_{th}
	Reactor temperature	850	°C
	Fuel feed rate	500-6000	kg/h
	Particle size	2-10	mm
	Syngas composition (Vol %)		vol %
	H_2	22-60	%
	CO	25-29	%

	CO_2	2-16	%
	CH_4	1-7	%
	N_2	2-37	%
	LHV	6-25	MJ/Nm^3
	Cold gas efficiency	80-95	%
	Pressure drops	0,15	bar
	Carbon conversion	90	%
	Gasifier heat loss	10	%
	Gasifier operation pressure	1-5	bar
	Steam preheat temperature	700	K
	Steam/biomass ratio	0,2-1,2	[-]
	Tar production	1-3	g/Nm^3
Hot cleaning	Particle removal unit temperature	700	K
	Pressure drops cyclone/filter	0,07	bar
	Pinch temperature difference	5	K
Alkaline electrolyzer	Area	3-3,6	m^2
	Current density	<0.45	A/cm^2
	Inlet temperature	300	K
	Outlet temperature	373	K
	Pressure	<30	bar
	Specific system energy consumption	4,2-4,8	kWh/Nm^3
	Capacity	4	MW
	Hydrogen purity	>99,8	%
	Cell temperature	353-373	K
Gas turbine	Pressure ratio (PR)	12	[-]
	Turbine inlet temperature	1293	K
	Stream excess ratio in post combustor	80	%
	Recuperator temperature	50	K
	Power turbine efficient	0,85	[-]
	Isentropic performance of the compressor	0,9	[-]
	generator efficient	0,92	[-]
District heating network (5G) 10,000 residents, 32 commercial establishments of various sizes, one floor of offices, and a school. One (1) local heat pump	Heating demand	$7,01x10^6$	kWh/yr
	Cooling demand	$4,38x10^6$	kWh/yr
	Electricity demand	$4,8x10^7$	kWh/yr
	Total floor area	$29x10^4$	m^2
	DH supply temperature	308	K
	DH return temperature	288	K
	Pump efficiency	0,9	[-]
	Pump motor efficiency	0,95	[-]

Hybrid heat pump (1,5 MW), and three (3) booster Sabro E Heat Pac HPX 704 (115 kW) .	Yearly average heat loss	10	%
	Yearly average permissible specific pressure drops	100	$\mathrm{Pa/m}$
	COP chiller compressor	3,8 -6,39	[-]
	Central heat pump	$2000 \leq \mathrm{kW} \leq 20000$	
	Local heat pump	$100 \leq \mathrm{kW} \leq 2000$	
	Booster heat pump	$30 \leq \mathrm{kW} \leq 100$	

For a fixed demand (cooling, heating, and electricity) of the Lachine area, two sizes of the turbine are considered. Second, the size of the turbine defines the capacity and operation of the gasification equipment. Third, the gasification system provides the syngas mass flow and can modify its performance by using different reaction agents to meet the specific demand on the turbine. Likewise, within this flexibility of operation, the electrical energy to operate the electrolyzer is supplied by the generation system coupled to the gasifier.

First, if the operation of the gasifier is with air, the system only has to cover the cooling, heating, and electricity demands of the Lachine area (2,2 MW_e). Second, if the operation changes to oxygen, the electrolyzer comes into operation; the electricity that the system requires to operate will be supplied by the same turbine that is forced to generate more electricity (6 MWe). Operating the gasifier with oxygen allows increasing the percentage of hydrogen in the synthesis gas. The hydrogen generated in the operation of the electrolyzer will serve to enrich the gas. These conditions require a greater or lesser amount of biomass to be consumed depending on the final calorific value of the gas before entering the turbine. Finally, figure 7-13 and 7-14 shows the consumption of fuel, biomass, and hydrogen on polygeneration system (2,2 MWe and 6 MWe) using the different oxidizing agents in gasification system in a low-temperature district energynetwork in Lachine-Est in Montreal, Canada. Likewise, figure 7-15 shows the Calorific value (LHV) of fuel used at the generation system (turbine) and LHV of syngas generated by the gasifier using the different oxidizing agents.

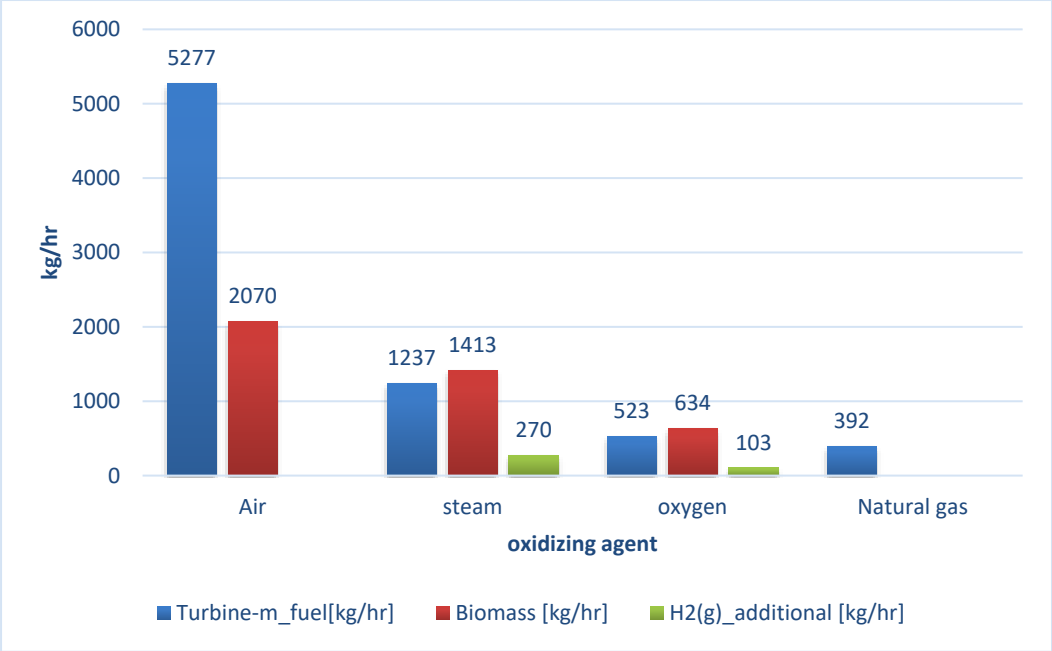

Figure 7-13: Consumption of syngas, biomass, and hydrogen oof the polygeneration system (2,2 MWe) using the different oxidizing agents in a low-temperature district energynetwork in Lachine-Est in Montreal, Canada

For a fixed demand (figure 7-6) and operation with air in the gasifier, 14392 kg/hr of syngas with a calorific value of 6.02 MJ/kg are required to operate the turbine and generate 6 MWe. To cover the gas mass flow, 5690 kg/hr of biomass with a composition of 48% C, 44% O, 6% H, 0,1% N, and 11% of moisture are required. In this operating condition, it does not require the participation of the electrolysis system to enrich the gas; therefore, this configuration represents the maximum consumption of biomass and greater storage of hydrogen.

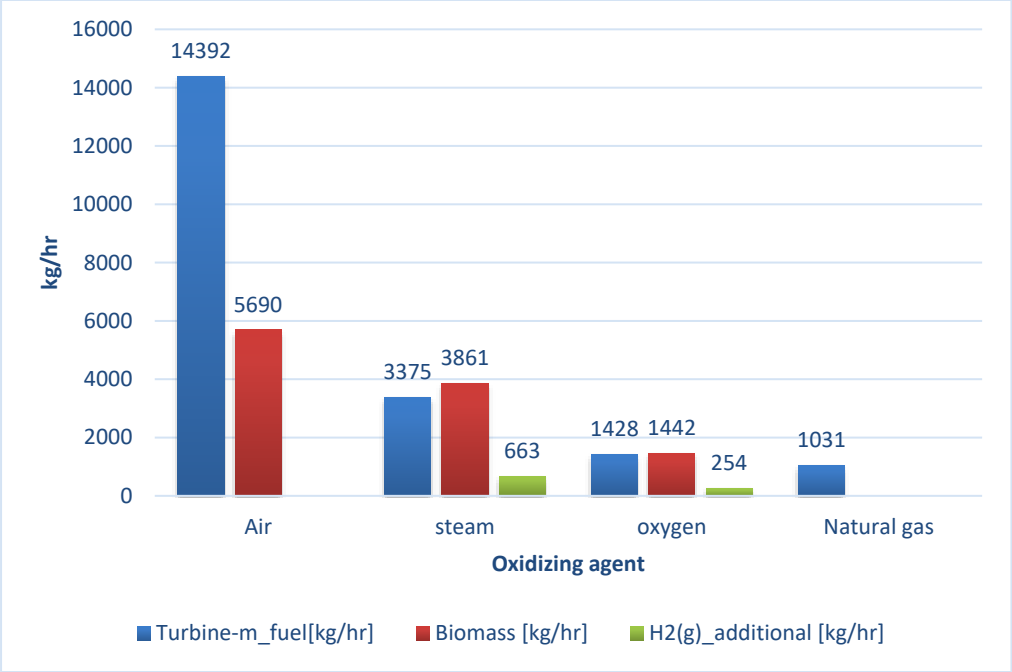

Figure 7-14: Consumption of syngas, biomass, and hydrogen on polygeneration system (6 MWe) using the different oxidizing agents in a low-temperature district energynetwork in Lachine-Est in Montreal, Canada

For a fixed demand (figure 7-6) and operation with steam in the gasifier, 3375 kg/hr of synthesis gas with a calorific value of 25,26 MJ/kg are required to operate the turbine and generate 6 MWe (2,2 MWe to cover energy demand in the Lachine area and 3,8 MWe to use the electrolyzer). To cover the gas mass flow, 3861 kg/hr of biomass with a composition of 48% C, 44% O, 6% H, 0,1% N, and 11% of moisture are required. This operating condition requires the participation of the electrolysis system to enrich the gas (oxygen is not used- it is stored). Therefore, an additional 663 kg/hr of hydrogen is required to enrich the gas and increase the heating value of syngas from 11,05 MJ/kg to 25,26 MJ/kg. This configuration represents lower biomass consumption and higher electricity consumption.

For a fixed demand (figure 7-6) and operation with oxygen in the gasifier, 1428 kg/hr of synthesis gas with a calorific value of 37,02 MJ/kg are required to operate the turbine and generate 6 MWe (2,2 MWe to cover energy demand in the Lachine area and 3,8 MWe to operate the electrolyzer). To cover the gas mass flow, 1442 kg/hr of biomass with a composition of 48% C, 44% O, 6% H, 0,1% N, and 11% of moisture are required. This operating condition requires the participation of the electrolysis system to enrich the gas (oxygen is used). Therefore, an additional 254 kg/hr of hydrogen is required to enrich the gas and increase the heating value from

24,62 MJ/kg to 37,02 MJ/kg. This configuration represents the lowest biomass consumption and the highest electrical consumption.

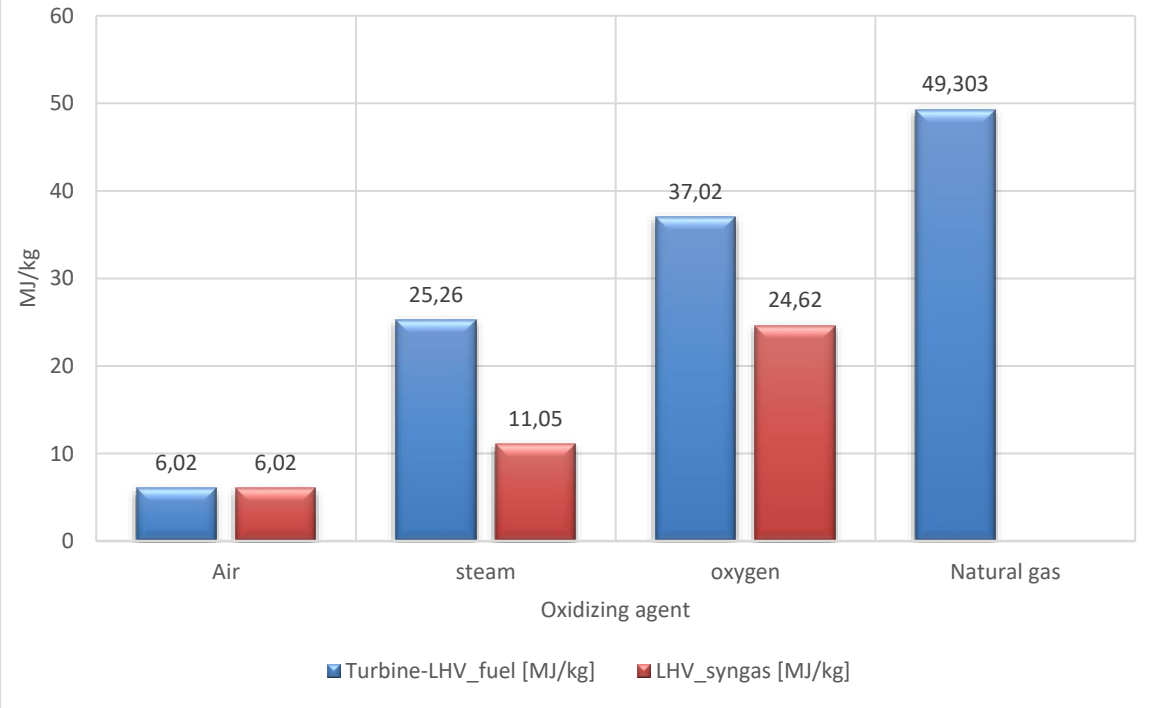

Figure 7-15: Low heating value (LHV) of fuel used in generation system (turbine) and LHV of syngas generated in gasifier using the different oxidizing agents in a low-temperature district energynetwork in Lachine-Est in Montreal, Canada

The results indicated in Table 7-9 shows that the electricity, heating, cooling, and hydrogen demand by the Lachine-Est area can be covered by the proposed plant concept. For the same electrical demand (MW_e), increasing the HC of the fuel by a factor of six (6) decreases the mass of fuel necessary to meet the demand defined for the Lachine area by a factor of ten (10). Likewise, by increasing the LHV_{gas} by a factor of four (4), the biomass fed into the gasifier is reduced by a factor of three (3) to cover the gas flow provided to the electrical generation system (turbine).

One of the ways to improve the LHV is to implement an oxidizing agent other than air in the gasification process. When gasification is carried out with air, it is unnecessary to use oxygen from the electrolyzer. Even so, the available energy could be used to generate and store hydrogen. For gasification with steam, a fraction of the hydrogen generated in the electrolyzer is used to increase the LHV, and the remainder flow rate is stored for future use. The first results indicate that when oxygen is implemented as an oxidizing agent, the electrolyzer equipment is

sized (700 kg/hr) to cover the oxygen demand required. The hydrogen generated enriches the gas, storing the remainder flow rate. For both analyzed scenarios in the Lachine area (2,2 MW_e and 6 MW_e), the lowest biomass feed rate (634 and 1413 kg/hr), the highest global efficiency (51.92 % and 88.3%), and the lowest amount of hydrogen stored (13 and 50 kg/hr) occur in gasification with steam and oxygen. Specifically, when comparing the fuel consumption in the turbine for a 6 MW_e demand, a reduction of 76,5 % of the fuel rate is presented when changing the reaction agent from air to steam. Likewise, biomass consumption is reduced by 32,14 % to cover the same demand in the Lachine Est area. On the other hand, to cover a 6 MWe demand in the gasification process with oxygen. When comparing the fuel consumption in the turbine, a reduction of 58 % is presented when changing the reaction agent from steam to oxygen. Likewise, biomass consumption is reduced by 62,6 % to cover the same demand in the Lachine Est area. Finally, to cover the same demand (6 MW_e), when comparing the fuel consumption in the turbine, a reduction of 90% is presented when changing the reaction agent from air to oxygen. Likewise, biomass consumption is reduced by 75 % to cover the same demand in the Lachine Est area.

Table 7-8: Model assumptions and operation values for polygeneration system (6 MW_e) in the Lachine area.

Section	Specification	Value	Unit
Biomass feedstock (dry weight basis)	C	48	%
	O	44	%
	H	6	%
	N	0.1	%
	Initial wood moisture content	11	%
Gasifier	Type	Downdraft	[-]
	Capacity	9	MW_{th}
	Reactor temperature	850	°C
	Fuel feed rate (biomass)	1300	kg/h
	Particle size	3-6	mm
	Syngas composition (Vol %)		vol %
	H_2	60,25	%
	CO	28,75	%
	CO_2	2,02	%
	CH_4	1,2	%
	N_2	2	%
	LHV	24,62	MJ/Nm^3
	Cold gas efficiency	94,35	%

	Pressure drops	0,15	bar
	Carbon conversion	90	%
	Gasifier heat loss	10	%
	Gasifier operation pressure	1,5	bar
	Oxygen and steam preheat temperature	700	K
	Steam/biomass ratio	-	[-]
	Tar production	1-3	g/Nm^3
Hot cleaning	Particle removal unit temperature	700	K
	Pressure drops cyclone/filter	0,07	bar
	Pinch temperature difference	5	K
Alkaline electrolyzer	Area	3-3,6	m^2
	Current density	<0,45	A/cm^2
	Inlet temperature	300	K
	Outlet temperature	373	K
	Pressure	<30	bar
	Specific system energy consumption	4,2-4,8	kWh/Nm^3
	Capacity	3	MW
	Hydrogen purity	>99,8	%
	Cell temperature	353-373	K
Gas turbine	Pressure ratio (PR)	12	[-]
	Power	5,5	MW_e
	Turbine inlet temperature	1293	K
	Stream excess ratio in post combustor	80	%
	Recuperator temperature	50	K
	Power turbine efficient	0,85	[-]
	Isentropic performance of the compressor	0,9	[-]
	Generator efficient	0,92	[-]
District heating network (5G) 10,000 residents, 32 commercial establishments of various sizes, one floor of offices, and a school. One (1) local heat pump Hybrid heat pump (1 MW), and five (5) booster Sabro E Heat Pac HPX 704 (115 kW)	Heating demand	$7{,}01x10^6$	kWh/yr
	Cooling demand	$4{,}38x10^6$	kWh/yr
	Electricity demand	$4{,}8x10^7$	kWh/yr
	Total floor area	$29x10^4$	m^2
	DH supply temperature	308	K
	DH return temperature	288	K
	Pump efficiency	0.9	[-]
	Pump motor efficiency	0.95	[-]
	Yearly average heat loss	10	%
	Yearly average permissible specific pressure drops	100	Pa/m
	COP chiller compressor	3,8 -6,39	[-]

.	Local heat pump	1000	kW
	Booster heat pump	115	kW

Table 7-9: Summary of performance of the integration of polygeneration system in low-temperature district energynetwork in Lachine-Est in Montreal, Canada.

		Air	Steam	Oxygen	Air	Steam	Oxygen
Demand (MW)	Electricity	1,1			4,8		
	Heating	0,7			0,7		
	Cooling	0,5			0,5		
Gas turbine	HC (MJ/kg)	6.02	25,26	37,02	6.02	25,26	37,02
	$\dot{m}_{fuel}$[kg/hr]	5277	1237	523	14392	3375	1428
	Power (MW_e)	2,2			6		
Fuel data	Type of fuel	**Biomass**					
	C (%)	48.2					
	H (%)	6					
	O (%)	40					
	N (%)	0,1					
	Moisture (%)	11					
	$LHV_{biomass}$ (MJ/kg)	16,14					
Operation conditions	Reactor temperature (°C)	850					
	H_2 (vol.%)	22,56	48,2	60,25	22,56	48,2	60,25
	CO (vol.%)	24,43	28,2	28,75	24,43	28,2	28,75
	CO_2 (vol.%)	8,053	15,9	2,04	8,053	15,9	2,04
	CH_4 (vol.%)	1,085	7,6	1,2	1,085	7,6	1,2
	N_2 (vol.%)	37,41	3	2	37,41	3	2
	LHV_{gas} (MJ/kg)	6,02	15,18	24,62	6,02	15,18	24,62
	Cold Gas efficiency (%)	90,09	80	94,1	90,09	84,5	94,35
	Steam/Biomass ratio	[-]	0,85	[-]	[-]	0,85	[-]
	Oxygen (%)	21	[-]	100	21	[-]	100
	Dry biomass (kg/h)	2070	1413	634	5690	3861	1442
	Indirect heating – syngas (kg/h)	633	200	100	1700	405	172
Energy Balance (MW)	Thermal Input (Biomass)	10,03	5,87	3,05	24,73	16,78	6,27
	Preheating dry biomass	0,751	0,438	0,229	1,85	1,26	0,46
	Preheating of Moisture	0,258	0,146	0,079	0,635	0,431	0,161
	Preheating of Air	0,418	0,051	0,0028	1,03	0,051	0,0048
	Preheating of Steam	0	0,91	0	0	2,693	0
	Gas cooling applied in DENN	1,8	1,6	0,309	4,43	4,69	0,618
	Energy in char out	0.165	0.096	0.05	0.406	0.275	0.102

	Turbine cooling system	0,6	0,4	0,3	0,9	0,7	0,6
	Heat loss	0,2	0,117	0,061	0,494	0,335	0,125
Electrolyzer	Hydrogen (%)	0	91	92	0	25	39
	$\dot{m}_{H_2}$ [kg/hr]	108	270	153	400	700	435
	$\dot{m}_{O_2}$l[kg/hr]	54	135	76.5	200	350	350
	$\dot{m}_{H_2}$ excess [kg/hr]	108	13	50	400	37	180
	$\mathbf{n_{plant}}$ (%)	40.15	10	62.9	51.92	15	88.3

7.6 **CONCLUSIONS**

The combination of biomass gasification and electrolyzer can be a potential solution to the emission problem and replace fossil fuels. The electrolyzer converts water into chemical products (i.e., O_2 or H_2) with the help of electricity from gasification. The gasification produces syngas and electricity from biomass, and at the same time provides heat for the heating demand. In this scheme, biomass plays a key role as a CO_2 capture system as it grows by consuming CO_2 from the air. The overall efficiency ranges from about 10 – 88 %, depending on the oxidizing agent and operating conditions used.

The syngas composition and heating value can be adjusted by changing the flow rate of O_2 as a gasifying agent. However, the flow rate of syngas strictly depends on the desired syngas properties (i.e., composition or heating value). In terms of chemical products, the production rate of CO or H_2 can be adjusted by changing the O_2 in the electrolyzer. While the proposed integration process is promising, there are several challenges to making this process efficient. We believe that the improvement in the geometry of the gasifier, the performance of the electrolyzer and heat exchanger system, and the development of the CO_2 electrolyzer will bring the proposed system to be an efficient in future.

The results indicate that when oxygen is implemented as an oxidizing agent, the electrolyzer equipment is sized (700 kg/hr) to cover the oxygen demand required. The hydrogen generated enriches the gas, storing the remainder flow rate. For both analyzed scenarios in the Lachine area (2,2 MWe and 6 MWe), the lowest biomass feed rate (634 and 1413 kg/hr), the highest global efficiency (51,92 % and 88,3 %), and the lowest amount of hydrogen stored (13 and 50 kg/hr) occur in gasification with steam and oxygen. Specifically, when comparing the fuel consumption in the turbine for a 6 MWe demand, a reduction of 76 % of the fuel rate is presented when changing the reaction agent from air to steam. Likewise, biomass consumption is reduced by 32% to cover the same demand in the Lachine

Est area. On the other hand, to cover a 6 MWe demand in the gasification process with oxygen. When comparing the fuel consumption in the turbine, a reduction of 58 % is presented when changing the reaction agent from steam to oxygen. Likewise, biomass consumption is reduced by 63 % to cover the same demand in the Lachine Est area. Finally, to cover the same demand (6 MWe), when comparing the fuel consumption in the turbine, a reduction of 90% is presented when changing the reaction agent from air to oxygen. Likewise, biomass consumption is reduced by 75 % to cover the same demand in the Lachine Est area.

7.7 **REFERENCES**

[1] "EnergyPlus." https://energyplus.net/ (accessed Sep. 22, 2021).
[2] "Building Component Library." https://bcl.nrel.gov/ (accessed Sep. 22, 2021).
[3] "| Building Energy Codes Program." https://www.energycodes.gov/ (accessed Sep. 22, 2021).
[4] O. Sarfraz, C. K. Bach, and C. K. Wilkins, "Plug load design factors," *ASHRAE J.*, vol. 60, no. 1, pp. 14–19, 2018.
[5] Y. J. Kim, S. H. Yoon, and C. S. Park, "Stochastic comparison between simplified energy calculation and dynamic simulation," *Energy Build.*, vol. 64, pp. 332–342, 2013, doi: 10.1016/j.enbuild.2013.05.026.
[6] A. S. Ancrossed D Signelković, I. Mujan, and S. Dakić, "Experimental validation of a EnergyPlus model: Application of a multi-storey naturally ventilated double skin façade," *Energy Build.*, vol. 118, pp. 27–36, 2016, doi: 10.1016/j.enbuild.2016.02.045.
[7] M. Wirtz, L. Kivilip, P. Remmen, and D. Müller, "5th Generation District Heating: A novel design approach based on mathematical optimization," *Appl. Energy*, vol. 260, no. July 2019, p. 114158, 2020, doi: 10.1016/j.apenergy.2019.114158.
[8] H. Energy, "5 Unitop ® 50FY heat pump / chiller units simultaneously generate 90 MW heat energy and 60 MW chilled water," 1990. [Online]. Available: www.friotherm.com.
[9] "Hybrid Energy – High temperature heat pumps." https://www.hybridenergy.no/ (accessed Oct. 29, 2020).
[10] A. B. Sab, "SAB heat SAB control SABROE HeatPAC HPX heat pumps SAB contr l SAB co tr l." https://www.sabroe.com/fileadmin/user_upload/Marketing/Brochures/Heat_pumps/HeatPAC_HPX_SB-4106_GB120dpi.pdf.
[11] L. Magistri, P. Costamagma, A. F. Massardo, C. Rodgers, and C. F. MacDonald, "A hybrid system based on a personal turbine (5 kW) and a solid oxide fuel cell stack: A flexible and high efficiency energy concept for the distributed power market," *J. Eng. Gas Turbines Power*, vol. 124, no. 4, pp. 850–857, 2002, doi: 10.1115/1.1473825.
[12] S. Katulić, M. Čehil, and D. R. Schneider, "Thermodynamic efficiency improvement of combined cycle power plant's bottom cycle based on organic working fluids," *Energy*, vol. 147, pp. 36–50, 2018, doi: 10.1016/j.energy.2018.01.033.
[13] F. J. Brooks, "GE Gas Turbine Performance Characteristics."
[14] K. Jana, A. Ray, M. M. Majoumerd, M. Assadi, and S. De, "Polygeneration as a future sustainable energy solution – A comprehensive review," *Appl. Energy*, vol. 202, pp. 88–111, 2017, doi: 10.1016/j.apenergy.2017.05.129.

[15] F. Calise, G. de Notaristefani di Vastogirardi, M. Dentice d'Accadia, and M. Vicidomini, "Simulation of polygeneration systems," *Energy*, vol. 163, pp. 290–337, 2018, doi: 10.1016/j.energy.2018.08.052.

[16] S. Murugan and B. Horák, "Tri and polygeneration systems-A review," *Renew. Sustain. Energy Rev.*, vol. 60, pp. 1032–1051, 2016, doi: 10.1016/j.rser.2016.01.127.

[17] A. K. Hossain, R. Thorpe, P. Vasudevan, P. K. Sen, R. E. Critoph, and P. A. Davies, "Omnigen: Providing electricity, food preparation, cold storage and pure water using a variety of local fuels," *Renew. Energy*, vol. 49, pp. 197–202, 2013, doi: 10.1016/j.renene.2012.01.032.

[18] Z. Ma, Y. Zhang, Q. Zhang, Y. Qu, J. Zhou, and H. Qin, "Design and experimental investigation of a 190 kWe biomass fixed bed gasification and polygeneration pilot plant using a double air stage downdraft approach," *Energy*, vol. 46, no. 1, pp. 140–147, 2012, doi: 10.1016/j.energy.2012.09.008.

[19] M. A. Rosen and I. Dincer, "Thermoeconomic analysis of power plants: An application to a coal fired electrical generating station," *Energy Convers. Manag.*, vol. 44, no. 17, pp. 2743–2761, 2003, doi: 10.1016/S0196-8904(03)00047-5.

[20] J. Mª, M. Villalón, and E. Q. Aragón, *Termoeconomía y optimización energética*. 2009.

[21] P. K. Govindasamy, S. Rajagopal, and A. Coronas, "Integrated polygeneration system for coastal areas," *Therm. Sci. Eng. Prog.*, vol. 20, no. September, p. 100739, 2020, doi: 10.1016/j.tsep.2020.100739.

[22] K. Jana and S. De, "Techno-economic evaluation of a polygeneration using agricultural residue - A case study for an Indian district," *Bioresour. Technol.*, vol. 181, pp. 163–173, 2015, doi: 10.1016/j.biortech.2015.01.060.

[23] Z. Hongtao, L. Zheng, N. Weidou, E. D. Larson, and R. Tingjin, "Case-study of a coal gasification-based energy supply system for China," *Energy Sustain. Dev.*, vol. 7, no. 4, pp. 63–78, 2003, doi: 10.1016/S0973-0826(08)60380-4.

[24] V. Eveloy, P. Rodgers, and S. Popli, "Trigeneration scheme for a natural gas liquids extraction plant in the Middle East," *Energy Convers. Manag.*, vol. 78, pp. 204–218, 2014, doi: 10.1016/j.enconman.2013.10.009.

[25] Y. a. Cengel and M. E. Boles, *Termodinamica - Cengel 7th*. 2011.

[26] K. Jana and S. De, "Sustainable polygeneration design and assessment through combined thermodynamic, economic and environmental analysis," *Energy*, vol. 91, pp. 540–555, 2015, doi: 10.1016/j.energy.2015.08.062.

Chapter8 CONCLUSIONS AND RECOMMENDATIONS

8.1 CONCLUSIONS

This doctoral thesis focuses on the improvement of the **Polygeneration plant based on integrating biomass gasifier and alkaline electrolyzer for district energy networks**. Specifically, the main components of the proposed system are a gasifier, electrolyzer, gas turbine, heat pumps and district heating network with the purpose to investigate a polygeneration concept that can produce or consume power and store electricity as biofuels (hydrogen).

Firstly, the present research aimed to examine power-to-heat technologies that can cost-effectively contribute to fossil fuel substitution, renewable energy integration, and decarbonization. In this context, integrating heat pumps into DEN systems provides significant environmental and performance improvements, being an innovative and profitable solution for different decarbonizing sectors. Specifically, small DH systems present the most significant potential for using HPs, significantly reducing the use of fossil fuels, while, in medium and large structures with efficient CHP production, the HP potential is lower. However, the optimal size of HPs for DH systems depends mainly on the system and its characteristics and external factors, such as electricity and fuel prices and other economic inputs. Likewise, available waste heat sources, heat requirements, and HP technology naturally affect the HP potential, being one reason why there are no single criteria for the potential of HPs in DH systems.

The DH literature identifies five generations of district heating networks. Additionally, several manufacturers can provide heat dissipation temperatures (T_{sink}) of at least 90 °C, with heating capacities varying from 20 kW to 20 MW with COP values ranging from 2,4 to 5,8, and with a temperature increase of 100 to 40 K. The experimental data of the operation of commercial heat pumps indicates that their efficiency oscillates between 40 and 60% of the maximum efficiency according to the second law of thermodynamics.

Twelve (12) possible heat pump configurations in DH networks have been identified, termed, and described. From our literature review, we could identify that eight of twelve heat pump configurations identified have been studied. Even so, four of twelve heat pump configurations have not been studied, and the authors recommend these cases be further investigated. The analysis focused on two key performance factors chosen to indicate the performance from a system perspective

and differences between system performance (COSP) and the heat pump component performance (COP). For example, three configurations $\mathbf{3-L\_HP\_DH_r\_DH_s}$,$\mathbf{4-L\_HP\_DH_s\_DH_s\_a}$, and $\mathbf{8-I\_HP\_T_s\_DH_s}$ do not perform well in a system feeding a CHP plant due to a more considerable impact on power production and higher condensation pressure in the heat pump than in the $\mathbf{10-I\_HP\_T_s\_DH_r}$ configuration. Likewise, configurations $\mathbf{10-I\_HP\_T_s\_DH_r}$ and $\mathbf{12-I\_HP\_T_s\_T_{demand}}$ have more advantages in terms of COSP at high DH network temperatures (3G).

Secondly, this study presents a numerical model capable of simulating the gasification process in a downdraft gasifier. The equilibrium model was used to predict the gas composition in the gasification of various biomass and oxidizing agents (air, air + steam, and steam). Likewise, the model is integrated into the "Engineering Equation Solver (EES)" equation solving program and includes a communication interface with the user that allows defining the inputs (mass flow rates, fuel data from the final analysis of the biomass, temperatures, ash percentage, and heat losses) to adjust the model to experimental conditions. Therefore, it is validated that the proposed equilibrium model reproduces the real operation with a 10 % of deviation and allows predicting, analyzing, and comparing gasification processes with different oxidizing agents (air, air + steam, and steam) to predict the trend in the composition of the gas, calorific value, and energy balance.

The numerical run indicated that temperature is the most crucial factor in the gasification process; low temperatures favor CO production, and high temperatures the production of H_2. Additionally, the concentration of CO_2 and CH_4 increase when temperatures decrease. These results are explained by the fact that at temperatures of 850 $^{\circ}C$, the heterogeneous water-gas reactions and the homogeneous water-gas displacement reaction (equations 20 and 21) favored the greater formation of H_2 at the expense of CO and CH_4.

Finally, when comparing the three oxidizing agents, steam showed a higher capacity to generate hydrogen than air + steam and air by 52% and 63%, respectively. Likewise, a higher capacity to generate higher LHV than air + steam and air by 44 % and 51%, respectively.

Thirdly, an N_2-free hydrogen-rich syngas yield was obtained from palm kernel shells (PKS) steam gasification in downdraft allothermal gasifier reactors. In this equipment, the temperature, biomass feeding rate, water concentration, and internal configuration of the equipment were adjusted for the correct experimental

execution. Special attention was paid to instrumentation to access information such as temperature, gas composition, and pressure throughout the equipment. On the other hand, increasing the heat exchange surface-to-volume ratio by introducing a new configuration in the reactor and integrating baffles in charge of obstructing the passage of combustion gases from the burners, in such a way that the minimum residence time of the gases is guaranteed, which allows the effective heat transfer to the biomass reduced the tar generation, appearance ash deposits, and agglomeration problems.

The gasification equipment was tested under gasification temperatures between $800 \text{ and } 950\ ℃$ and steam-biomass mass ratios between 0,2 and 1,2. The reliability of both the equipment and the operating methodology was confirmed by obtaining N_2-free syngas. Likewise, it was shown that the steady-state could be reached during the experiments in a downdraft allothermal gasifier with a maximum generation of $95,4\ Nm^3$ of fuel gas with a syngas volume fraction of $48,2\ \%\ H_2$, $28{,}2\ \%\ CO$, $15{,}9\ \%\ CO_2$, $7{,}6\ \%CH_4$ and average lower calorific value of $11{,}5\ MJ/Nm^3$.

The experimental run indicated that temperature is the most crucial factor in the gasification process; low temperatures favor CO production, and high temperatures the production of H_2. Additionally, the concentration of CO_2 and CH_4 increase when temperatures decrease. These results are explained by the fact that at temperatures of 850 ℃, the heterogeneous water-gas reactions and the homogeneous water-gas displacement reaction (equations 6 and 7) favored the greater formation of H_2 at the expense of CO and CH_4.

In fourth place, this thesis discusses the performance of an alkaline electrolysis cell for the application of remote area hydrogen using photovoltaic panels. Maximum efficiencies of 31% were achieved for the alkaline electrolysis cell and 4,6 % for the entire system including a 360 W solar panel.

The distribution of temperatures on the electrodes was determined, identifying the interaction between the electrical and thermal phenomena present in the anode and cathode. From the analysis of the data, it became evident that the Joule-Thomson effect dominates. This explains the existence of temperature gradients on the electrode surface and areas of higher activity for oxidation and reduction reactions in metals such as stainless steel with measured temperature differences in the anode of ΔT = 209 ° C and ΔT = -139 ° C. Temperature differences in the cathode of ΔT = 125 ° C and ΔT = -214 ° C were measured.

The gas bubble formation was analyzed, and it could be shown that in nucleation the generated vapor bubbles are trapped and accumulated on the surface of the electrode to form a supersaturation layer with dissolved gas molecules due to a high current density and surface roughness on electrodes. These conditions generated temperature gradients and specific areas on the surface of the electrodes where oxidation-reduction reactions are favored and therefore, a greater generation of bubbles take place. The growth and departure of the bubble depending on the balance of forces in the area triphasic contact between the electrolyte, gas bubble, and the electrode surface influenced by the high current density and temperature gradients. These conditions described and explained by the Joule-Thomson effect generate higher gas formation, premature depart of bubbles from the bottom of the electrodes and greater natural convection or micro concentration of the electrolyte. These results are useful to improve the efficiency of alkaline electrolysis cells by managing and modifying temperature profiles.

Finally, the combination of biomass gasification and electrolyzer can be a potential solution to the emission problem and replace fossil fuels. The electrolyzer converts water into chemical products (i.e., O_2 or H_2) with the help of electricity from gasification. The gasification produces syngas and electricity from biomass, and at the same time provides heat for the heating demand. In this scheme, biomass plays a key role as a CO_2 capture system as it grows by consuming CO_2 from the air. The overall efficiency ranges from about 10 – 88 %, depending on the oxidizing agent and operating conditions used.

The syngas composition and heating value can be adjusted by changing the flow rate of O_2 as a gasifying agent. However, the flow rate of syngas strictly depends on the desired syngas properties (i.e., composition or heating value). In terms of chemical products, the production rate of CO or H_2 can be adjusted by changing the O_2 in the electrolyzer. While the proposed integration process is promising, there are several challenges to making this process efficient. We believe that the improvement in the geometry of the gasifier, the performance of the electrolyzer and heat exchanger system, and the development of the CO_2 electrolyzer will bring the proposed system to be an efficient in future.

The results indicate that when oxygen is implemented as an oxidizing agent, the electrolyzer equipment is sized (700 kg/hr) to cover the oxygen demand required. The hydrogen generated enriches the gas, storing the remainder flow rate. For both analyzed scenarios in the Lachine area (2,2 MWe and 6 MWe), the lowest biomass feed rate (634 and 1413 kg/hr), the highest global efficiency (51,92 % and 88,3

%), and the lowest amount of hydrogen stored (13 and 50 kg/hr) occur in gasification with steam and oxygen. Specifically, when comparing the fuel consumption in the turbine for a 6 MWe demand, a reduction of 76 % of the fuel rate is presented when changing the reaction agent from air to steam. Likewise, biomass consumption is reduced by 32% to cover the same demand in the Lachine Est area. On the other hand, to cover a 6 MWe demand in the gasification process with oxygen. When comparing the fuel consumption in the turbine, a reduction of 58 % is presented when changing the reaction agent from steam to oxygen. Likewise, biomass consumption is reduced by 63 % to cover the same demand in the Lachine Est area. Finally, to cover the same demand (6 MWe), when comparing the fuel consumption in the turbine, a reduction of 90% is presented when changing the reaction agent from air to oxygen. Likewise, biomass consumption is reduced by 75 % to cover the same demand in the Lachine Est area.

8.2 **RECOMMENDATIONS**

Based on the result obtained in this work a number of possible research line are suggested:

- Further work based on classification made in chapter 2 will address the effect of district grid configuration, the difference between high-temperature supply lines and low-temperature returns lines on the thermal performance of a district heating system that integrates commercial high-temperature heat pumps using the twelve configurations identified.

- Expand the thermodynamic model developed in chapter 3 for the gasification of municipal solid waste and improve the prediction when using oxygen and hydrogen as an oxidizing agent.

- The gas outlet ducts must be modified for a larger diameter to avoid plugging and achieve a longer operating time in the gasifier. A suction blower with a higher capacity (> 221 lpm) should be selected to cover the high gas production rates in the fixed bed gasifier. A better cooling system must be implemented in the endless screw to avoid thermal decomposition due to high temperatures of the stored biomass, which causes jamming in the screw. A more significant number of experiments must be carried out to evaluate the influence of temperature and the reaction agent on the final composition of the gas.

- Propose geometric and thermal optimization in electrodes using the conditions described and explained by the Joule-Thomson effect to generate higher gas formation, premature depart of bubbles from the bottom of the electrodes, and greater natural convection or micro concentration of the electrolyte. These results are useful to improve the efficiency of alkaline electrolysis cells by managing and modifying temperature profiles.

- An exhaustive thermo-economic and exergy study considering several integration modes. This evaluation would be interesting as it could lead to reduced costs. Furthermore, an optimization of the combined process (Torrefaction, gasification, and electrolyzer) would potentially improve the whole process and hence the final cost for liquid fuels production. The integration of energy balances and detailed simulation should be explored in this domain.

A. APPENDIX

Research articles

- J.Barco-Burgos., J.Carles-Bruno., U.Eickera., A.L.Saldana-Roblesc., V.Alcántar-Camarena "Hydrogen-rich syngas production from palm kernel shells (PKS) biomass on a downdraft allothermal gasifier using steam as a gasifying agent**", Energy Conversion and Management,** https://doi.org/10.1016/j.enconman.2021.114592.
- J.Barco-Burgos., J.Carles-Bruno., U.Eickera., A.L.Saldana-Roblesc., V.Alcántar-Camarena "Review on the integration of high-temperature heat pumps in district energynetworks", **Energy,** https://doi.org/10.1016/j.energy.2021.122378
- J.Barco-Burgos., U.Eickera., Saldana-Robles,N.,A.L.Saldana-Roblesc., V.Alcántar-Camarena "Thermal characterization of an alkaline electrolysis cell for hydrogen production at atmospheric pressure", **Fuel**, https://doi.org/10.1016/j.fuel.2020.117910

Scientific events

Simposio internacional de ingeniería agrícola Tipo de evento: Simposio Ámbito: Internacional Realizado el: 2021-11-09 00:00:00.0, 2021-11-11 00:00:00.0 en Irapuato - Sede Copal del Campus

Associated products

- Nombre del producto: Diseño, Biorrefinerías y poligeneración Tipo de producto: Producción técnica - Presentación de trabajo - Ponencia

Associated institutions

- Nombre de la institución: Universidad de Guanajuato Tipo de producto: Patrocinadora

Participants

- Nombre: JIMMY BARCO BURGOS Rol en el evento: Ponente

D-FEST Tipo de evento: Simposio Ámbito: Internacional Realizado el: 2021-07-07 00:00:00.0, 2021-07-09 00:00:00.0 en Irapuato - Universidad Politécnica Bicentenario

Associated products

- Nombre del producto: Syngas and hydrogen for power generation systems Tipo de producto: Producción técnica - Presentación de trabajo - Ponencia

Associated institutions

- Nombre de la institución: UNIVERSIDAD POLITÉCNICA DEL BICENTENARIO Tipo de producto: Patrocinadora

Participants

- Nombre: JIMMY BARCO BURGOS Rol en el evento: Ponente

10 th INTERNATIONAL SEMINAR ON THERMODYNAMIC ENGINEERING OF FLUIDS Tipo de evento: Seminario Ámbito: Internacional Realizado el:2021-07-22 00:00:00.0, 2021-07-23 00:00:00.0 en Tarragona - Universitat Rovira i Virgili

Associated products

- Nombre del producto: Hydrogen-rich syngas production from biomass/MSW and their integration in energy systems Tipo de producto: Producción técnica - Presentación de trabajo - Ponencia

Associated institutions

- Nombre de la institución: Universitat Rovira i Virgili (URV) Tipo de producto:Patrocinadora

Participants

- Nombre: JIMMY BARCO BURGOS Rol en el evento: Ponente

Great success for the clean hydrogen networking event between Canada, Switzerland, and Wallonia! Tipo de evento: Taller Ámbito: Internacional Realizado el: 2021-09-29 00:00:00.0, 2021-09-29 00:00:00.0 en Montreal - https://wallonia.be/en/news/great-success-clean-hydrogen-networking-event-between-canada-switzerland-and-wallonia

Associated products

- Nombre del producto:Clean hydrogen networking event between Canada, Switzerland and Wallonia Tipo de producto:Producción técnica - Presentación de trabajo - Ponencia

Associated institutions

- Nombre de la institución: Concordia University Tipo de producto: Gestionadora

Participants

- Nombre: JIMMY BARCO BURGOS Rol en el evento: Ponente, Traductor simultaneo

9th International Seminar in Thermodynamic Engineering of Fluids Tipo de evento: Seminario Ámbito: Internacional Realizado el:2019-07-25 00:00:00.0, 2019-07-26 00:00:00.0 en Tarragona - Avinguda Països Catalans, 26, 43007 Tarragona

Associated products

- Nombre del producto: Integration of commercial high-temperature heat pumps in district heating networks Tipo de producto:Producción técnica - Presentación de trabajo - Seminario

Associated institutions

- Nombre de la institución: Universitat Rovira i Virgili Tipo de producto:Patrocinadora

Participants

- Nombre: JIMMY BARCO BURGOS Rol en el evento: Ponente

7° Simposio Nacional y 1er Internacional de Ingeniería Química y Bioquímica Aplicada, SNIQBA 2018 Tipo de evento: Simposio Ámbito: Internacional Realizado el: 2018-09-12 00:00:00.0, 2018-09-14 00:00:00.0 en Irapuato - Universidad de Guanajuato

Associated products

- Nombre del producto: Determinación de Rendimientos de alquitrán, agua, gas y carbonizado de residuos forestales colombianos y su potencial para la Biorremediación de suelos Tipo de producto: Producción técnica - Presentación de trabajo - Ponencia

Associated institutions

- Nombre de la institución:Universidad De Guanajuato Tipo de producto:Patrocinadora

Participants Nombre: JIMMY BARCO BURGOS Rol en el evento: Ponente magistral

UNIVERSITAT
ROVIRA i VIRGILI